



저작자표시-비영리-변경금지 2.0 대한민국

이용자는 아래의 조건을 따르는 경우에 한하여 자유롭게

- 이 저작물을 복제, 배포, 전송, 전시, 공연 및 방송할 수 있습니다.

다음과 같은 조건을 따라야 합니다:



저작자표시. 귀하는 원저작자를 표시하여야 합니다.



비영리. 귀하는 이 저작물을 영리 목적으로 이용할 수 없습니다.



변경금지. 귀하는 이 저작물을 개작, 변형 또는 가공할 수 없습니다.

- 귀하는, 이 저작물의 재이용이나 배포의 경우, 이 저작물에 적용된 이용허락조건을 명확하게 나타내어야 합니다.
- 저작권자로부터 별도의 허가를 받으면 이러한 조건들은 적용되지 않습니다.

저작권법에 따른 이용자의 권리는 위의 내용에 의하여 영향을 받지 않습니다.

이것은 [이용허락규약\(Legal Code\)](#)을 이해하기 쉽게 요약한 것입니다.

[Disclaimer](#)





A THESIS  
FOR THE DEGREE OF DOCTOR OF PHILOSOPHY

**A Study on the Synthesis and Electrochemical  
Properties of Nanostructured Materials towards  
High Energy Density Hybrid Supercapacitors**

Ganesh Kumar Veerasubramani

Department of Mechatronics Engineering

GRADUATE SCHOOL

JEJU NATIONAL UNIVERSITY

February – 2017



# A Study on the Synthesis and Electrochemical Properties of Nanostructured Materials towards High Energy Density Hybrid Supercapacitors

**Ganesh Kumar Veerasubramani**

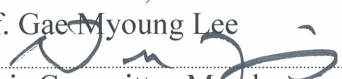
(Supervised by Professor Sang Jae Kim)

A thesis submitted in partial fulfillment of the requirement for the degree of

Doctor of Philosophy

2016. 12

The thesis has been examined and approved.

 Thesis Director, Prof. Gaemyoung Lee	Professor, Department of Electrical Engineering, College of Engineering, Jeju National University
 Thesis Committee Member, Prof. Nam-Jin Kim	Professor, Department of Energy Engineering, College of Engineering, Jeju National University
 Thesis Committee Member, Prof. Hye-Won Seo	Associate Professor, Department of Physics, College of Natural Science, Jeju National University
Thesis Committee Member Dr. Ji-Yong Eom	Senior Researcher, Clean & Energy Materials R&D Center, Korea Automotive Technology Institute
 Thesis Committee Member, Prof. Sang-Jae Kim	Professor, Department of Mechatronics Engineering, College of Engineering, Jeju National University

December, 2016

**Department of Mechatronics Engineering**

**GRADUATE SCHOOL**

**JEJU NATIONAL UNIVERSITY**

**REPUBLIC KOREA**





**Dedicated to My  
Beloved Family,  
All My Teachers &  
Friends**



## Acknowledgement

காலத்தி னாற்செய்த நன்றி சிறிதெனினும்

ஞாலத்தின் மாணப் பெரிது

A timely benefit, -though thing of little worth,

The gift itself, -in excellence transcends the earth

----- **Thiruvalluvar**

It is my great pleasure to thank so many people who have made this thesis possible. I sincerely acknowledge all the people who helped and supported me during my doctoral course.

Foremost, I express my sincere gratitude to my research supervisor, **Prof. Sang Jae Kim** for making it possible for me to realize my hopes and dreams of my research career. I am also grateful to him for guiding me to gain some expertise in the exciting field of nanomaterials research. With a deep sense of gratitude, I would like to thank for his guidance, joviality, support, encouragement and suggestions. During some of my initial critical times in the research, he is the real guardian for me to overcome.

I extend my sincere thanks to thesis committee members, Prof. Ji-Yong Eom, Prof. Nam-Jin Kim, Prof. Hye-Won Seo and Prof. Lee Gae Myuong for their excellent suggestions and support to finish my thesis. I would like to thank Prof. Young Sun Mok for his constant support for collaboration work. I also thank Prof. K. Natarajan for his constant support and encouragement.

I would like to express my sincere thanks to my cousin Dr. Lakshminarayanan Raghupathy for his encouragement and motivation throughout my research career. I also would like to thank Dr. Malligarjunan, Dr. T. Esakkidurai, Mrs. Hemalatha, Dr. P. Subbaraj, Dr. S. Kumar, and Dr. M. Ganapathi for their excellent support and encouragement since my Bachelor degree in Chemistry.



Staying away from home country is always challenging. My immense sense of gratitude to my friend Mr. Sudhakaran MSP and his family for their constant help, advice, care and encouragement in research as well as in life.

Without my lab mates, I couldn't able to finish this degree. I sincerely thank Dr. Karthikeyan Krishnamoorthy, Dr. Ananthakumar Ramadoss, Dr. Kaliannan Thiyagarajan, and Dr. Saravanakumar Balasubramaniam for their valuable support. I also thank them for their continuous encouragement to my life even at outside lab during my research carrier. I am very much grateful to my friends and colleagues Mr. Nagamalleswara Rao Alluri, Mr. Arunkumar Chandrasekhar, Ms. Sophia Selvarajan, Mr. Parthiban Pazhamalai, Ms. Yuvasree Purusothaman, Mr. Vivek Venkateswaran, Ms. Kausalya Ganesan, Mr. Surjit Sahoo, Mr. Nitthin Ananth, Mrs. Saipriya, Mr. Eui-Youg Hong, Ms. Shin So Yoon, Mr. Kim Taehyun, Mr. Ko Eunhyung, Ms. Park Minhee and Mr. Seong Mingeon for their timely help and support. I thank all of them for useful discussion of our work and lab presentations, and the fun we have together after work inside the campus, especially at coffee shop.

I am glad to have friends in Jeju who always given good environment in the campus. I would like to thank Dr. Navaneethan, Dr. Radhakrishnan and Dr. Gandhi for their fun filled moment and constant support during my initial days. I would like to thank Dr. Anilkumar, Dr. Dharaneedharan, Dr. Antony Ananth, Dr. Sridhar, Dr. Umasuthan, Dr. Sodhi, Dr. Raj Mogre, Mr. Srikanth, Mr. Sravan Kumar, Mr. Sakthivel, Mr. Rajveer, Mr. Nilojan, and Mr. Kugan for giving me so many wonderful memories to cherish during my stay in Jeju.

I extend my sincere thanks to Dr. S.T. Senthilkumar for his help, guidance, and encouragement to complete my thesis successfully. I would like to thank Mr. Goli Nagaraju for his valuable support, and discussion to complete this thesis. I also thank Dr. Parthiban Ramasamy, Dr. B. Senthilkumar, Dr. K. Anand and Mr. Vijayaraj for their support and fruitful discussion during my research career.



I would like to thank the following Jeju friends, who made homely environment during my stay in Korea “Dr. Trinh, Mr. Suresh, Mr. Moker, Mr. Adikari, Dr. Kalpa, Dr. Kamran, Dr. Zubair, Dr. Adanan, Dr. Murtaza, Dr. Safdar, Dr. Farrukh, Dr. Razhid, Dr. Sohail, Dr. Junaid, Dr. Zahid, Mr. Siddique, Mr. Memoon, Dr. Shahid, Mr. Zubair, Dr. Waqar, Mr. Gul, Mr. Harsad, Mr. Muqet, Mr. Lakmal, Mr. Anushka, Mr. Sachith and Mr. Rahman”. My special thanks to Mr. Viet for his sacrifice as my room buddy. I also thank all the JISO members who have been very co-operative and supporting during my stay in Jeju. I am very much thankful to Research Instrument Center at JNU for providing the instrumental facilities during my study.

I sincerely thank my dearest friends Mr. Kannan, Mr. Ravikumar, Mr. Ravisankar, Mr. Saravanakumar, Mr. Mathiarul, Mr. Dhanasekar, Mr. Mahendran, Mr. Mariyappan, Mr. JP, Mrs. Vaidhegi, Mr. Muthusamy, Mr. Raghu, Mr. Balamurugan, Mr. Saravana, Mr. Karpagaraj and Mr. Sathish, for their generous love and support.

Last but certainly not least, I would like to express my deepest gratitude to my parents (**Mr. M. Veerasubramani and Mrs. V. Saraswathi**), my dear brother Mr. V. Muthu Kumar and family, my dear sister Mrs. Malathi and family, my bro Mr. R. Thulasiraman, and my love Ms. Karthigaiselvi for their tolerance, cheering, compassion and cherish support. My thanks are bountiful for their wholehearted love and care.

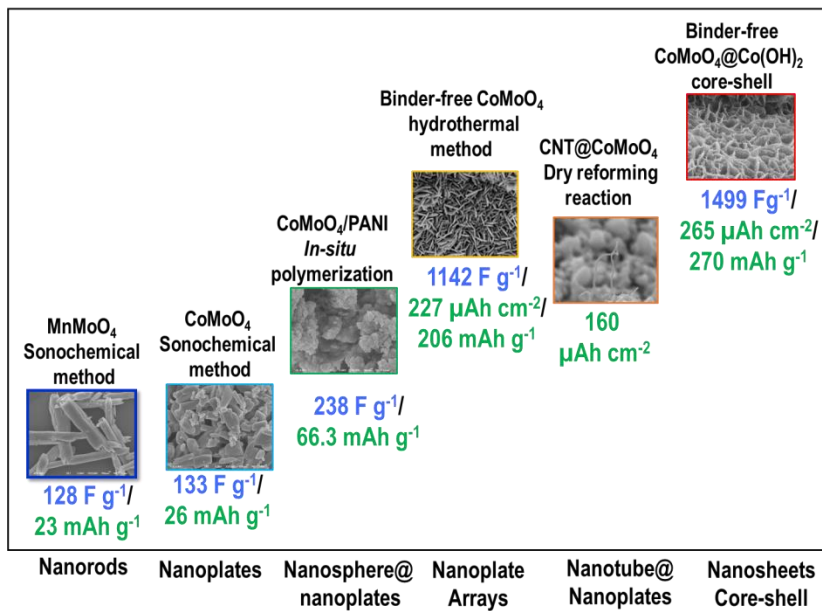
***Ganesh Kumar Veerasubramani***



# Thesis Overview

Specific capacitance

Specific capacity



## Types of Morphology



## Contents

<b>Contents</b>	i
<b>Nomenclature</b>	vii
<b>List of Tables</b>	ix
<b>List of Figures</b>	x
<b>Abstract – Hangul</b>	xxiv
<b>Abstract</b>	xxviii

### CHAPTER -1

#### Introduction

1.1. Background	1
1.2. Importance of electrochemical energy storage devices	2
1.3. Principle of electrochemical capacitors	4
1.3.1. Electrical double layer capacitor (EDLC)	4
1.3.1.1. Materials for EDLCs	7
1.3.2. Pseudocapacitors	9
1.3.2.1. Materials for pseudocapacitors	12
1.3.3. Hybrid supercapacitors	13
1.3.3.1. Materials for hybrid capacitors	15
1.4. Scope of this present work	19
1.5. Structure of this thesis	22
1.6. References	24

### CHAPTER -2

#### Materials and methods

2.1.	Chemicals	32
2.2.	Synthesis procedure	35
	2.2.1. Sonochemical method	35
	2.2.2. <i>In-situ</i> polymerization	35
	2.2.3. Hydrothermal method	36
	2.2.4. Dry reforming reaction	37
	2.2.5. Electrochemical deposition	37
	2.2.6. Hummer's method	38
2.3.	Materials characterization	
	2.3.1. X-ray diffraction	39
	2.3.2. Raman spectroscopy	39
	2.3.3. Fourier transform infrared spectrometer	40
	2.3.4. Field-emission scanning electron microscopy	40
	2.3.5. High-resolution transmission electron microscopy	40
	2.3.6. Energy dispersive X-ray spectroscopy	40
	2.3.7. X-ray photoelectron microscopy	41
	2.3.8. Brunauer Emmett and Teller Surface area analyzer	41
2.4.	Electrode fabrication	
	2.4.1. Single electrode	42
	2.4.2. Hybrid device	43
2.5.	Electrochemical characterization	
	2.5.1. Cyclic voltammetry	45
	2.5.2. Galvanostatic charge discharge	45
	2.5.3. Electrochemical impedance spectroscopy	46
	2.5.4. Calculation of electrochemical parameters	47
2.6.	References	49

## CHAPTER -3

### Transition metal molybdates $M\text{MoO}_4$ ( $M = \text{Co}, \text{Mn}$ ) and their electrochemical properties for supercapacitors

3.1. Synthesis and electrochemical performances of $\text{CoMoO}_4$ nanostructures	
3.1.1. Introduction	53
3.1.2. Experimental methods	56
3.1.2.1. Preparation of $\text{CoMoO}_4$ by sonochemical method	56
3.1.2.2. Preparation of $\text{CoMoO}_4$ electrode	56
3.1.3. Results and discussion	57
3.1.3.1. Structural characterization	57
3.1.3.2. Morphological analysis	60
3.1.3.3. Electrochemical characterization	62
3.1.4. Conclusion	67
3.1.5. References	68
3.2. Synthesis and electrochemical performances of $\text{MnMoO}_4$ nanostructures	
3.2.1. Introduction	73
3.2.2. Experimental methods	74
3.2.2.1. Preparation of $\text{MnMoO}_4$ by sonochemical method	74
3.2.2.2. Preparation of $\text{MnMoO}_4$ electrode	74
3.2.3. Results and discussion	75
3.2.3.1. Structural characterization	75
3.2.3.2. Morphological analysis	79
3.2.3.3. Electrochemical characterization	81
3.2.4. Conclusion	84
3.2.5. References	86
3.3. Summary	89

## CHAPTER -4

### Synthesis of hybrid nanostructure with conducting polymer with CoMoO<sub>4</sub> and fabrication of CoMoO<sub>4</sub>/rGO hybrid supercapacitors

4.1.	Synthesis and electrochemical performances of CoMoO <sub>4</sub> /PANI nanocomposite	
4.1.1.	Introduction	91
4.1.2.	Experimental methods	92
4.1.2.1.	Preparation of CoMoO <sub>4</sub> /PANI by <i>in-situ</i> polymerization	92
4.1.2.2.	Preparation of CoMoO <sub>4</sub> /PANI electrode	93
4.1.3.	Results and discussion	94
4.1.3.1.	Structural characterization	94
4.1.3.2.	Morphological analysis	97
4.1.3.3.	Electrochemical characterization	98
4.1.4.	Conclusion	103
4.1.5.	References	103
4.2.	Fabrication of CoMoO <sub>4</sub> /reduced graphene oxide hybrid supercapacitors	
4.2.1.	Introduction	107
4.2.2.	Experimental methods	109
4.2.2.1.	Preparation of rGO nanosheets	109
4.2.2.2.	Preparation of CoMoO <sub>4</sub> nanostructures	110
4.2.2.3.	Preparation of CoMoO <sub>4</sub> and rGO electrodes	110
4.2.3.	Results and discussion	111
4.2.3.1.	Structural characterization	111
4.2.3.2.	Electrochemical characterization	116
4.2.4.	Conclusion	123
4.2.5.	References	124
4.3.	Summary	128

## CHAPTER - 5

### **Improved electrochemical properties of CoMoO<sub>4</sub> by binder-less method and redox additive electrolyte as positive electrode for hybrid supercapacitor**

5.1.	Introduction	130
5.2.	Experimental methods	134
5.2.1.	Preparation of CoMoO <sub>4</sub> by hydrothermal method	134
5.2.2.	Electrode and electrolyte preparation	134
5.2.3.	Fabrication of hybrid supercapacitor	135
5.3.	Results and discussion	136
5.3.1.	Structural characterization	136
5.3.2.	Morphological analysis	139
5.3.3.	Electrochemical characterization	140
5.4.	Conclusion	154
5.5.	References	154
5.6.	Summary	159

## CHAPTER - 6

### **Deposition of CNT on CoMoO<sub>4</sub> by sustainable method and its electrochemical performance as positive electrode for hybrid supercapacitor**

6.1.	Introduction	161
6.2.	Experimental methods	164
6.2.1.	Preparation of CoMoO <sub>4</sub> /Ni foam catalyst	164
6.2.2.	Preparation of CNT on CoMoO <sub>4</sub> /Ni foam by DRR	165
6.2.3.	Fabrication of hybrid supercapacitor	166
6.3.	Results and discussion	166
6.3.1.	Structural characterization before DRR	166

6.3.2.	DRR of propane	169
6.3.3.	Structural characterization after DRR	172
6.3.4.	Electrochemical characterization	179
6.4.	Conclusion	191
6.5.	References	192
6.6.	Summary	198

## CHAPTER - 7

### **Preparation of CoMoO<sub>4</sub>@Co(OH)<sub>2</sub> core-shell structure on conductive textile as positive electrode for hybrid supercapacitor**

7.1.	Introduction	199
7.2.	Experimental methods	203
7.2.1.	Preparation of CoMoO <sub>4</sub> shell @ Co(OH) <sub>2</sub> core-shell on conductive textile by electrochemical deposition technique	203
7.2.2.	Preparation of activated carbon via lab-waste tissue paper	204
7.2.3.	Fabrication of pouch-type flexible hybrid supercapacitor	205
7.3.	Results and discussion	205
7.3.1.	Structural characterization of CoMoO <sub>4</sub> @Co(OH) <sub>2</sub> core-shell	205
7.3.2.	Electrochemical characterization of CoMoO <sub>4</sub> @Co(OH) <sub>2</sub> core – shell	219
7.3.3.	Structural characterization of porous carbon	221
7.3.4.	Electrochemical characterization of porous carbon	224
7.3.5.	Electrochemical characterization of hybrid supercapacitor	225
7.4.	Conclusion	232
7.5.	References	233
7.6.	Summary	239

## CHAPTER - 8

### Summary and suggestions for the future work

8.1.	Summary	240
8.2.	Suggestions for the future work	245
<b>APPENDIX A: List of Publications</b>		246
<b>APPENDIX B: List of Conferences</b>		249

## Nomenclature

AC	Activated carbon
BET	Brunauer-Emmet-Teller
CV	Cyclic voltammetry
CNT	Carbon nanotube
CT	Conductive textile
DI	De-ionized
DRR	Dry reforming reaction
ECD	Electrochemical deposition
ECs	Electrochemical capacitors
EDLC	Electrochemical double layer capacitor
EES	Energy storage systems
EDS	Energy dispersive X-ray Spectroscopy
EIS	Electrochemical Impedance spectroscopy
ESR	Equivalent series resistance
FE-SEM	Field-emission scanning electron microscopy
FT-IR	Fourier transform-infrared
GC	Gas chromatography
GCD	Galvanostatic charge discharge
GO	Graphene oxide
HK	Horvath-Kawazae

HT	Hydrothermal
HR-TEM	High-resolution transmission electron microscopy
HSCs	Hybrid supercapacitors
JCPDS	Joint committee on powder diffraction standard
LEDs	Light emitting diodes
LPG	Liquid petroleum gas
PANI	Polyaniline
PC	Porous carbon
RGO	Reduced graphene oxide
SAED	Selected area electron diffraction
SCs	Supercapacitors
SCE	Saturated calomel electrode
SEM	Scanning electron microscope
SNG	Syngas
SS	Stainless steel
TEM	Transmission electron microscope
XRD	X-ray diffraction
XPS	X-ray photo electron spectroscopy

## List of Tables

Table 1.1	Comparison between energy storage devices	3
Table 2.1	Chemicals used in this research work	29
Table 2.2	Apparatus used in this research work	31

## List of Figures

Figure - 1.1.1	Comparison of energy storage devices by Ragone plot	3
Figure - 1.1.2	Models of the electrical double layer at a positively charged surface	6
Figure - 1.1.3	Schematic representation of the pseudocapacitors in the charged condition	9
Figure - 2.1.1	Photographic images of current collectors used in this study	43
Figure - 2.1.2	Electrochemical workstation	45
Figure - 3.1.1	X-ray diffraction pattern (A) and Fourier transform infrared spectrum of CoMoO <sub>4</sub> nanostructures (B)	58
Figure - 3.1.2	Molecular structure of CoMoO <sub>4</sub>	59
Figure - 3.1.3	Field-emission scanning electron micrographs of CoMoO <sub>4</sub> nanostructures (A) low magnification (scale bar = 1 μm) and (B) high magnification (scale bar = 100 nm) micrographs	60
Figure - 3.1.4	High-resolution transmission electron micrographs of CoMoO <sub>4</sub> nanostructures (A-C) low magnification (scale bar = 1 μm to 200 nm) and SAED pattern (D)	61
Figure - 3.1.5	Cyclic voltammetric curves of CoMoO <sub>4</sub> electrodes in 2M KOH electrolyte. (A) at a scan rate of 10 mV s <sup>-1</sup> and (B) at different scan rates from 5 to 100 mV s <sup>-1</sup>	62
Figure - 3.1.6	Electrochemical impedance spectroscopy of CoMoO <sub>4</sub> electrodes. (A) Nyquist plot and (B) Bode phase angle plot	63

Figure - 3.1.7	Galvanostatic discharge curves of $\text{CoMoO}_4$ electrodes. (A) with different discharge current densities and (B) Variation of specific capacitance with respect to discharge current density	64
Figure - 3.1.8	(A) Cyclic stability tests of $\text{CoMoO}_4$ using galvanostatic charge discharge measurements at a constant current density of $6 \text{ mA cm}^{-2}$ for 1000 cycles. The inset shows the Nyquist plot of $\text{CoMoO}_4$ electrodes before and after cyclic stability test. FE-SEM micrographs (scale bar -100 nm) of electrode materials before (B) and after (C) cyclic tests	66
Figure - 3.2.1	X-ray diffraction pattern of sonochemically synthesized $\alpha\text{-MnMoO}_4$ nanorods	76
Figure - 3.2.2	Raman spectrum of sonochemically synthesized $\alpha\text{-MnMoO}_4$ nanorods	77
Figure - 3.2.3	XPS spectra of synthesized $\alpha\text{-MnMoO}_4$ nanorods (A) the Mn2p core-level, (B) Mo3d <sub>3/2</sub> , Mo3d <sub>5/2</sub> core-level peaks, (C) the O 1s core-level spectra	78
Figure - 3.2.4	FE-SEM images of the prepared $\text{MnMoO}_4$ nanorods (A-D)	80
Figure - 3.2.5	HR-TEM image of the synthesized $\alpha\text{-MnMoO}_4$ nanorods at $0.5\mu\text{m}$ (A), 200nm (B), 100 nm (C) and 50 nm (D), SAED pattern (inset of D).	80
Figure - 3.2.6	(A) Cyclic voltammetric curves of $\alpha\text{-MnMoO}_4$ nanorods in 2M NaOH electrolyte at different scan rates. (B) Variation of specific capacitance with respect to scan rates	81
Figure - 3.2.7	Electrochemical impedance spectroscopy of $\text{MnMoO}_4$ electrodes represented as Nyquist plot	82
Figure - 3.2.8	(A) Galvanostatic discharge curves of $\alpha\text{-MnMoO}_4$ with different discharge current densities. (B) Variation of specific capacitance with respect to discharge current density	83

Figure - 3.2.9	Cyclic stability tests of $\alpha$ -MnMoO <sub>4</sub> using cyclic voltammetry measurements at a scan rate of 100 mV s <sup>-1</sup> for 2000 cycles. The inset shows the Nyquist plot of $\alpha$ -MnMoO <sub>4</sub> electrodes before and after 2000 cycles	85
Figure - 4.1.1	X-ray diffraction pattern of PANI and CoMoO <sub>4</sub> /PANI composite material. Inset shows the XRD pattern of CoMoO <sub>4</sub>	96
Figure - 4.1.2	Raman spectrum (A), FT-IR spectrum (B) of PANI and CoMoO <sub>4</sub> /PANI composite material. Inset shows the FT-IR spectrum of CoMoO <sub>4</sub>	97
Figure - 4.1.3	FE-SEM images of PANI (A and B) and CoMoO <sub>4</sub> /PANI composite (C and D) material at the different magnifications	99
Figure - 4.1.4	Comparison of cyclic voltammetry curves for pristine CoMoO <sub>4</sub> , pristine PANI and CoMoO <sub>4</sub> /PANI composite at a scan rate of 5 mV s <sup>-1</sup> in H <sub>2</sub> SO <sub>4</sub> electrolyte	99
Figure - 4.1.5	Cyclic voltammetry curves of CoMoO <sub>4</sub> /PANI at the different scan rates (from 5 to 50 mV s <sup>-1</sup> ) (A), galvanostatic charge-discharge curves of CoMoO <sub>4</sub> /PANI at the different current densities (from 2 to 5 mA cm <sup>-2</sup> ) (B), specific capacitances of CoMoO <sub>4</sub> /PANI with respect to scan rates (C), and specific capacitances of CoMoO <sub>4</sub> /PANI with respect to current densities	100
Figure - 4.1.6	Cyclic performance of CoMoO <sub>4</sub> /PANI at current density of 4 mA cm <sup>-2</sup> (inset Nyquist plot for before and after cyclic stability test)	102
Figure - 4.2.1	XRD pattern for the synthesized GO from Hummers method and rGO by hydrothermal method (A), CoMoO <sub>4</sub> nanostructures by sonochemical method (B).	111

Figure – 4.2.2	FE-SEM image of rGO by hydrothermal method at low (A) and high magnifications (B), FE-SEM image of GO (inset of (A)), CoMoO <sub>4</sub> nanostructures by sonochemical method at low (C) and high magnifications (D).	112
Figure – 4.2.3	FT-IR spectrum of CoMoO <sub>4</sub> nanostructures (A), GO and rGO nanosheets (B).	113
Figure – 4.2.4	Raman spectrum of CoMoO <sub>4</sub> nanostructures (A), GO and rGO nanosheets (B).	114
Figure – 4.2.5	Nitrogen adsorption/desorption isotherm of rGO (A) and CoMoO <sub>4</sub> (B)	116
Figure – 4.2.6	Cyclic voltammetry curve for rGO at the various scan rates (A), comparison of specific capacitances with respect to the scan rates (B).	117
Figure – 4.2.7	Cyclic voltammetry curve for CoMoO <sub>4</sub> at the various scan rates (A), comparison of specific capacitances with respect to the scan rates (B).	118
Figure – 4.2.8	Schematic representation of fabricated ASC (A), photograph of fabricated device (inset of A), cyclic voltammetry comparison of negative (rGO) and positive (CoMoO <sub>4</sub> ) electrodes at the scan rate of 5 mV s <sup>-1</sup> , cyclic voltammetry curve for fabricated ASC at the different voltage levels (C), galvanostatic charge discharge curve for fabricated ASC at the different voltage levels (D).	120
Figure – 4.2.9	Cyclic voltammetry curve for ASC at the various scan rates (A), comparison of specific capacitances with respect to the scan rates (B), charge discharge curve for ASC at the various current densities comparison (C), comparison of specific capacitances with respect to the current densities (D).	121
Figure – 4.2.10	Cyclic performance of ASC measured by the galvanostatic charge discharge measurement at the current density of 1.0 mA cm <sup>-2</sup> .	122

Figure – 5.1.1	X-ray diffraction pattern (A), (* Ni foam), and Raman spectrum of CoMoO <sub>4</sub> NPAs grown on nickel foam (B)	136
Figure – 5.1.2	X-ray photoelectron spectroscopy of Co 2p core-level spectrum (A), Mo 3d core-level spectrum (B), and O 1s core-level spectrum (C) of CoMoO <sub>4</sub> NPAs on Ni foam	138
Figure – 5.1.3	Field-emission scanning electron micrographs of CoMoO <sub>4</sub> NPAs directly grown on nickel foam at different magnifications, 20 μm (A), 10 μm (B), 1 μm (C), 200 nm (D). Cross sectional view images at the different regions (E) and (F)	139
Figure – 5.1.4	Cyclic voltammetry curves measured at different scan rates (5 to 100 mV s <sup>-1</sup> ) (A), galvanostatic discharge curves measured at different current densities (2.5 to 25 mA cm <sup>-2</sup> ) (B), Areal charge capacities with respect to current densities (C) of CoMoO <sub>4</sub> NPAs directly grown on nickel foam in 2 M KOH electrolyte	141
Figure – 5.1.5	Comparison of cyclic voltammetry curves at 5 mV s <sup>-1</sup> (A), discharge curves measured at 25 mA cm <sup>-2</sup> (B) and Nyquist plot (C) of CoMoO <sub>4</sub> NPAs directly grown on nickel foam measured with and without addition of 0.02M K <sub>3</sub> Fe(CN) <sub>6</sub> redox additive in 2M KOH electrolyte	142
Figure – 5.1.6	Cyclic voltammetry curves at different scan rates (measured at 5 to 100 mV s <sup>-1</sup> ) (A), galvanostatic discharge curves at different current densities (measured at 2.5 to 25 mA cm <sup>-2</sup> ) (B), Areal charge capacities with respect to current densities (C) of CoMoO <sub>4</sub> NPAs directly grown on nickel foam in 2M KOH electrolyte with addition of 0.02 M K <sub>3</sub> Fe(CN) <sub>6</sub> redox additive electrolyte	144

Figure – 5.1.7	Annotation of hexacyanoferrate ions during charge (A) and discharge (B) with the synthesized CoMoO <sub>4</sub> NPAs on Ni foam electrode	145
Figure – 5.1.8	Cyclic stability test for CoMoO <sub>4</sub> NPAs on Ni foam using charge discharge analysis measured at the current density of 15 mA cm <sup>-2</sup>	147
Figure – 5.1.9	XRD pattern of CoMoO <sub>4</sub> NPAs on Ni foam after cycles	147
Figure – 5.1.10	Raman spectrum of CoMoO <sub>4</sub> NPAs on Ni foam after cycles	148
Figure – 5.1.11	FE-SEM images of CoMoO <sub>4</sub> NPAs on Ni foam after cycles at low (A) and high (B) magnifications	149
Figure – 5.1.12	Self-discharge curve CoMoO <sub>4</sub> NPAs on Ni foam electrode with and without redox additive	149
Figure – 5.1.13	Cyclic voltammetry curves at the different scan rates (measured at 5 to 100 mV s <sup>-1</sup> ) (A), charge discharge curves at the different current densities (measured at 2.5 to 5 mA cm <sup>-2</sup> ) for AC using three electrode system	150
Figure – 5.1.14	Cyclic voltammetry curves of AC and CoMoO <sub>4</sub> NPAs on Ni foam at the scan rate of 50 mV s <sup>-1</sup> in three electrode system	151
Figure – 5.1.15	Cyclic voltammetry curves at the different potentials (measured at 50 mV s <sup>-1</sup> ) (A), charge discharge curves at the different potentials (measured at 5 mA cm <sup>-2</sup> ) (B), cyclic voltammetry curves at the different scan rates (C), charge discharge curves at the different current densities (D), Ragone plot (E) and cyclic stability test measured at 25 mA cm <sup>-2</sup> (F) of fabricated CoMoO <sub>4</sub> NPAs on Ni foam//activated carbon asymmetric supercapacitors with redox additive electrolyte.	153

Figure – 6.1.1	Structural characterization of binder-free CoMoO <sub>4</sub> on nickel Ni foam catalyst before the dry reforming reaction (DRR): the X-ray diffraction (XRD) pattern (A) and Field-emission –scanning electron microscopy (FE-SEM) images at different magnifications, 20 μm (B), 10 μm (C), 2 μm (inset of Fig.1C), 200 nm (D), (B–D) suggest that uniform CoMoO <sub>4</sub> plate-like arrays grew on the Ni foam (~400 nm in length, 50–100 nm in breadth), which was used directly as a catalyst for the DRR of propane	167
Figure – 6.1.2	Raman spectrum of CoMoO <sub>4</sub> NPAs on Ni foam after calcination	168
Figure – 6.1.3	Schematic representation of the reactor used for DRR of propane	169
Figure – 6.1.4	Catalytic activity of the catalyst: Conversion efficiencies of propane and carbon dioxide (CO <sub>2</sub> ) (A), concentrations of SNG obtained (B) for bare Ni foam and binder-free CoMoO <sub>4</sub> /Ni foam catalysts, H <sub>2</sub> /CO ratios obtained (C) at different temperatures, and conversion efficiencies of propane at 630°C over a period of 1,440 min (D) for binder-free CoMoO <sub>4</sub> /Ni foam catalyst.	170
Figure – 6.1.5	Structural morphology of carbon-deposited binder-free CoMoO <sub>4</sub> /Ni foam catalyst after DRR: FE-SEM images (A–D) and HR-TEM (E–H) at different magnifications suggest that carbon nanotubes (CNTs) at the diameter of ~20 nm have been deposited over the catalyst, Inset of G and H, SAED pattern of CoMoO <sub>4</sub> and CNT respectively	173
Figure – 6.1.6	FE-SEM images of bare Ni foam, before DRR (A), after DRR (B).	174

Figure – 6.1.7	Structural characterization of carbon-deposited binder-free CoMoO <sub>4</sub> /Ni foam catalyst after DRR: the XRD pattern (A) and Raman spectrum of CNT-deposited catalyst after DRR at different laser powers at a laser wavelength of 514 nm. The laser power dependence was examined for samples exposed in air to examine both the bonding nature of metal-oxygen vibrations for CoMoO <sub>4</sub> /Ni foam and the D/G bands for the CNT (B)	175
Figure – 6.1.8	XPS spectrum: survey spectrum (A), Co2p core-level spectrum (B), Mo3p core-level spectrum (C), Mo3d core-level spectrum, C1s core-level spectrum (E), O1s core-level spectrum of CNT deposited CoMoO <sub>4</sub> on Ni foam after DRR	177
Figure – 6.1.9	XRD pattern (A) and Raman spectrum (B) of CoMoO <sub>4</sub> /Ni foam after treated at 630 °C for 24 h. (Δ – CoMoO <sub>4</sub> , ◆ – Ni foam, ● – NiO)	178
Figure – 6.1.10	Schematic annotation of this work. The binder-free CoMoO <sub>4</sub> /Ni foam was used as a catalyst for the dry reforming reaction (DRR) of propane with carbon dioxide (CO <sub>2</sub> ). During the DRR, propane reacts with CO <sub>2</sub> to generate synthesis gas (CO + H <sub>2</sub> ) in the presence of the catalyst. In addition, carbon becomes deposited over the catalyst over time. This carbon-deposited catalyst was further used as a positive electrode for supercapacitor applications	179
Figure – 6.1.11	Electrochemical performances of CNT-deposited binder-free CoMoO <sub>4</sub> /Ni foam catalyst in three electrode systems: cyclic voltammetry curves (CVs) at different scan rates (5–100 mVs <sup>-1</sup> ) (A), square root of the scan rates versus charge and discharge peak current (B), galvanostatic charge-discharge (GCD) curves at different current densities (1–10 mA cm <sup>-2</sup> ) (C), and comparison of areal capacity with respect to various current densities	180

Figure – 6.1.12	CV curve at the different scan rates (A), GCD curves (B), areal capacities with respect current densities (C) of CoMoO <sub>4</sub> /Ni foam after treated at 630 °C for 24 h without propane and CO <sub>2</sub>	182
Figure – 6.1.13	Cyclic stability test for CNT deposited CoMoO <sub>4</sub> /Ni foam for 3000 cycles using GCD measurement	183
Figure – 6.1.14	Cyclic voltammetry curves at the different scan rates (A), galvanostatic charge discharge analysis at the different current densities (B).	184
Figure – 6.1.15	Fabricated asymmetric supercapacitor: photographic image of a fabricated coin cell-type device (A), schematic representation of the fabricated asymmetric supercapacitor in the charged state; the device consists of CNT-deposited CoMoO <sub>4</sub> /Ni foam as the positive electrode, reduced graphene oxide (rGO)-coated carbon cloth (CC) as the negative electrode, a separator, and electrolyte solution (B), comparison of CV curves at a scan rate of 50 mVs <sup>-1</sup> (C), comparison of charge-discharge curves at a current density of 2 mA cm <sup>-2</sup> (D) for the positive and negative electrodes	185
Figure – 6.1.16	Electrochemical performance of an asymmetric supercapacitor: CV curves at different potential windows (at a scan rate of 100 mVs <sup>-1</sup> ) (A), GCD curves at different potential windows (at a current density of 2 mA cm <sup>-2</sup> ) (B), CV curves at a 1.6 V potential window (at different scan rates from 5 to 100 mVs <sup>-1</sup> ) (C), and GCD curves at the 1.6 V potential window (at different current densities from 2 to 10 mA cm <sup>-2</sup> ) (D), cyclic stability over many cycles (E), Nyquist plot of before and after cyclic study (inset in E), Ragone plot of energy density vs. power density (F), for the fabricated CNT-deposited CoMoO <sub>4</sub> /Ni foam // rGO asymmetric supercapacitors	186

Figure – 6.1.17	<p>Demonstration of driving low power electronic devices for switching applications: series connection of fabricated supercapacitor devices could power up the red (A), white (B), green (C), and blue (D) LEDs, driving a UV light sensor circuit for detection in dark environments (E), switching response of UV photodetector in ON and OFF conditions (<math>\lambda</math>-365 nm) (F), optical photograph of UV light sensor triggering red LED under various illumination intensities, <math>0.5 \text{ mW cm}^{-2}</math> and <math>8 \text{ mW cm}^{-2}</math>, along with fabricated supercapacitors (G).</p>	189
Figure – 6.1.18	<p>Photographic images of various LEDs at the different time intervals of two serially connected asymmetric supercapacitors</p>	190
Figure – 7.1.1	<p>Preparation of positive electrode material: Schematic representation of the formation of core-shell (A). The binder-free <math>\text{Co(OH)}_2</math> core has been initially grown on the CT by cyclic voltammetry method for 30 cycles. <math>\text{CoMoO}_4</math> shell has been grown on the <math>\text{Co(OH)}_2/\text{CT}</math> core by chronoamperometry method for 240 sec. FE-SEM images of Bare CT (B), magnified part of bare CT (C), <math>\text{Co(OH)}_2/\text{CT}</math> core (D) and <math>\text{CoMoO}_4@\text{Co(OH)}_2/\text{CT}</math> core-shell (E).</p>	206
Figure – 7.1.2	<p>FE-SEM images of the conductive textile at the different magnifications (from <math>10 \mu\text{m}</math> to <math>200 \text{ nm}</math>)</p>	207
Figure – 7.1.3	<p>FE-SEM images of the <math>\text{Co(OH)}_2</math> on conductive textile by 10 CV cycles at the different magnifications (from <math>10 \mu\text{m}</math> to <math>200 \text{ nm}</math>)</p>	208
Figure – 7.1.4	<p>FE-SEM images of the <math>\text{Co(OH)}_2</math> on conductive textile by 20 CV cycles at the different magnifications (from <math>10 \mu\text{m}</math> to <math>200 \text{ nm}</math>)</p>	209

Figure – 7.1.5	FE-SEM images of the $\text{Co(OH)}_2$ on conductive textile by 30 CV cycles at the different magnifications (from 10 $\mu\text{m}$ to 200 nm)	210
Figure – 7.1.6	FE-SEM images of the $\text{Co(OH)}_2$ on conductive textile by 40 CV cycles at the different magnifications (from 10 $\mu\text{m}$ to 200 nm)	211
Figure – 7.1.7	FE-SEM images of the $\text{CoMoO}_4 @ \text{Co(OH)}_2$ on conductive textile by CP for 180 sec at the different magnifications (from 10 $\mu\text{m}$ to 200 nm)	212
Figure – 7.1.8	FE-SEM images of the $\text{CoMoO}_4 @ \text{Co(OH)}_2$ on conductive textile by CP for 210 sec at the different magnifications (from 10 $\mu\text{m}$ to 200 nm)	213
Figure – 7.1.9	FE-SEM images of the $\text{CoMoO}_4 @ \text{Co(OH)}_2$ on conductive textile by CP for 240 sec at the different magnifications (from 10 $\mu\text{m}$ to 200 nm)	214
Figure – 7.1.10	FE-SEM images of the $\text{CoMoO}_4 @ \text{Co(OH)}_2$ on conductive textile by CP for 270 sec at the different magnifications (from 10 $\mu\text{m}$ to 200 nm)	215
Figure – 7.1.11	TEM images of $\text{CoMoO}_4 @ \text{Co(OH)}_2$ nanosheets on conductive textile at different magnifications (240 sec). The images clearly suggest that the formation crumpled $\text{CoMoO}_4$ shell on the $\text{Co(OH)}_2$ core. SAED pattern in inset of Figure 7.1.11 suggest that the polycrystalline nature of core-shell structure.	216
Figure – 7.1.12	Structural characterization of positive electrode material: XRD pattern (A) (inset shows the magnified part of maximum intensity peak of $\text{CoMoO}_4$ ), Raman spectrum (B) of $\text{CoMoO}_4 @ \text{Co(OH)}_2 / \text{CT}$ . XPS core-level spectra: Survey spectrum (C), $\text{Co}2\text{p}$ core-level spectrum (D), $\text{Mo}3\text{d}$ core-level (E) and $\text{O}1\text{s}$ core-level (F) of $\text{CoMoO}_4 @ \text{Co(OH)}_2 / \text{CT}$ .	217

Figure – 7.1.13	Photographic images of flexibility of the deposited $\text{CoMoO}_4@\text{Co}(\text{OH})_2$ on conductive textile at the different bending conditions.	219
Figure – 7.1.14	Electrochemical performance of the prepared positive core-shell electrode: Cyclic voltammetry curves at different scan rates (100 to $5 \text{ mV s}^{-1}$ ) (A), Galvanostatic charge-discharge curves at different current densities ( $50\text{-}1 \text{ mA cm}^{-2}$ ) (B), areal capacity with respect to the current densities calculated from the charge-discharge analysis (C) of $\text{CoMoO}_4 @ \text{Co}(\text{OH})_2/\text{CT}$	220
Figure – 7.1.15	Preparation of negative electrode material: Schematic representation of the formation of porous nature (A), FE-SEM images of the prepared lab waste derived activated carbon at different magnifications (B–D)	222
Figure – 7.1.16	XRD pattern (A), Raman spectrum (B) of $\text{CoMoO}_4@\text{Co}(\text{OH})_2/\text{CT}$ . XPS core-level spectra: Survey spectrum (C), C1s core-level spectrum (D), O1s core-level (E) and elemental mapping (F) of lab waste tissue paper derived activated carbon	223
Figure – 7.1.17	Electrochemical performance of the prepared negative porous electrode: Cyclic voltammetry curves at different scan rates ( $100$ to $5 \text{ mV s}^{-1}$ ) (A), Galvanostatic charge-discharge curves at different current densities ( $50\text{-}1.5 \text{ mA cm}^{-2}$ ) (B), specific capacitance with respect to the current densities calculated from the charge-discharge analysis (C) of porous LTAC respectively	224
Figure – 7.1.18	Electrochemical performance of the Pouch cell: Cyclic voltammetry curves at different scan rates ( $200$ to $5 \text{ mV s}^{-1}$ ) (A), Galvanostatic charge-discharge curves at different current densities ( $25\text{-}2 \text{ mA cm}^{-2}$ ) (B), specific capacitance with respect to the current densities calculated from the charge-discharge analysis (C) and Ragone plot (D).	226

Figure – 7.1.19	Flexibility test of the Pouch cell: Photographic images of the fabricated pouch cell at normal and at different bending conditions (A), Cyclic voltammetry curves for the device at normal and different bending conditions (B), the obtained specific capacitance from the area of the each CV curves at normal and bending conditions (C)	230
Figure – 7.1.20	Self-powered application by solar cell charging: Circuit-diagram (A), charging and self-discharging curve (B), photographic images of self-powered set-up (C), lightening 30 blue LEDs (D), 24 green LEDs (E) and 7-segment display (F) of the two serially connected solar cells, four serially connected fabricated pouch devices	231
Figure – 8.1.1	Overall outlook of this thesis	240

## 초록

현대 산업사회의 발전과 화석 연료의 급속한 고갈로 인해 새로운 에너지원의 수요가 증가하고 있으며 운송, 산업, 군사 및 우주 탐사를 포함한 다양한 분야의 인류의 진보를 위한 대체 에너지 및 저장 시스템의 개발이 필요하다. 특히 여러가지 종류의 에너지 저장 장치 중 전기화학 커패시터 (슈퍼커패시터)는 고출력 밀도, 빠른 충·방전 속도, 긴 수명 및 우수한 안전성의 전기화학적 특성으로 인해 고전력 응용 분야에서 가장 유망한 소자 중 하나로 간주되어 왔지만 에너지 밀도는 배터리와 비교하여 다소 부족하기 때문에 이를 향상시키기 위해 수많은 연구자들이 많은 연구를 진행하고 있다. 일반적으로, 페러데이 전극은 높은 비정전용량을 가지지만, 에너지 저장 분야에서 전기 활성 물질의 사용은 전도성 및 주기적인 안정성측면에서는 안정성의 열화로 인해 그 효과가 일부 제한된다. 반면에, 탄소계 물질의 전기화학 이중층 커패시터(EDLC)의 특성은 높은 전기 전도성 및 양호한 주기 안정성을 제공하지만 비정전용량은 더 낮은 편이다. 양호한 전기 전도성 및 높은 표면적을 갖는 적합한 전극 물질은 에너지 저장 시스템을 개발하기 위한 중요한 핵심 쟁점 중 하나이다. 또한 나노 스케일의 전극-전해질 계면특성은 슈퍼커패시터의 특성을 결정하는 중요한 요소 중의 하나이며,

소자의 에너지 저장 용량을 결정한다.

본 논문은 슈퍼커패시터의 상대적인 저에너지밀도의 문제점을 극복하기 위한 나노구조의 이원전이 금속 산화물을 이용하여 에너지밀도 및 비용량의 향상을 위하여 전극소재개발을 위한 체계적인 연구를 수행하였다. 또한 페러데이 반응을 가지는 양극물질을 양극으로 사용하고 다양한 탄소계 재료(활성 탄소, 나노튜브 및 그래핀)를 음극으로 사용하여 하이브리드 슈퍼커패시터 소자를 제작하였다.

본 논문의 제 3장에서는 전기화학 커패시터 응용을 위하여 음파화학적 (sonochemical) 방법을 이용하여 나노 구조 합성을 통하여  $M\text{MoO}_4$  (M은 Co 및 Mn) 전극을 제작하였고, 제작과정에서 발생하는 물질형성의 상세 메커니즘에 관하여 분석하였다.  $\text{MnMoO}_4$ 와 비교하여,  $\text{CoMoO}_4$ 는 우수한 전기화학적 성질을 나타내지만, 다른 금속 산화물 기반의 페러데이 전극 재료에 비해 낮은 전기화학적 특성을 보였다. 또한,  $\text{CoMoO}_4$  전극의 전도성 및 표면적을 향상시키기 위해 4장에서  $\text{CoMoO}_4/\text{PANI}$  복합체를  $\text{CoMoO}_4$ 와 아닐린 단량체의 in-situ 화학 산화 중합방법에 의하여 제조하였다. 그리고 하이브리드 소자를 제조하기 위해 페러데이  $\text{CoMoO}_4$  전극(양극 단자), 분리막(separator)과 환원그래핀산화물(RGO) 전극(음극 단자)와 함께 제조하였다. 제조된 하이브리드 소자는 1.5 V까지 작동하며 에너지 밀도가

8.17 Wh kg<sup>-1</sup> 그리고 전류 밀도가 0.5mAcm<sup>-2</sup>일 때 최대 비정전용량은 26.16Fg<sup>-1</sup>로 나타났다. 집전체 상에 페러데이 전극 물질의 수동 슬러리(manual slurry) 코팅은 여전히 폴리머바인더(polymer binder)의 사용으로 인해 보다 낮은 비정전용량을 보였다. 이를 개선하기 위하여 CoMoO<sub>4</sub> 나노 플레이트 어레이(NPAs)는 수열합성 합성법을 사용하여 Ni 폼 집전체 위에 직접 성장하는 프로세스를 제 5장에서 제시하였다. 바인더가 함유하지 않은 CoMoO<sub>4</sub>@Ni 폼의 NPAs는 견고한 접착력을 가진 KOH 전해질에서 227μAh<sup>-2</sup>의 우수한 표면정전용량(areal specific capacity)을 나타낸다. 본 연구에서는 다양한 농도의 산화 환원 첨가제로 페리시안화칼륨(K<sub>3</sub>Fe(CN)<sub>6</sub>)을 사용하여 전기화학 실험을 하였다. 2M KOH에서 0.02M K<sub>3</sub>Fe(CN)<sub>6</sub>을 첨가하면 다른 전해질 물질에 비해 더 우수한 출력 및 603 μAhcm<sup>-2</sup>의 최대 면적용량을 보이며 초기 전해질보다 거의 3배 증가하였다. 이 결과는 바인더 물질이 없는 패러데이 전극의 성능개선을 위하여 산화환원 첨가제를 추가한 최초의 접근 방법을 제시하였다.

제 6장에서는 폐기물 에너지의 새로운 활용에 관한 기발한 아이디어를 활용한 연구결과를 소개한다. 바인더가 없는 CoMoO<sub>4</sub>@Ni 폼을 촉매로 사용하여 슈퍼커패시터의 전극 재료용 CoMoO<sub>4</sub>@Ni 폼 위에 카본 나노튜브(CNT)를 증착하기 위해 프로판 건식개질반응(DRR)을 수행하였다. 고온의 DDR 과정에서 프로판

이 이산화탄소와 반응하여 일산화탄소 및 수소 가스(합성 가스)를 생성되면 추가로 탄화수소가  $\text{CoMoO}_4@Ni$  폼 촉매 위에 CNT 형태로 침전된다. 여기서 탄소는 제거되면 지구 온난화의 원인인  $\text{CO}_2$ 로 배출하게 된다.  $\text{CO}_2$  가스 배출을 방지하기 위해 이 탄소가 증착 된 촉매는 우수한 전기적 특성을 가진 전극 재료로서 슈퍼커패시터의 응용을 위해 폐탄소 침전 된 촉매로 활용하는 방법에 대해 처음으로 보고하였다. 이는 소규모 및 휴대용 기기에 응용하기 위한 전원 및 에너지 저장 시스템에 대한 수요가 증가에 부응할 수 있는 친환경적인 접근방법이다. 제 7장은  $\text{Co(OH)}_2$ 를 중심으로 한 페러데이 코어-셀 구조와  $\text{CoMoO}_4$  직물 셀을 다른 사이클 및 시간 간격을 가진 쉬운 전기화학 증착법을 사용한 유연한 슈퍼커패시터 제조에 대해 설명하였으며, 체계적인 최적화프로세스를 통하여 면적용량을 증가시키는 우수한 결과를 도출하였다. 또한 실험에 사용 한 활성탄이 묻은 폐박엽지 (LTAC)를 사용하여 고표면적 활성탄을 합성하였으며, 유연한 코어-셀 구조를 같은 물질과 LTAC를 이용하여 파우치 형태의 하이브리드 슈퍼커패시터를 제작하였다. 이 장치의 유연성을 다양한 굽힘 조건을 사용하여 실험을 하였으며, 제작된 에너지저장장치는  $33.5\text{Wh kg}^{-1}$ 의 최대 에너지 밀도 우수한 전기화학적 성능을 보여주었으며, 상업용 태양 전지등과의 하이브리드화를 통하여, 자체구동에너지원으로써 활용이 가능할 것으로 기대된다.

## **Abstract**

The advent of modern times and increasing demand in the need of global energy due to rapid deterioration of fossil fuels drives the development of alternate energy conversion and storage systems for the progress of mankind including residential, transportation, industry, military and space exploration. Among the various kinds of energy storage devices, electrochemical capacitors (often called as supercapacitors) have been considered as one of the most promising candidates for high-power applications due to their eminent properties, such as high power density, fast charge-discharge rate, long cycle life, and better safety, but it lacks in storing the specific energy (or energy density) compared to the batteries. Many attempts are under the progressive research by the researchers to improve this specific energy. Generally, faradaic electrodes have high specific capacity, but suffer in conductivity and cyclic stability which limits the effective use of these electroactive materials in the energy storage field. On the other hand, electrochemical double layer capacitance (EDLC) behavior of carbon based materials provides high electrical conductivity and good cyclic stability, but lower in specific capacitance. The suitable electrode materials having good electrical conductivity and high surface area is one of the key issues in the field of energy storage systems. Also, the nano scaled electrode-electrolyte interface is one of the main things in every supercapacitor, which determines the energy storage capacity of the device. By considering all the benefits and to overcome the issues of the supercapacitor, the main

focus of this thesis is that the improving the specific energy by design of nanostructured binary transition metal oxide and their systematic enhancement in the capacity by various strategies. In addition, the hybrid supercapacitor devices have been studied by using this faradaic material as positive electrode and various carbon based materials (activated carbon, carbon nanotube, and graphene) as negative electrode.

Chapter-3 of this thesis covers the synthesis of  $\text{MMoO}_4$  ( $\text{M} = \text{Co}$  and  $\text{Mn}$ ) nanostructures as an electrode materials under sonochemical method for electrochemical capacitor applications. The detailed mechanism of the formation of the materials under sonochemical process has been explored. Compared to  $\text{MnMoO}_4$ ,  $\text{CoMoO}_4$  shows the excellent electrochemical properties and however it shows less compared to other metal oxide based faradaic materials. Further, to improve the conductivity and surface area of  $\text{CoMoO}_4$ , *in-situ* chemical oxidative polymerization of aniline monomer in the presence of  $\text{CoMoO}_4$  has been performed to prepare  $\text{CoMoO}_4/\text{PANI}$  composite in Chapter-4 of this thesis. In order to fabricate the hybrid device, the faradaic  $\text{CoMoO}_4$  electrode (as positive terminal) is assembled with the hydrothermally reduced graphene oxide electrode (as negative terminal) with the separator and shown in Chapter-4. The assembled hybrid device works up to 1.5V and shows a maximum specific capacitance of  $26.16 \text{ F g}^{-1}$  at a current density of  $0.5 \text{ mA cm}^{-2}$  with an energy density of  $8.17 \text{ Wh kg}^{-1}$ . The manual slurry coating of faradaic electrode material on the current collector still shows less specific capacity because of the use of polymer binder. Hence, the hierarchical  $\text{CoMoO}_4$  nanoplate arrays (NPAs) are directly grown on the Ni foam

current collector by hydrothermal method and presented in the Chapter-5. This binder-free  $\text{CoMoO}_4@Ni$  foam NPAs shows excellent areal specific capacity of  $227 \mu\text{Ah cm}^{-2}$  in KOH electrolyte with robust adhesion. In this study, another impressive approach has been made with the use of potassium ferricyanide ( $\text{K}_3\text{Fe}(\text{CN})_6$ ) as redox additive electrolyte with the various concentrations. The addition of 0.02 M  $\text{K}_3\text{Fe}(\text{CN})_6$  into 2M KOH shows the better output compared to others and shows the maximum areal capacity of  $603 \mu\text{Ah cm}^{-2}$  which is nearly three order higher than the pristine electrolyte. This is the first time approach that the addition of redox additive to the improvement of binder-free faradaic electrode.

Chapter-6 of this thesis is an innovative waste-to-energy concept. With the use of binder-free  $\text{CoMoO}_4@Ni$  foam as catalyst, dry reforming reaction of propane (DRR) has been performed to deposit the carbon nanotube (CNT) over the  $\text{CoMoO}_4@Ni$  foam for supercapacitor electrode material. During high temperature DRR, with the presence of  $\text{CoMoO}_4@Ni$  foam catalyst, propane reacts with  $\text{CO}_2$  and liberates the CO and  $\text{H}_2$  (called as syngas), the additional hydrocarbon are deposited as carbon (in the form of CNT) over the catalyst. This carbon can be removed as  $\text{CO}_2$  again into the atmosphere which might be cause of global warming to our earth. In order to avoid  $\text{CO}_2$  emission, this carbon deposited catalyst has been investigated as an electrode material for supercapacitor application with the excellent electrochemical properties. This is the first time approach to utilizing the waste carbon deposited catalyst for an interesting approach. The modern trend in the technology towards small scale and portable

electronic devices has increased the demand of the power sources and energy storage systems. Chapter-7 shows the fabrication of flexible supercapacitor using the faradaic core-shell structure based on  $\text{Co(OH)}_2$  as the core and  $\text{CoMoO}_4$  as the shell on the conductive textile by facile electrochemical deposition method with different cycles and time intervals. The systematic optimization has been performed to achieve the excellent morphology which leads to improved areal capacity. On the other hand, the high surface area activated carbon is synthesized using the lab waste tissue paper derived activated carbon (LTAC). The flexible core-shell structure has been assembled with the LTAC to fabricate hybrid supercapacitor device and it covered with pouch. The flexibility of the pouch cell has been tested at the different bending conditions. This fabricated flexible pouch cell shows excellent electrochemical performances and achieved a maximum energy density of  $33.5 \text{ Wh kg}^{-1}$ . Also, this pouch cell has been integrated with commercial solar cell to show the self-powered applications.



## **CHAPTER-I**

### **Introduction**

#### **1.1. Background**

An emergence of modern era and increasing demand in the need of global energy due to rapid deterioration of fossil fuels drives the development of alternate energy conversion and storage systems for the progress of mankind including residential, transportation, industry, military and space exploration [1-3]. The energy demand increases day-to-day gradually in domestic applications and industries but the available conventional energy resources fail to meet out our requirements. Because it is impossible to achieve the renewable energy resources such as solar and wind for all the years and the non-renewable (fossil fuels) sources of energy are not utilized to the thorough potential due to their own demerits. Another difficulty of the same extent is that the demolitions of environmental hazards like nuclear waste from non-renewable sources. Then again, global warming is also a rising problem due to increase in atmospheric CO<sub>2</sub> content due to more numbers of vehicles and industries. Furthermore, over the last few years the cost of liquid fuels has enormously increasing day by day which makes more stress on economic development of the developing and growing countries. These problems can be solved by advancing effective electrical energy storage systems which can promote efficient energy storage and utilize of power. This can significantly help us to reduce our dependence on combustible and thermal sources of

energy (like petroleum extracts) and above all the problems, there is no perpetual resource of power, avert us from grieving about our future.

## **1.2. Importance of electrochemical energy storage devices**

All the above issues are now days supportively reduced by modern energy storage device, specifically battery (Li-ion battery, LIB), supercapacitors (SCs), and hydrogen energy storage system and so on. Electrochemical energy storage systems (EES) play an important role in storing electrical energy in terms of transforming chemical into electrical energy and inversely. The EES has fascinated among other classes of energy storage systems because of its several advantages like high efficiency of energy conversion, direct energy conversion without intermediate step, absence of moving parts and hence minimum noise level, portability, miniaturization, convenience to scale up and minimum pollution [4-6]. However, the SCs and LIBs are nowadays encouraged as representative promising gadgets. However due to cost, more than a sector of the world's population cannot access to modern energy devices. Because essential tasks and problem headed for the commercialization of ECs, LIBs, have been extensively deliberate in different fields of technology essentially on electrode active materials and electrolyte etc., Subsequently, there yet continue numerous problem interrelated to commercialization viz. materials synthesis cost, life cycle, international environment regulation and so on. Along with some practical issues and when considering the SCs and LIBs, the utilization with lower cost electrode material is a major issues.

However, new devices namely SCs are offered today as an alternative energy storage device compared to LIBs. Because, the SCs possess intermediate value of power density (P) and energy density (E), when compared to classical capacitors and batteries or fuel cells i.e., higher power density (in  $\text{k W kg}^{-1}$ ) than batteries or fuel cells and higher energy density (in  $\text{Wh kg}^{-1}$ ) than classical capacitors (Fig. 1.1) [7, 8]. Thereby supercapacitors are characterized by their long cyclic life i.e., more number of charge-discharge cycle ( $\sim 10^6$ ) and fast charge/discharge rate (within  $\sim 3\text{s}$ ) [9].

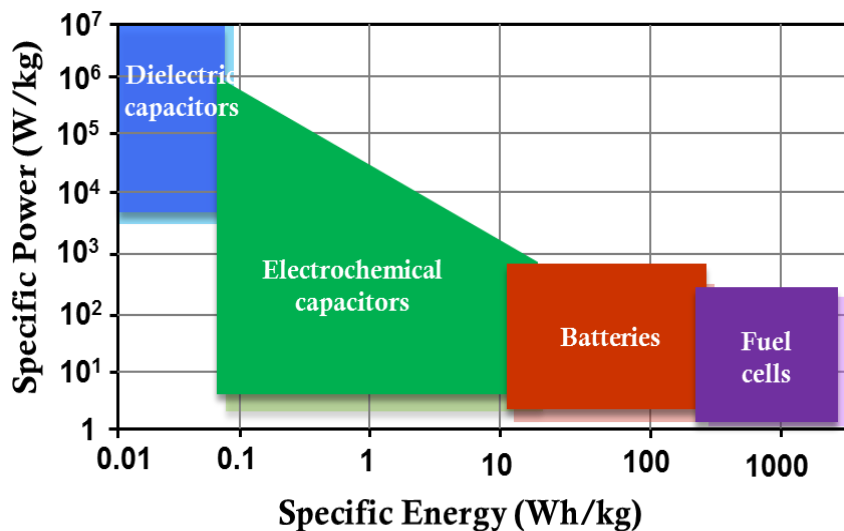


**Figure 1.1.1** Comparison of energy storage devices by Ragone plot

Hence, the supercapacitors are considered as high efficiency (95%) system with longer life time and lighter weight than the other energy storage devices [10]. In addition, due to its high power density, nowadays ECs are mostly used in space and military applications. ECs are also used in mobile phones, digital cameras, digital

communication devices, industrial equipment (cranes, elevators and fork-lifts) and pulse laser technique, electric hybrid vehicles, UPS and electric tools [11].

**Table. 1.1.** Comparison between typical supercapacitors and battery characteristics

Parameters	Capacitor	Supercapacitor	Battery
<b>Storage mechanism</b>	Electrostatic	Electrostatic	Chemical
<b>Charge Time</b>	$10^{-6}$ – $10^{-3}$ s	1–30 s	0.3–3 h
<b>Discharge Time</b>	$10^{-6}$ – $10^{-3}$ s	1–30 s	1–5 h
<b>Energy Density (Wh kg<sup>-1</sup>)</b>	< 0.1	1–10	20–100
<b>Power Density (W kg<sup>-1</sup>)</b>	>10 000	1000–2000	50–200
<b>Cycle Life</b>	> 500 000	> 100 000	500–2000
<b>Charge/Discharge Efficiency</b>	~1.0	0.90–0.95	0.7–0.85
<b>Discharge Profile</b>	Linear trend	Linear trend	discharge

Based on the charge storage mechanism and the electrode materials, supercapacitors are classified into three types including (i) Electrical double layer capacitors (EDLCs), (ii) Pseudocapacitors and (iii) Hybrid capacitors. The detailed explanations are given below

### 1.3. Principle of electrochemical capacitors

#### 1.3.1. Electrical double layer capacitors (EDLCs)

In EDLCs, the capacitance is related to accumulation of charge as double layer, between the electrode and electrolyte interface via non-Faradaic process [12, 13]. Here,

different types of carbon materials (activated carbon, carbon nanotubes and graphene) [14] have been used to store charges in EDLCs. However, the amount of charge accumulation is estimated by using the following equation to that of parallel-plate capacitor, therefore [9]

$$C = \frac{\varepsilon \cdot A}{d} \quad \mathbf{1.1}$$

Where,  $\varepsilon = \varepsilon_0 \cdot \varepsilon_r$ ,  $\varepsilon_0$  is the permittivity of free space ( $8.854 \times 10^{-12} \text{ F m}^{-1}$ ) and  $\varepsilon_r$  the relative dielectric constant of the electrolyte as liquid or solid, A is the surface area of the electrodes ( $\text{m}^2 \text{ g}^{-1}$ ) and d is the thickness of the electrical double-layer (EDL) or Debye length (DL). Moreover, an energy storage mechanism in EDLC is based on the electric double layer (EDL) theory [3]. This EDL theory was firstly proposed by Helmholtz in 1853 as similar to that of parallel plate capacitor therefore this model tells that two layers of opposite charges build up at the electrode-electrolyte interface with some atomic distance (**Figure. 1.1.2a**). Although, this presented model does not examine the adsorption of counter ions and water molecules. In the earlier 1900's, it is further modified by Gouy and Chapman, thus theory states that distribution of electrolyte ions in the electrolyte medium due to the thermal motion, named as a diffuse layer (**Figure. 1.1.2b**).

But this modified theory exhibits an overestimation of EDL capacitance. Afterwards, in 1924 Stern developed a modified theory by combined the Helmholtz and Gouy-

Chapman model. Therefore, explains that possibility of two layers of ion distribution. First is compact layer or Stern layer or Helmholtz layer which is formed by adsorbed ions and non-specifically adsorbed counter ions on electrode where this two type of adsorbed ions are distinguished as outer Helmholtz plane (OHP) and inner Helmholtz plane (IHP) (**Figure. 1.1.2c**). Second is diffuse layer which is same as what the Gouy-Chapman model describes. So, total capacitance ( $C_t$ ) is build up by both layer i.e., compact layer (Helmholtz layer) and the diffuse layer and stored capacitance termed as compact/Helmholtz double layer capacitance ( $C_H$ ) and diffusion layer capacitance ( $C_{diff}$ ). So, therefore the total capacitance is expressed as follow [9],

$$\frac{1}{C_t} = \frac{1}{C_H} + \frac{1}{C_{diff}} \quad 1.2$$

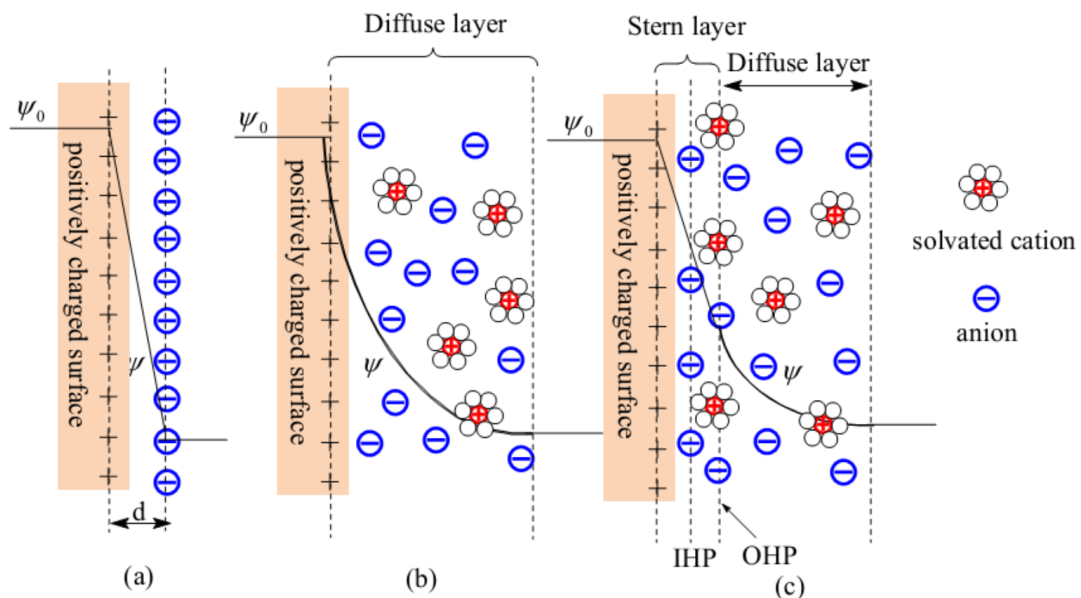


**Figure 1.1.2** Models of the electrical double layer at a positively charged surface: (a) the Helmholtz model, (b) the Gouy–Chapman model, and (c) the Stern model, showing the inner Helmholtz plane (IHP) and outer Helmholtz plane (OHP). The IHP refers to the distance of closest approach of specifically adsorbed ions (generally anions) and OHP refers to that of the non-specifically adsorbed ions. The OHP is also the plane where the diffuse layer begins. “d” is the double layer distance described by the Helmholtz model.  $\Psi_0$  and  $\Psi$  are the potentials at the electrode surface and the electrode/electrolyte interface, respectively (Reprinted with permission from RSC) [9].

### 1.3.1.1. Materials for EDL capacitor

#### a. Activated carbon

Activated carbon (AC) is a non-graphitic (disordered carbon) carbon and it has maximum amount of porous nature. Similarly, the interplanar spacing (0.335 nm) of activated carbon is smaller than the graphite (0.34-0.35 nm) and this AC is composed of many number of disorder graphene layers or basal layer which is known as turbostatic carbon [15]. Currently, ACs is mainly used as electrode material in commercial SCs because of their high surface area, good electrochemical stability, electrical conductive properties and better porous nature [16, 17]. Therefore, the conventional raw materials such as petroleum coke, tar pitches and coal could not meet our demand for the large scale production of ACs due to their less availability as well as they are not renewable in nature and cost effective. Therefore biomass is considered as the suitable precursor for the preparation of ACs, due to its availability and renewable in nature, waste management and cost effective [18, 19].

#### b. Carbon nanotube

CNTs show advantages of unique inter-connected mesoporous structure, high electronic conductivity, good mechanical and thermal stability [20-23]. These excellent properties of CNTs make them an interesting electrode material for EDLCs. The open and accessible network of mesopores in CNTs compared to other carbon materials provides a continuous charge distribution. CNTs also have low ESR than activated carbon; the ESR can be further decreased by using suitable fabrication technique. Aligned CNTs is more efficient than tangled CNTs, due to the fast ionic transportation [21-23]. However, due to contact resistance at the interface between electrode and electrolyte, CNT-based supercapacitors show lower electrochemical performances [24, 25].

### **c. Graphene**

Graphene, a 2D monolayer of  $sp^2$ -hybridized carbon atoms, has much considered in recent years due to its exceptional mechanical, optical, thermal properties, outstanding electrical properties, and extreme large specific surface area (over  $2600 \text{ m}^2 \text{ g}^{-1}$ ). It is contributing stupendous new advances in the various fields, such as field-effect transistors, biological/chemical sensors, transparent conductors, and energy storage and conversion devices [26-34]. The merit of graphene in energy storage devices is quite large due to its interesting properties. Many methods such as thermal reduction, chemical reduction, electrochemical reduction, microwave assisted reduction and multi-step reduction methods etc. have been used to synthesize graphene based materials. Graphene based EDLCs was first reported by Stoller et al [35]. They have prepared

graphene by chemical modification and showed a capacitance of  $135 \text{ F g}^{-1}$  in aqueous electrolyte. Graphene prepared by the thermal treatment of graphite exhibited a capacitance of  $117 \text{ F g}^{-1}$  in  $\text{H}_2\text{SO}_4$  aqueous electrolyte [36]. Very recently, Wang et al. demonstrated a synthesis of graphene using microwave method and reported a capacitance of  $185 \text{ F g}^{-1}$  in KOH electrolyte [37]. However, the agglomeration of graphene sheets during electrochemical process has limited its applications. The energy density of EDLCs is still unsatisfactory with the severe requirements and development of EES devices.

### **1.3.2. Pseudocapacitors**

The source of “pseudocapacitance” can be established in the association of the prefix “pseudo” and capacitance. It can be applied to define something that is fake or false, illusive, a sham (example: pseudoscience, methodology, a theory, or practice that is referred to be without scientific base) [38]. In other words, (i) not actually but having the appearance of; (ii) nearly, more or less, approaching, or trying to be (example: pseudo-classicism, the imitative utilization of classicism in art and literature, widespread during the 18th century). Because the word “pseudocapacitance” was created in order to confine the properties of an electrode that behaves like a capacitor in its electrochemical signature, this second definition of “pseudo” is the more correct use in the present case [39].

In the field of electrochemical capacitors, the word “pseudocapacitance” is used to indicate the electrode materials ( $\text{MnO}_2$  and  $\text{RuO}_2$ ) that have the electrochemical

signature of a capacitive electrode (such as noticed with activated carbon), i.e., exhibiting a linear dependence of the charge stored with the wideness of the potential window, but where charge storage arises from different reaction mechanisms. Pseudocapacitance arises at the surface of the electrodes where a totally distinct charge-storage mechanism occurs. It is faradaic in nature, undergoing the passing of charge crossing the double layer, as in battery charging or discharging, but capacitance arises in account of the appropriate relation that can originate for thermodynamic reasons between the extent of charge acceptance ( $\Delta q$ ) and the change in potential ( $\Delta V$ ), so that the derivative  $d(\Delta q)/d(\Delta V)$  or  $dq/dV$ , which is equivalent to a capacitance, can be formulated and experimentally measured by dc, ac, or transient methods [8, 39-43]. In addition, the average capacitance of redox electrodes are denoted as,  $C = C_{dl} + C\Phi$ , where,  $C_{dl}$  is EDL capacitance and  $C\Phi$  is pseudocapacitance.

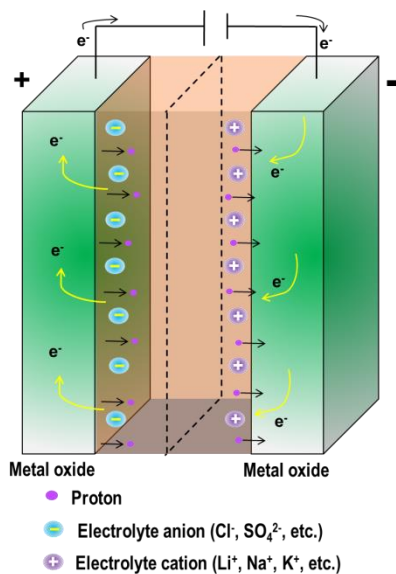
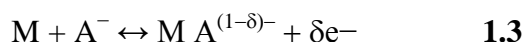


**Figure 1.1.3** Schematic representation of the pseudocapacitors in the charged condition

Generally, the electrosorption process occurs while the electron-donating anions such as Cl<sup>-</sup>, Br<sup>-</sup>, I<sup>-</sup> and CNS<sup>-</sup> contributing to the chemisorption process [44] such as,



Electro-sorption reaction of anions (A<sup>-</sup>) at the electrode surface and the quantity are correlated to the so-called “electro-sorption valence”. Then, by exchanging of charge across the double layer, rather than a static partition of charge across a fixed distance, resulting in oxidation-reduction reactions [44]. Hence,



The exchange of charge  $ne^{-}$  is happened in this reaction and the storing of energy is indirect which is similar to that of a battery. These reactions may tolerate pseudocapacitors in achieving superior capacitance and energy densities. The principle difference of pseudocapacitors and EDLCs are that there is no net ion-exchange involving along with the electrode and electrolyte in EDLCs which implies that the electrolyte concentration remains stable all through the charge-discharge process. But notably the EDL capacitance in such system always co-exists with pseudocapacitance. However the number of ions to build an EDL formation is normally slighter than the number of protons exchanged between the electrodes. The values of pseudocapacitance are usually few times higher than EDL capacitance, results in both rapid adsorptions/desorption obvious reaction or multi-electron-transfer reaction through fast charge/discharge properties [45].

### 1.3.2.1. Materials for pseudocapacitors

#### a. $\text{MnO}_2$

Among various metal oxides, manganese oxide plays a prominent interest due to its low cost, nature abundance, environmental compatibility and high specific capacitance with excellent cycling stability and wide voltage range (1 V) [46-48].  $\text{MnO}_2$  with its multi-valance characteristics of Mn (Mn (0), Mn (II), Mn (III), Mn (IV), Mn (V), Mn (VI) and Mn (VII)) states gifted to the pseudocapacitors electrode owing to their cost effective and more environmental friendly than other available metal oxides. Theoretical specific capacitance of  $\text{MnO}_2$  was about  $\sim 1370 \text{ F g}^{-1}$  due to one-electron transfer (Mn IV to Mn III) over a potential window of about 0.9 V [49]. However, the SC and electrochemical stability of  $\text{MnO}_2$  was strongly influenced by its surface morphology, crystal structure, porous size, pore volume and surface area [50]. On the other hand, crystalline nature improved the stability by avoiding dissolution of the active material [51]. Very recently, birnessite- $\text{MnO}_2$  prepared by polyol method which delivered a capacitance of about  $130 \text{ F g}^{-1}$  [51]. Lu et al. synthesized large surface area  $\text{MnO}_2$  nanorod arrays and exhibited a high capacitance of  $485 \text{ F g}^{-1}$  [52]. Compared to bulk,  $\text{MnO}_2$  thin films delivered a high capacitance for example, sol-gel derived  $\text{MnO}_2$  film showed a capacitance of  $698 \text{ F g}^{-1}$  which was the maximum capacitance reported so far [53]. However, the electronic conductivity of  $\text{MnO}_2$  was low and so it delivered only low capacitance compared to its theoretical capacitance.

## **b. RuO<sub>2</sub>**

Among metal oxides, ruthenium oxide (RuO<sub>2</sub>) has very high metallic conductivity and excellent supercapacitive performance with high specific capacitance [54]. It was observed that RuO<sub>2</sub> has a large over-potential for oxygen evolution in acid solution [55]. However, RuO<sub>2</sub> has a very less over-potential for hydrogen evolution in acid solution [56]. Recently, a novel symmetric RuO<sub>2</sub>/RuO<sub>2</sub> supercapacitor with a high-operating voltage of 1.6 V is also built using the nanocrystalline hydrous RuO<sub>2</sub> electrode, exhibiting an energy density of 18.77 Wh kg<sup>-1</sup> at 500 W kg<sup>-1</sup> of power density [57]. However, RuO<sub>2</sub> has excellent specific capacitance; it is quite difficult to utilize RuO<sub>2</sub> in real application, owing to its very high cost and environmental toxicity. These drawbacks can be partially conquered by hybridization of other conductive materials with RuO<sub>2</sub>.

### **1.3.3. Hybrid supercapacitors**

The term “hybrid” supercapacitor (is quite different from the “asymmetric” supercapacitor) which should be used when pairing two electrode with different charge storage behavior, i.e., one faradaic and one capacitive, and the resulting device is in-between a supercapacitor and a battery [39]. Whereas, “asymmetric” supercapacitor covers a wider range of electrode combinations because it can be used for supercapacitors use electrodes of the same nature but with various mass loading, or two

electrodes using different materials. Brousse et al, recently suggested the term “asymmetric” should be used only when pseudocapacitive or capacitive electrodes are involved (such as  $\text{MnO}_2$ //activated carbon asymmetric supercapacitor) in order to avoid confusion with true “hybrid” devices [39, 58-60]. There are many literatures on the usage of faradaic electrode materials for electrochemical capacitor applications including our published reports. Unfortunately, some of these materials are denoted as “pseudocapacitive” materials although the reason that their electrochemical signature (i.e., charge/discharge curve and cyclic voltammogram) is akin to that of “battery electrodes”, as commonly found for  $\text{Ni}(\text{OH})_2$  in KOH electrolyte [39]. Generally, positive electrodes for hybrid supercapacitors are based on same faradaic reaction as we discussed in previous section. But, it is potential independent charge storage behavior which should be denoted as “battery like electrodes” of faradaic electrodes. Hybrid devices constitute a special case of asymmetric cells. In hybrid devices, various charge storage mechanisms are implemented in the positive and negative electrode materials. For instance, one electrode uses the double-layer storage mechanism (that is, porous carbon) while the other charge storage by means of faradaic reactions, that is, as occurs in transition metal oxides, except  $\text{MnO}_2$ ,  $\text{RuO}_2$  (which is called as asymmetric device as named by Brousse et al). Thus, the possible way to boosting the specific energy of the supercapacitor is to congregating the EDLC material as one electrode and faradaic material (ex, NiO) as another electrode.

### 1.3.3.1. Materials for hybrid supercapacitors

#### a. Ni(OH)<sub>2</sub>

Many advances have been published for Ni(OH)<sub>2</sub> in recent years, but unfortunately their effect has been alleviated by a uncertainty of nomenclature that was initiated to the scientific community working in that field at its early stages, whereby the Ni(OH)<sub>2</sub> electrode was denoted as “pseudocapacitive” rather than faradaic (battery type electrode) [61]. However, this is battery type faradaic electrode which can be used to fabricate hybrid supercapacitors. Generally, Ni(OH)<sub>2</sub> exhibits two types of polymorphs such as  $\alpha$  and  $\beta$  phase and both are in the form of hexagonal-crystal structure, where Ni(OH)<sub>2</sub> layers stacked along the c-axis. Presence of intercalated species such as water and charge-balancing anions (OH<sup>-</sup>) in the interlayer galleries differentiate  $\alpha$  and  $\beta$  phases [62]. Earlier, there are few reports on Ni(OH)<sub>2</sub> which mentioned its behavior like capacitance. The electrochemical performance of Ni(OH)<sub>2</sub> improved to a greater extend by tuning the basal spacing and morphology. Various synthetic methods have been adopted to prepare morphologically different nanostructured nickel hydroxides. Ultrathin nanoflakes of Ni(OH)<sub>2</sub> exhibited the SC of 1715 Fg<sup>-1</sup> with 0.6 V when compared with stacked nanoplatelets (1268 Fg<sup>-1</sup>) and hexagonal sheets (1029 Fg<sup>-1</sup>). Electrodeposited  $\alpha$ -Ni(OH)<sub>2</sub> exhibited a maximum capacitance of 3125 F g<sup>-1</sup>. But it delivered poor electrochemical stability due to the slow conversion of alpha-Ni(OH)<sub>2</sub> to beta-Ni(OH)<sub>2</sub> [63]. Ni(OH)<sub>2</sub> has much attention for the research by considering to its low toxicity, high stability, low cost and high theoretical capacity, which leads for useful

energy storage [64-68]. The electrochemical performance for freestanding Ni(OH)<sub>2</sub> particles was reported to largely compare with several parameters, including structural defects, crystallite size, and surface area [68, 69]. Ni(OH)<sub>2</sub> powders in the form of nanoflower-like, hollow microsphere-like, and nanoplate-like architecture show strong structural property relationship [70–72]. Therefore, successful preparation of Ni(OH)<sub>2</sub> with desired nanostructures is of predominant importance.

#### **b. Co<sub>3</sub>O<sub>4</sub>**

Cobalt-containing materials, such as Co<sub>3</sub>O<sub>4</sub> and Co(OH)<sub>2</sub>, have received great attentions due to their predominant advantages of natural abundance, high electroactivity, environmental friendliness and easy fabrication [73-76]. Amidst the battery-type electrode materials such as nickel or cobalt based oxides or hydroxides which undergo faradaic reactions, Co<sub>3</sub>O<sub>4</sub> is found to be one of potential alternatives owing to its high theoretical specific capacity, controllable size and shape, good redox performance, and structural identities [73]. As its capacity is directly associated with surface properties, any change in the surface morphology of this electroactive material has a great impact on its electrochemical performance. Recently, The Co<sub>3</sub>O<sub>4</sub>/MWCNTs nanohybrid shows superior electrochemical performance as positive electrode material in 1 M KOH solution [77]. More recently, Pan et al reported that A novel three-dimensional (3D) Co<sub>3</sub>O<sub>4</sub>@Co(OH)<sub>2</sub> hybrid nanostructure is synthesized by using two-step hydrothermal and electrodeposition methods [78]. The composite can be employed as an efficient electrode of a high-performance supercapacitor. However, the

supercapacitor applications of molybdenum oxide and its composites were limited because of their poor cycling stability, low energy density and/or slow reaction kinetics.

**c. Metal molybdates (M<sub>2</sub>MoO<sub>4</sub>; M – Co, Mn)**

To overcome these difficulties, after the pioneering work of Mai *et al.*, extensive work has been focused on metal molybdates [79]. Mai *et al.* have been synthesized heterostructured MnMoO<sub>4</sub>/CoMoO<sub>4</sub> nanowires by micro-emulsion method and its capacitance behavior was investigated. Heterostructured MnMoO<sub>4</sub>/CoMoO<sub>4</sub> nanowires showed a capacitance of 187 F g<sup>-1</sup> and excellent cycling stability [79]. Actually, metal molybdates are the significant class of semiconducting materials which widely used as catalysis [80], photoluminescence [81], sensors [82], magnetic [83], and energy storage applications especially in Li-ion batteries and supercapacitors [84 - 95]. More recently, Purushothaman *et al.* has synthesized  $\alpha$ -MnMoO<sub>4</sub> by using sol-gel spin coating method and achieved a specific capacitance of 998, 784 and 530 F g<sup>-1</sup> in three electrolytes such as H<sub>2</sub>SO<sub>4</sub>, *para*-toluene sulfonic acid (P-TSA) and HCl electrolytes respectively [87]. Xu *et al.* studied about the microwave synthesized CoMoO<sub>4</sub>/MWCNTs and achieved a specific capacitance of 170 F g<sup>-1</sup> at the current density of 1 A g<sup>-1</sup> for [88]. Liu *et al.* demonstrated a capacitance of 326 F g<sup>-1</sup> at 5 mA cm<sup>-2</sup> for CoMoO<sub>4</sub>·0.9H<sub>2</sub>O synthesized by hydrothermal process [89]. In recent work on combustion synthesized metal molybdates, the samples MnMoO<sub>4</sub> and CoMoO<sub>4</sub>·xH<sub>2</sub>O delivered a high specific capacitance of 126 and 401 F g<sup>-1</sup> at 5 mA cm<sup>-2</sup> respectively [90]. Hierarchical bismuth

molybdates nanowires have been prepared by facile electrodeposition-heat method, which exhibited a capacitance of  $1075 \text{ F g}^{-1}$  at  $1 \text{ A g}^{-1}$  and excellent cycle life up to 1000 cycles. Very recently a  $\text{CoMoO}_4$  nanorod was synthesized by chemical co-precipitation method and exhibited excellent supercapacitive performance ( $286 \text{ F g}^{-1}$  at  $5 \text{ mA cm}^{-2}$ ).

#### 1.4. Scope of this present work

The literature review depicts that the metal molybdates are one of the prominent electrode material for the high performance supercapacitor and their specific capacity value is mainly depends on the synthesis and morphology of the material. Hence, it is mandatory to identify the suitable synthesis procedure and new fabrication technique to prepare metal molybdate for the hybrid supercapacitors. In this regard, two different metal molybdates were chosen and evaluated their physico-chemical properties very carefully using different sophisticated techniques. From that, we chose one transition metal molybdate to improve their specific capacity and energy density by possible ways. Also, in order to make hybrid supercapacitors, we have fabricated the device with various types of carbon materials and novel strategies are also implemented. The objectives of this work are briefly outlined as follows,

- ❖ To synthesize nanostructured transition metal molybdates ( $\text{MMoO}_4$ ; M – Co and Mn) by sonochemical approach
- ❖ To synthesize  $\text{CoMoO}_4/\text{PANI}$  by in-situ polymerization chemical oxidative polymerization of aniline with the presence of  $\text{CoMoO}_4$  (prepared by sonochemical method)
- ❖ To investigate the structural properties of the prepared materials by X-ray diffraction (XRD), Raman spectroscopy, Fourier transform Infrared spectroscopy (FT-IR), X-ray photoelectron spectroscopy (XPS), scanning

- electron microscopy (FE-SEM), transmission electron microscopy (HR-TEM) and N<sub>2</sub> adsorption/desorption are used to characterize the synthesized materials
- ❖ To investigate the electrochemical properties of the prepared electrodes using cyclic voltammetry (CV), electrochemical impedance spectroscopy (EIS) and galvanostatic charge-discharge (GCD) techniques
  - ❖ To fabricate the hybrid supercapacitor using sonochemically prepared CoMoO<sub>4</sub> as positive electrode and hydrothermally prepared reduced graphene oxide as negative electrode
  - ❖ To prepare binder-free CoMoO<sub>4</sub> by hydrothermal method and study the effect of addition of potassium ferricyanide redox additive electrolyte into the electrode for improving the energy storage performances
  - ❖ To prepare the CNT deposited CoMoO<sub>4</sub>/Ni foam by dry reforming method and to use of waste catalysts instead CO<sub>2</sub> emission for fabricate the hybrid supercapacitors with the reduced graphene oxide
  - ❖ Finally to prepare CoMoO<sub>4</sub>@Co(OH)<sub>2</sub> core-shell structure on conductive textile for the fabrication of flexible, portable pouch-type supercapacitors which integrated with the solar cell for self-powered application

The results presented in this thesis may provide simple and effective approaches to preparing transition metal molybdates and their improved electrochemical performances via various approaches as electrode materials for hybrid supercapacitors. In addition, the demonstration of the capability of the fabricated flexible hybrid supercapacitors which

integrating with other energy harvesting technique provide a new promising direction in the field supercapacitor research for the development of next generation self-powered sustainable power source for wearable and flexible electronic devices

## 1.5. Structure of this thesis

This thesis is systematized into eight chapters,

**Chapter - 1** describes that the detailed introduction about the energy storage systems, electrochemical capacitors, mechanism of the different types of electrochemical capacitors, materials used in the different electrochemical capacitors.

**Chapter - 2** provides details of the chemicals and reagents, experimental setups and methods used in the thesis. Also it accords with the different characterization performed in the analysis of properties of the materials like structural, optical, composition, morphological and electrochemical properties. The details about the device and working electrodes preparation, electrolyte preparation, electrochemical measurement techniques and equations used for linear and non-linear profiles are presented.

**Chapter – 3** presents the synthesis of transition metal molybdates  $\text{MMoO}_4$  (M-Co, Mn) and their structural and electrochemical properties as a positive electrode material for supercapacitor applications.

**Chapter – 4** describes the synthesis of  $\text{CoMoO}_4/\text{PANI}$  composite as a positive electrode material for supercapacitor applications. Also it deals with the performance of hybrid supercapacitors using  $\text{CoMoO}_4$  as positive electrode and rGO as negative electrode.

**Chapter – 5** emphasizes the improved electrochemical performances of  $\text{CoMoO}_4$  by binder-free approach and followed by addition of redox additive electrolyte. The

mechanism of the addition of redox additive into the electrolyte has been outlined in detail.

**Chapter – 6** annotates the effective utilization of an idle carbon coated  $\text{CoMoO}_4/\text{Ni}$  foam catalyst for supercapacitor applications. The structural characterization has been before and after dry reforming reaction was investigated in detail. The mechanism of formation deposition of CNT over the catalyst by dry reforming reaction was explored in detail. This study suggests that use of this waste-to-energy material for supercapacitor application will be the effective way to fabricate low-cost electrode material without  $\text{CO}_2$  emission.

**Chapter – 7** defines the preparation of both positive and negative electrodes for flexible supercapacitors. The optimization in the preparation of  $\text{CoMoO}_4@\text{Co}(\text{OH})_2$  core-shell on conductive textile by electrochemical deposition technique has been explained in detail. The preparation of negative electrode by bio-waste derived carbon as negative electrode was studied in detail. The fabrication of flexible, portable pouch-type hybrid supercapacitor was performed using the prepared material and integration with the solar cell is demonstrated in detail.

**Chapter – 8** summarizes the salient features of this present work and suggestion for the future work.

## 1.6. References

1. P. Simon, Y. Gogotsi, *Nat. Mater.* **2008**, 7, 845.
2. L. Schlapbach, A. Züttel, *Nature*. **2001**, 414, 353.
3. G.Q. Zhang, H.B. Wu, H.E. Hoster, M.B. Chan-Park, X.W. Lou, *Energy Environ. Sci.* **2012**, 5, 9453.
4. C. A. Vincent and B. Scrosati, “Modern Batteries: An introduction to Electrochemical Power Sources”, Arnold, London (**1997**).
5. S. U. Falk and S. J. Salkind, “Alkaline Storage Batteries”, Wiley, New York (**1969**).
6. A. J. Salkind, J. J. Kelly and A. G. Cennone, in Hand Book of Batteries, D. Linden (Editor), McGraw Hill, New York (**1995**).
7. R. Koltz and M. Carlen, *Electrochem. Acta*, **2000**, 45, 2483.
8. B. E. Conway, *Electrochemical Supercapacitors: Scientific Fundamentals and Technological Applications*, New York (USA): Kluwar Academic (1999).
9. L. L. Zhang and X. S. Zhao, *Chem. Soc. Rev.*, **2009**, 38, 2520.
10. P. J. Hall and E. J. Bain, *Energy Policy*, **2008**, 36, 4352.
11. M. Conte, *Fuel Cells*, **2010**, 10, 806.
12. M. Inagaki, H. Konno and O. Tanaike, *J. Power Sources*, **2010**, 195, 7880.
13. G. Wang, L. Zhang and J. Zhang, *Chem. Soc. Rev.*, **2012**, 41, 797.

14. S. T. Senthilkumar, R. Kalai Selvan and J. S. Melo, *J. Mater. Chem. A*, **2013**, 1, 12386.
15. R. C. Bansal and M. Goyal, *Activated Carbon Absorption*, New York (USA), CRC Press Taylor and Francies (**2005**).
16. S. T. Senthilkumar, B. Senthilkumar, S. Balaji, C. Sanjeeviraja and R. Kalai Selvan, *Mater. Res. Bull.*, **2011**, 46, 413
17. E. Frackowiak and F. Beguin, *Carbon*, **2001**, 39, 937.
18. L. Wei and G. Yushin, *Nano Energy*, **2012**, 1, 552.
19. S. T. Senthilkumar, R. Kalai Selvan and J. S. Melo, *AIP Proceed*, **2013**, 124, 1538.
20. H. Zhang, G. Cao, Z. Wang, Y. Yang, Z. Shi and Z. Gu, *Nano Lett.*, **2008**, 8, 2664.
21. E. Frackowiak, K. Metenier, V. Bertagna and F. Beguin, *Applied Physics Letters*, **2000**, 77, 2421.
22. K. H. An, W. S. Kim, Y. S. Park, Y. C. Choi, S. M. Lee, D. C. Chung, D.J. Bae, S. C. Lim, and Y. H. Lee, *Adv. Mat.*, **2001**, 13, 497.
23. K. H. An, W. S. Kim, Y. S. Park, J. M. Moon, D. J. Bae, S. C. Lim, Y. S. Lee and Y. H. Lee, *Adv. Funct. Mater*, **2001**, 11, 387.
24. M. M. Shaijumon, F. S. Ou, L. J. Ci, P. M. Ajayan, *Chem. Commun.*, **2008**, 20, 2373.
25. B. J. Yoon, S. H. Jeong, K. H. Lee, H. S. Kim, C. G. Park, J. H. Han, *Chem. Phys. Lett.*, **2004**, 388, 170.
26. D. Li, R.B. Kaner, Graphene-based materials, *Science*, **2001**, 320, 1170.

27. S. Stankovich, D.A. Dikin, G.H.B. Dommett, K.M. Kohlhaas, E.J. Zimney, E.A. Stach, et al., *Nature* **2006**, 442, 282.
28. Y.B. Tan, J.M. Lee, *J. Mater. Chem. A* **2013**, 1, 14814.
29. C. Xu, B. Xu, Y. Gu, Z. Xiong, J. Sun, X.S. Zhao, *Energy Environ. Sci.* **2013**, 6, 1388.
30. D. Zhang, X. Zhang, Y. Chen, C. Wang, Y. Ma, *Electrochim. Acta* **2001**, 69, 364.
31. D. Sun, X. Yan, J. Lang, Q. Xue, *J. Power Sources* **2013**, 222, 52.
32. B. Zhan, C. Li, J. Yang, G. Jenkins, W. Huang, X. Dong, *Small* **2014**, 10 4042.
33. L. Vicarelli, M.S. Vitiello, D. Coquillat, A. Lombardo, A.C. Ferrari, W. Knap, et al., *Nat. Mater.* **2012**, 11, 865.
34. F. Li, S. Gan, D. Han, L. Niu, *Electroanalysis* **2015**, 27, 2098.
35. M. D. Stoller, S. J. Park, Y. W. Zhu, J. H. An and R. S. Ruoff, *Nano Lett.*, **2008**, 8, 3498.
36. S. R. C. Vivekchand, C. S. Rout, K. S. Subrahmanyam, A. Govindaraj and C. N. R. Rao, *J Chem. Sci.*, **2008**, 120, 9.
37. K. Wang, L. Li and X. Wu, *Int. J. Electrochem. Sci.*, **2013**, 8, 6763
38. Collins English Dictionary - Complete & Unabridged 10th Edition, Harper Collins Publishers, <http://dictionary.reference.com/browse/pseudo>.
39. T. Brousse, D. Bèlanger, J. W. Long, *J. Electrochem. Soc* **2015**, 162 (5) A5185.
40. S. Ardizzone, G. Fregonara, and S. Trasatti, *Electrochim. Acta*, **1990**, 35, 263.
41. J. P. Zheng, P. J. Cygan, and T. R. Jow, *J. Electrochem. Soc.*, **1995**, 142, 2699.

42. H. Y. Lee and J. B. Goodenough, *J. Solid State Chem.*, **1999**, 144, 220.
43. T. Brousse, M. Toupin, R. Dugas, L. Athouël, O. Crosnier, and D. Bélanger, *J. Electrochem. Soc.*, **2006**, 153, A2171.
44. Y. Zhang, H. Feng, X. Wu, L. Wang, A. Zhang, T. Xia, H. Dong, X. Li and L. Zhang, *Int. J. Hydro. Energy*, **2006**, 34, 4889.
45. C. Lin, J. A. Ritter, B. N. Popov, and R. E. White, *J. Electrochem. Soc.*, **1999**, 146, 3168.
46. G. Zhang and S. Zhang, *J. App. Electrochem.*, **2008**, 39, 1033.
47. J. Li, F. Gao, Y. Jing, R. Miao, K. Wu and X. Wang, *Int. J. Miner. Metall. Mater.*, **2009**, 16, 576.
48. M. Toupin, T. Brousse and D. Bélanger, *Chem. Mater.*, **2004**, 16, 3184.
49. W. Xing, F. Li, Z. Yan and G. Q. Lu, *J. Power Sources*, **2004**, 134, 324.
50. J. N. Broughton and M. J. Brett, *Electrochim. Acta*, **2005**, 50, 4814.
51. E. Goikolea, B. Daffos, P. L. Taberna and P. Simon, *Mater. Renew Sustain. Energy*, **2013**, 2, 16.
52. X. Lu, D. Zheng, T. Zhai, Z. Liu, Y. Huang, S. Xie and Y. Tong, *Energy Environ. Sci.*, **2011**, 4, 2915.
53. S. C. Pang, M. A. Anderson and T. W. Chapman, *J. Electrochem. Soc.*, **2000**, 147, 444.
54. T. S. Hyun, J. E. Kang, H. G. Kim, J. M. Hong, and I. D. Kim, *Electrochem. Solid-State Lett.*, **2009**, 12, A225.

55. T. C. Liu, W. G. Pell, and B. E. Conway, *Electrochim. Acta*, **1997**, 42, 3541.
56. T. C. Wen and C. C. Hu, *J. Electrochem. Soc.*, **1992**, 139, 2158.
57. H. Xia, Y. S. Meng, G. Yuan, C. Cui, L. Lu, *Electrochem. Solid-State Lett.* **2012**, 15  
A60.
58. T. Brousse, M. Toupin, and D. B´elanger, *J. Electrochem. Soc.*, **2005**, 151, A614.
59. D. B´elanger, T. Brousse, and J. W. Long, *Interface*, **2008**, 17, 49.
60. J. W. Long, D. B´elanger, T. Brousse, W. Sugimoto, M. B. Sassin, and O. Crosnier,  
*MRS Bull.*, **2011**, 36, 513.
61. G. Hu, C. Tang, C. Li, H. Li, Y. Wang, and H. Gong, *J. Electrochem. Soc.*, **2011**,  
**158**, A695.
62. H. Jiang, T. Zhao, C. Li and J. Ma, *J. Mater. Chem.*, **2011**, 21, 3818.
63. GW. Yang, CL. Xu and HL. Li, *Chem. Commun.*, **2008**, 48, 6537.
64. H. Wu, M. Xu, H. Wu, J. Xu, Y. Wang, Z. Peng, G. Zheng, *J. Mater. Chem.*  
**2012**, **22**, 19821.
65. G. Wang, X. Lu, T. Zhai, Y. Ling, H. Wang, Y. Tong, Y. Li, *Nanoscale* **2012**, 4,  
3123.
66. G. Li, X. Wang, H. Ding, T. Zhang, *RSC Advances* **2012**, 2, 13018.
67. J. Li, W. Zhao, F. Huang, A. Manivannan, N. Wu, *Nanoscale* **2005**, 3, 5103.
68. C. Tang, X. Yin, H. Gong, *ACS Appl. Mater. Interfaces* **2013**, 5, 10574.
69. D. P. Dubal, V. J. Fulari, C. D. Lokhande, *Microporous Mesoporous Mater.* **2012**,  
151, 511.

70. X. Ni, Y. Zhang, S. Wang, Z. Zhang, L. Fei, Y. Qian. *Chem. Lett.* **2005**, 34, 1408.
71. Y. Wang, Q. Zhu, H. Zhang, *Chem. Commun.* **2005**, 41, 5231.
72. X. Wang, L. Liu, R. Liu, F. Shen, Z. Cui, W. Chen, T. Zhang, **2015**, 11(6), 731.
73. P. Balaya, *Energy Environ. Sci.*, **2008**, **1**, 645.
74. H. Zhang, G.P. Cao, Z.Y. Wang, Y.S. Yang, Z.J. Shi, Z.N. Gu, *Nano Lett.* **2008**, 8, 2664.
75. X.X. Qing, S.Q. Liu, K.L. Huang, K.Z. Lv, Y.P. Yang, Z.G. Lu, D. Fang, X.X. Liang, *Electrochim. Acta* **2011**, 56, 4985.
76. X.H. Xia, J.P. Tu, Y.J. Mai, X.L. Wang, C.D. Gu, X.B. Zhao, *J. Mater. Chem.* **2011**, 21, 9319.
77. X. Wang, M. Li, Z. Chang, Y. Wang, B. Chen, L. Zhang, Y. Wu, *J. Electrochem. Soc.*, **2015**, 162 (10), A1966.
78. X. Pan, F. Ji, L. Kuang, F. Liu, Y. Zhang, X. Chen, K. Alameh, B. Ding, *Electrochim. Acta* **2016**, 215, 298.
79. L-Q. Mai, F. Yang, Y-L. Zhao, X. Xu, L. Xu and Y-Z. Luo, *Nat. Commun.* **2011**, 2, 381.
80. R. Rangel, P. Bartolo-Perez, E. Martinez, X. A. Trejo-Cruz, G. Diaz and D. H. Galvan, *Catalysis Science and Technology*, **2012**, 2, 847.
81. W-S. Wang, L. Zhen, C-Y. Xu and W-Z. Shao, *Cryst. Growth Des.*, **2009**, 9, 1558.
82. Q. Dai, G. Zhang, P. Liu, J. Wang and J. Tang, *Inorg. Chem.* **2012**, 51, 3232.
83. D. M. Bubb, D. Cohen and S. B. Qadri, *Appl. Phys. Lett.*, **2005**, 87, 131909.

84. J. Haetge, I. Djerdj and T. Brezesinski, *Chem. Commun.*, **2012**, 48, 6726.
85. Y. Dong, Y. Wan, Y-L. Min, W. Zhang, S-H. Yu, *Inorg. Chem.*, **2008**, 47, 7813.
86. W. Xiao, J. S. Chen, C. M. Li, R. Xu and X. W. Lou, *Chem. Mater.*, **2010**, 22, 746.
87. K. K. Purushothaman, M. Cuba and G. Muralidharan, *Mater. Res. Bull.* **2012**, 47 (2012) 3348.
88. Z. Xu, Z. Li, X. Tan, C. M. B. Holt, L. Zhang, B. S. Amirkhiz and D. Mitlin, *RSC Adv.*, **2012**, 2, 2753.
89. M-C. Liu, L-B. Kong, X-J. Ma, C. Lu, X-M. Li, Y-C. LuO and L. Kang, *New. J. Chem.* **2012**, 36, 1713.
90. B. Senthilkumar, K. Vijaya Sankar, R. Kalai Selvan, M. Danielle and M. Manickam, *RSC Adv.*, **2013**, 3, 352.
91. Z-Q. Liu, L-Y. Tang, N. Li, K. Xiao, J. Wang, J-H. Zhang, Y-Z. Su and Y-X. Tong, *J. Electrochem. Soc.* **2012**, 159, D582.
92. M-C. Liu, L-B. Kong, C. Lu, X-J. Ma, X-M. Li, Y-C. LuO and L. Kang, *Mater. Lett.*, **2013**, 94, 197.
93. M-C. Liu, L. Kang, L-B. Kong, C. Lu, X-J. Ma, X-M. Li and Y-C. LuO, *RSC Adv.*, **2013**, 3, 6472.
94. K-S. Park, S-D. Seo, H-W. Shim and D-W. Kim, *Nano Res. Let.*, **2012**, 7, 35.
95. M-C. Liu, L-B. Kong, C. Lu, X-J. Ma, X-M. Li, Y-C. LuO, L. Kang, *J. Mater. Chem. A*, **2013**, 1, 1380.

## CHAPTER-2

### Materials Characterization and Electrochemical Techniques

This chapter narrates the detailed experimental methods and the characterization techniques, which are adopted for the present investigation. To achieve the research objective, experimental work was done in the laboratory, followed by physicochemical characterization and evaluation of the electrochemical properties of the obtained materials. The typical materials synthesis methods such as sonochemical, hydrothermal, dry reforming, *in-situ* polymerization, electrodeposition and modified hummers method for graphene oxide synthesis; basic materials characterization techniques for structure, morphology, composition, surface area and optical properties confirmation; electrode fabrication, cell assembly, and electrochemical measurement is discussed in detail.

## 2.1. Chemicals and Apparatus

All chemicals were used in these thesis experiments were of research grade and were used without any further purification. The list of materials and chemical used in this thesis are given in **Table 2.1**.

**Table 2.1** Materials and chemicals used in this thesis.

<b>Chemicals</b>	<b>Formula</b>	<b>Purity</b>	<b>Supplier</b>
Cobalt nitrate hexahydrate	$\text{Co}(\text{NO}_3)_2 \cdot 6\text{H}_2\text{O}$	97%	Daejung Chemicals & Metals Co. Ltd, Korea
Cobalt chloride hexahydrate	$\text{CoCl}_2 \cdot 6\text{H}_2\text{O}$	97%	Daejung Chemicals & Metals Co. Ltd, Korea
Hydrochloric acid	HCl	35%	Daejung Chemicals & Metals Co. Ltd, Korea
Sodium sulfate (anhydrous)	$\text{Na}_2\text{SO}_4$	99%	Daejung Chemicals & Metals Co. Ltd, Korea
Potassium permanganate	$\text{KMnO}_4$	99.3%	Daejung Chemicals & Metals Co. Ltd, Korea
Aniline	$\text{C}_6\text{H}_5\text{NH}_2$	98%	Daejung Chemicals & Metals Co. Ltd, Korea
Potassium hydroxide	KOH	85%	Daejung Chemicals & Metals Co. Ltd, Korea
Sodium molybdate	$\text{Na}_2\text{MoO}_4$	98%	Sigma Aldrich
Potassium chloride	KCl	99%	Daejung Chemicals & Metals Co. Ltd, Korea
Polyvinylidene fluoride (PVDF)	$(\text{CH}_2\text{CF}_2)_n$	-	Sigma Aldrich
<i>N</i> -Methyl-2-pyrrolidinone (NMP)	$\text{C}_5\text{H}_9\text{NO}$	99.7%	Daejung Chemicals & Metals Co. Ltd, Korea

Ethanol	$\text{CH}_3\text{CH}_2\text{OH}$	99.9%	Fisher Scientific
Acetone	$\text{C}_3\text{H}_6\text{O}$	99.8%	Fisher Scientific
Phosphoric acid	$\text{H}_3\text{PO}_4$	98%	Daejung Chemicals & Metals Co. Ltd, Korea
Polyvinyl alcohol (PVA)	$(\text{C}_2\text{H}_4\text{O})_x$	99+%	Sigma Aldrich
Graphite	C	75%	Sigma Aldrich
Sulfuric acid	$\text{H}_2\text{SO}_4$	98%	Daejung Chemicals & Metals Co. Ltd, Korea
Hydrogen peroxide	$\text{H}_2\text{O}_2$	30%	Junsei Chemical Co. Ltd. Japan
Sodium hydroxide	NaOH	98%	Daejung Chemicals & Metals Co. Ltd, Korea
Potassium hydroxide	NaOH	98%	Daejung Chemicals & Metals Co. Ltd, Korea
Hydrazine hydrate	$\text{NH}_2\text{NH}_2 \cdot x\text{H}_2\text{O}$	80%	Daejung Chemicals & Metals Co. Ltd, Korea
Methanol	$\text{CH}_4\text{O}$	99.8%	Daejung Chemicals & Metals Co. Ltd, Korea
Dimethyl formamide (DMF)	$\text{C}_3\text{H}_7\text{NO}$	99.8%	Daejung Chemicals & Metals Co. Ltd, Korea
Poly(tetrafluoroethylene) (PTFE)	$(\text{C}_2\text{F}_4)_n$	-	Sigma Aldrich
Nickel foam	Ni	-	Heze Jiaotong Group Corporation, China
Stainless steel	316L SS	-	Nilaco, Japan
Ammonium persulfate	$(\text{NH}_4)_2\text{S}_2\text{O}_8$	98%	Kanto Chemical Co. Inc, Japan
Nitric acid	$(\text{HNO}_3)$	60-62%	Junsei Chemical Co. Ltd. Japan
Carbon fabric	C	-	FCC International, Korea

The general equipment's used for materials preparation and electrochemical measurements are given **Table 2.2**.

**Table 2.2** Apparatus used in the research project

<b>Apparatus</b>	<b>Model or Specification</b>	<b>Manufacturer</b>
Hot plate & Magnetic stirrer	MS300HS	M TOPS
Autoclave	PTFE container	Latech
Oven	OF-02 GW	JEIO Tech
Microwave	MW-202BG	LG
Furnace	CRF-M15	Ceber
Tube furnace		
Centrifuge	GYROZEN -1580 MG	Gyrozen
Ultrasonicator	SONIC VCX 500 model (20 kHz, 500 W)	Sonics Materials, Inc.
Ultrasonic cleaner	ELMASONIC S15H	Elmasonic
Balance	AUW220D	Shimadzu
Electrochemical work station	AUTOLAB PGSTAT302N	Eco Chemie
Keithley Nano voltmeter& picoammeter	2182A & 6485	Keithley
Spin coater	SPIN-1200	Midas System

## **2.2. Materials synthesis**

The syntheses of nanomaterials with controlled size and shape have attracted rapidly growing interest for many practical and technological applications. To fulfill the research tasks, the electroactive materials were mainly synthesized using following methods such as hydrothermal, microwave, electrodeposition, thermal treatment, etc.,

### **2.2.1. Sonochemical synthesis**

Sonochemical method becomes more potential candidate in the synthesis of variety of nanomaterials including nano chalcogenides, metal and metal oxide nanoparticles [1, 2]. The mechanism of sonochemistry depends on the acoustic cavitation phenomenon, i.e., the formation, growth, and collapse of bubbles in liquid medium [3, 4]. According to the hot spot theory, extremely high temperature about 5000 K, pressure about 20 MPa and very high cooling rate about  $10^{10}$  Ks<sup>-1</sup> arises during the acoustic cavitation, thus enabling reaction conditions which further results in unique properties of the synthesized particles. CoMoO<sub>4</sub>, MnMoO<sub>4</sub> nanostructures are prepared using sonochemical method and presented in first two chapters.

### **2.2.2. *In-situ* polymerization**

In other words, it is also called as an in-situ chemical oxidative polymerization reaction. The conductive polymers such as polyaniline (PANI), polypyrrole (Ppy) and so on are widely used in the field of organic polymer electronics because of its tunable electrical conductivity and easy preparation. Oxidative polymerization is a method, in

which monomer undergoes a chain reaction with the formation of regular macromolecules, and growing chains are simultaneously organized into complex supramolecular structures [5, 6]. As a result, conducting polymer containing stable supramolecular structures with various morphologies is formed. Most of these structures cannot be dissolved or melted without destruction of polymer chains and changing properties of the polymer. Therefore, synthesis is the only unique instrument allowing us to control structure of polymer chains and obtain nanostructured forms of the conducting polymer and its composites with other materials [7, 8].

### **2.2.3. Hydrothermal synthesis**

Hydrothermal approach is one important technique that has many advantages, such as low cost, environmentally friendly, excellent morphology, and the possibility of achieving high accessible active sites. Hydrothermal method has considered as one of the popular promising approaches for preparing nanomaterials with different morphologies. Hydrothermal synthesis is a process that utilizes \homo- or heterogeneous phase reactions in liquid aqueous medium at the pressure more than 1 atm and at the temperature above 100 °C to crystallize nanostructured materials directly from precursor solution [9, 10]. The chemical reaction was performed in a sealed stainless steel autoclave, that can sustain even at high temperatures and pressures for a long time in which a nutrient is supplied along with water. A temperature slope was maintained between the two ends of opposite side of growth chamber. At the side of hotter end, the

precursor solute dissolves, while at the side of cooler end, it is deposited on a seed crystal, growing the desired shape of crystal [11, 12]. The reduced graphene oxide, binder-free CoMoO<sub>4</sub> on Ni foam, lab waste tissue paper derived activated carbon were prepared through hydrothermal technique as presented in this thesis.

#### **2.2.4. Dry reforming reaction**

Dry (CO<sub>2</sub>) reforming of hydrocarbon (DR) is a well-studied reaction that is of both scientific and industrial importance [13, 14]. This reaction produces syngas that can be used to produce a wide range of products, such as higher alkanes and oxygenates by means of Fischer–Tropsch synthesis [15]. DR is inevitably accompanied by deactivation due to carbon deposition. DRM is also a highly endothermic reaction and requires operating temperatures of 800–1000 °C to attain high equilibrium conversion of hydrocarbon (such as methane, propane) and CO<sub>2</sub> to H<sub>2</sub> and CO and to minimize the thermodynamic driving force for carbon deposition DRR shows advantages, combining SNG production and greenhouse gas utilization [16]. It uses hydrocarbons (e.g., methane, propane) with CO<sub>2</sub> gas to produce SNG. DR has been performed to grow carbon on the CoMoO<sub>4</sub>/Ni foam electrode and presented in **Chapter-6**.

#### **2.2.5. Electrochemical deposition**

The electrochemical deposition or e-coating, cathodic electrodeposition, or anodic electrodeposition, is a deposition process in which metal ions (colloidal particles)

suspended in a solution are migrated by an electric field and deposit on the surface of the substrate [17]. The deposition process can be either cathodic or anodic reaction depending on the work piece to be coated (cathode or anode). The process is useful for applying materials to any electrically conductive surface. It possesses some advantages process, possibility of large scale application, low temperature processing and direct control of thickness.  $\text{CoMoO}_4@\text{Co}(\text{OH})_2$  core-shell nanostructure on conductive textile was prepared by using electrodeposition method as presented in **Chapter 7**.

#### **2.2.6. Graphene oxide synthesis by modified Hummer's method**

Graphene oxide was successfully synthesized from expandable graphite powder by the modified Hummer's method [18, 19]. Briefly, graphite powder (2 g) was stirred in 98%  $\text{H}_2\text{SO}_4$  (35 mL) for 2 h.  $\text{KMnO}_4$  (6 g) was gradually added to the above solution while keeping the temperature less than 20 C. The mixture was then stirred at 35–40 °C for 30 min. The resulting solution was diluted by adding 90 mL of water under vigorous stirring and a dark brown color suspension was obtained. The resulting solution was diluted by adding 50 mL of water and the mixture was heated at 90 °C for 30 min, leads to the formation of dark brown solution. The reaction was terminated by the addition of 150 mL of distilled water and 30%  $\text{H}_2\text{O}_2$  solution (10 mL). After continuously stirred for 2 h, the mixture was washed by repeated centrifugation and filtration using 5% HCl aqueous solution in order to remove the residual metal ions. Further, the centrifugation process was repeated with distilled water until the pH of the solution becomes neutral.

The prepared GO was used for the synthesis of reduced graphene oxide (rGO) for negative electrode and to prepare CoMoO<sub>4</sub>/rGO composite and presented in **Chapter 4**.

### **2.3. Materials characterization**

The synthesized nanomaterials were analyzed using several characterization techniques to identify the crystal phase, morphology, microstructure, size, composition and surface area. The detailed experimental conditions are given below.

#### **2.3.1. X-ray diffraction (XRD)**

X-ray diffractometer (XRD) is an important analytical technique to determine the phase purity, phase of the crystal, structure, and crystal size. The synthesized samples were performed by using Rigaku X-ray diffractometer (XRD) operated at the power of 40 kV and current of 40 mA with CuK<sub>α</sub> radiation in the range 2θ angle of 10-80° with a step of 0.02°.

#### **2.3.2. Raman spectroscopy**

The Raman spectrum is a non-destructive tool towards and sensitive technique the structural defects and disorders, crystallization in nanostructures. Further, it is also used to study the bonding nature of various carbon materials such as graphene oxide, carbon nanotube and reduced graphene oxide. Raman spectra of the prepared CoMoO<sub>4</sub> and carbon samples were studied using a Model: LabRam HR800 micro Raman spectroscope (manufacturer: Horiba Jobin-Yvon, France). The Raman spectrum was operated at an excitation wavelength of 514 nm at the different laser power using Ar<sup>+</sup>

ion laser. The spectral region of 100–3500  $\text{cm}^{-1}$  was used to collect the data were using an acquisition time of 10-s data point.

### **2.3.3. Fourier transform infrared (FT-IR) spectrometer**

FT-IR spectroscopy is an important technique for the direct monitoring of interaction between adsorbed molecules and the material. FT-IR spectra were measured at room temperature with an FT-IR spectrometer (Thermo Scientific Systems, Nicolet-6700) using the KBr pellet technique in the range of 4000 to 400  $\text{cm}^{-1}$ .

### **2.3.4. Field-emission scanning electron microscopy**

The morphology and particle size of the prepared material is very important to investigate the electrochemical reaction and it was easily identified using the Field-emission scanning electron microscope. Here we used, FE-SEM (Model: FE-SEM, JSM-6700F, JEOL Ltd) with a 5 kV of acceleration voltage and 10  $\mu\text{A}$  of filament current. Prior to measurement, the as-prepared samples were fixed onto a double-face conducted tape mounted on a metal stud and coated with platinum with a sputter coater (Cressing ton sputter coater -108 auto).

### **2.3.5. High-resolution transmission electron microscopy**

The particle size, microstructure, and crystalline phase of the nanomaterials were studied by the high-resolution transmission electron microscopy (HR-TEM, JEOL–JEM 200CX) with an accelerating voltage of 200 kV, The samples used for TEM observations were prepared by dispersing the NPs in ethanol followed by ultrasonic

vibration for 5 min, and then placing a drop of the dispersion onto a copper grid before loading in to the instrument.

### **2.3.6. Energy dispersive X-ray spectroscopy analysis (EDS)**

The elemental composition of the prepared samples was measured using Energy Dispersive X-ray Spectroscopy (EDS). The EDS analysis was done with the Field-emission Scanning Electron Microscopy (FE-SEM) instrument (Zeiss ultra FE-SEM instruments) with a separate EDS detector (INCA) connected to that instrument.

### **2.3.7. X-ray photoelectron spectroscopy (XPS)**

The chemical composition and the state of elements present in the outermost part of samples was obtained by X-ray photoelectron spectroscopy (XPS) techniques using ESCA- 2000, VG Microtech Ltd and Theta Probe AR-XPS system (Thermo Fisher Scientific, U.K). Here a monochromatic X-ray beam source at 1486.6 eV (Aluminum anode) and 14 kV was used to scan upon the sample surface. A high flux X-ray source with Aluminum anode was used for X-ray generation, and a quartz crystal monochromatic was used to focus and scan the X-ray beam on the sample.

### **2.3.8. Brunauer, Emmett and Teller (BET) surface area analysis**

Nitrogen (N<sub>2</sub>) adsorption-desorption isotherm measurement was carried out to determine the surface area, pore-volume and pore-size distribution of the as-prepared samples. The Brunauer-Emmett-Teller (BET) analysis was performed with Quantachrome RASiQwin™ c 1994-2012, Quantachrome Instruments v2.02 and nitrogen (N<sub>2</sub>) gas was used as an adsorptive for the determination of the above

parameters. The specific surface area of the samples was calculated by using the multiple-point BET model. The pore size distributions were obtained from the adsorption/ desorption branch of the isotherm by the Horvath-Kawazae (HK) method. The total pore volume was calculated from the volume of nitrogen adsorbed at a relative pressure of  $P/P_0 = 0.95$ .

## **2.4. Electrode fabrication**

### **2.4.1. Single electrode**

The working electrodes were prepared by various methods depends on the nature of the electroactive materials. Briefly, the as-prepared samples, carbon black, and poly(tetrafluoroethylene) (PTFE) or polyvinylidene difluoride (PVDF) were mixed in a mass ratio of 75:20:5 or 80:10:10 and dispersed in the ethanol or N-methyl pyrrolidone (NMP), solution, resulting in a homogeneous paste. For manual coating, the resulting solution mixture was coated onto a current collector substrate (stainless steel, nickel foam, carbon cloth, and conductive fabric) in  $1\text{ cm} \times 1\text{ cm}$  with a spatula for the fabrication of the electrodes. For hierarchical growth, these substrates directly to grow the active material. The electrodes were then dried at  $80\text{ }^\circ\text{C}$  for overnight in a vacuum oven. The loading mass of the electrode active material was measured using balance before and after loading of mass on current collector. The photographs of current collector used in this study are shown in **Figure 2.1.1**.

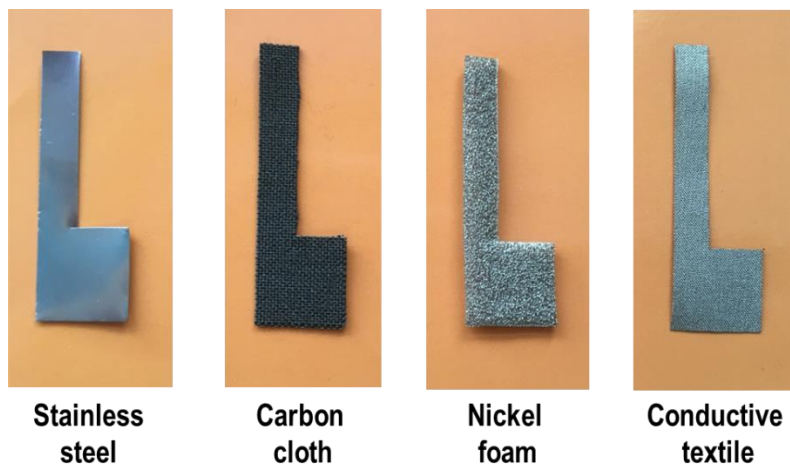


**Figure 2.1.1** Photographic images of current collectors used in this study.

#### **2.4.2. Hybrid device**

Since this study focuses the improvement on the positive electrode and its efficiency on hybrid device, hybrid supercapacitors are fabricated using  $\text{CoMoO}_4$  based electrode as positive electrode and carbon based electrode as negative electrode. The as-prepared positive and negative electrode were pressed together and separated by a commercial filter paper separator. Prior to assembling process, both the electrodes are charge balanced by balancing the mass of the electrode. The electrochemical measurements of the hybrid supercapacitors were carried out in 2 M KOH aqueous electrolyte using the electrochemical working station in a two electrode cell (such as sandwich type, coin cell type and pouch-type) at room temperature.

## 2.5. Electrochemical characterization

To confirm the capacitive behavior and quantify the specific capacity, specific capacitance of the fabricated electrodes, cyclic voltammetry (CV), and galvanostatic charge/discharge (GCD) and electrochemical impedance spectroscopy (EIS) tests were performed. All of the electrochemical experiments were investigated using an AUTOLAB PGSTAT302N electrochemical work station (**Figure 2.1.2**). A typical three-electrode experimental cell, equipped with a working electrode, platinum foil as a counter electrode, and an Ag/AgCl or SCE reference electrode, was used for measuring the electrochemical properties of the working electrodes. Three electrode configurations are common in fundamental research where it allows one electrode to be studied in isolation, without complications from the electrochemistry of the other electrodes. For measuring packaged supercapacitors (two electrode cell configuration), both reference and counter electrode leads are connected to the negative (-) terminal of the capacitor. The working electrode and working sense leads are connected to the positive (+) terminal. Various aqueous solutions were used as the electrolytes, which include 1 M  $\text{H}_2\text{SO}_4$ , 2 M NaOH, and 2 M KOH.



**Figure 2.1.2.** Electrochemical workstation.

### **2.5.1. Cyclic voltammetry (CV)**

CV measurement is popularly known to be a suitable tool for evaluating the difference between capacitor type EDLC behaviors, battery like faradaic nature in an electrochemical reaction. In CV measurement, the ranges of voltage scan rates have been given from a lower to an upper limit at constant voltage. The evolution of current was measured as voltage function. The characteristics of the linear sweep voltammogram recorded depend on a rate of the electron transfer reaction, chemical reactivity of the active species and the voltage scan rate. The CV data of the electrodes were received by using the changing of scan rates: 5, 10, 25, 50, 75, 100, 150 and 200  $\text{mV s}^{-1}$ .

### **2.5.2. Galvanostatic charge/discharge (GCD)**

The GCD technique are the most essential and direct strategy to investigate the applicability of energy storage devices. A repetitive loop of charge and discharge is

denoted as a cycle. Principally, charge and discharge are measured at constant current density until the reach of set potential. The GCD curves were produced at the various current densities.

### **2.5.3. Electrochemical impedance spectroscopy (EIS)**

EIS is a most powerful and non-destructive tool to evaluate the capacitive behavior and resistance for the surface of the electrode material. This makes the possibility for further electrochemical measurements. EIS is the most common method for measuring the equivalent series resistance of energy storage devices. It also permits developing models to annotate, underlying reaction mechanisms. Using these models, capacitor non idealities can be found. A sinusoidal alternate current (AC) excitation signal is applied during an EIS experiment to the investigated system and AC response is measured. Scanning of frequency in a wide range from lower to higher creates the reaction steps with different rate constants, such as charge transfer, mass transport, and chemical reaction. In the study, EIS experiment for prepared electrodes was conducted between the frequency ranges of 0.1 Hz and 100 kHz. Nyquist plot was used to analyze the data and, are the plotted with the real component ( $Z'$ ) against imaginary component ( $-Z''$ ) which show the response of frequency for the electrode/electrolyte system.

#### 2.5.4. Calculation of electrochemical parameters

The electrochemical parameters, such as the specific capacitance, Coulombic efficiency ( $\eta$ ), energy ( $E$ ), and power density ( $P$ ) are important parameters for the investigation of the capacitive behavior of electrochemical cells [20-26].

##### **For linear charge/discharge profiles:**

The specific capacitance ( $C_{sp}$ ) of the electrodes can be calculated from the CV curves according to the following equation,

$$C_{sp} = \frac{\int I(V)dv}{v(morA)\Delta V} \quad (2.1)$$

Where,  $m$  indicates the mass of the electroactive material (g),  $A$  is the area of the electrode ( $\text{cm}^2$ ),  $v$  represents the potential scan rate ( $\text{Vs}^{-1}$ ),  $\Delta V$  is the voltage range of one sweep segment (V) and  $\int I(V)dv$  is the integrated area under the CV curve loop (AV).

The specific capacitance of the electrodes can also be calculated from GCD curves according to the following formula,

$$C_s = \frac{I\Delta t}{(MorA)\Delta V} \quad (2.2)$$

where,  $C_s$  is the specific capacitance ( $\text{F g}^{-1}$ ),  $I$  is the discharge current (A),  $\Delta t$  is the discharge time (s),  $M$  is the mass of the electroactive material (g),  $A$  is the area of the electrode ( $\text{cm}^2$ ) and  $\Delta V$  is the potential range (V).

The suitability of electrodes for supercapacitor applications was further evaluated by examining its Coulombic efficiency ( $\eta$ ), energy ( $E$ ) and power density ( $P$ ). The Coulombic efficiency, energy density and power density values were calculated from galvanostatic charge/discharge curves by using the following equations:

$$E = \frac{C_m (\Delta V)^2}{7.2} \quad (2.3)$$

$$P = \frac{E}{\Delta t} \quad (2.4)$$

Where  $E$  is the energy density ( $\text{Wh Kg}^{-1}$ ),  $\Delta V$  is the potential window (V),  $P$  is the power density ( $\text{W kg}^{-1}$ ) and  $\Delta t$  is the discharge time (s).

**For non-linear charge/discharge profile;**

$$Q = \frac{I \times \Delta t}{A(\text{or})M} \quad (2.5)$$

$$E = \frac{I \int V(t) dt}{A(\text{or})M} \quad (2.6)$$

$$P = \frac{E}{\Delta t} \quad (2.7)$$

Where  $Q$  is the specific capacity ( $\text{Ah cm}^{-2}$  or  $\text{Ah g}^{-1}$ ),  $I$  is the current (A),  $\Delta t$  is the discharge time (s),  $E$  is the energy density ( $\text{Wh kg}^{-1}$  or  $\text{Wh cm}^{-2}$ ),  $\int V(t) dt$  is the area of the discharge curve (V.s),  $A$  is the area of the electrode ( $\text{cm}^2$ ),  $M$  is the mass of the electrode (g) and  $P$  is the power density ( $\text{W kg}^{-1}$  or  $\text{W cm}^{-2}$ ).  $A^+$  and  $Q^+$  are the area and

areal capacity of the positive electrode respectively, and  $m^-$ ,  $\Delta V^-$ , and  $C_s^-$  are the mass, potential, and specific capacitance of the rGO electrode, respectively.

The mass balance equation for hybrid supercapacitor to achieve charge balance ( $q^+ = q^-$ ) [27],

$$\frac{m^-}{m^+} = \frac{(C^+ \times \Delta V^+)}{(C^- \times \Delta V^-)} \quad (2.8)$$

$$\frac{m^-}{A^+} = \frac{Q^+}{(C^- \times \Delta V^-)} \quad (2.9)$$

where  $m^-$  and  $m^+$  represent the mass of the negative and positive electrodes,  $C^-$  and  $C^+$  are the specific capacitance of the negative and positive electrodes,  $A^+$  is the area of the positive electrode material,  $Q^+$  is the specific capacity of the positive electrode material ( $\text{Ah cm}^{-2}$  or  $\text{Ah g}^{-1}$ ) and,  $\Delta V^-$ ,  $\Delta V^+$  are the potential window of the negative and positive electrodes obtained using the three-electrode system, respectively.

## 2.6. References

1. A. Gedanken. *Ultrason Sonochem*, **2004**, 11 47.
2. C. Deng, H. Hub, X. Ge, C. Han, D. Zhao, G. Shao. *Ultrason Sonochem* **2011**, 18 932.
3. V. Safarifard, A. Morsali. *Ultrason Sonochem* **2012**, 19, 823.
4. M. Veerapandian, R. Subbiah, G. S. Lim, S. H. Park, K. S. Yun, M. H. Lee. *Langmuir* **2011**, 27, 8934.

5. S. J. Tang, A. T. Wang, S. Y. Lin, K. Y. Huang, C. C. Yang, J. M. Yeh, K. C. Chiu, *Polymer Journal* 2011, 43, 667.
6. C. Meng, C. Liu, L. Chen, C. Hu, S. Fan, *Nano Lett.* **2010**, 10, 4025.
7. Q. Wu, Y. Xu, Z. Yao, A. Liu, G.Q. Shi, *ACS Nano* **2010**, 4, 1963.
8. C. Li, H. Bai, G.Q. Shi, *Chem. Soc. Rev.* **2009**, 38, 2397.
9. H. Jiang, L. P. Yang, C. Z. Li, C. Y. Yan, P. S. Lee, and J. Ma, *Energy Environ Sci.* **2011**, 4, 1813.
10. W. F. Wei, X. W. Cui, W. X. Chen, and D. G. Ivey, *Chem. Soc. Rev.* **2011**, 40, 1697.
11. Y. Tan, Q. Gao, C. Yang, K. Yang, W. Tian, L. Zhu, *Sci. Rep.* **2015**, 5, 12382.
12. X. Yu, B. Lu, Z. Xu, *Adv. Mater.* **2014**, 26, 1044.
13. M. C. J. Bradford, M. A. Vannice, *Appl Catal., A*, **1996**, 142, 73.
14. M. C. J. Bradford, M. A. Vannice, *Catal Rev.* **1999**, 41, 1.
15. M. He, Y. Sun and B. Han, *Angew. Chem., Int. Ed.*, **2013**, 52, 9620.
16. T. V. Choudhary, V. R. Choudhary, *Angew. Chem., Int. Ed.*, **2008**, 47, 1828.
17. I. Gurrappa and L. Binder, *Sci. Technol. Adv. Mater.* **2008**, 9, 043001.
18. W. S. Hummers, and R. E. Offeman, *J. Am. Chem. Soc.* **1958**, 80, 1339.
19. Y. Zhu, S. Murali, W. Cai, X. Li, J. W. Suk, J. R. Potts, R. S. Ruoff, *Adv. Mater.* **2010**, 22 3906–3924.
20. A. Paravannoor, R. Ranjusha, A. M. Asha, R. Vani, S. Kalluri, K. R. V. Subramanian N. Sivakumar, T.N. Kim, S. V. Nair, A. Balakrishnan, *Chem Eng J* **2013**, 220,360.

21. G. K. Veerasubramani, K. Krishnamoorthy, S. Radhakrishnan, N.-J. Kim, S. J. Kim, *Int. J. Hydrogen Energy* **2014**, 39 (10), 5186.
22. C.G. Liu, Z.N. Yu, D. Neff, A. Zhamu, B.Z. Jang, *Nano. Lett.* 2010, 10, 4863.
23. J.W. Lang, X.B. Yan, X.Y. Yuan, J. Yang, Q.J. Xue, *J. Power Sources* **2011**, 196, 10472.
24. G. K. Veerasubramani, K. Krishnamoorthy, S. J. Kim, *J. Power Sources* **2016**, 306, 378.
25. B. Akinwolemiwa, C. Peng, G.Z. Chen, *J. Electrochem. Soc.* **2015**, 162 (5), A5054.
26. S.E. Chun, B. Evanko, X. Wang, D. Vonlanthen, X. Ji, G.D. Stucky, S.W. Boettcher, *Nat. Commun.* **2015**, 6, 7818.
27. P. Ahuja, V. Sahu, S.K. Ujjain, R. K. Sharma and G. Singh, *Electrochim. Acta* **2014**, 146, 429.
28. A. Ramadoss, Hybrid Nanostructured Materials for Supercapacitors and Self-Powered Systems, Thesis dissertation. **2015**

## CHAPTER – 3

### Transition metal molybdates $\text{MMoO}_4$ ( $\text{M} = \text{Co}, \text{Mn}$ ) and their electrochemical properties for supercapacitors

#### Chapter–3.1: Synthesis, characterization, and electrochemical properties of $\text{CoMoO}_4$ nanostructures

##### Highlights

- ❖ A facile sonochemical approach for the synthesis of cobalt molybdate ( $\text{CoMoO}_4$ ) nanostructures and their application as electrodes for supercapacitors
- ❖ The surface morphology was investigated using a field-emission scanning electron microscope, which showed the formation of plate-like  $\text{CoMoO}_4$  nanostructures
- ❖ The growth mechanism and formation of the  $\text{CoMoO}_4$  nanostructures is discussed
- ❖ The CV curves showed the presence of redox pairs and, along with the EIS data (using Nyquist and Bode plots), demonstrated the pseudocapacitance nature of the synthesized  $\text{CoMoO}_4$
- ❖ The galvanostatic studies showed non-symmetric discharge curves, and a maximum specific capacitance of  $133 \text{ F g}^{-1}$  (specific capacity of  $25.89 \text{ mAh g}^{-1}$ ) was obtained at a constant discharge current density ( $1 \text{ mA cm}^{-2}$ )
- ❖ The cyclic stability tests demonstrated capacitance retention of about 84% after 1000 cycles, suggesting the potential application of  $\text{CoMoO}_4$  in energy-storage devices

### 3.1.1. Introduction

As we discussed in chapter-1, electrochemical capacitors, also called supercapacitors or ultracapacitors, are considered to be emerging energy-storage devices due to their high power density and long cycling life [1]. In general, there are two mechanisms for charge storage in electrochemical supercapacitors: (i) electrical double-layer capacitance (EDLC) and (ii) pseudocapacitance [2]. EDLC is due to reversible electrolyte ion adsorption at the electrode/electrolyte interface; pseudocapacitance is due to redox reactions at the electrode surface [3]. Carbonaceous materials, such as activated carbon, mesoporous carbon, carbon nanotubes (CNTs), and graphene nanosheets, have all been widely investigated for EDLC devices [4, 5]. In contrast, several metal oxide/hydroxides with various nanostructured morphologies have been investigated for pseudocapacitance applications [5]. Extensive research has focused on materials for pseudocapacitors due to their high energy density compared to carbon-based EDLC devices [6]. A variety of transition metal oxides, such as  $\text{RuO}_2$ ,  $\text{MnO}_2$ ,  $\text{CuO}$ ,  $\text{NiO}$ ,  $\text{MoO}_3$ ,  $\text{MoO}_2$ ,  $\text{Co}_3\text{O}_4$ , and their corresponding hydroxides, having various nanostructures, such as nanoparticles, nanosheets, nanowires, nanorods, and hierarchical structures, have been investigated for their pseudocapacitance behavior over the last decade [7 - 9]. Although these materials possess higher specific capacitances, they have several disadvantages, such as the high cost and toxicity of  $\text{RuO}_2$  and poor electrical conductivity of  $\text{MnO}_2$ , which limit their use in commercial applications [10, 11]. The

increasing demand for energy-storage devices has motivated researchers to develop novel materials for this application.

Recently, research has focused on the development of novel nanostructures that are environmentally benign and possess enhanced electrochemical properties [12]. With respect to these criteria, metal molybdate nanostructures are well suited for energy-storage devices because they are environmentally safe and exhibit enhanced performance compared to their corresponding oxides. Nanostructured  $\text{NiMoO}_4$ ,  $\text{CoMoO}_4$ ,  $\text{MnMoO}_4$ , and their hierarchical structures showed superior electrochemical performance [13–15]. Electrochemical studies based on metal molybdates motivated us to examine the detailed supercapacitive behavior of  $\text{CoMoO}_4$  nanostructures.  $\text{CoMoO}_4$  is advantageous because it is low cost, non-toxic, and exhibits enhanced electrochemical properties [16, 17]. There have been few reports on the supercapacitive behavior of  $\text{CoMoO}_4$ . Mai et al. reported the hydrothermal synthesis of  $\text{CoMoO}_4$  nanowires with a specific capacitance  $62.8 \text{ F g}^{-1}$  and improved the specific capacitance to  $187 \text{ F g}^{-1}$  by forming hierarchical structures of  $\text{MnMoO}_4/\text{CoMoO}_4$  nanowires; the improvement was due to the high surface-to-volume ratio [14]. Xu et al. demonstrated that  $\text{CoMoO}_4/\text{CNTs}$  composites possess a specific capacitance of  $170 \text{ F g}^{-1}$  [18]. Recently, Xia et al. reported hydrothermally synthesized  $\text{CoMoO}_4$  nanoparticles with a specific capacitance of  $72 \text{ F g}^{-1}$  [19]. Recent studies by other groups also demonstrated that  $\text{CoMoO}_4 \cdot \text{H}_2\text{O}$  has a higher specific capacitance than pure  $\text{CoMoO}_4$  [17, 20].

Various synthetic strategies, such as hydrothermal synthesis, microwave-assisted synthesis, and wet chemical routes, have been used to achieve CoMoO<sub>4</sub> nanostructures [13, 14, and 18]. It is known that synthesis method, starting materials, and reaction parameters play a vital role in the physico-chemical properties of nanomaterials, which can strongly influence their optical, electrical, and electrochemical properties [1]. Moreover, the size, shape, and surface effects of nanostructures can also significantly alter their electrochemical properties [21]. Recently, sonochemical synthesis has become a popular approach for the fabrication of nanostructured materials, such as metals, metal oxides, metal chalcogenides, and graphene [22, 23]. In this study, we used a facile sonochemical approach for the synthesis of CoMoO<sub>4</sub> nanostructures. The advantage of sonochemical synthesis, compared to conventional methods, is the acoustic cavitation phenomenon (i.e., the formation, growth, and collapse of bubbles in liquid medium) [24]. The reaction conditions used in the sonochemical approach, including high temperature (5000 K), pressure (20 MPa), and cooling rate (10<sup>10</sup> Ks<sup>-1</sup>), provide a large number of reactive sites, which are typically not available during conventional reactions. This results in the unique properties of the synthesized nanomaterials [25, 26]. To our knowledge, this is the first report on the sonochemical synthesis of CoMoO<sub>4</sub> nanostructures.

In this initial study, we used a facile sonochemical approach for the synthesis of CoMoO<sub>4</sub> nanostructures and investigated their electrochemical properties for supercapacitor applications. Techniques such as cyclic voltammetry, electrochemical

impedance spectroscopy, and galvanostatic charge-discharge cycles were used to study the electrochemical properties of the prepared  $\text{CoMoO}_4$ .

### **3.1.2. Experimental methods**

#### **3.1.2.1. Preparation of $\text{CoMoO}_4$ by sonochemical method**

The  $\text{CoMoO}_4$  nanostructures were synthesized by a facile sonochemical approach using sodium molybdate and cobalt chloride as the starting precursors. Briefly, two solutions containing 1 M sodium molybdate in water and 1 M cobalt chloride in methanol were prepared separately. The solution containing cobalt chloride was exposed to ultra sonication (US, using a probe-type sonicator) followed by dropwise addition of sodium molybdate solution; the entire solution was stirred continuously using a Teflon-coated magnetic stir bar. The reaction progressed for 1.5 h, resulting in the formation of a violet-colored precipitate containing  $\text{CoMoO}_4 \cdot \text{H}_2\text{O}$ . Next, the  $\text{CoMoO}_4 \cdot \text{H}_2\text{O}$  was washed thoroughly with distilled water and ethanol, and the process was repeated several times until the synthesized product was free from impurities or residual ions. Finally, the  $\text{CoMoO}_4 \cdot \text{H}_2\text{O}$  precipitate was allowed to dry at  $100^\circ\text{C}$  for 3 h followed by calcination at  $500^\circ\text{C}$  for 3 h, forming  $\text{CoMoO}_4$ .

#### **3.1.2.2. Preparation of $\text{CoMoO}_4$ electrode**

The working electrode was prepared by taking active material  $\text{CoMoO}_4$  (37.5 mg), carbon black (10 mg), and PVDF (2.5 mg) in the weight ratio of 75:20:5 and mixed

together with N-methylpyrrolidone (NMP) into slurry form. Then the slurry was coated onto the stainless steel substrate ( $1 \times 1 \text{ cm}^2$ ) and allowed to dry at  $80^\circ\text{C}$  overnight. The mass of the active material on the electrode was  $\sim 5 \text{ mg}$ . A solution containing  $2 \text{ M}$  potassium hydroxide (KOH) was used as the electrolyte.

The electrochemical measurements were carried out at room temperature using a three-electrode system consisting of  $\text{CoMoO}_4$  as the working electrode, a saturated calomel electrode (SCE) as the reference electrode, and platinum as the counter electrode. The CV curves were recorded in the potential range of  $-0.3$  to  $+0.4 \text{ V}$  under different scan rates from  $5$  to  $100 \text{ mV s}^{-1}$ . The EIS measurements were carried out in the frequency range from  $0.01 \text{ Hz}$  to  $100 \text{ kHz}$ . Galvanostatic charge-discharge analysis was performed from the current density of  $1$  to  $10 \text{ mA cm}^{-2}$ .

### **3.1.3. Results and discussion**

#### **3.1.3.1. Structural characterization**

In this study, a facile sonochemical approach was used for the synthesis of  $\text{CoMoO}_4$  nanostructures. Solutions of sodium molybdate and cobalt chloride were mixed under US, resulting in the formation of  $\text{CoMoO}_4 \cdot \text{H}_2\text{O}$ . It is difficult to achieve pure metal molybdate using a wet chemistry approach due to the formation of hydrates by the intercalation of water molecules between the interlayers. To achieve pure  $\text{CoMoO}_4$ , the  $\text{CoMoO}_4 \cdot \text{H}_2\text{O}$  was calcined at  $500^\circ\text{C}$ , forming  $\text{CoMoO}_4$  as follows:

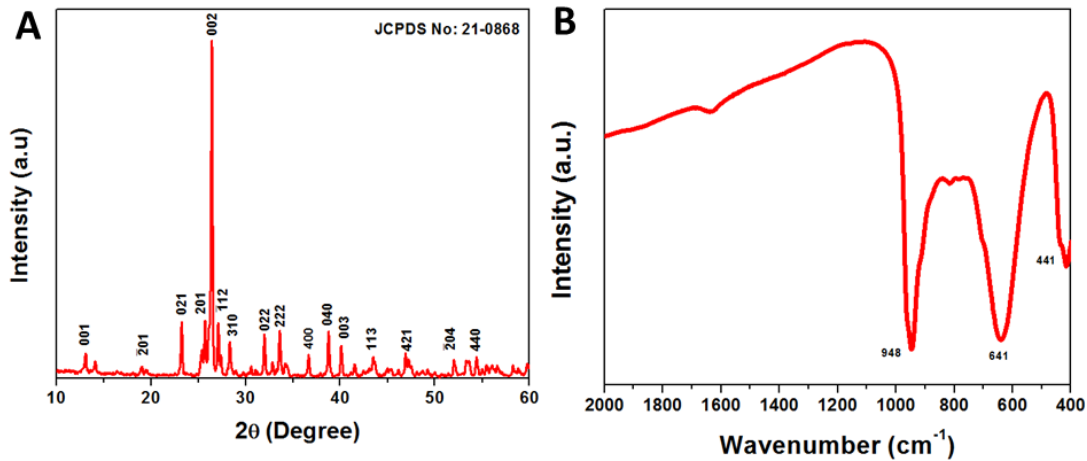
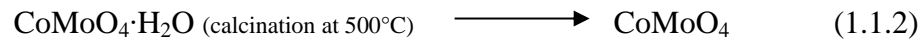
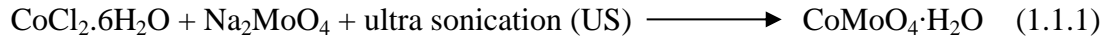


**Figure 3.1.1** X-ray diffraction pattern (A) and Fourier transform infrared spectrum of  $\text{CoMoO}_4$  nanostructures (B).

The crystalline nature of the sonochemically prepared  $\text{CoMoO}_4$  was examined by XRD; results are shown in **Figure 3.1.1 (A)**. The sharp diffraction peak at  $26.43^\circ$  corresponds to the reflections of the (002) plane. The other diffraction peaks at  $13.09^\circ$ ,  $19.04^\circ$ ,  $23.24^\circ$ ,  $25.69^\circ$ ,  $27.09^\circ$ ,  $28.30^\circ$ ,  $31.97^\circ$ ,  $33.65^\circ$ ,  $36.64^\circ$ ,  $38.74^\circ$ ,  $40.08^\circ$ ,  $43.46^\circ$ ,  $46.89^\circ$ ,  $51.98^\circ$ , and  $54.38^\circ$  can be assigned to the reflections of the (001), (201), (021), (201), (112), (310), (022), (222), (400), (040), (003), (113), (421), (204), and (440) planes, respectively. The observed diffraction peaks are in good agreement with the standard patterns for monoclinic  $\text{CoMoO}_4$  (JCPDS card no. 21-0868). Moreover, there were no peaks due to impurities or other residuals, indicating the high purity of the

sonochemically synthesized  $\text{CoMoO}_4$  nanostructures. The average crystallite size of the  $\text{CoMoO}_4$  was calculated as 64 nm using the Debye–Scherer equation [27]. FT-IR spectroscopy was used to examine the bonding nature in the prepared  $\text{CoMoO}_4$  nanostructures, as shown in **Figure 3.1.1 (B)**. The spectra revealed the presence of three major bands at 948, 641, and 441  $\text{cm}^{-1}$ . The band observed at 948  $\text{cm}^{-1}$  corresponds to the vibrational modes of distorted  $\text{MoO}_4$  present in  $\text{CoMoO}_4$  [28]. The band at 641  $\text{cm}^{-1}$  corresponds to the vibrational mode of Mo-O in the  $\text{CoMoO}_4$ , and the band at 441  $\text{cm}^{-1}$  represents vibrations due to the Co and Mo building blocks of  $\text{CoMoO}_4$  [29].

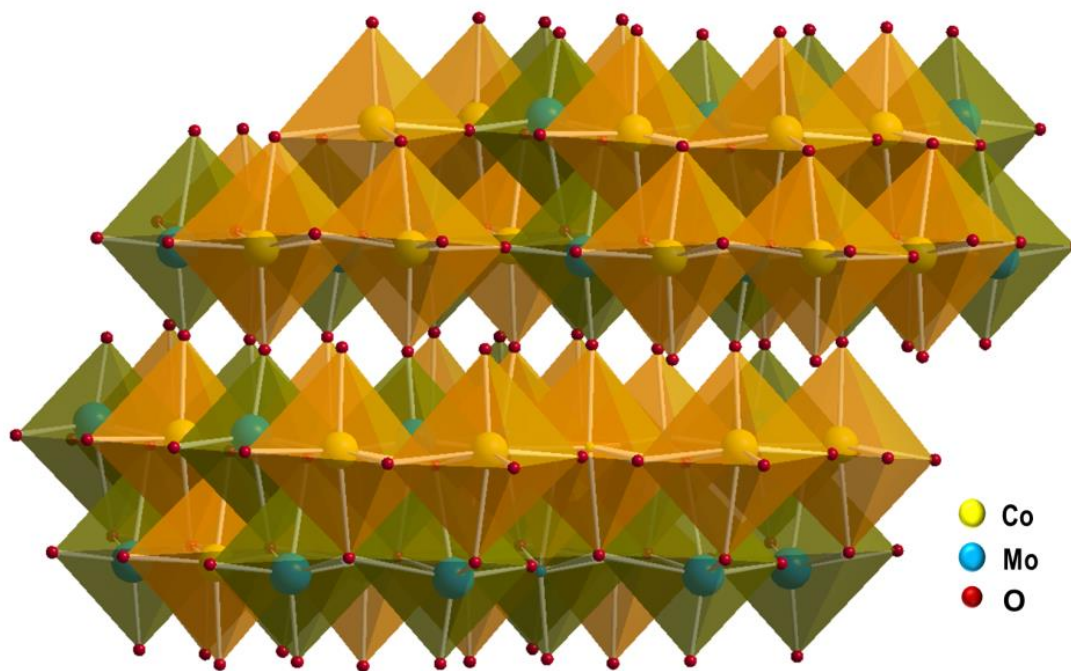


**Figure 3.1.2** Molecular structure of  $\text{CoMoO}_4$

**Figure 3.1.2** shows the crystal structure of  $\alpha$ -CoMoO<sub>4</sub> drawn by using Diamond crystallographic software. It consist chains of CoO<sub>6</sub> and MoO<sub>6</sub> octahedra which form the total crystal structure. The  $\alpha$ -CoMoO<sub>4</sub> has z-shaped condensed type [CoO<sub>6</sub>]<sub>4</sub> units which are isolated and similar [MoO<sub>6</sub>]<sub>4</sub> units exists. The condensed [CoO<sub>6</sub>]<sub>4</sub> units constitute of two dimers of edge-shared CoO<sub>6</sub> octahedra. Likewise, in the [MoO<sub>6</sub>]<sub>4</sub> units, the MoO<sub>6</sub> octahedra are directly linked by sharing edges to form z-shaped unit. Unlike the other phases ( $\beta$ -, hp-) of the compound, the condensed units of Co and Mo were found only in the  $\alpha$ -phase of CoMoO<sub>4</sub>.

### 3.1.3.2. Morphological analysis

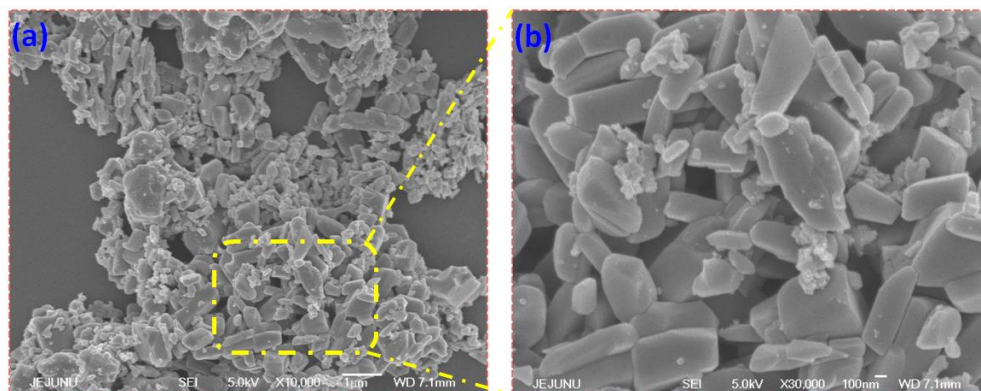


**Figure 3.1.3** Field-emission scanning electron micrographs of CoMoO<sub>4</sub> nanostructures (a) low magnification (scale bar = 1  $\mu$ m) and (b) high magnification (scale bar = 100 nm) micrographs.

The surface morphology of the prepared CoMoO<sub>4</sub> was examined using FE-SEM analysis. **Figure 3.1.3** shows the FE-SEM micrographs of the CoMoO<sub>4</sub> in both low (A) and high (B) magnifications. The low-magnification micrograph shows the presence of

plate-like nanostructures in  $\text{CoMoO}_4$ . The high-magnification micrograph shows that the dimensions of the  $\text{CoMoO}_4$  nanoplate were  $\sim 500$  nm in length and  $\sim 200$  nm in width. During the synthesis reaction, sodium molybdate dissolves into sodium and molybdate ions, and the molybdate ions react with cobalt ions from cobalt chloride. In the solution phase, the molybdate ions can be easily hydrolyzed to form  $\text{MoO}_4 \cdot \text{H}_2\text{O}$ , which later reacts with cobalt ions to form  $\text{CoMoO}_4 \cdot \text{H}_2\text{O}$ . After heat treatment for 3 h, the decomposition of  $\text{CoMoO}_4 \cdot \text{H}_2\text{O}$  into two-dimensional nanoplates of  $\text{CoMoO}_4$  was occurred.

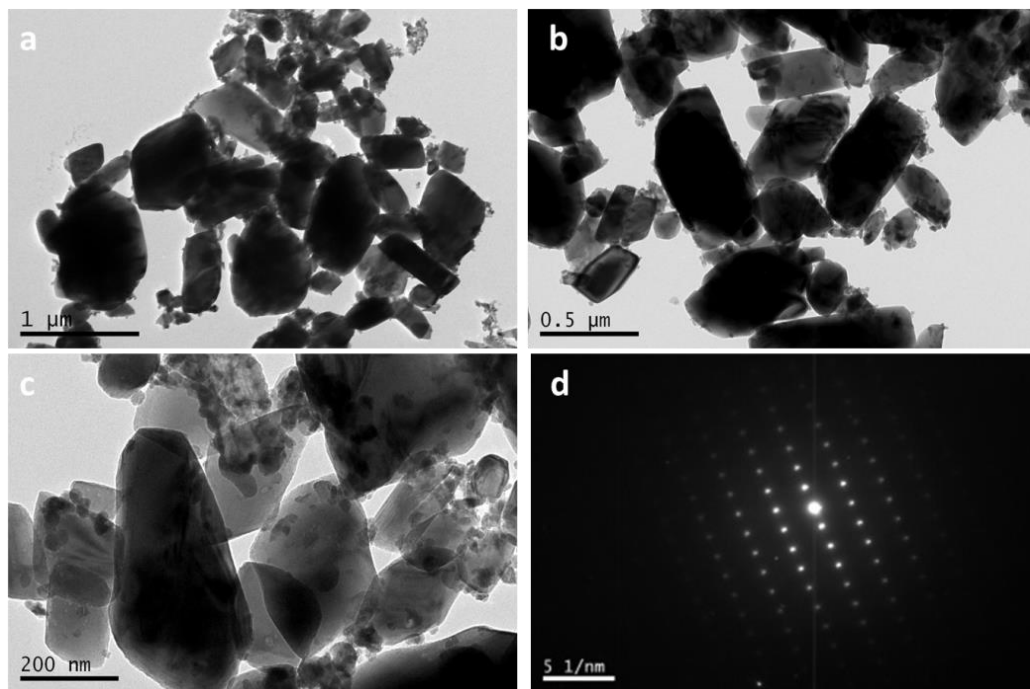


**Figure 3.1.4** High-resolution transmission electron micrographs of  $\text{CoMoO}_4$  nanostructures (A-C) low magnification (scale bar =  $1\ \mu\text{m}$  to  $200\ \text{nm}$ ) and SAED pattern (D).

**Figure 3.1.4 (A-C)** illustrates that the HR-TEM micrographs of synthesized  $\alpha$ -MnMoO<sub>4</sub> nanorods. It shows that the presences of nanoplates are in the range of about 500 - 200 nm in diameter which clearly matched with FE-SEM analysis. Also, the plate-like shape of the  $\alpha$ -CoMoO<sub>4</sub> is in accordance with the FE-SEM observations. The selected area electron diffraction (SAED) pattern of  $\alpha$ -CoMoO<sub>4</sub> nanorods (as shown in inset of **Figure 3.1.4 (D)**) shows clear diffraction patterns which indicates that the high crystallinity of the prepared nanorods

### 3.1.3.3. Electrochemical characterization

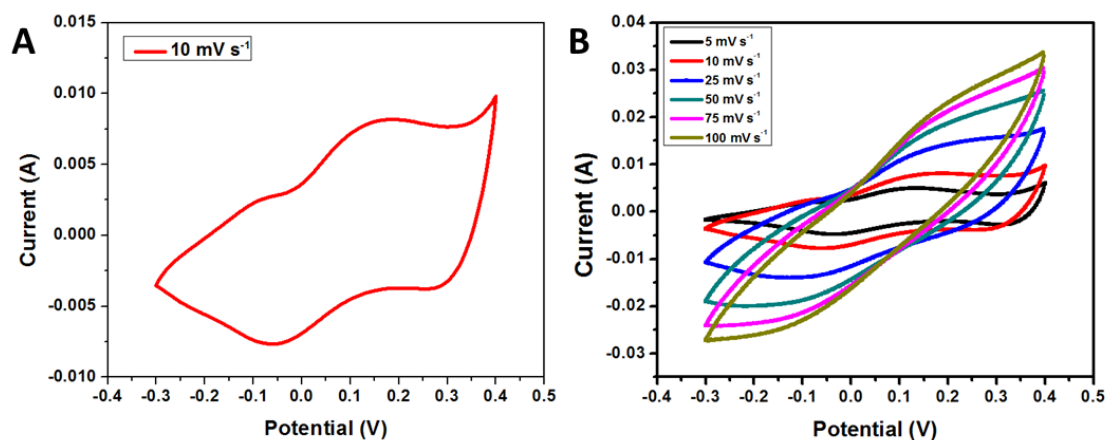


**Figure 3.1.5** Cyclic voltammetric curves of CoMoO<sub>4</sub> electrodes in 2 M KOH electrolyte (A) at a scan rate of 10 mV s<sup>-1</sup> and (B) at different scan rates from 5 to 100 mVs<sup>-1</sup>.

Novel structures, such as one- and two-dimensional nanomaterials, possess enhanced optical, electronic, and electrochemical properties. In this study, we investigated the application of CoMoO<sub>4</sub> nanoplates for electrochemical energy-storage devices. First, we examined the CV profiles of the CoMoO<sub>4</sub> electrode in 2 M KOH as

the electrolyte. The CV profile of CoMoO<sub>4</sub> under a scan rate of 10 mV s<sup>-1</sup> (**Figure 3.1.5 (A)**) shows the presence of a redox pair, indicating the pseudocapacitive nature of the material. The observed redox peak is due to the charge-transfer kinetics of Co<sup>2+</sup>/Co<sup>3+</sup> in the metal molybdate. Previous work by Mai et al. also demonstrated a similar redox reaction in CoMoO<sub>4</sub> with the aid of Pourbaix diagrams [14]. The CV profiles at different scan rates (**Figure 3.1.5 (B)**) revealed the presence of these redox peaks even at higher scan rates. However, a slight deviation in the shape of the CV curve was observed at high scan rates (100 mV s<sup>-1</sup>); the shape became quasi-rectangular which was due to the fact that at high scan rates, the active material is not completely utilized by the electrolyte ions [30]. The voltammetric current increased gradually with increasing scan rate, suggesting that the kinetics of the interfacial Faradaic redox reactions and the rates of electronic and ionic transport were sufficient [31, 32]. The specific capacitance of CoMoO<sub>4</sub> increased with decreasing scan rate, reaching a maximum of about 117 F g<sup>-1</sup> (specific capacity of 22.77 mAh g<sup>-1</sup>) at a scan rate of 5 mV s<sup>-1</sup>.

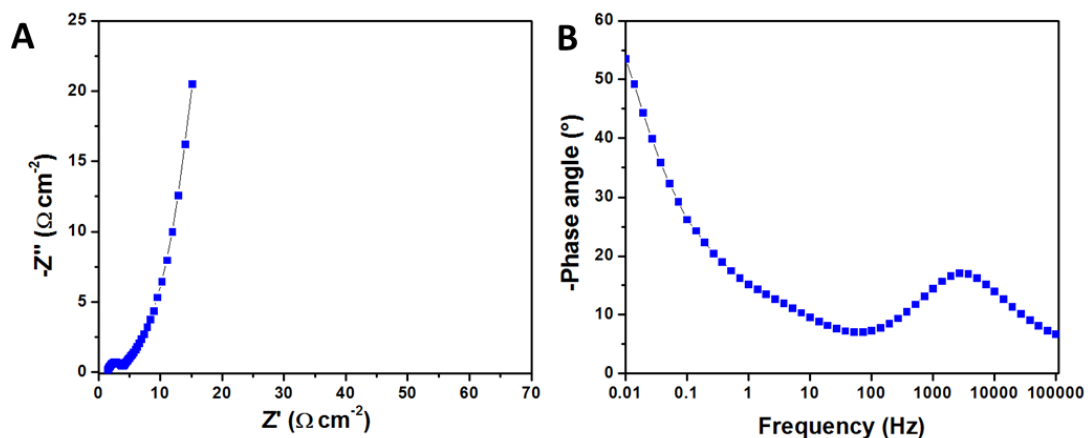


**Figure 3.1.6** Electrochemical impedance spectroscopy of CoMoO<sub>4</sub> electrodes (A) Nyquist plot and (B) Bode phase angle plot.

EIS was used to investigate the mechanism of charge storage in the CoMoO<sub>4</sub> electrode. EIS is a common technique used to characterize the electrochemical behavior of any material [33]. The EIS data were analyzed using Nyquist and Bode plots. The Nyquist plot represents the frequency response of the electrode/electrolyte system by examining the imaginary component ( $-Z''$ ) of the impedance compared to the real component ( $Z'$ ) [34]. The Nyquist plot of the CoMoO<sub>4</sub> electrode is shown in **Figure 3.1.6(A)**, revealing the presence of a semicircle at the high-frequency region and a linear section at the low-frequency region. The semicircle in the Nyquist plot indicates the charge-transfer resistance ( $R_{ct}$ ) of the CoMoO<sub>4</sub> electrode/electrolyte interfacial region; the obtained  $R_{ct}$  value was  $\sim 3.8 \Omega \text{ cm}^2$ . The linear section at the low-frequency region, or the slope of the  $45^\circ$  portion, is referred to as the Warburg resistance ( $Z_w$ ), which results from frequency-dependent ion diffusion or transport from the electrolyte to the electrode surface [35]. The Bode plot is shown in **Figure 3.1.6(B)** and represents the change in the Bode phase with applied frequency. It is well known that a phase angle of  $90^\circ$  indicates ideal capacitive behavior; otherwise, the material has pseudocapacitive behavior [36, 37]. In the case of CoMoO<sub>4</sub>, the low phase angle of  $53.5^\circ$  indicates the pseudocapacitive nature of the material.

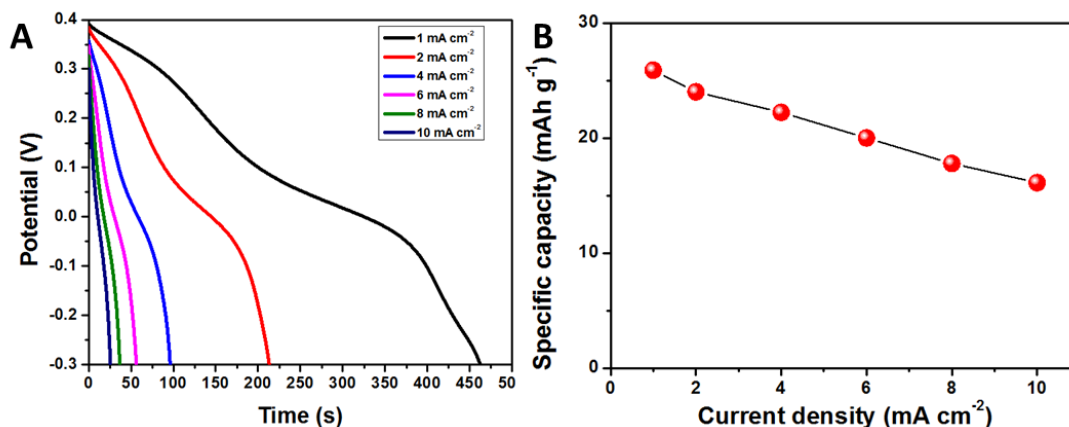


**Figure 3.1.7** Galvanostatic discharge curves of CoMoO<sub>4</sub> electrodes, (A) with different discharge current densities and (B) Variation of specific capacitance with respect to discharge current density.

Galvanostatic charge-discharge studies of CoMoO<sub>4</sub> were performed at various discharge current densities (1 to 10 mA cm<sup>-2</sup>), and the corresponding curves are shown in **Figure 3.1.7 (A)**. The results showed semi-symmetric discharge curves due to the pseudocapacitive nature of the material. The maximum specific capacitance of CoMoO<sub>4</sub> was about 133 F g<sup>-1</sup> (specific capacity of 25.89 mAh g<sup>-1</sup>) at a constant discharge current density (1 mA cm<sup>-2</sup>). The observed specific capacitance agreed well with the specific capacitance obtained from the CV curves. Moreover, the obtained specific capacitance is relatively high compared with previous reports on the supercapacitive behavior of CoMoO<sub>4</sub>. Xia et al. reported a specific capacitance of 72 F g<sup>-1</sup> for CoMoO<sub>4</sub> nanoparticles [19]. The obtained specific capacitance is also high compared with conventional metal oxide nanoparticles used for supercapacitor applications, such as MoO<sub>3</sub>, Co<sub>3</sub>O<sub>4</sub>, CuO, and Mn<sub>3</sub>O<sub>4</sub>, suggesting the potential application of this material in

energy-storage devices [39–42]. The higher specific capacitance obtained in this study can be attributed to the plate-like morphology of the sonochemically synthesized  $\text{CoMoO}_4$ . **Figure 3.1.7 (B)** shows the variation in specific capacitance with respect to the discharge current density. The specific capacitance decreased with increasing discharge current density. This is due to the fact that at a high discharge current density, the electrolyte ions are not effectively utilized by the active material, resulting in a decrease in specific capacitance [43, 44]. The maximum specific capacitance of about  $133 \text{ F g}^{-1}$  (at a current density of  $1 \text{ mA cm}^{-2}$ ) was reduced to  $82.5 \text{ F g}^{-1}$  at a discharge current density of  $10 \text{ mA cm}^{-2}$ . Thus, almost 62% of the specific capacitance was retained after the discharge current density was increased 10 times, demonstrating the enhanced capacitive behavior of  $\text{CoMoO}_4$ .

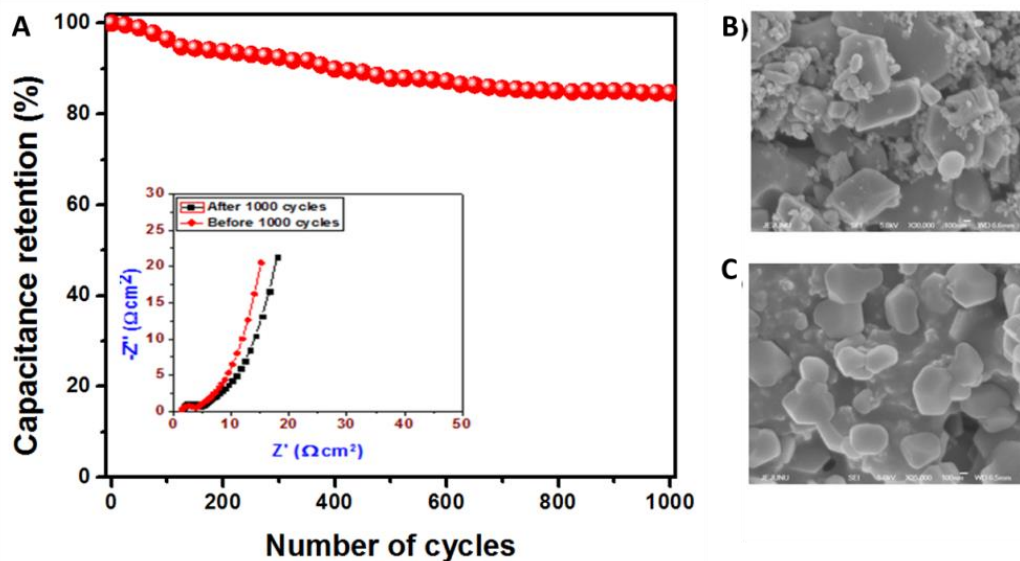


**Figure 3.1.8** (A) Cyclic stability tests of  $\text{CoMoO}_4$  using galvanostatic charge discharge measurements at a constant current density of  $6 \text{ mA cm}^{-2}$  for 1000 cycles. The inset

shows the Nyquist plot of CoMoO<sub>4</sub> electrodes before and after cyclic stability test. FE-SEM micrographs (scale bar -100 nm) of electrode materials before (B) and after (C) cyclic tests

Long-term cyclic stability is an important parameter and is essential for practical applications of an electrode material in supercapacitor devices [45]. The cyclic stability of CoMoO<sub>4</sub> was examined using galvanostatic charge discharge cycles (at a current density of 6 mA cm<sup>-2</sup>) for 1000 cycles. A plot of capacitance retention against the number of cycles is shown in **Figure 3.1.8 (a)**. A decrease in specific capacitance was observed after 1000 cycles; this can be attributed to dissolution, aggregation, and the volume change occurred in the electrode material [46]. The decrease in specific capacity after a certain number of cycles is in agreement with previous studies [19]. In order to investigate this, we examined the FE-SEM images of the electrode materials before and after the long term stability tests and is shown in inset of **Figure 3.1.8 (b and c)**. Significant changes in the electrode materials have been observed after the long term stability tests. The FE-SEM image of the electrodes after 1000 cycles (**Figure 3.1.8 (c)**) revealed the aggregation of the materials which can decrease the specific capacitance of the electrodes. Further, the EIS measurements after 1000 cycles show a remarkable increase in charge transfer resistance from 3.8 to 4.5 Ω cm<sup>2</sup>. This further leads to the decrease in specific capacitance after long term cyclic stability test. Nearly 84% of the specific capacitance was retained after 1000 cycles, demonstrating the enhanced long-term stability of the sonochemically synthesized CoMoO<sub>4</sub> compared to the previous work [19].

### 3.1.4. Conclusion

In conclusion, CoMoO<sub>4</sub> nanostructures were successfully synthesized by a facile sonochemical approach, and the structure, morphology, and bonding nature were investigated. The electrochemical studies, including CV and EIS analysis, demonstrated the pseudocapacitance nature of the prepared CoMoO<sub>4</sub> nanostructures. A maximum specific capacitance of ~133 F g<sup>-1</sup> (specific capacity of 25.89 mAh g<sup>-1</sup>) was obtained during discharge cycles at a constant discharge current density (1 mA cm<sup>-2</sup>). Nearly 62% of the specific capacitance was retained after the current density was increased 10 times, indicating the enhanced electrochemical behavior of the material. Cyclic stability studies showed 84% retention after 1000 cycles, indicating the potential of CoMoO<sub>4</sub> for use in energy-storage devices.

### 3.1.5. References

1. Y. Zhang, H. Feng, X. Wu, L. Wang, A. Zhang, T. Xia, H. Dong, X. Li, L. Zhang. *Int.J.Hydrogen Energy* **2009**, 34, 4889.
2. A.V. Murugan, T. Muraliganth, A. Manthiram. *Chem. Mater* **2009**, 21, 5004.
3. S. Biswas, L.T. Drzal. *ACS Appl. Mater. Interfaces* **2010**, 2, 2293.
4. M. Kumar, K. Singh, S. K. Dhawan, K. Tharanikkarasu, J. S. Chung, B. S. Kong, E. J. Kim, S. H. Hur, *Chem. Eng. J* **2013**, 31, 397–405.
5. K. Krishnamoorthy, A. Ananth, Y. S. Mok, S. J. Kim, *Sci. Adv. Mater* **2014**, 6, 349.
6. G. Wang, L. Zhang, J. Zhang. *J. Chem. Soc. Rev* **2012**, 41, 797.

7. C. D. Lokhande, D. P. Dubal, O. S. Joo, *Curr. Appl. Phy*, **2011**, 11, 255.
8. K. Krishnamoorthy, S. J. Kim, *Mater. Res. Bull* **2013**, 48, 3136.
9. J. Rajeswari, P. S. Kishore, B. Viswanathan, T. K. Varadarajan. *Electrochem Commun.* **2009**, 11, 572.
10. H. Wang, L. Zhang, X. Tan, C. M. B. Holt, B. Zahiri, B. C. Olsen, D. Mitlin, *J. Phys. Chem. C* **2011**, 115, 17599.
11. B. O. Park, C. D. Lokhande, H-S. Park, K. D. Jung, O. S. Joo. *J. Mater. Sci* **2004**, 39, 4313.
12. G. X. Pan, X. Xia, F. Cao, P. S. Tang, H. F. Chen. *Electrochim. Acta* **2012**, 63, 335.
13. B. Senthilkumar, K. V. Sankar, Selvan RK, Danielle M, Manickam M. *RSC Adv* **2013**, 3, 352.
14. L. Q. Mai, F. Yang, Y. L. Zhao, X. Xu, L. Xu, Y. Z. Luo. *Nat. Commun* **2011**, 2, 381.
15. B. Senthilkumar, D. Meyrick, Y. S. Lee, R. K. Selvam. *RSC Adv* **2013**, 3, 16542.
16. Y. Ding, Y. Wan, L. Min, W. Zhang, S. H. Yu. *Inorg. Chem* **2008**, 47, 7813.
17. J. Zhao, Q. S. Wu, M. Wen. *J. Mater. Sci* **2009**, 44, 6356.
18. Z. Xu, Z. Li, X. Tan, C.M.B. Holt, L. Zhang, B. S. Amirkhiz. *RSC Adv* **2012**, 2, 2753.
19. X. Xia, W. Lei, L. Hao, W. Wang, X. Wang. *Electrochim. Acta* **2013**, 99, 253.
20. M. C. Liu, L. B. Kong, X. J. Ma, C. Lu, X. M. Li, Y. C. Luo. *New J. Chem* **2012**, 36, 1713.

21. R. Mohan, K. Krishnamoorthy, S. J. Kim. *Chem. Phys. Lett* **2012**, 539–540, 83.
22. A. Gedanken *Ultrason. Sonochem* **2004**, 11, 47.
23. K. Krishnamoorthy, G. S. Kim, S. J. Kim. *Ultrason. Sonochem* **2013**, 20, 644.
24. C. Deng, H. Hub, X. Ge, C. Han, D. Zhao, G. Shao. *Ultrason. Sonochem* **2011**, 18, 932.
25. V. Safarifard, A. Morsali, *Ultrason. Sonochem* **2012**, 19, 823.
26. M. Veerapandian, R. Subbiah, G. S. Lim, S. H. Park, K. S. Yun, M. H. Lee. *Langmuir* **2011**, 27, 8934.
27. K. Krishnamoorthy, G. Manivannan, S. J. Kim, K. Jeyasubramanian, M. Premanathan, *J. Nanopart. Res* **2012**, 14, 1063.
28. K. Nakamoto. *Infrared and Raman Spectra of Inorganic and Coordination Compounds*. 5th ed. New York: Wiley; **1997**.
29. G. Kianpour, M. S. Niasari, H. Emadi. *Superlattice Microst.* **2013**, 58, 120.
30. G. Guo, L. Huang, Q. Chang, L. Ji, Y. Liu, Y. Xie. *Appl. Phys. Lett* **2011**, 99, 083111-1.
31. R. K. Selvan, I. Perelshtein, N. Perkas, A. Gedanken. *J. Phys. Chem. C* **2008**, 112, 1825.
32. A. Paravannoor, R. Ranjusha, A. M. Asha, R. Vani, S. Kalluri, K. R. V. Subramanian. *Chem. Eng. J.* **2013**, 220, 360.
33. K. Liu, Z. Hu, R. Xue, J. Zhang, J. Zhu. *J. Power Sources* **2008**, 179, 858.

34. S. T. Senthilkumar, R. K. Selvan, N. Ponpandian, J. S. Melo. *RSC Adv* **2012**, 2, 8937.
35. K. K. Purushothaman, M. Cuba, G. Muralidharan. *Mater. Res. Bull* **2012**, 47, 3348.
36. L. Yuan, X. H. Lu, X. Xiao X, T. Zhai, J. Dai, F. Zhang. *ACS Nano* **2012**, 6, 656.
37. K. Krishnamoorthy, G. K. Veerasubramani, S. Radhakrishnan, S. J. Kim. *Mater. Res. Bull.* **2014**, 50, 499.
38. J. Yan, J. Liu, Z. Fan, T. Wei, L. Zhang. *Carbon* **2012**, 50, 2179.
39. I. Shakir, M. Shahid, H. W. Yang, D. J. Kang. *Electrochim. Acta* **2010**, 56, 376.
40. L. Wang, X. Liu, X. Wang, X. Yang, L. Lu. *Curr. Appl. Phys* **2010**, 10, 1422.
41. V. D. Patake, S. S. Joshi, C. D. Lokhande, O-S. Joo. *Mater. Chem. Phys* **2009**, 114, 6.
42. K. V. Sankar, D. Kalpana, R. K. Selvan. *J. Appl. Electrochem* **2012**, 42, 463.
43. J. Xu, L. Gao, J. Cao, W. Wang, Z. Chen. *Electrochim. Acta* **2010**, 56, 732.
44. J. Yan, T. Wei, W. Qiao, B. Shao, Q. Zhao, L. Zhang, *Electrochim. Acta* **2010**, 55, 6973.
45. P. Justin, G. R. Rao. *Int.J.Hydrogen Energy* **2010**, 35: 9709.
46. S. Park, S. Kim. *Electrochim. Acta* **2013**, 89, 516.
47. Z. Li, Z. Zhou, G. Yun, K. Shi, L. V. Xiaowei, B. Yang. *Nanoscale Res. Lett.* **2013**, 8, 473.

## 3.2 - Synthesis, characterization, and electrochemical properties of MnMoO<sub>4</sub> nanorods for supercapacitor applications

### Highlights:

- ❖ The preparation of manganese molybdate (MnMoO<sub>4</sub>) nanorods by a facile sonochemical method and investigated its electrochemical properties for supercapacitor applications
- ❖ The microstructure, surface morphology and composition were characterized by using Field-emission scanning electron microscope (FE-SEM), High-resolution-transmission electron microscopy (HR-TEM), X-ray diffraction analysis (XRD), Raman spectroscopy and X-ray photo electron microscopy (XPS)
- ❖ The cyclic voltammetry (CV) curves of sonochemically synthesized  $\alpha$ -MnMoO<sub>4</sub> nanorods revealed the presence of redox pairs suggesting the pseudocapacitive nature of MnMoO<sub>4</sub>
- ❖ A maximum specific capacitance of the  $\alpha$ -MnMoO<sub>4</sub> nanorods was about 168.32 F g<sup>-1</sup> (specific capacity of 30.3 mAh g<sup>-1</sup>) as observed from the galvanostatic charge-discharge (GCD) analysis at a constant current density of 0.5 mA cm<sup>-2</sup>
- ❖ Long term cyclic stability study revealed that about 96 % of initial capacitance was retained after 2000 cycles

### 3.2.1. Introduction

In recent years, researches on pseudocapacitive materials such as Ni(OH)<sub>2</sub>, Co(OH)<sub>2</sub>, RuO<sub>2</sub>, MnO<sub>2</sub>, Co<sub>3</sub>O<sub>4</sub>, NiO, CuO have been investigated [1-7]. Even though, these materials possess higher specific capacitance, there are several demerits such as high cost and toxicity of RuO<sub>2</sub>, and poor electrical conductivity of MnO<sub>2</sub> which limits their applications in commercialization [8, 9]. In recent years, the researchers focused on developing novel pseudocapacitive materials for improving the performance of the supercapacitors. The studies on nanostructured metal molybdates showed superior electrochemical performances [10-14]. Manganese molybdate (MnMoO<sub>4</sub>) is one of the metal molybdate nanostructures with excellent electrochemical properties. Considering the recent works performed on the supercapacitive behavior of MnMoO<sub>4</sub>, only limited reports are available. Mai et al, reported the hydrothermal synthesis of MnMoO<sub>4</sub> nanowires with specific capacitance 9.7 F g<sup>-1</sup> and improved their specific capacitance into 187 F g<sup>-1</sup> at 1 A g<sup>-1</sup> of current density by forming hierarchical structures of MnMoO<sub>4</sub>/CoMoO<sub>4</sub> nanowires which is due to the high surface/ body ratio [11]. Senthilkumar et al reported synthesis of MnMoO<sub>4</sub> by solution combustion method with specific capacitance of 126 F g<sup>-1</sup> at 5 mA cm<sup>-2</sup> of current density [13]. However, the development of molybdate materials with simple and reliable synthetic method still remains massive challenge [15]. To best of our knowledge, there are no reports available on the synthesis of MnMoO<sub>4</sub> nanorods using facile sonochemical method towards electrochemical capacitor applications. The aim of this study is to examine the

electrochemical properties of sonochemically synthesized  $\alpha$ -MnMoO<sub>4</sub> nanorods with presented CoMoO<sub>4</sub> for supercapacitor applications.

### **3.2.2. Experimental methods**

#### **3.2.2.1. Preparation of MnMoO<sub>4</sub> by sonochemical method**

The  $\alpha$ -MnMoO<sub>4</sub> nanorods are prepared via facile sonochemical approach using manganese acetate and sodium molybdate as the starting precursors. In a typical procedure, 1 M of sodium molybdate in water and 1 M of manganese acetate tetrahydrate in absolute alcohol were taken in 100 ml beaker separately. At first, manganese acetate solution was allowed to ultrasound irradiation followed by the dropwise addition of sodium molybdate by keeping entire solution under mild stirring. The overall reaction was carried out for 90 min at the room temperature which results the formation of MnMoO<sub>4</sub>.xH<sub>2</sub>O precipitate. Then the precipitate was washed thoroughly with excess distilled water and ethanol at 6000 rpm for 10 min in order to remove the residuals. This procedure was repeated for several times until the synthesized product becomes free from trace amount of impurities. Then the precipitate was separated and dried at 80 °C for overnight to obtain MnMoO<sub>4</sub>.xH<sub>2</sub>O followed by calcined at 500 °C for 3 hrs which results in the formation of  $\alpha$ -MnMoO<sub>4</sub> nanorods.

#### **3.2.2.2. Preparation of MnMoO<sub>4</sub> electrodes**

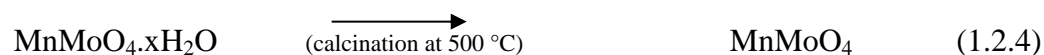
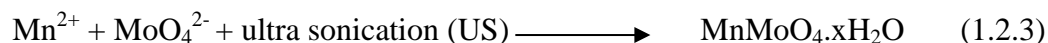
A three-electrode system consisting of a working electrode, platinum foil and Ag/AgCl as counter and reference electrodes were used. The working electrode was

prepared by mixing  $\alpha$ -MnMoO<sub>4</sub> powder, carbon black as a conducting agent and polyvinylidene difluoride (PVDF) as a binder with the mass ratio of 75:20:5. Then this mixture was grinded homogeneously with NMP and coated on the Ni foam substrate (1×1 cm<sup>2</sup>) current collector and dried at 80 °C for overnight. The mass loading of the material on single electrode was about 1.7 mg.

### 3.2.3. Results and discussion

#### 3.2.3.1. Structural characterization

In this study,  $\alpha$ -MnMoO<sub>4</sub> nanorods was prepared by a facile sonochemical method using manganese acetate and sodium molybdate as starting precursors. Under sonochemical conditions, the molybdate and manganese ions reacts with each other which results in the formation of MnMoO<sub>4</sub>.xH<sub>2</sub>O. It is known that achieving pure metal molybdates via wet chemistry approach is difficult due to the formation of hydrates. In order to achieve the pure MnMoO<sub>4</sub>, the MnMoO<sub>4</sub>.xH<sub>2</sub>O is calcined at 500 °C which further leads to the formation of MnMoO<sub>4</sub>. The overall reaction is given as follows:



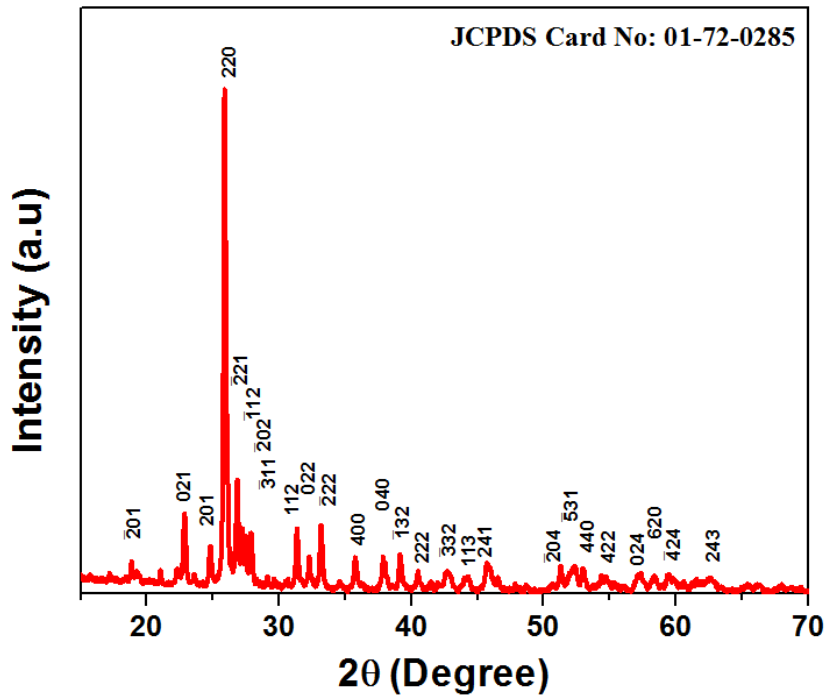


**Figure 3.2.1** X-ray diffraction pattern of sonochemically synthesized  $\alpha$ -MnMoO<sub>4</sub> nanorods

The XRD pattern of the as-prepared MnMoO<sub>4</sub> nanorods (shown in **Figure 3.2.1**) clearly indicates the presence of monoclinic  $\alpha$ -MnMoO<sub>4</sub> with space group C2/m [15]. The major diffraction peak at  $2\theta = 25.8^\circ$  which corresponds to the reflections of (220) plane. The observed diffraction peaks and the interplanar spacing were matched well with the standard diffraction pattern of  $\alpha$ -MnMoO<sub>4</sub> (Joint Committee on Powder Diffraction Standards card no: 01-72-0285). There is no peaks related to any such impurities were found in the XRD pattern suggesting the high quality of  $\alpha$ -MnMoO<sub>4</sub> has been synthesized. The crystallite size of the  $\alpha$ -MnMoO<sub>4</sub> was calculated from the Debye–Scherer equation [16].

$$D = [(0.9\lambda)/(\beta\cos\theta)] \quad (1.2.5)$$

Where  $D$  is the crystallite size,  $\lambda$  ( $= 1.5405 \text{ \AA}$ ) is the wavelength of X-rays used ( $\text{CuK}\alpha$ ),  $\beta$  is the broadening of diffraction line measured at half its maximum intensity in radians and  $\theta$  is the angle of diffraction. The crystallite size of the  $\text{MnMoO}_4$  nanorods was found to be 21nm using maximum intensity peak.

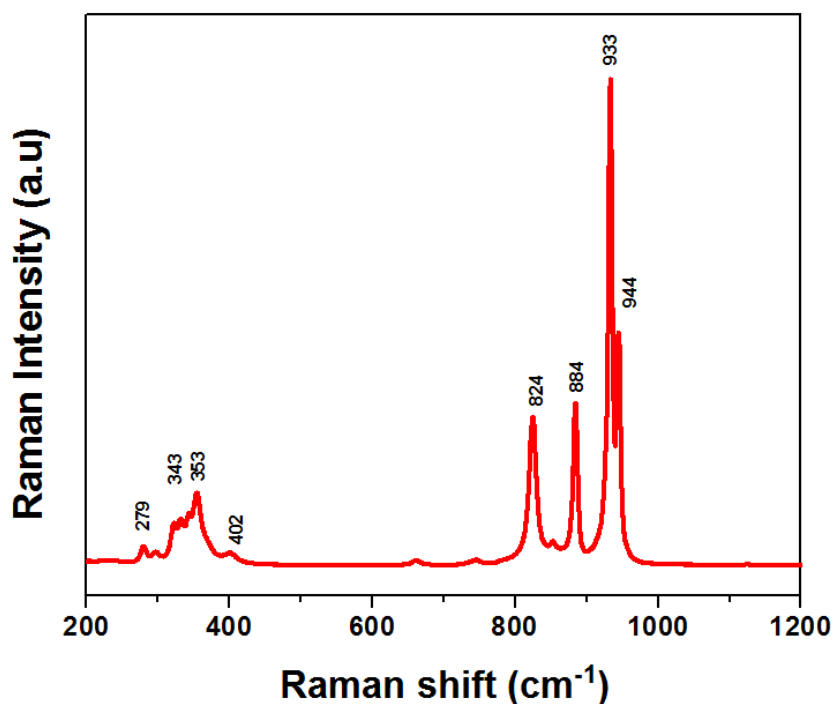


**Figure 3.2.2** Raman spectrum of sonochemically synthesized  $\alpha\text{-MnMoO}_4$  nanorods

Raman spectroscopy is one of the prominent tools for analyzing the crystallinity, bonding nature and defect states of nanocrystalline materials [17, 18]. It is reported that  $\alpha\text{-MnMoO}_4$  possess 13 Raman active modes of vibrations ( $3\text{Ag} + 5\text{Bg} + 5\text{Eg}$ ) based on group theory [15]. **Figure 3.2.2** shows the Raman spectra for  $\alpha\text{-MnMoO}_4$  nanorods. The

bands observed at 944, 933, 824  $\text{cm}^{-1}$  are assigned to  $A_g$ , peaks 884  $\text{cm}^{-1}$ , 343  $\text{cm}^{-1}$  are assigned to  $B_g (+A_g)$  and  $A_g (+B_g)$  respectively, peak 402  $\text{cm}^{-1}$  is assigned to  $B_g$ , the peaks 353, 279  $\text{cm}^{-1}$  are assigned to  $A_g^b (+B_g)$ . The high intensity bands at 933 and 820  $\text{cm}^{-1}$  correspond to the Mo(1)O(2) and Mo(1)O(1) symmetric stretching vibration respectively. The obtained bands are in good agreement with the reported values by Kanesaka et al. [19].

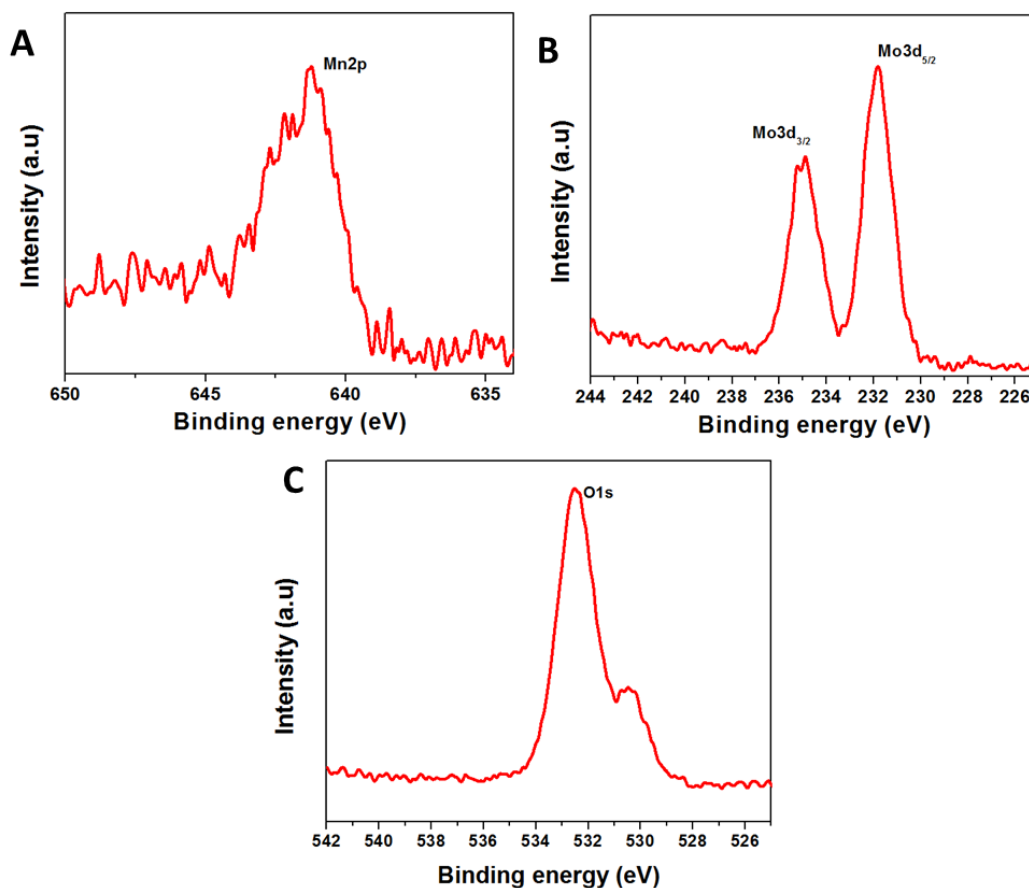


**Figure 3.2.3** XPS spectra of synthesized  $\alpha$ - $\text{MnMoO}_4$  nanorods (A) the Mn2p core-level, (B) Mo3d<sub>3/2</sub>, Mo3d<sub>5/2</sub> core-level peaks, (C) the O 1s core-level spectra.

Further, the chemical states of the elements present in the prepared  $\alpha$ -MnMoO<sub>4</sub> were investigated using XPS analysis. The survey spectrum (data not shown) revealed the presence of Mn, Mo, and O components respectively. The presence of Mn 2p in the  $\alpha$ -MnMoO<sub>4</sub> was observed at the binding energy 641.2 eV as shown in **Figure 3.2.3 (A)** [20]. The chemical state of Mo in the  $\alpha$ -MnMoO<sub>4</sub> is shown in **Figure 3.2.3 (B)**, which indicates the presence of two peaks observed at binding energies 231.86 and 234.87 eV respectively. The peak observed at 231.86 eV corresponds to the Mo 3d<sub>5/2</sub> and the peak observed at 234.87 eV corresponds to the Mo 3d<sub>3/2</sub> states respectively. The binding energy and splitting width ( $\Delta$ Mo3d = 3.01 eV) are in good agreement with the previous studies [21, 22]. The state of O 1s present in  $\alpha$ -MnMoO<sub>4</sub> is shown in **Figure 3.2.3 (C)** [23]. A small additional peak observed in the O 1s spectra is usually associated with hydroxyl groups of surface adsorbed water molecules.

### 3.2.3.2. Morphological analysis

The surface morphology of the sonochemically synthesized MnMoO<sub>4</sub> is examined using Field-emission scanning electron microscopy (FE-SEM) and is shown in **Figure 3.2.4 (A-D)**. The FE-SEM micrographs revealed the presence of nanorods in the range of 100 to 400 nm in diameter and 1 to 2  $\mu$ m in length. The formation of rod like nanostructures of  $\alpha$ -MnMoO<sub>4</sub> is due to the use of ultrasound irradiation employed in the reaction condition. A previous study demonstrated the use of sonochemical method for achieving NiMoO<sub>4</sub> nanorods [24].

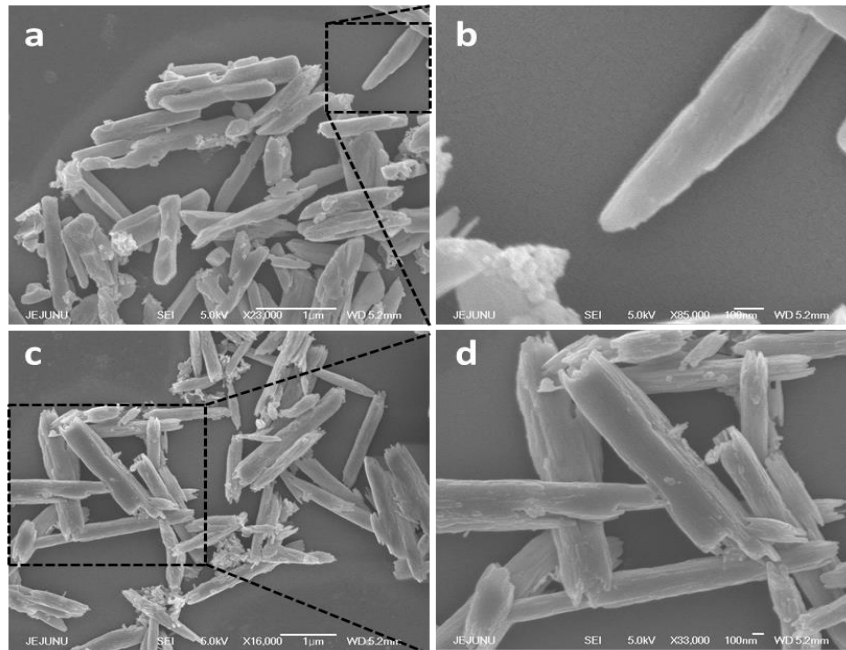


**Figure 3.2.4** FE-SEM images of the prepared  $\text{MnMoO}_4$  nanorods (a-d).

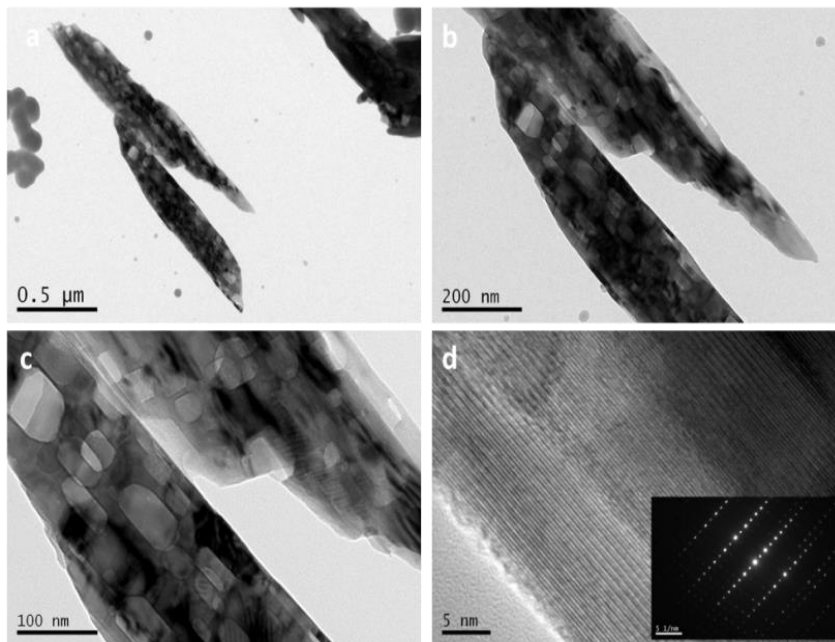


**Figure 3.2.5** HR-TEM I mage of the synthesized  $\alpha\text{-MnMoO}_4$  nanorods at 0.5  $\mu\text{m}$  (a), 200 nm (b), 100 nm (c) and 50 nm (d), SAED pattern (inset of d).

**Figure 3.2.5 (A-D)** illustrates that the HR-TEM micrographs of synthesized  $\alpha$ -MnMoO<sub>4</sub> nanorods. It shows that the presence of nanorods in the range of about 200 nm in diameter and nearly 2  $\mu$ m in length. The rod-like shape of the  $\alpha$ -MnMoO<sub>4</sub> is in accordance with the FE-SEM observations. The selected area electron diffraction (SAED) pattern of  $\alpha$ -MnMoO<sub>4</sub> nanorods (as shown in inset of **Figure 3.2.5 (d)**) shows clear diffraction patterns which indicates that the high crystallinity of the prepared nanorods [25].

### 3.2.3.3. Electrochemical characterization

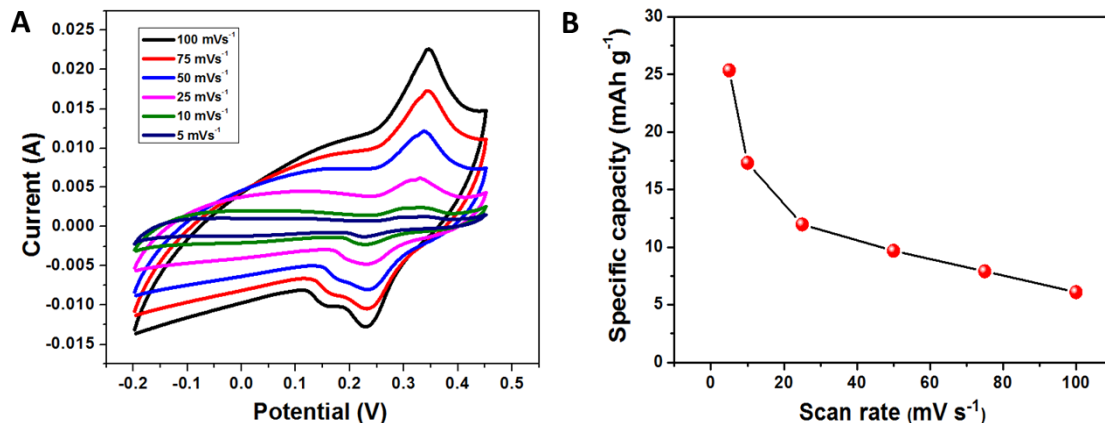


**Figure 3.2.6 (A)** Cyclic voltammetric curves of  $\alpha$ -MnMoO<sub>4</sub> nanorods in 2 M NaOH electrolyte at different scan rates. **(B)** Variation of specific capacitance with respect to scan rates.

In order to evaluate the electrochemical properties of the prepared  $\alpha$ -MnMoO<sub>4</sub>, at first, we studied the cyclic voltammetric (CV) analysis using 2 M NaOH electrolyte in the potential range of -0.2 – 0.45 V. **Figure 3.2.6 (A)** shows the CV curves of MnMoO<sub>4</sub> at different scan rates from 5 mV s<sup>-1</sup> to 100 mVs<sup>-1</sup>. The CV curves shows the presence of

a pair of redox peak which is attributed to the transition of Mn(II)/Mn(III) [11]. This evidences the pseudocapacitive nature of the  $\alpha$ -MnMoO<sub>4</sub>. With an increase in scan rate, the voltammetric current gradually increases which suggests that the kinetics of the interfacial faradaic redox reactions and the rates of electronic and ionic transport are rapid enough in the present scan [11].

where, 'S' is scan rate (mV s<sup>-1</sup>), ' $\Delta V$ ' is potential window (V), 'm' is mass of the active material (mg). **Figure 3.2.6 (B)** shows the variation of specific capacitance with respect to the scan rate. A specific capacitance of about 110.29 F g<sup>-1</sup> (specific capacity of 21.9 mAh g<sup>-1</sup>) was achieved for  $\alpha$ -MnMoO<sub>4</sub>nanorods at a lower scan rate of about 5 mV s<sup>-1</sup>. With an increase in scan rate, the specific capacitance is decreased which is due to the fact that at higher scan rates, the electrolyte ions are not able to utilize the active material completely [26, 27].

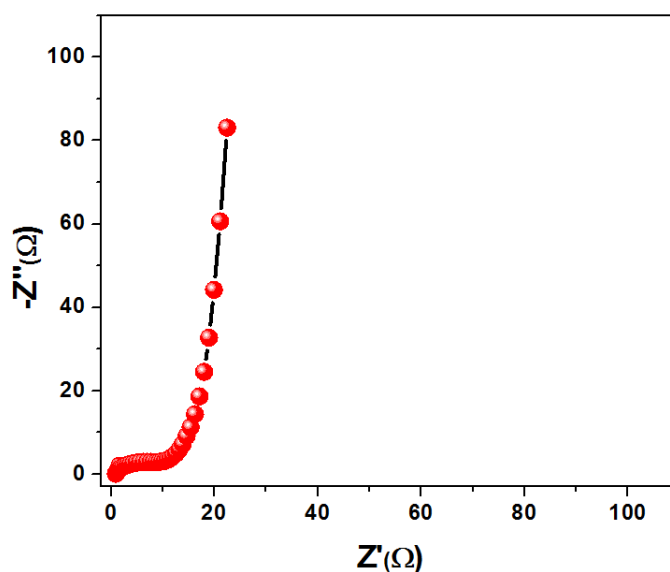


**Figure 3.2.7** Electrochemical impedance spectroscopy of  $\text{MnMoO}_4$  electrodes represented as Nyquist plot.

In order to understand the charge storage mechanism in  $\alpha\text{-MnMoO}_4$  nanorods, the EIS study has been performed in the frequency range from 0.01 Hz to 100 kHz and is presented as Nyquist plot as shown in **Figure 3.3.7**. It shows the presence of a semi-circle at the higher frequency range, which is due to the capacitance in parallel with the ionic charge transfer resistance ( $R_{ct} = 10.2\Omega$ ). In addition to this, the presence of linear part at the low frequency region or the slope of the  $45^\circ$  portion is called as Warburg resistance ( $Z_w$ ) is also observed which is due to the frequency dependent ion diffusion or transport in the electrolyte to the electrode surface [28, 29].

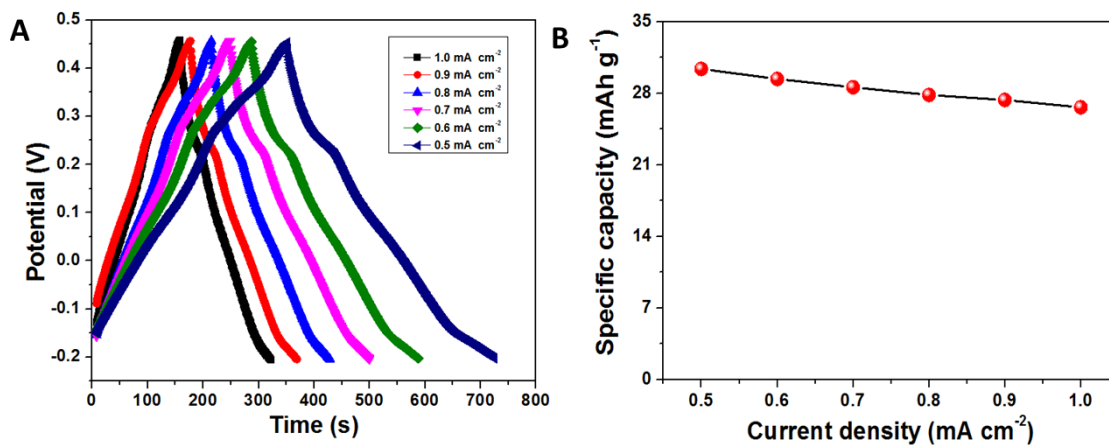


**Figure 3.2.8** (A) Galvanostatic discharge curves of  $\alpha\text{-MnMoO}_4$  with different discharge current densities. (B) Variation of specific capacitance with respect to discharge current density.

**Figure 3.2.8** (A) illustrates that the galvanostatic charge-discharge curves of the synthesized  $\text{MnMoO}_4$  at the various current densities. The observed quasi-symmetric

charge-discharge profile suggests that the pseudo capacitive behavior of the material. **Figure 3.2.8 (B)** shows the variance of specific capacitances with respect to the different discharge current densities. When increasing the current density, capacitance values decrease due to decrease in diffusion to the inner active sites of electrode material [30]. A specific capacitance of about  $168.32 \text{ F g}^{-1}$  was achieved for sonochemically synthesized  $\alpha\text{-MnMoO}_4$  nanorods at a lower current density of about  $0.5 \text{ mA cm}^{-2}$ . However the bare Ni foam is contributed to this obtained specific capacitance. We have performed the electrochemical characterization of bare Ni foam in same environment. About 13.5% of specific capacitance has been contributed by the bare Ni foam. Hence, the true output of  $\text{MnMoO}_4$  nanorods is calculated to be  $145.62 \text{ F g}^{-1}$  (specific capacity of  $30.39 \text{ mAh g}^{-1}$ ) at the scan rate of  $0.5 \text{ mA cm}^{-2}$ . The true capacitance of  $127.6 \text{ F g}^{-1}$  (specific capacity of  $23 \text{ mAh g}^{-1}$ ) is obtained at the scan rate of  $1 \text{ mA cm}^{-2}$ . The observed specific capacitance of  $\text{MnMoO}_4$  is relatively higher than that of the previous reports [11, 13].

The long-term cyclic stability of electrode material is an important criterion for supercapacitor applications [31]. The cyclic stability test of sonochemically synthesized  $\alpha\text{-MnMoO}_4$  using CV measurement (at a scan rate of  $100 \text{ mV mVs}^{-1}$ ) for 2000 cycles.

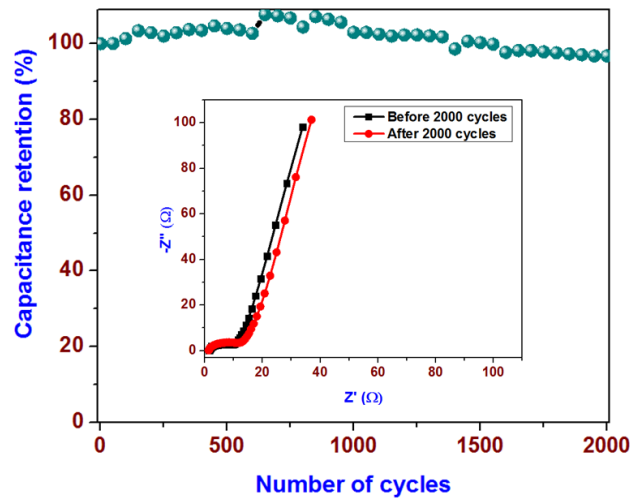


**Figure 3.2.9** Cyclic stability tests of  $\alpha$ -MnMoO<sub>4</sub> using cyclic voltammetry measurements at a scan rate of 100 mV s<sup>-1</sup> for 2000 cycles. The inset shows the Nyquist plot of  $\alpha$ -MnMoO<sub>4</sub> electrodes before and after 2000 cycles.

**Figure 3.2.9** showed the specific capacitance retentions with respect to number of cycles. About 96 % of initial capacitance was retained even after 2000 cycles which demonstrates that the good cyclic stability of sonochemically synthesized  $\alpha$ -MnMoO<sub>4</sub>. The inset of **Figure 3.2.9** shows the EIS analyses of electrode before and after cyclic tests. A significant increase in charge transfer resistance was observed for the electrode after 2000 cycles which may be attributed to the aggregation of the electrode material [32]. The increase in  $R_{ct}$  value from 10.2 to 11.4  $\Omega$  after cyclic test may cause decrease in specific capacitance after cyclic test.

### 3.2.4. Conclusion

In conclusion, a facile sonochemical approach for the preparation of  $\alpha$ -MnMoO<sub>4</sub> nanorods has been demonstrated. The XRD analysis, Raman spectrum, and HR-TEM studies revealed the high crystallinity of the prepared  $\alpha$ -MnMoO<sub>4</sub> nanorods. The electrochemical studies using CV and EIS measurements suggested the pseudocapacitive nature of the  $\alpha$ -MnMoO<sub>4</sub> nanorods. A maximum specific capacitance value of 168.32 F g<sup>-1</sup> (specific capacity of 30.3 mAh g<sup>-1</sup>) was obtained from the galvanostatic charge discharge analysis at the current density of 0.5 mA cm<sup>-2</sup>. When removing the contribution of Ni foam current collector, at 1 mA cm<sup>-2</sup> current density, the capacitance is about 127.6 F g<sup>-1</sup> (specific capacity of 23 mAh g<sup>-1</sup>). The  $\alpha$ -MnMoO<sub>4</sub> shows capacitance retention of about 96 % of its initial capacitance suggesting the good cyclic stability of the prepared material for supercapacitor applications. The overall results suggested that the sonochemically synthesized  $\alpha$ -MnMoO<sub>4</sub> is a good candidate as electrode material for supercapacitor applications.

### 3.2.5. References

1. G.W. Yang, C.L. Xu, H.L. Li, *Chem. Commun*, **2008**, 48, 6537.
2. G.X. Pan, X. Xia, F. Cao, P.S. Tang, H.F. Chen, *Electrochim. Acta*, **2012**, 63, 335.
3. A. Devadas, S. Baranton, T.W. Napporn, C. Christophe, *J. Power Sources*, **2011**, 196, 4044.
4. W. Wei, X. Cui, W. Chen, D.G. Ivey, *J. Power Sources*, **2009**, 186, 543.

5. R. Tummala, R.K. Guduru, P.S. Mohanty, *J. Power Sources*, **2012**, 209. 44.
6. Q. Lu, M.W. Lattanzi, Y. Chen, X. Kou, W. Li, X. Fan, K.M. Unruh, J.G. Chen, J.Q. Xiao, *Angew. Chem., Int. Ed.*, **2011**, 50, 6847.
7. K. Krishnamoorthy, S.J. Kim, *Mater. Res. Bull.*, **2013**, 48, 3136.
8. H. Wang, L. Zhang, X. Tan, C.M.B. Holt, B. Zahiri, B.C. Olsen, D. Mitlin, *J. Phys. Chem. C*, **2011**, 115, 17599.
9. B.O. Park, C.D. Lokhande, H.S. Park, K.D. Jung, O.S. Joo, *J. Mater. Sci.*, **2004**, 39, 4313.
10. Y. Ding, Y. Wan, Y.L. Min, W. Zhang, S.H. Yu, *Inorg. Chem.*, **2008**, 47, 7813.
11. L.Q. Mai, F. Yang, Y.L. Zhao, X. Xu, L. Xu, Y.Z. Luo, *Nat. Commun.*, **2011**, 2, 381.
12. D. Guo, H. Zhang, X. Yu, M. Zhang, P. Zhang, Q. Li, T. Wang, *J. Mater. Chem. A*, **2013**, 1, 7247.
13. B. Senthilkumar, K.V. Sankar, R.K. Selvan, M. Danielle, M. Manickam, *RSC Adv.*, **2013**, 3, 352.
14. D. Guo, P. Zhang, H. Zhang, X. Yu, J. Zhu, Q. Li, T. Wang, *J. Mater. Chem. A*, **2013**, 1, 9024.
15. C. Sekar, R.K. Selvan, S.T. Senthilkumar, B. Senthilkumar, C. Sanjeeviraja, *Powder Technol.*, **2013**, 215-216, 98.
16. G. Kianpour, M.S. Niasari, H. Emadi, *Ultrason. Sonochem.* **2013**, 20, 418.
17. C. Peng, L. Gao, S. Yang, J. Sun, *Chem. Commun.*, **2008**, 5601.

18. K. Karthikeyan, N. Poornaprakash, N. Selvakumar, K. Jeyasubramanian, *J. Nanostruct. Polym. Nanocompos.* **2009**, 5, 83.
19. M. Maczka, M. Ptak, K. Hermanowicz, A. Majchrowski, A. Pikul, J. Hanuza, *Phys. Rev. B* **2011**, 83, 174439.
20. M. N. Coelho, P. T. C. Freire, M. Maczka, C. Luz-Limac, G. D. Saraiva, W. Paraguassue, A. G. Souza Filhoa, P. S. Pizani, *Vib. Spectrosc* **2013**, 68, 34.
21. I. Kanesaka, H. Hashiba, I. Matsuura, *J Raman Spectrosc*, **1988**, 19,213.
22. G.C. Allen, S.J. Harris, J.A. Jutson, *Appl. Surf. Sci.* **1989**, 37, 111.
23. F. Werfeli, E. Minni, *J. Phys. Chem C* **1983**, 16, 6091.
24. X. Xia, W. Lei, Q. Hao, W. Wang, X. Wang, *Electrochim. Acta* **2013**, 99, 253.
25. T. Choudhury, S. O. Saied, J. L. Sullivan, A. M. Abbot, *J. Phys. D: Appl. Phys.* **1989**, 22, 1185.
26. S. Saranya, R.K. Selvan, N. Priyadharsini, *Appl. Surf. Sci.* **2012**, 258, 4881.
27. K. Krishnamoorthy, G. K. Veerasubramani, R. Sivaprakasam, S. J. Kim, *Chem Eng Chem Eng J.* **2014**, 251, 116.
28. K. Liu, Z. Hu, R. Xue, J. Zhang, J. Zhu, *J. Power Sources* **2008**, 179, 858.
29. C. Fu, H. Zhou, R. Liu, Z. Huang, J. Chen, Y. Kuang, *Mater. Chem. Phys.* **2012**, 132, 596.
30. J. Xu, L. Gao, J. Cao, W. Wang, Z. Chen, *Electrochim. Acta* **2010**, 56, 736.
31. P. Justin, G. R. Rao. *Int. J Hydrogen Energy*, **2010**, 35, 9709.

32. G. K. Veerasubramani, K. Krishnamoorthy, R. Sivaprakasam, N. J. Kim, S. J. Kim, *Int. J. Hydrogen Energy*. **2014**, 39, 5186.

### 3.3. Summary

In this chapter, we have synthesized transition metal (Co and Mn) molybdates using sonochemical method and investigated their electrochemical properties for supercapacitor applications. According to the result, the performance of CoMoO<sub>4</sub> exhibit quite better electrochemical performances due to their nano-sized structure compared to the MnMoO<sub>4</sub>. Also, the working current range is 10 times higher for the prepared plate-like CoMoO<sub>4</sub> (10 to 1 mA cm<sup>-2</sup>) whereas rod-shaped MnMoO<sub>4</sub> (1 to 0.5 mA cm<sup>-2</sup>). Hence, from next chapter, we are focused to improve the performance of CoMoO<sub>4</sub> and investigated its physico-chemical and electrochemical properties in detail.

## CHAPTER-4

### Synthesis of hybrid nanostructure with conducting polymer with CoMoO<sub>4</sub> and fabrication of CoMoO<sub>4</sub>//rGO hybrid supercapacitors

#### 4.1. *In-situ* chemical oxidative polymerization of aniline monomer in the presence of cobalt molybdate for supercapacitor applications

##### Highlights

- ❖ A simple and green approach for the preparation of cobalt molybdate/polyaniline (CoMoO<sub>4</sub>/PANI) composite via *in-situ* polymerization method has been reported
- ❖ The growth of PANI conductive layer on the surface of plate-like CoMoO<sub>4</sub> nanostructures has been confirmed by XRD, FT-IR, Raman and FE-SEM techniques
- ❖ The prepared CoMoO<sub>4</sub>/PANI composite delivered a maximum specific capacitance of 246 Fg<sup>-1</sup> (specific capacity of 68.3 mAh g<sup>-1</sup>) at scan rate of 5 mVs<sup>-1</sup>, whereas pristine PANI exhibits only 160 Fg<sup>-1</sup> which attributed to the synergic effect on the conducting network between CoMoO<sub>4</sub> and PANI
- ❖ The cyclic stability measurement revealed that above 80 % of its initial capacitance is retained even after long cycles

#### 4.1.1 Introduction

In recent times, conducting polymers are generally considered to be an ideal electrode material for flexible energy storage devices [1-4]. Among them, PANI is a unique conducting polymer due to its environmentally friendly nature, facile synthesis, and promising optical, electrical, electrochemical properties [5]. But it suffers from the poor electrochemical cyclic stability of PANI. To overcome this demerit, many researchers are focused to make composites with carbon based materials, and metal chalcogenides and metal oxides to enhance the electrochemical cyclic stability [6, 7]. More significantly, it is reported that some binary metal oxides acquires a much better electronic conductivity and higher electrochemical activity than single component metal oxide [8, 9]. In addition, it is well known that the rate capability of electrode materials is mainly determined by the kinetics of ion diffusion and electronic conductivity [10-12]. Nowadays, abundant researches focused on the metal molybdates due to their various important properties [13]. In order to enhance the electrochemical properties of PANI, researchers are focusing with incorporating the binary metal oxide into the PANI [14]. However, the development of PANI based materials with simple, reliable synthetic method and improved electrochemical properties are still remains massive challenge. Only few reports are available on the binary metal oxide based PANI composite for electrochemical supercapacitor applications. On the basis of this strategy, we have successfully synthesized  $\text{CoMoO}_4/\text{PANI}$  for electrochemical supercapacitor applications. Briefly, in this article,  $\text{CoMoO}_4/\text{PANI}$  was synthesized via *in-situ* chemical

polymerization of aniline monomer in the presence of  $\text{CoMoO}_4$  nanostructures. The spherical shaped PANI was uniformly spreading over  $\text{CoMoO}_4$  nanostructures. The synthesized  $\text{CoMoO}_4/\text{PANI}$  composite based electrode material demonstrated a high specific capacitance, high energy density than the pristine PANI and also better long term cyclic stability showing the auspicious evidences for this synthesized  $\text{CoMoO}_4/\text{PANI}$  material could be utilized for supercapacitor applications.

#### 4.1.2 Experimental

##### 4.1.2.1 Preparation of $\text{CoMoO}_4/\text{PANI}$ by *in-situ* polymerization

$\text{CoMoO}_4$  was synthesized by sonochemical method as described in our previous report [16]. Briefly,  $\text{CoMoO}_4$  nanostructures were synthesized by a facile sonochemical approach using sodium molybdate and cobalt chloride as the starting precursors. The solution containing cobalt chloride was allowed to ultrasound irradiation followed by the drop-wise addition of sodium molybdate solution by keeping the entire solution under mild stirring using a Teflon coated magnetic stir bar. The obtained precipitate was washed thoroughly with distilled water and ethanol and the process was repeated several times until the synthesized product is free from any impurities or residual ions and dried in electric oven. Finally, the dried powder was calcined at  $500\text{ }^\circ\text{C}$  for 3 h, which results in the formation of  $\text{CoMoO}_4$ . The  $\text{CoMoO}_4/\text{PANI}$  composite was synthesized by *in-situ* polymerization of aniline monomer using  $\text{CoMoO}_4$  nanostructures. In a typical procedure, 0.425 g of  $\text{CoMoO}_4$  nanostructure was dispersed in 50 ml of 1 M HCl by

Teflon coated magnetic stirrer under room temperature. Then 0.5 ml of aniline monomer was added drop-wise to the  $\text{CoMoO}_4$  dispersed solution. Then 10 ml of 2.2 g of APS in water was added drop-wise to the above mixture. Further, the polymerization reaction was carried out for 4 h under room temperature with maintained in stirring. The obtained precipitate was washed with ethanol and deionized water to remove the residual ions. Then the precipitate was dried at 60 °C for overnight to obtain  $\text{CoMoO}_4/\text{PANI}$  composite. The same procedure was followed to synthesize pristine PANI without addition of  $\text{CoMoO}_4$ .

#### **4.1.2.2 Preparation of $\text{CoMoO}_4/\text{PANI}$ electrodes**

The working electrode was prepared as follows: In detail, the active material ( $\text{CoMoO}_4/\text{PANI}$ ), carbon black and PVDF were mixed in the weight ratio of 75:20:5 using N-methyl pyrrolidone (NMP) into slurry form. The slurry was coated on the stainless steel substrate (area of  $1 \times 1 \text{ cm}^2$ ) and allowed to dry at 50 °C for 48 h. The mass of an active material on the electrode is about 2.8 mg. A solution containing 1 M  $\text{H}_2\text{SO}_4$  was used as the electrolyte. The electrochemical behavior of the  $\text{CoMoO}_4/\text{PANI}$  electrode was examined by cyclic voltammetry and galvanostatic charge-discharge tests using an AUTOLAB PGSTAT302N electrochemical workstation. The electrochemical measurements were carried out at room temperature in a three electrode system consisting of the  $\text{CoMoO}_4/\text{PANI}$  as working electrode, silver/silver chloride (Ag/AgCl) as reference electrode and platinum as counter electrode.

### 4.1.3 Results and discussion

#### 4.1.3.1 Structural characterization

In this study, an *in-situ* chemical oxidative polymerization of aniline monomer was performed in the presence of sonochemically synthesized  $\text{CoMoO}_4$  nanostructures. **Figure 4.1.1**, shows XRD pattern of PANI and  $\text{CoMoO}_4/\text{PANI}$  composites. The presence of broad peaks at  $20.3^\circ$  and  $25.3^\circ$  corresponds to the planes (020) and (110) respectively, indicating the periodicity parallel and perpendicular characteristics of polymer chain and also no sharp peak was observed which suggesting the semi crystalline nature and emeraldine salt form of the synthesized PANI polymer [15].

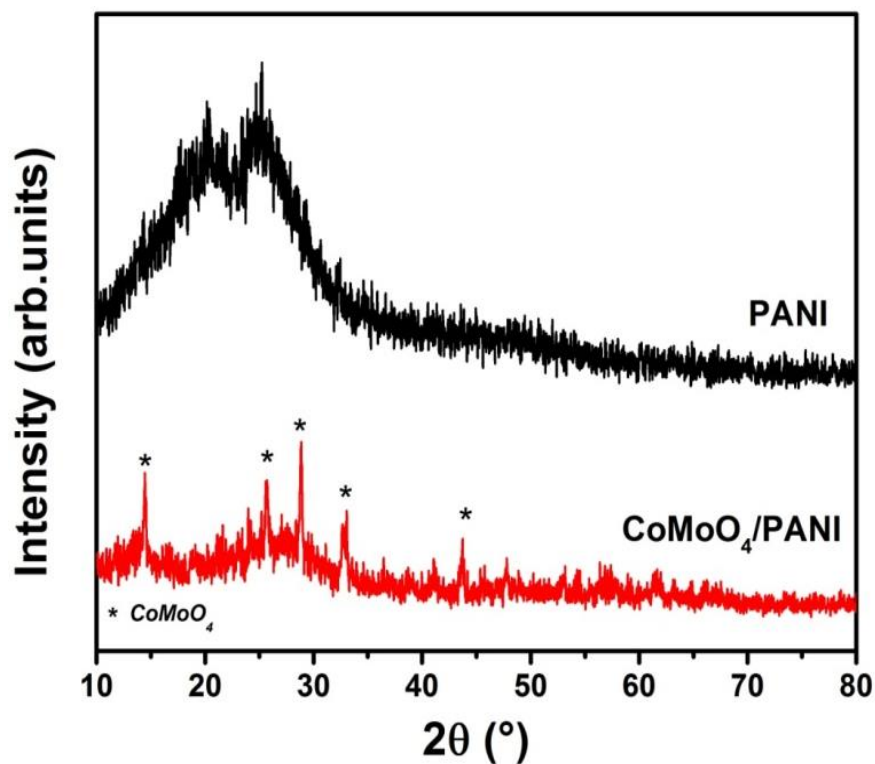


**Figure 4.1.1** X-ray diffraction pattern of PANI and CoMoO<sub>4</sub>/PANI composite material. Inset shows the XRD pattern of CoMoO<sub>4</sub>.

The monoclinic phase of CoMoO<sub>4</sub> by sonochemical approach as shown in **Figure 3.1.1**. In the composite of CoMoO<sub>4</sub>/PANI, the maximum intensity peak of CoMoO<sub>4</sub> was totally diminished and the characteristic peaks of PANI was observed majorly except few peaks of CoMoO<sub>4</sub>, which indicated that the CoMoO<sub>4</sub> was fully covered with PANI. Raman spectroscopy is one of the non-destructive tools to identify the bonding nature of the polymeric materials.

The Raman spectrum has been measured between the ranges of 500 and 2000 cm<sup>-1</sup> and presented in **Figure 4.1.2 (A)**.

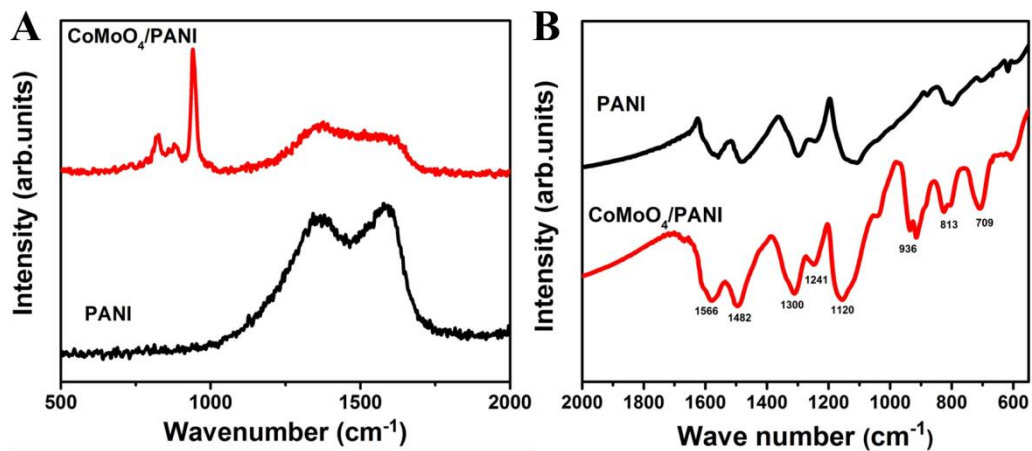


**Figure 4.1.2** Raman spectrum (a), FT-IR spectrum (b) of PANI and CoMoO<sub>4</sub>/PANI composite material. Inset shows the FT-IR spectrum of CoMoO<sub>4</sub>.

The broad peak has been observed from 1100 cm<sup>-1</sup> to 1700 cm<sup>-1</sup> which corresponds to the presence of PANI. The band at 1342 cm<sup>-1</sup> corresponds to the C-N<sup>+</sup> stretching

modes of delocalized polaronic charge carriers, which are characteristic of the protonated imine form of polyaniline [16]. The small band at  $1509\text{ cm}^{-1}$  may be assigned to the N–H deformation vibrations associated with the semi-quinonoid structures. The bands at  $1588$  and  $1618\text{ cm}^{-1}$  may be assigned to the C=C stretching vibrations of the quinonoid ring and C–C stretching vibrations of the benzene ring [17]. In case of CoMoO<sub>4</sub>/PANI composite, all the above specified peaks have been observed for PANI and remaining peaks below  $1000\text{ cm}^{-1}$  which corresponds to the presence of CoMoO<sub>4</sub>. **Figure 3.1.2 (a)** shows the Raman spectrum of CoMoO<sub>4</sub>. In order to investigate the bonding nature of synthesized composite material, FT-IR was performed. **Figure 4.1.2 (B)** shows the FT-IR spectrum of pristine PANI and CoMoO<sub>4</sub>/PANI composite. The bands at  $1565$ ,  $1482$ ,  $1300$ ,  $1241$ ,  $1120$ ,  $800$ ,  $504\text{ cm}^{-1}$  are corresponds to the characteristics peaks of PANI. The band  $1565\text{ cm}^{-1}$  and  $1482\text{ cm}^{-1}$  are attributed to the C=C stretching frequency of quinoid and benzenoid ring respectively, band  $1300\text{ cm}^{-1}$  is assigned to the C–N stretching of secondary aromatic amine, the band  $1241\text{ cm}^{-1}$  is due to C–N<sup>+</sup> stretching vibration in the polarized structure of PANI. The band  $1120\text{ cm}^{-1}$  is attributed to the C=N stretching vibration (–N=quinoid=N–). The bands at  $800$  and  $504\text{ cm}^{-1}$  are assigned to the C–H out-of-plane deformation and C=C stretching in 1, 4-disubstituted benzene [18, 19]. **Figure 3.1.2** shows the FT-IR spectrum of CoMoO<sub>4</sub> which is exactly matched with our previous report [20]. When compared to PANI, new bands are found for CoMoO<sub>4</sub>/PANI composites which are assigned to the presence of CoMoO<sub>4</sub>. The peak at  $936\text{ cm}^{-1}$  corresponds to the vibrational modes of distorted MoO<sub>4</sub>

tetrahedral present in  $\text{CoMoO}_4$ . The band at  $700\text{-}900\text{ cm}^{-1}$  is attributed to the ordinary bond Mo-O [20].

#### 4.1.3.2 Morphological analysis

The structural morphology of pristine PANI,  $\text{CoMoO}_4$  and  $\text{CoMoO}_4/\text{PANI}$  composite was investigated by using the FE-SEM analysis (**Figure 4.1.3A-D**). **Figure 4.1.3A** shows the pristine PANI is random spherical granulated particles. The high magnification of PANI (**Figure 4.1.3 (B)**) showed the spherical particles are less than 100 nm. **Figure 3.1.3** shows the plate like structure of  $\text{CoMoO}_4$ . After polymerization of aniline in the presence of  $\text{CoMoO}_4$ , the homogeneous aggregated spherical like PANI particles were uniformly covered on the  $\text{CoMoO}_4$  surface. (**Figure 4.1.3 (C and D)**).

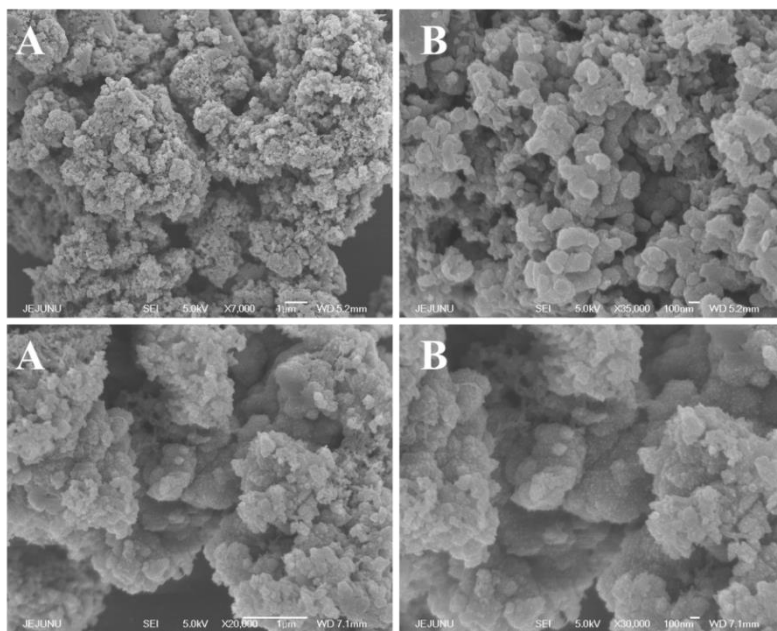


**Figure 4.1.3** FE-SEM images of PANI (A and B) and  $\text{CoMoO}_4/\text{PANI}$  composite (C and D) material at the different magnifications.

#### 4.1.3.3 Electrochemical characterization

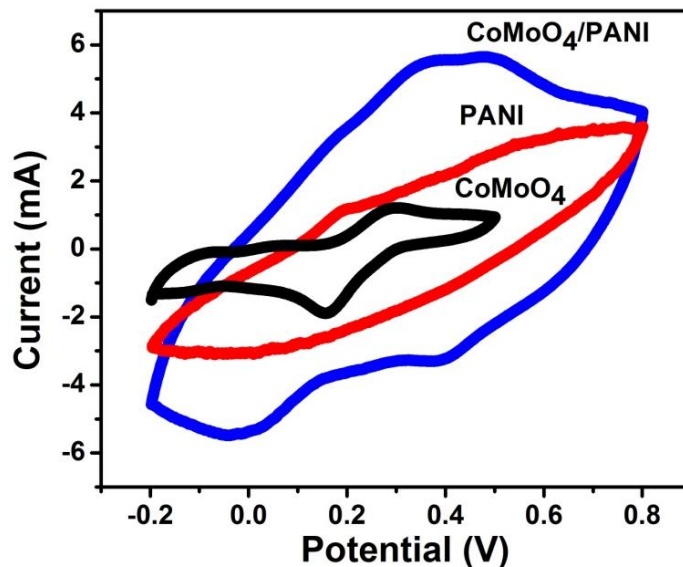


**Figure 4.1.4** Comparison of cyclic voltammetry curves for pristine CoMoO<sub>4</sub>, pristine PANI and CoMoO<sub>4</sub>/PANI composite at a scan rate of 5 mV s<sup>-1</sup> in H<sub>2</sub>SO<sub>4</sub> electrolyte.

In order to evaluate the electrochemical properties of synthesized CoMoO<sub>4</sub>/PANI composites, cyclic voltammetry, galvanostatic charge-discharge and electrochemical impedance spectroscopy measurements were performed using 1 M sulfuric acid as an electrolyte solution. **Figure 4.1.4** shows the comparison curve of pristine PANI, CoMoO<sub>4</sub>, and CoMoO<sub>4</sub>/PANI composites at the scan rate of 5 mV s<sup>-1</sup>. The working potential window of CoMoO<sub>4</sub> was found to be -0.2 to +0.5 V whereas PANI and CoMoO<sub>4</sub>/PANI was found of -0.2 to 0.8 V. It shows that the presence of redox pair which indicates the pseudocapacitive behavior of the material. Also, the area under CV curve of CoMoO<sub>4</sub>/PANI composite is higher than the PANI may be due to the

availability of active sites of PANI and increasing the conducting network through intermolecular interaction between PANI and CoMoO<sub>4</sub> [21-23]. The maximum specific capacitance value of 52.95, 159.8 and 245.9 F g<sup>-1</sup> was obtained for pristine CoMoO<sub>4</sub>, pristine PANI and CoMoO<sub>4</sub>/PANI respectively, in H<sub>2</sub>SO<sub>4</sub> electrolyte solution.

**Figure 4.1.5** cyclic voltammetry and charge discharge analysis of CoMoO<sub>4</sub>/PANI composite. In **Figure 4.1.5 (A)**, the area under the CV curve was significantly increased when increasing the scan rates, which indicates that the scan rate is directly proportional to the area under CV curve. However, a slight deviation in the shape of the CV curve was observed at high scan rates (50 mV s<sup>-1</sup>); the shape became quasi-rectangular which was due to the fact that at high scan rates, the active material is not completely utilized by the electrolyte ions [24]. **Figure 4.1.5 (B)** illustrates that the galvanostatic charge-discharge curve for pristine PANI and CoMoO<sub>4</sub>/PANI composite at the current density from 2 to 5 mA cm<sup>-2</sup>. It can be seen that the charge-discharge profiles are semi-symmetric behavior and indicates the pseudocapacitive behavior of the CoMoO<sub>4</sub>/PANI composite material. It is well known that at low current density, ions in the electrolyte have more time to diffuse into the inner surface of the electrode material. Hence, at lower current density both the inner and outer surfaces contribute to the electrochemical activity then finally it leads to the higher specific capacitance of the material. In similar way, high discharge current density, the electrolyte ions are not effectively utilized the active material. On the other hand, only the outer surface of the electrode material contributed to the reaction with the electrolytes because of limited

access time of electrolyte ions which further results in the decrease in specific capacitance value [25, 26].

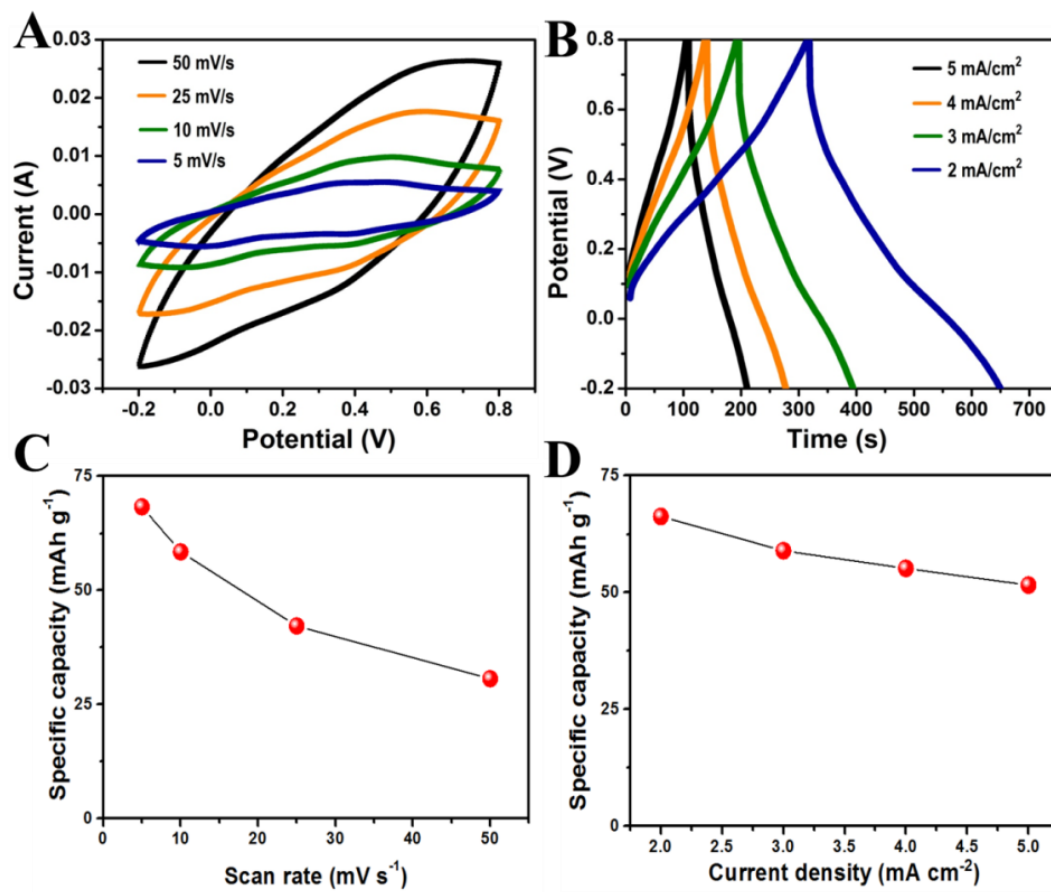


**Figure 4.1.5** Cyclic voltammety curves of CoMoO<sub>4</sub>/PANI at the different scan rates (from 5 to 50 mV s<sup>-1</sup>) (A), galvanostatic charge-discharge curves of CoMoO<sub>4</sub>/PANI at the different current densities (from 2 to 5 mA cm<sup>-2</sup>) (B), specific capacitances of CoMoO<sub>4</sub>/PANI with respect to scan rates (C), and specific capacitances of CoMoO<sub>4</sub>/PANI with respect to current densities (D).

**Figure 4.1.5 (C)** represents the variation of specific capacitance with respect to the scan rates. The maximum specific capacitance 248.9 F g<sup>-1</sup> (specific capacity of 68.3 mAh g<sup>-1</sup>) at the scan rate of 5 mV s<sup>-1</sup> was achieved from cyclic voltammety and 238.6

F/g (specific capacity of 66.269 mAh g<sup>-1</sup>) at the current density of 2 mA cm<sup>-2</sup> from charge discharge analysis **Figure 4.1.5 (D)**. This observed capacitance value of CoMoO<sub>4</sub>/PANI composite is relatively higher than when compared to some reported metal oxide and conducting polymer based composites. Such as, the organically soluble bifunctional PANI/Fe<sub>3</sub>O<sub>4</sub> composite (213 F g<sup>-1</sup> at 1 mA cm<sup>-2</sup>) by Radhakrishnan et al., [27], PANI/mesoporous carbon based nano-composite electrode (87.5 F g<sup>-1</sup>) by Cai et al., [28] and PANI/MoO<sub>3</sub> composite (200 F g<sup>-1</sup>) by Zheng et al., [29].

Long term cyclic stability is one of the important parameter which is essential for the practical applications of the electrode materials in super capacitor devices [12]. To study the cyclic stability of CoMoO<sub>4</sub>/PANI composite, galvanostatic charge discharge analysis was performed for 500 cycles at the current density of 4 mA cm<sup>-2</sup> (**Figure 4.1.6**). At the end of the 500<sup>th</sup> cycle, 82.35% of the initial specific capacitance was retained. A decrease in specific capacitance is observed after 500 cycles which can be attributed to the aggregation of the electrode material. It may also be attributed to the decrease in adhesion between electrode material and current collector [30, 31]. It also confirmed by electrochemical impedance spectroscopy. The inset of **Figure 4.1.6** shows that the Nyquist plot of electrode materials before and after cyclic study. We can easily observe that the solution and charge transfer resistance significantly increased after 500 cycles. It might be due to the aggregation of the electrode materials during continuous cycles.

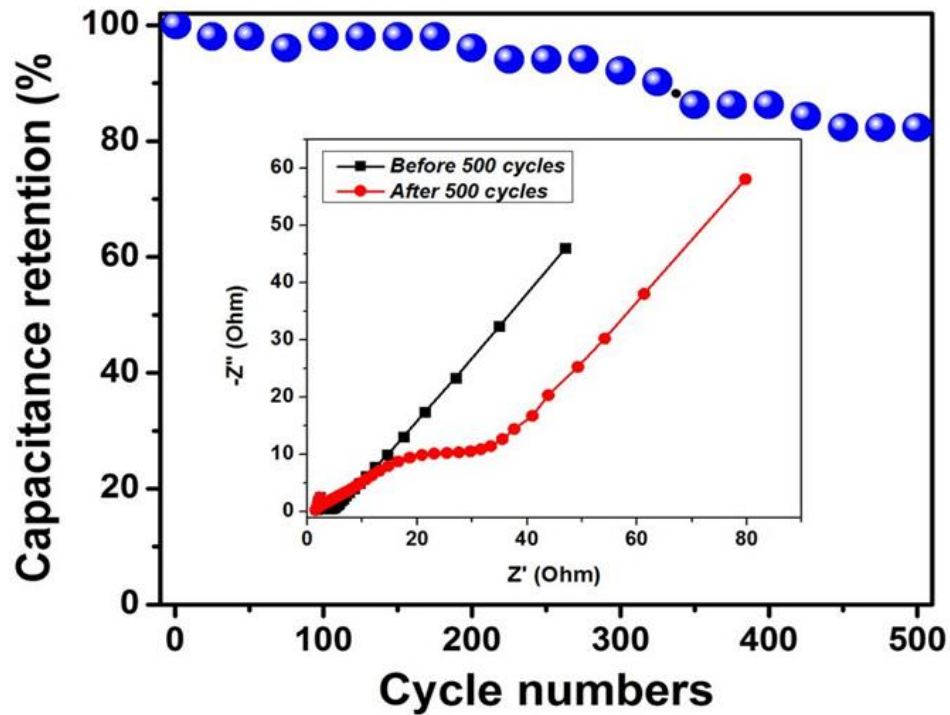


**Figure 4.1.6** Ragone plot of  $\text{CoMoO}_4/\text{PANI}$  at different current densities (a), cyclic performance of  $\text{CoMoO}_4/\text{PANI}$  at current density of  $4 \text{ mA cm}^{-2}$  (inset Nyquist plot for before and after cyclic stability test).

The observed stability is relatively higher than PANI covered on carbon microspheres [32]. This behavior suggests that the better long term stability of  $\text{CoMoO}_4/\text{PANI}$  composite. Overall results suggest that the synthesized  $\text{CoMoO}_4/\text{PANI}$  composite is a potential candidate as an electrode material for supercapacitor applications.

#### 4.1.4 Conclusion

In conclusion, CoMoO<sub>4</sub>/PANI composite was successfully synthesized by an *in-situ* chemical oxidative polymerization approach and successfully applied for supercapacitor applications. The structure, surface morphology and electrochemical behavior of synthesized material were thoroughly investigated. A maximum specific capacitance of 245.9 F g<sup>-1</sup> was achieved for CoMoO<sub>4</sub>/PANI composite material which is significantly higher than the pristine PANI (159.8 F g<sup>-1</sup>). The prepared CoMoO<sub>4</sub>/PANI composites exhibit good cyclic stability of 82.35 % even after 500 cycles of charge-discharge analysis at current density of 4 mA cm<sup>-2</sup>. These improved electrochemical properties suggest that the prepared CoMoO<sub>4</sub>/PANI composite material as a highly suitable promising electrode material for supercapacitor applications.

#### 4.1.5 References

1. C. Meng, C. Liu, L. Chen, C. Hu, S. Fan, *Nano Lett.* **2010**, 10, 4025.
2. Q. Wu, Y. Xu, Z. Yao, A. Liu, G. Q. Shi, *ACS Nano* **2010**, 4, 1963.
3. S. Mu, C. Chen, J. Wang, *Synt. Met.* **1997**, 88, 249-254.
4. J.E. Yang, I. Jang, M. Kim, S.H. Baeck, S. Hwang, S.E. Shim, *Electrochim. Acta* **2013**, 111, 136.
5. K.J. Huang, L. Wang, Y.J. Liu, H.B. Wang, Y. M. Liu, L.L. Wang, *Electrochim. Acta* **2013**, 109, 587.

6. H. Jiang, J. Ma, C.Z. Li, *Chem. Commun.* **2012**, 48, 4465.
7. Q.F. Wang, B. Liu, X.F. Wang, S.H. Ran, L.M. Wang, D. Chen, G.Z. Shen, *J. Mater. Chem.* **2012**, 22, 21647.
8. M.D. Stoller, R.S. Ruoff, *Energy Environ. Sci.* **2010**, 3, 1294.
9. D.W. Wang, F. Li, M. Liu, G.Q. Lu, H.M. Cheng, *Angew. Chem.* **2007**, 46, 379.
10. Y. Liang, M. G. Schwab, L. Zhi, E. Mugnaioli, U. Kolb, X. Feng, K. Mullen, *J. Am. Chem. Soc.* **2010**, 132, 15030.
11. S. Radhakrishnan, C.R.K. Rao, M. Vijayan, *J Appl Polym Sci* **2011**, 122, 1510.
12. C. Li, H. Bai, G. Q. Shi, *Chem. Soc. Rev.* **2009**, 38, 2397.
13. W. Xiao, J.S. Chen, C.M. Li, R. Xu, X.W. Lou, *Chem Mater* **2010**, 22, 746.
14. B. Senthilkumar, K. Vijayasankar, C. Sanjeeviraja, R. Kalaiselvan, *J. Alloy Compd* **2013**, 553, 350.
15. N.R. Chiou, A.J. Epstein, *Adv. Mater.* **2005**, 17, 1679.
16. A. Shakoor, T.Z. Rizvi, A. Nawaz, *J. Mater. Sci.: Mater. Electron*, **2011**, 22, 1076.
17. Z. Morávková, M. Trchová, M. Exnerová, J. Stejskal, *Thin Solid Films*, **2012**, 520, 6088.
18. C. Li, J. Wang, Y. Wen, Y. Ning, Y. Wen, X. Yuan, M. Li, D. Yang, *ECS Electrochem. Lett.* **2013**, 2, H1.
19. X.B. Yan, Z.J. Han, Y. Yang, B.K. Tay, *J. Phys. Chem. C* **2007**, 111, 4125.

20. Yu.A. Agafonov, N.V. Nekrasov, N.A. Gaidai, M.A. Botavina, P.E. Davydov, A.L. Lapidus. *Kinet. Catal.* **2009**, 50, 599-604.
21. K.R. Prasad, N. Miura, *Electro chem. Solid State Lett.* **2004**, 7, A425.
22. L. Chena, L.J. Suna, F. Luana, Y. Lianga, Y. Li, X.X. Liu, *J. Power Sources* **2010**, 195, 3742.
23. Z.A. Hu, Y.L. Xie, Y.X. Wang, L.P. Mo, Y.Y. Yang, Z.Y. Zhang, *Mater. Chem. Phys.* **2009**, 114, 990.
24. G. Guo, L. Huang, Q. Chang, L. Ji, Y. Liu, Y. Xie, W. Shi, and N. Jia, *Appl. Phys. Lett* **2011**, 99, 083111-1.
25. C.C. Hu, E. Chen, and J.Y. Lin, *Electrochim. Acta*, **2002**, 47, 2741.
26. S.T. Senthilkumar, R.K. Selvan, N. Ponpandian, J.S. Melo. *RSC Adv* **2012**, 2, 8937.
27. S. Radhakrishnan, S. Prakash, C.R.K. Rao, M. Vijayan, *Electrochem Solid St*, **2009**, 12, A84.
28. J.J. Cai, L.B. Kong, J. Zhang, Y.C. Luo, L. Kang, *Chinese Chem Let*, **2010**, 21, 1509.
29. L. Zheng, Y. Xu, D. Jin, Y. Xie, *Chem. Asian J.* **2011**, 6, 1505.
30. J. Yan, Z. Fan, T. Wei, W. Qian, M. Zhang, F. Wei, *Carbon* **2010**, 48, 3825.
31. D. Zhang, X. Zhang, Y. Chen, C. Wang, Y. Ma. *Electrochim. Acta* **2012**, 69, 364.
32. Y.T. Tan, F. Ran, L.B. Kong, J. Liu, L. Kang, *Synt. Met*, **2012**, 162, 114.

## 4.2. Fabrication of CoMoO<sub>4</sub>//reduced graphene oxide hybrid supercapacitors

### Highlights

- ❖ In this part, we report the fabrication of hybrid supercapacitor based on a reduced graphene oxide (rGO) negative electrode and a cobalt molybdate (CoMoO<sub>4</sub>) positive electrode
- ❖ The electrode materials were synthesized hydrothermally (as rGO nanosheets) and sonochemically (as CoMoO<sub>4</sub> nanostructures)
- ❖ X-ray diffraction, field-emission scanning electron microscopy, Fourier-transform infrared spectroscopy, Raman spectroscopy, and nitrogen adsorption–desorption isotherm analysis were used to characterize the electrode materials
- ❖ In a three-electrode configuration, rGO nanosheets and CoMoO<sub>4</sub> nanostructures delivered a specific capacitance of ~168.8 and 98.34 F g<sup>-1</sup>, respectively
- ❖ Furthermore, the rGO||CoMoO<sub>4</sub> HSC device demonstrated a maximum specific capacitance of 26.16 F g<sup>-1</sup> (at a current density of 0.5 mA cm<sup>-2</sup>), an energy density of 8.17 Wh kg<sup>-1</sup>, and a maximum working voltage of 1.5 V
- ❖ The fabricated device possessed excellent capacitance retention: >84.7% for 4000 cycles at a current density of 1.0 mA cm<sup>-2</sup>

#### 4.2.1. Introduction

Two strategies have been investigated to increase the potential window (*i.e.*, the chemical stability of the electrolyte under redox reaction initiation): (1) the use of organic electrolytes instead of aqueous electrolytes and (2) the use of asymmetric SCs (ASCs). The system using organic electrolytes show low capacitive performance and low power capability due to their limited ion concentration and ionic conductivity [1]. In contrast, the enhancement in the potential window displayed by ASCs has been impressive, resulting in higher energy density in aqueous electrolytes. ASCs commonly have an electrochemical double-layer (capacitor-type) electrode created from carbon materials and a second electrode constructed from a pseudocapacitive (battery-type) material; together, the two components allow the ASC to exhibit two different potential windows in the same electrolyte [2-4]. Thus, ASCs are configured to fully utilize the different potential windows of the two electrodes to maximize the operation voltage of the cell system [5].

Recently, considerable research effort has been devoted to increasing the working voltage levels of various asymmetric electrochemical SCs using different materials for the negative and positive electrodes [5-7]. In these studies, the negative electrode is mainly composed of carbonaceous materials, such as activated carbon, carbon nanotubes (CNTs), and graphene [8-10]. Among these, graphene is an ultrathin two-dimensional hexagonal lattice of  $sp^2$  carbon atoms, covalently bonded along two plane directions

[11]. Graphene has been investigated extensively for its electrical, electrochemical, and electronic applications due to its high strength, as well as its excellent thermal and electrical conductivity [12, 13]. The exceptional electrochemical behavior of graphene can be explained by its high specific surface area, providing the electrolyte ions easy access to the electrode [14]. Additionally, graphene-based materials can be easily fabricated by simple chemical synthesis of graphite oxide. Besides, graphene has been extensively studied as a negative electrode material for ASCs [10, 13, 15, and 16]. Hitherto, metal oxides/hydroxides, binary metal oxides, and conducting polymers, among other materials, have been investigated for use as a positive electrode material for ASCs [15-19]. Among them, binary metal oxides/hydroxides are considered to be especially effective due to their multiple oxidation states and high electrical conductivities [20, 21]. Recently, metal molybdates, such as  $\text{CoMoO}_4$ ,  $\text{NiMoO}_4$ , and  $\text{MnMoO}_4$ , have demonstrated enhanced electrochemical performance over the single-component oxides [21-23]. In particular, cobalt molybdate ( $\text{CoMoO}_4$ ) SCs exhibit a high electrochemical performance, high rate capability, and high durability [24], in addition to being nontoxic, environmentally safe, and inexpensive. Several studies have investigated  $\text{CoMoO}_4$ -based ASCs. Liu et al. fabricated an ASC based on  $\text{CoMoO}_4$ - $\text{NiMoO}_4 \cdot x\text{H}_2\text{O}$  as the positive electrode and activated carbon as the negative electrode [25], while Senthilkumar et al. synthesized an ASC using  $\beta$ - $\text{NiMoO}_4$ - $\text{CoMoO}_4 \cdot x\text{H}_2\text{O}$  as the positive electrode and activated carbon as the negative electrode [26].

In this chapter, we report an ASC fabricated using  $\text{CoMoO}_4$  nanostructures as the positive electrode and reduced graphene oxide (rGO) nanosheets as the negative electrode material, with 1.0 M sodium hydroxide (NaOH) used as the electrolyte. Commercial filter paper was used as a separator. This ASC device achieved a specific capacitance of  $26.16 \text{ F g}^{-1}$  and an energy density of  $8.17 \text{ Wh kg}^{-1}$  at a constant discharge current density of  $0.5 \text{ mA cm}^{-2}$  for an operational voltage of 1.5 V. To our knowledge, this is the first report of a  $\text{CoMoO}_4/\text{rGO}$ -based ASC.

## **4.2.2. Experimental methods**

### **4.2.2.1. Preparation of reduced graphene oxide nanosheets (rGO)**

The rGO nanosheets were prepared using graphene oxide (GO; synthesized via the modified Hummers method [27]) as the starting material. A hydrothermal method was used to reduce GO into graphene nanosheets, with water as the solvent. Briefly, 80 mg of GO was dispersed in water and sonicated in a bath-type sonicator for 1 h to obtain a uniform brown-colored GO dispersion. The solution was then transferred to a 100-mL Teflon autoclave, covered by a stainless steel reactor, and kept at a constant temperature of  $150^\circ\text{C}$  for 10 h. After the reaction, the Teflon was cooled to room temperature naturally; the color of the suspension turned black, indicating the reduction of GO into rGO. The rGO suspension was washed thoroughly and centrifuged several times with

distilled water and ethanol to remove the residual ions. Finally, the sample was dried at 60°C for 5 h in a hot-air oven.

#### **4.2.2.2. Preparation of CoMoO<sub>4</sub> nanostructures**

The CoMoO<sub>4</sub> nanostructures were synthesized via a sonochemical approach using Na<sub>2</sub>MoO<sub>4</sub> and CoCl<sub>2</sub> as the starting precursors, as reported in **Chapter 3.1** [28]. Briefly, 1 M of CoCl<sub>2</sub>·6H<sub>2</sub>O in CH<sub>3</sub>OH and 1 M of Na<sub>2</sub>MoO<sub>4</sub> in water were prepared in two separate beakers. The CoCl<sub>2</sub> solution underwent ultrasound irradiation, followed by dropwise addition of the Na<sub>2</sub>MoO<sub>4</sub> solution. Note that during this process, the entire solution was stirred gently with a Teflon-coated magnetic stir bar for 1.5 h to obtain violet-colored precipitates of CoMoO<sub>4</sub>·xH<sub>2</sub>O. The precipitate was thoroughly washed with distilled water and ethanol until the impurities and residual ions were eliminated from the final product. Lastly, the CoMoO<sub>4</sub>·xH<sub>2</sub>O precipitate was allowed to dry at 100°C for 3 h, followed by calcination at 500°C for 3 h, resulting in the formation of CoMoO<sub>4</sub> nanostructures.

#### **4.2.2.3. Preparation of positive and negative electrodes**

The working electrodes were prepared using the following procedure. The active material (CoMoO<sub>4</sub> or rGO) was ground with carbon black and polyvinylidene difluoride (PVDF; mixture ratio: 75:20:5) using *N*-methyl pyrrolidone (NMP). A stainless steel substrate (1 × 1 cm<sup>2</sup>) was then coated with the mixture, and the coated substrate was allowed to dry at 80°C overnight. The mass of the active material on the electrode was

~1.6 mg, and a solution containing 1 M NaOH was used as the electrolyte. The electrochemical behavior of the positive and negative electrodes was examined at room temperature using a three-electrode system: CoMoO<sub>4</sub> or rGO as the working electrode, silver/silver chloride (Ag/AgCl) as the reference electrode, and platinum as the counter electrode. Finally, ASCs were fabricated in the form of a sandwich-type electrode, with an electrolyte-immersed filter paper used as the separator.

### 4.2.3. Results and discussion

#### 4.2.3.1. Structural characterization

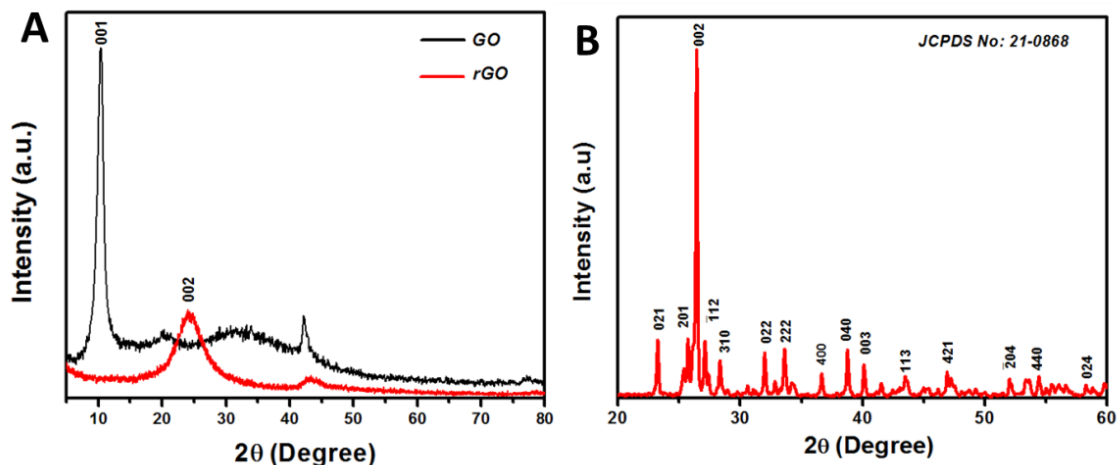


**Figure 4.2.1** XRD pattern for the synthesized GO from Hummers method and rGO by hydrothermal method (A), CoMoO<sub>4</sub> nanostructures by sonochemical method (B).

**Figure 4.2.1** shows an XRD pattern of the synthesized material; XRD patterns for GO and rGO are shown in **Figure 4.2.1 A**. The prepared GO exhibited a sharp dominant peak at 10.43° (with an interlayer spacing of 0.847 nm), which was assigned to (001) reflection. After hydrothermal reduction of GO, these peaks disappeared

completely; a strong, broad peak appeared at a  $2\theta$  value of  $24.29^\circ$  (with an interlayer spacing of 0.365 nm), which was assigned to the (002) plane of the graphitic domains [29, 30]. **Figure 4.2.1 B** shows the diffraction pattern for monoclinic  $\text{CoMoO}_4$ . The maximum intensity was observed at  $2\theta = 26.43^\circ$ , corresponding to the (002) plane. All of the diffraction peaks matched exactly the standard patterns for monoclinic  $\text{CoMoO}_4$ , as determined by the Joint Committee on Powder Diffraction Standards (card no. 21-0868). The calculated interlayer spacing of  $\text{CoMoO}_4$  (002) was  $\sim 0.336$  nm, in good agreement with the value reported by Mai et al. [22].

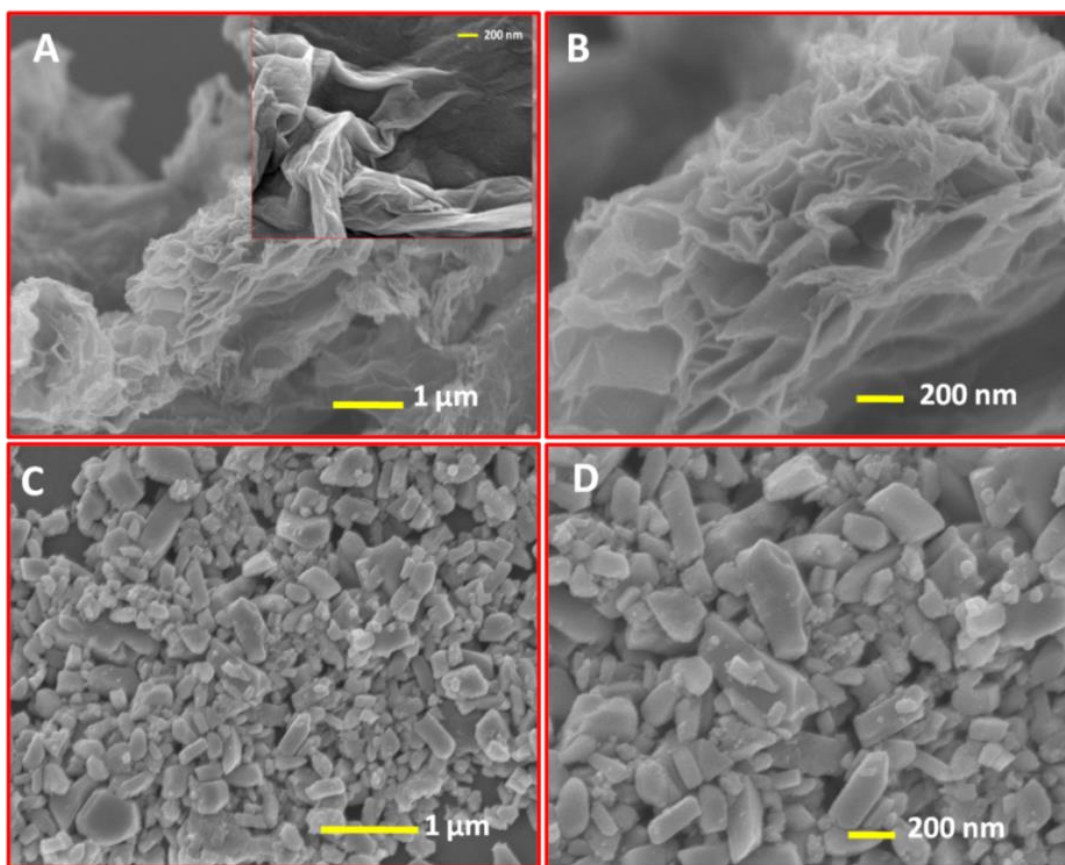


**Figure 4.2.2** FE-SEM image of rGO by hydrothermal method at low (A) and high magnifications (B), FE-SEM image of GO (inset of (A)), CoMoO<sub>4</sub> nanostructures by sonochemical method at low (C) and high magnifications (D).

FE-SEM was used to examine the morphology of the prepared materials. **Figure 4.2.2** presents FE-SEM images of rGO and CoMoO<sub>4</sub>. **Figure 4.2.2 A and B** show low and high magnification images of hydrothermally synthesized rGO, respectively, with the inset of **Figure 4.2.2 A** displaying the GO structure; rGO exhibited a sheet like form. **Figure 4.2.2 C and D** display low and high magnification images of sonochemically synthesized CoMoO<sub>4</sub>, respectively; a plate like structure was revealed, approximately several hundreds of nanometers in size.

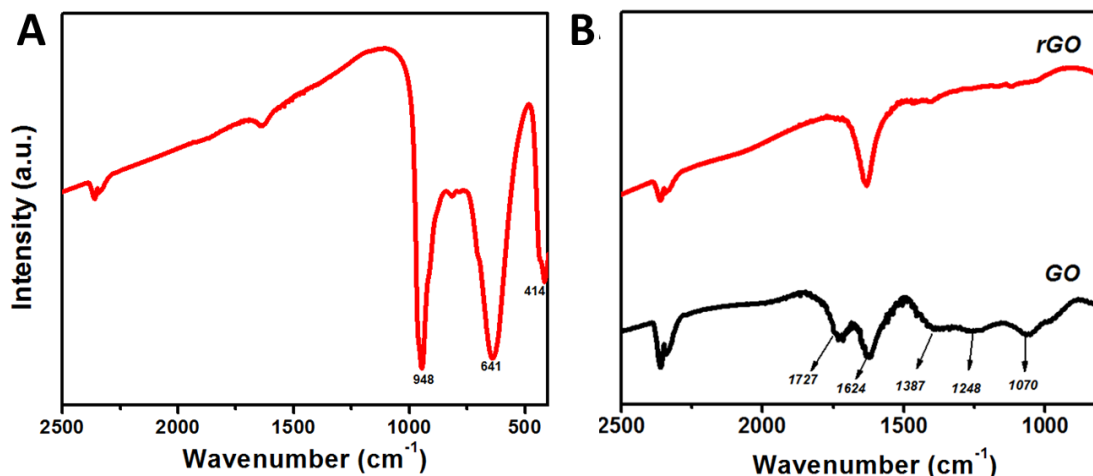


**Figure 4.2.3** FT-IR spectrum of CoMoO<sub>4</sub> nanostructures (A), GO and rGO nanosheets (B).

**Figure 4.2.3 A and B** show FTIR spectra of CoMoO<sub>4</sub>, GO and rGO, respectively. Three major bands were observed in the CoMoO<sub>4</sub> spectra (Fig. 3A) at 948,

641, and 441  $\text{cm}^{-1}$ , corresponding to the vibrational modes of distorted  $\text{MoO}_4$ , Mo-O in  $\text{CoMoO}_4$ , and vibrations due to the Co and Mo building blocks of  $\text{CoMoO}_4$ , respectively [28]. The peak at 1638  $\text{cm}^{-1}$  indicates that the presence of physically adsorbed water molecule on the surface of the  $\text{CoMoO}_4$ . In the GO and rGO spectra, shown in Fig. 3B, the peaks at 2355  $\text{cm}^{-1}$  (Also in **Figure 4.2.3A**) for both GO and rGO indicated the presence of atmospheric  $\text{CO}_2$ ; other oxygen-containing functional groups were revealed by the bands at 1727, 1387, 1248, and 1070  $\text{cm}^{-1}$ , associated with carboxyl, hydroxyl, epoxy, and carbonyl stretching frequency vibrations, respectively [13]. The graphitic domains (C-C) at band 1624  $\text{cm}^{-1}$  were observed for both GO and rGO. In case of rGO, the single peak at 1624  $\text{cm}^{-1}$  indicated that the other oxygenated functional groups, such as carboxyl, hydroxyl, epoxy, and carbonyl, had nearly disappeared due to the reduction of GO and the formation of rGO.

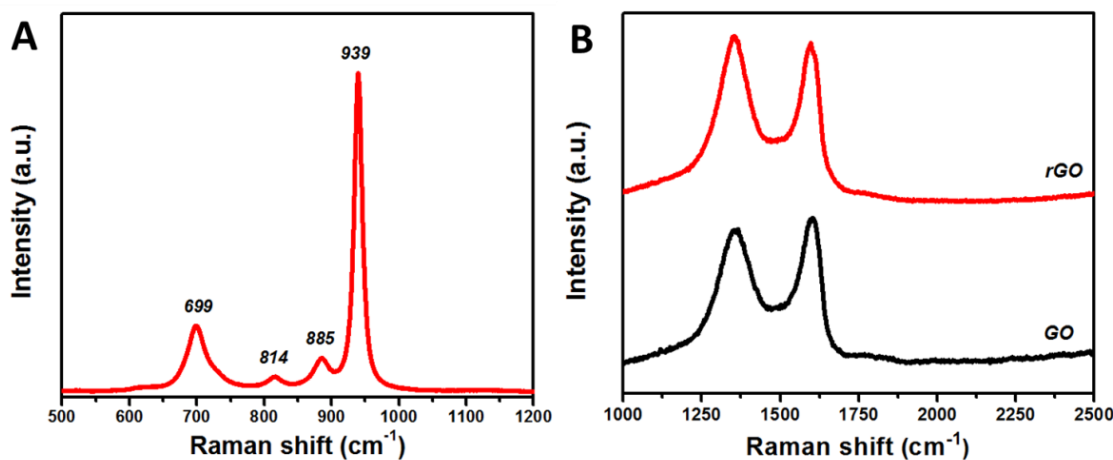


**Figure 4.2.4** Raman spectrum of  $\text{CoMoO}_4$  nanostructures (A), GO and rGO nanosheets (B).

Raman spectroscopy results for CoMoO<sub>4</sub>, and GO and rGO are shown in **Figure 4.2.4 A and B**, respectively. The Raman spectrum of CoMoO<sub>4</sub> (**Figure 4.2.4 A**) was measured over the range from 500 to 1200 cm<sup>-1</sup>. Raman vibrational modes were revealed at 939, 885, 814, and 699 cm<sup>-1</sup>; the band at 939 cm<sup>-1</sup> is associated with the symmetric stretching mode of the Mo–O bond, and the bands observed at 885 and 814 cm<sup>-1</sup> correspond to the asymmetric stretching modes of oxygen in the O–Mo–O bond. The band located at 698 cm<sup>-1</sup> was attributable to the symmetric stretching mode of the Co–O–Mo bond [22, 31]. The Raman spectra of GO and rGO were measured over the range of 1000–2500 cm<sup>-1</sup> (**Figure 4.2.4 B**). Generally, the Raman spectrum of graphene-based materials is characterized by two main features: the G band and the D band; the former arises from first-order scattering of the E<sub>2g</sub> phonon of sp<sup>2</sup>-bonded carbon, while the latter is associated with vacancies, grain boundaries, and amorphous carbon species [32, 33]. The Raman spectra of the GO nanosheets show the presence of G and D bands at 1602 and 1356 cm<sup>-1</sup>, respectively. After hydrothermal reduction of GO into rGO, significant changes in the Raman spectra were observed: (i) the G band shifted toward a lower wave number, suggesting that re-graphitization had occurred, and (ii) the D band became more prominent due to an increase in the defect level from the reduction reaction. The observed findings are consistent with our earlier report on the reduction of GO into rGO [32]. **Figure 4.2.5 A** shows the typical N<sub>2</sub> adsorption/desorption isotherm of rGO.

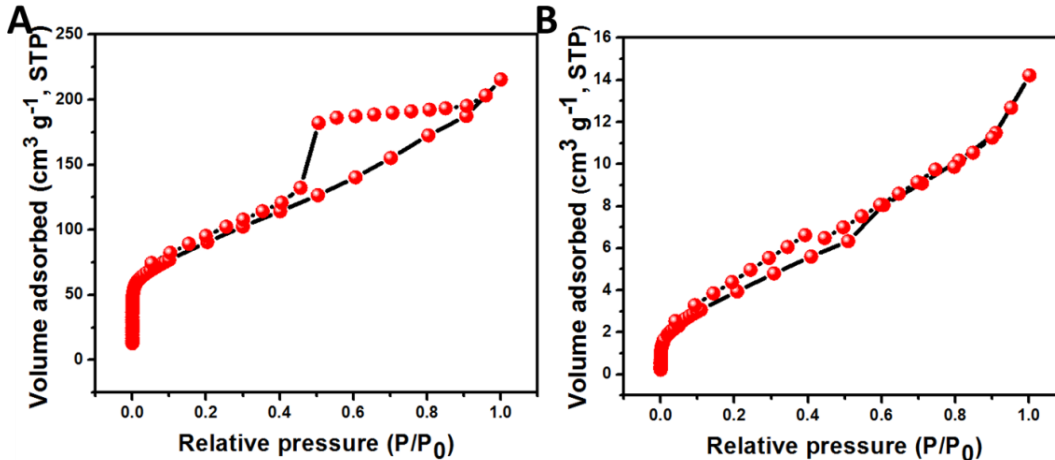


**Figure 4.2.5** Nitrogen adsorption/desorption isotherm of rGO (A) and CoMoO<sub>4</sub> (B)

The isotherm can be characterized as Type IV, with hysteresis displayed over the relative pressure range from 0.4 to 0.9; this result indicates the availability of mesopores fractions [34]. The obtained Brunauer–Emmett–Teller (BET) surface area ( $S_{BET}$ ) of hydrothermally synthesized rGO was 317.44 m<sup>2</sup> g<sup>-1</sup>. **Figure 4.2.5 B** shows the N<sub>2</sub> adsorption–desorption isotherm of CoMoO<sub>4</sub>. The measured BET surface area ( $S_{BET}$ ) of sonochemically synthesized CoMoO<sub>4</sub> was 15.76 m<sup>2</sup> g<sup>-1</sup>, which was mainly due to the porous structure of the CoMoO<sub>4</sub> nanostructures [25].

#### 4.2.3.2. Electrochemical characterization

The electrochemical performance evaluation of the synthesized material was carried out using CV and GCD. Initially, the positive and negative electrodes were tested individually in 1.0 M NaOH using the three-electrode system.

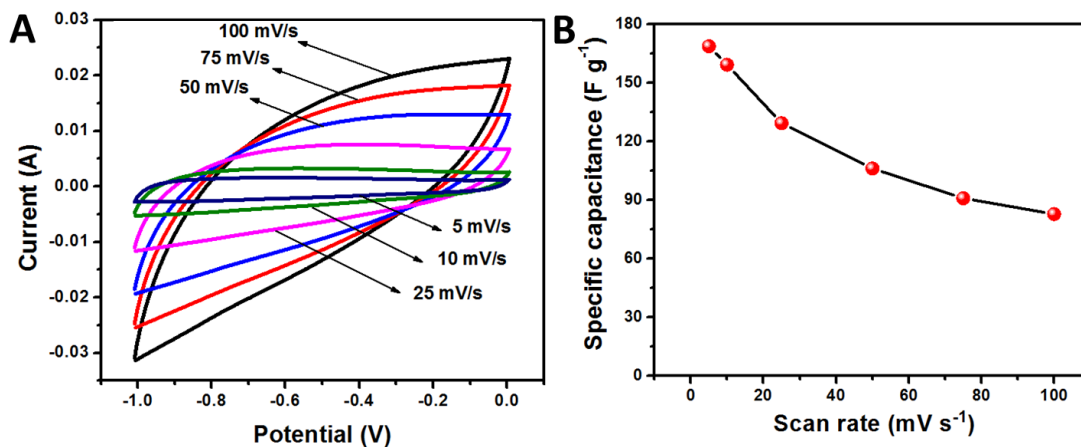


**Figure 4.2.6** Cyclic voltammety curve for rGO at the various scan rates (A), comparison of specific capacitances with respect to the scan rates (B).

**Figure 4.2.6** shows the electrochemical performance of the rGO negative electrode; cyclic voltammograms were recorded over the potential range of  $-1$  to  $0$  V, for a variable scan rate ranging from  $5$  to  $100$   $\text{mV s}^{-1}$ . Quasi-rectangular shapes were revealed, suggesting that the electrode had excellent electrochemical double-layer capacitance (**Figure 4.2.6 A**). The increase in the voltammetric current with the scan rate confirmed that the voltammetric current was directly proportional to the scan rate, an indicator of ideal capacitive behavior. **Figure 4.2.6 B** shows the calculated specific capacitances of the rGO electrode with respect to the current density. A specific capacitance of  $168.8$   $\text{F g}^{-1}$  was achieved at a scan rate of  $5$   $\text{mV s}^{-1}$ ; this value is comparable to that reported previously [35] and high compared with that obtained by Yan et al. [36]. For a high scan rate of  $100$   $\text{mV s}^{-1}$ , electrolyte ions can only access the outer surface of the electrode, which decreases both the active sites and the specific capacitance of the electrode material. For a low scan rate of  $5$   $\text{mV s}^{-1}$ , the electrolyte

ions can interact with both the inner and outer surfaces of the electrode material, resulting in a higher specific capacitance [37].

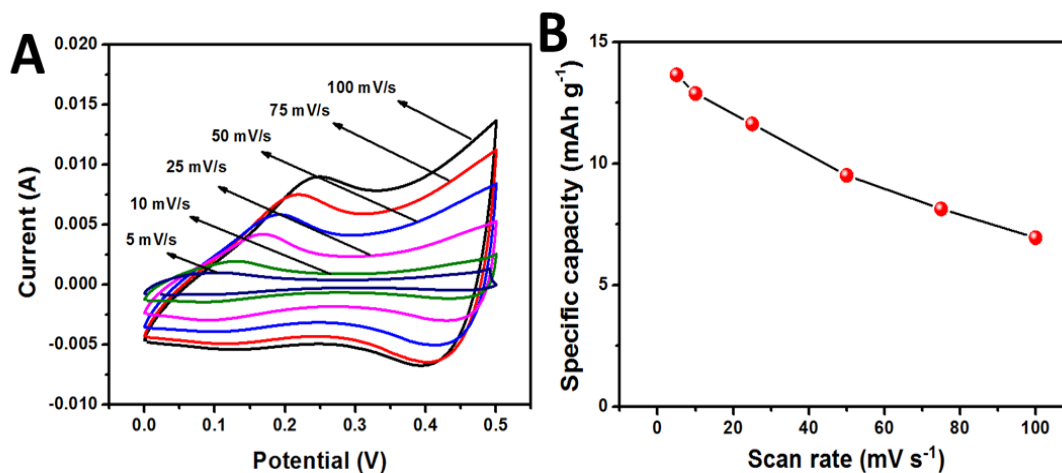


**Figure 4.2.7** Cyclic voltammety curve for CoMoO<sub>4</sub> at the various scan rates (A), comparison of specific capacitances with respect to the scan rates (B).

**Figure 4.2.7** shows the electrochemical performance of CoMoO<sub>4</sub> as a positive electrode. Cyclic voltammograms were recorded over the potential range of 0–0.5 V for scan rates varying from 5 to 100 mV s<sup>-1</sup>. The CV profile of CoMoO<sub>4</sub> (**Figure 4.2.7A**) shows the presence of a redox pair, indicating the pseudocapacitive behavior of the material. When the scan rate increased, the voltammetric current increased gradually, suggesting that the kinetics of the interfacial Faradaic redox reactions and the rates of electronic and ionic transport were sufficient for the given scan rates. **Figure 4.2.7 B** shows the calculated specific capacitance of the CoMoO<sub>4</sub> electrode with respect to the current density. The maximum specific capacitance of 98.34 F g<sup>-1</sup> was achieved for a

scan rate of  $5 \text{ mV s}^{-1}$ , which is comparable to that obtained in our previous studies [22, 28].

An ASC was assembled using rGO as the negative electrode and  $\text{CoMoO}_4$  as the positive electrode, denoted as  $\text{rGO}||\text{CoMoO}_4$  (**Figure 4.2.8A**); the inset of **Figure 4.2.8 A** shows a photograph of the fabricated device. **Figure 4.2.8 B** shows the CV curve of both rGO and  $\text{CoMoO}_4$  for a scan rate of  $5 \text{ mV s}^{-1}$ . The potential range for rGO was  $-1$  to  $0 \text{ V}$  and that for  $\text{CoMoO}_4$  was  $0$  to  $0.5 \text{ V}$  versus  $\text{Ag}/\text{AgCl}$ . Therefore, the  $\text{rGO}||\text{CoMoO}_4$  device was expected to achieve a maximum working voltage of  $1.5 \text{ V}$ . To attain the maximum device capacitance, the mass of the negative and positive electrodes should be balanced to equate the specific capacitance of the individual electrodes. Because the specific capacitances and the operational potential window of the positive and negative electrodes are different, the charge storage capacities of both electrodes were balanced by fine-tuning the mass loading between these electrodes.

Subsequently, the ASC device was fabricated using rGO as the negative electrode and  $\text{CoMoO}_4$  as the positive electrode in a  $1.0 \text{ M NaOH}$  electrolyte solution. **Figure 4.2.8 C** shows the CV curves of the  $\text{rGO}||\text{CoMoO}_4$  ASC device measured over the voltage range of  $0$ – $1.5 \text{ V}$ , for a scan rate of  $100 \text{ mV s}^{-1}$ . The results in **Figure 4.2.8 C** confirm that the fabricated ASC device can operate with a potential window of  $1.5 \text{ V}$ , without instability. GCD analysis was also performed for operating voltages over the range of  $0$ – $1.5 \text{ V}$ , as shown in **Figure 4.2.8 D**. The charge–discharge profile was

symmetric for a current density of  $0.5 \text{ mA cm}^{-2}$ , confirming the excellent capacitive behavior of the device over the entire voltage range.

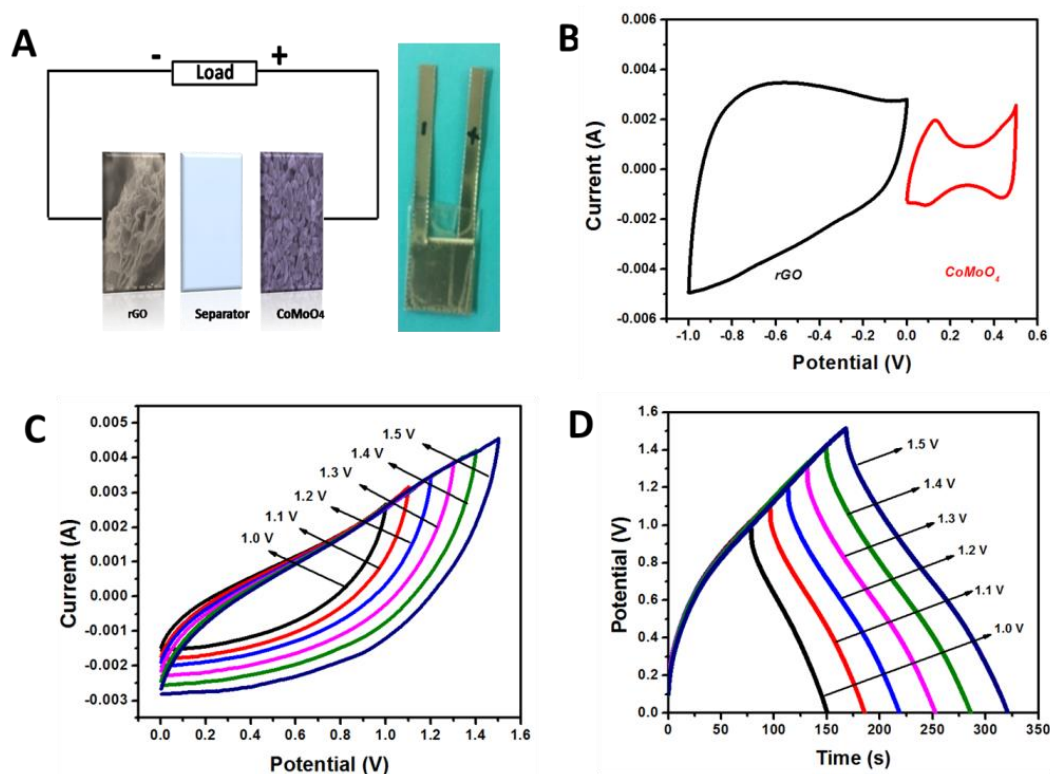


**Figure 4.2.8** Schematic representation of fabricated ASC (A), photograph of fabricated device (inset of A), cyclic voltammetry comparison of negative (rGO) and positive (CoMoO<sub>4</sub>) electrodes at the scan rate of  $5 \text{ mV s}^{-1}$ , cyclic voltammetry curve for fabricated ASC at the different voltage levels (C), galvanostatic charge discharge curve for fabricated ASC at the different voltage levels (D).

**Figure 4.2.9 A** shows the CV curve of the ASC device, for a variable scan rate of  $5\text{--}200 \text{ mV s}^{-1}$ . No significant change was observed in the nature of the CV curves, even for a scan rate of  $200 \text{ mV s}^{-1}$ , which indicates the better rate capability of the

fabricated asymmetric device. A maximum capacitance of  $27.7 \text{ F g}^{-1}$  was achieved for a scan rate of  $5 \text{ mV s}^{-1}$ .

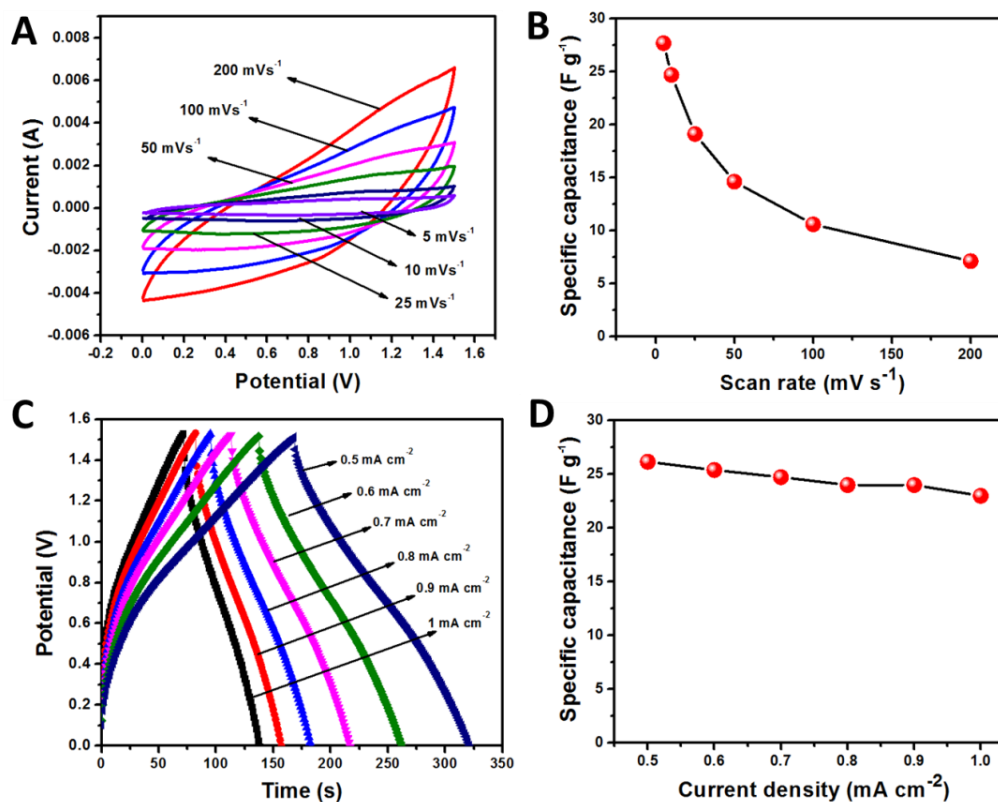


**Figure 4.2.9** Cyclic voltammetry curve for ASC at the various scan rates (A), comparison of specific capacitances with respect to the scan rates (B), charge discharge curve for ASC at the various current densities comparison (C), comparison of specific capacitances with respect to the current densities (D).

**Figure 4.2.9 B** shows the variation in the specific capacitance as a function of the scan rate. The specific capacitance decreased as the scan rate increased; in this case, the electrolyte ions were not fully utilized by the electrode material due to the faster scan rates. **Figure 4.2.9 C** shows the GCD curve of the ASC collected at different current densities ranging from  $0.5$  to  $1 \text{ mA cm}^{-2}$ . The fabricated device exhibited symmetric

charge–discharge profiles, suggesting good charge-storage capability. **Figure 4.2.9 D** shows the variation in the specific capacitance with respect to the current density. A maximum specific capacitance of  $26.16 \text{ F g}^{-1}$  was achieved for a current density of  $0.5 \text{ mA cm}^{-2}$ . The observed specific capacitance from the GCD analysis was well matched with the specific capacitance value obtained from CV measurements.

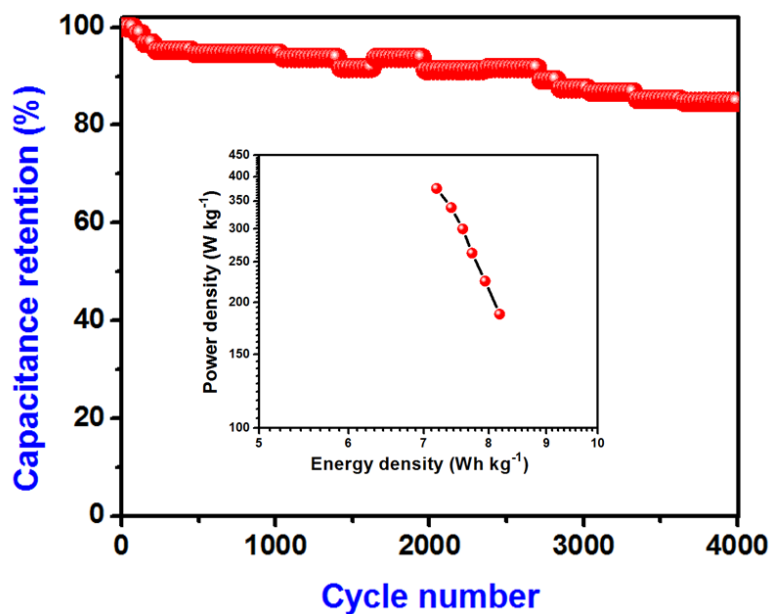


**Figure 4.2.10** Cyclic performance of ASC measured by the galvanostatic charge discharge measurement at the current density of  $1.0 \text{ mA cm}^{-2}$ .

The amount of energy stored and delivered by SC devices can be evaluated using the energy and power densities, which play an important role in the capacitive behavior of electrochemical devices. From Eqns. (4) and (5) [20], the calculated energy and power densities were  $8.17 \text{ Wh kg}^{-1}$  and  $187.5 \text{ W kg}^{-1}$ , respectively, for a current density of  $0.5 \text{ mA cm}^{-2}$ . The cyclic stability of the fabricated  $\text{rGO}||\text{CoMoO}_4$  ASC device was evaluated via GCD measurements for an operating voltage of  $1.5 \text{ V}$  and a current density of  $1 \text{ mA}$

$\text{cm}^{-2}$ . The ASC device exhibited superior cyclic performance,  $>84.7\%$  specific capacitance retention after 4000 cycles (**Figure 4.2.10**); the decrease in capacitance was attributable to electrode aggregates in the electrolytes. Thus, our results demonstrated the excellent cyclic stability of the fabricated  $\text{rGO}||\text{CoMoO}_4$  ASC device.

#### 4.2.4. Conclusion

In summary, we demonstrated an ASC device composed of an  $\text{rGO}$  negative electrode and  $\text{CoMoO}_4$  positive electrode. The negative and positive electrode materials were synthesized by hydrothermal and sonochemical methods respectively. The ASC used a 1 M NaOH electrolyte and commercially available filter paper spacers. By integrating these positive and negative electrodes, the device achieved an operating voltage of 1.5 V, a maximum specific capacitance of  $26.16 \text{ F g}^{-1}$ , an energy density of  $8.17 \text{ Wh kg}^{-1}$ , and a power density of  $187.5 \text{ W kg}^{-1}$ , for a current density of  $0.5 \text{ mA cm}^{-2}$ . Additionally, the fabricated device exhibited excellent cyclic stability ( $>84.7\%$  retention of its initial specific capacitance) over 4000 cycles of charge–discharge analysis at a current density of  $1 \text{ mA cm}^{-2}$ . Collectively, our results show that the  $\text{rGO}||\text{CoMoO}_4$  ASC device has great potential for application to energy storage and electrochemical devices.

#### 4.2.5. References

1. L. Demarconnay, E. Raymundo-Piñero, F.Béguin, **2011**, 196, 580.
2. Q.T. Qu, Y. Shi, L.L. Li, W.L. Guo, Y.P. Wu, H.P. Zhang, S.Y. Guan and R. Holze, *Electrochem. Commun.* **2009**, 11, 1325.
3. X. Hu, Y. Huai, Z. Lin, J. Suo and Z.A. Deng, *J. Electrochem. Soc.* **2007**, 154, A1026-.
4. D.W. Wang, H.T. Fang, F. Li, Z.G. Chen, Q.S. Zhong, G.Q. Lu and H.M. Cheng, *Adv. Funct. Mater.* **2008**, 18, 3787.
5. P.C. Chen, G. Shen, Y. Shi, H. Chen and C. Zhou, *ACS Nano* **2010**, 4, 4403.
6. L.J. Xie, J.F. Wu, C.M. Chen, C.M. Zhang, L. Wan, J.L. Wang, Q.Q. Kong, C.X. Lv, K.X. Li, and G.H. Sun, *J. Power Sources* **2013**, 242, 148.
7. B.X. Zou, Y. Liang, X.X. Liu, D. Diamond and K.T. Lau, *J. Power Sources* **2011**, 196, 4842.
8. D. Salinas-Torres, J.M. Sieben, D. Lozano-Castelló, D. Cazorla-Amorós and E. Morallón, *Electrochim. Acta* **2013**, 89, 326.
9. Z. Niu, W. Zhou, J. Chen, G. Feng, H. Li, W. Ma, J. Li, H. Dong, Y. Ren, D. Zhao and S. Xie, *Energy Environ. Sci.*, **2011**, 4, 1440.
10. J. Cao, Y. Wang, Y. Zhou, J.H. Ouyang, D. Jia and L. Guo, *J. Electroanal. Chem*, **2013**, 689, 201.
11. K.S. Novoselov, A.K. Geim, S.V. Morozov, D. Jiang, Y. Zhang, S.V. Dubonos, I.V. Grigorieva, and A.A. Firsov, *Science*, **2004**, 306, 666.

12. S. Park and R.S. Ruoff, *Nat. Nanotechnol.* **2009**, 4, 217.
13. K. Zhang, L.L. Zhang, X.S. Zhao and J.S. Wu, *Chem. Mater.* **2010**, 22, 1392-1401.
14. J. Xia, F. Chen, J. Li, N. Tao, *Nat. Nanotechnology*, **2009**, 4, 505.
15. F. Luan, G. Wang, Y. Ling, X. Lu, H. Wang, Y. Tong, X.X. Liu and Y. Li, *Nanoscale*, **2013**, 5, 7984.
16. J. Yan, Z. Fan, W. Sun, G. Ning, T. Wei, Q. Zhang, R. Zhang, L. Zhi and F. Wei, *Adv. Funct. Mater.* **2012**, 22, 2632.
17. H. Wang, C.M.B. Holt, Z. Li, X. Tan, B.S. Amirkhiz, Z. Xu, B.C. Olsen, T. Stephenson, D. Mitlin, *Nano Res.* **2012**, 5(9), 605.
18. C.T. Hsu and C.C. Hu, *J. Power Sources* **2013**, 242, 662.
19. H. Peng, G. Ma, J. Mu, K. Sun and Z. Lei, *J. Mater. Chem. A*, **2014**, 2, 10384.
20. H. Chen, J. Jiang, L. Zhang, T. Qi, D. Xia and H. Wan, *J. Power Sources* **2014**, 248, 28.
21. D. Guo, Y. Luo, X. Yu, Q. Lin and T. Wang, *Nano Energy* 2014, 8, 174–182
22. L.Q. Mai, F. Yang, Y.L. Zhao, X. Xu, L. Xu and Y.Z. Luo, *Nature Commun.* **2011**, 2, 381.
23. G.K. Veerasubramani, K. Krishnamoorthy, S. Radhakrishnan and S.J. Kim, *Mat Chem Phys* **2014**, 147, 836.
24. M.C. Liu, L.B. Kong, X.J. Ma, C. Lu, X.M. Li, Y.C. Luo and L. Kang, *New J. Chem.*, **2012**, 36, 1713.

25. M.C. Liu, L.B. Kong, C. Lu, X.J. Ma, X.M. Li, Y.C. Luo and L. Kang, *J. Mater. Chem. A*, **2013**, 1, 1380.
26. B. Senthilkumar, D. Meyrick, Y.S. Lee, R.K. Selvan, *RSC Adv.*, **2013**, 3, 16542.
27. K. Krishnamoorthy, K. Jeyasubramanian, M. Premanathan, G. Subbiah, H.S. Shin and S.J. Kim. *Carbon* **2014**, 72, 328.
28. G.K. Veerasubramani, K. Krishnamoorthy, S. Radhakrishnan, N.J. Kim and S.J. Kim, *Int J Hydrogen Energy*, **2014**, 39, 5186.
29. D.Y. Pan, S. Wang, B. Zhao, M.H. Wu, H.J. Zhang, Y. Wang, Z. Jiao, *Chem. Mater.* **2009**, 21, 3136.
30. K. Krishnamoorthy, M. Veerapandian, L.H. Zhang, K. Yun and S.J. Kim, *J. Phys. Chem. C*, **2012**, 116, 17280.
31. Ana P. de Moura, Larissa H. de Oliveira, Paula F.S. Pereira, Ieda L.V. Rosa, Máximo S. Li, Elson Longo and José A. Varela, *Adv. Chem. Engineer. Sci.*, **2012**, 2, 465.
32. Y. Zhu, S. Murali, W. Cai, X. Li, J.W. Suk, J.R. Potts and R.S. Ruoff, *Adv Mater* **2010**, 22(35), 3906.
33. S. Stankovich, D.A. Dikin, R.D. Piner, K.A. Kohlhaas, A. Kleinhammes, Y. Jia, Y. Wu, S.B.T. Nguyen and R.S. Ruoff, *Carbon* **2007**, 45, 1558.
34. S. Yang, X. Feng, L. Wang, K. Tang, J. Maier and K Müllen. *Angew Chem Int Ed* **2010**, 49(28), 4795.
35. D. Ma, Z. Wu and Z. Cao, *J Energy Chemistry* **2014**, 23, 346.

36. J. Yan, T. Wei, B. Shao, F. Ma, Z. Fan, M. Zhang, C. Zheng, Y. Shang, W. Qian and F. Wei, *Carbon* **2010**, 48, 1731.
37. Y. Wang, J. Chen, J. Cao, Y. Liu, Y. Zhou, J.H. Ouyang, D. Jia, *J. Power Sources*, **2014**, 271, 269.
38. Y. Hou, L. Chen, P. Liu, J. Kang, T. Fujita, M Chen, *J. Mater. Chem. A*, **2014**, 2, 10910.

### 4.3 Summary

In this chapter, we have discussed two sections. First one is, we have investigated that the sonochemically prepared  $\text{CoMoO}_4$  to make composite with conducting polymer. Second one is, the prepared  $\text{CoMoO}_4$  has been investigated for hybrid supercapacitor with reduced graphene oxide. From this chapter, the prepared  $\text{CoMoO}_4$ /polyaniline composite showed the improved electrochemical performances in acidic electrolyte. But the cyclic stability is too poor due to acid electrolyte might etches the transition metal oxide leading to the electrode dissolution into the electrolytes. Hence, in order to make the composite of  $\text{CoMoO}_4$  with conducting polymer, suitable materials and electrolyte should be chosen to improve the capacity as well as stability. In the second section, we have fabricated hybrid supercapacitor device based on sonochemically prepared  $\text{CoMoO}_4$  as positive electrode and hydrothermally reduced graphene oxide as negative electrode. This device exhibits good electrochemical performances in terms of capacitance ( $26 \text{ Fg}^{-1}$ ), energy density ( $8.17 \text{ Wh kg}^{-1}$ ), and cyclic stability. However, the achieved energy density is quite low for hybrid device. Hence, we need to improve the energy density by changing the structure of the electrode materials and we will discuss from next chapter.

## CHAPTER - 5

### Improved electrochemical performances of binder-free CoMoO<sub>4</sub> nanoplate arrays@Ni foam electrode using redox additive electrolyte

#### Highlights

- ❖ Herein, we are successfully prepared cobalt molybdate (CoMoO<sub>4</sub>) grown on nickel foam as a binder free electrode by hydrothermal approach for supercapacitors and improved their electrochemical performances using potassium ferricyanide (K<sub>3</sub>Fe(CN)<sub>6</sub>) as redox additive
- ❖ The formation of CoMoO<sub>4</sub> on Ni foam with high crystallinity is confirmed using XRD, Raman, and XPS measurements. The nanoplate like arrays (NPAs) of CoMoO<sub>4</sub> was uniformly grown on Ni foam which is confirmed by FE-SEM analysis
- ❖ The prepared binder-free CoMoO<sub>4</sub> NPAs achieved maximum areal capacity of 227 μAh cm<sup>-2</sup> with KOH electrolyte at 2.5 mA cm<sup>-2</sup>. The achieved capacity was further improved ~2.65 times using the addition of K<sub>3</sub>Fe(CN)<sub>6</sub> as redox additive
- ❖ The increased electrochemical performances of CoMoO<sub>4</sub> NPAs on Ni foam electrode via redox additive are discussed in detail and the mechanism has been explored. Moreover, the assembled CoMoO<sub>4</sub> NPAs on Ni foam // activated carbon asymmetric supercapacitor device with an extended operating voltage window of 1.5 V exhibits an excellent performances such as high energy density and cyclic stability.

## 5.1. Introduction

Presently, portable electronic devices (such as laptops, mobile phones and digital cameras) have fascinated much consideration due to the increasing demand in the modern electronic industries [1, 2]. Among various power sources, batteries are one of the important energy storage devices in the past decades. As the next alternative-generation energy storage, supercapacitors have the potential (often called as electrochemical capacitors, ECs) to overcome lithium-ion batteries for their fast charge/discharge rates, high power density, and long cycle life [3-5]. However, without sacrificing the power density and cyclic stability, a strategic idea can be brought to achieve the high energy density by increasing operating cell voltage. One of the promising avenue towards this target is the introduction of a battery-type faradaic electrode (as the positive electrode) to replace one terminal of the capacitor-type electrodes in the electric double layer capacitor (EDLC) [1]. Hence, the hybrid system can create the use of various potential windows of the two electrodes to increase the maximum operation voltage while also providing the advantages of both supercapacitors (power density) and batteries (energy density) [6]. Transition metal oxides have been widely investigated as positive electrode material for supercapacitors due to its multiple oxidation states [7-9]. However, due to the short diffusion distance of electrolytes into electrode materials and intrinsic poor electrical conductivity of metal oxides, a maximum portion of electrode material is blocked from the contact of electrolyte ions in the participation of faradaic reactions which leads to a less satisfactory level of

capacitances [10]. Therefore, it is quite a great dispute to develop alternate electrode materials with excellent electrochemical performances.

Nowadays, one dimensional (1D) nanostructures of metal oxides/hydroxides (such as nanobelts, nanowires, nanotubes) [10-12], two dimensional (2D) nanostructures (such as nanosheets and nanoflakes) [13, 14], and three dimensional (3D) nanostructures (nanoflowers) [15] have been extensively studied for energy storage applications [16]. Thus, the formation of different nanostructures supports many reaction sites for fast charge transfer and penetration of electrolyte ions. Hence, there is an increasing demand for the developing these kind of nanostructures for advanced supercapacitor applications, especially to enhance the energy density of electrode materials with high specific capacities. In the recent years, researchers are focused on the hierarchical growth of nanostructured material on any substrates, especially on conducting substrates for supercapacitor applications has been extensively studied. Recently, Yang et al., have discussed about the metal oxide/ hydroxides nanoarrays on conducting substrates by hydrothermal synthesis and their supercapacitor applications [17]. Our earlier study demonstrated the high performance supercapacitive properties of hierarchical nanostructured  $\text{Ni}_3\text{S}_2$  on Ni foam based binder free electrodes [18]. Hence, one of the potential ways is to enhance the performances of electrode materials that the direct growing of electrode materials on conducting substrate as binder-free electrodes. In this effective approach, tremendous benefits such as highly accessible electro-active sites, fast diffusion of the electrolyte ions and access of fast ion transport can be achieved.

Due to these synergetic properties, contact of electrolyte ions into the electrode material is highly activated to participate faradaic reactions which leads to the high specific capacities and rich cyclic stability and better rate performances [19]. Binary metal oxides have been attracted much attention due to multiple oxidation states and high electrical conductivity compared to the single component metal oxides [20-22]. The families of metal molybdates such as  $\text{MnMoO}_4$ ,  $\text{CoMoO}_4$ , and  $\text{NiMoO}_4$  have been believed as a promising effective and scalable alternatives compared to other binary metal oxides [23-25]. Among these,  $\text{CoMoO}_4$  has attracted much research interest because of its low cost, environmentally friendly and enhanced electrochemical performances [26-28]. The electrochemical properties of  $\text{CoMoO}_4$  have been studied using electrodes prepared by conventional slurry coating method, in which the use of polymer binder in the electrode leads to decrease in conductivity of electrode materials [19,29]. Hence, it is highly attractive to fabricate  $\text{CoMoO}_4$  on conducting substrate which leads to better electrochemical performances compared to conventional slurry coating methods [19, 30, 31].

Another impressive approach to increase the charge capacity of the supercapacitor can be achieved by the addition of small quantities of redox additives/mediators into the electrolytes. Recently, Rolden *et al.* reported an increasing capacitance of activated carbon from 72 to 220  $\text{F g}^{-1}$  by introducing hydroquinone/quinine redox additives into the 1 M  $\text{H}_2\text{SO}_4$  solution [32]. Su *et al.* have reported capacitance of Co-Al layered double hydroxides was improved through the addition of  $\text{K}_3\text{Fe}(\text{CN})_6$  and  $\text{K}_4\text{Fe}(\text{CN})_6$  as

redox additive electrolytes when compared to bare KOH electrolyte [33]. More recently, p-benzenediol incorporated into a PVA-H<sub>2</sub>SO<sub>4</sub> gel electrolyte for activated carbon shows an increased capacitance of 474.29 F g<sup>-1</sup> compared to the absence of p-benzenediol (specific capacitance of 129.29 F g<sup>-1</sup>) [34]. Senthilkumar et al. have reported specific capacitance was improved for activated carbon from 472 F g<sup>-1</sup> to 912 F g<sup>-1</sup> by the addition of KI into H<sub>2</sub>SO<sub>4</sub> electrolytes [35]. The use of redox additive electrolytes has been highly recognized as a novel method for improving the energy storage performance of supercapacitor devices which is evidenced from the recent trends. In this scenario, Akinwolemiwa et al. presented a critical review article on the pros and cons of the applications of redox electrolytes in supercapacitors which clearly demonstrates that the importance of appropriate methods for determining the performance of electrode materials without over estimated specific energy [36]. Brousse et al. presented the detailed discussion on the representation of electrode materials for supercapacitors [37]. By considering these factors, in this study, we have used appropriate metric to represent the faradaic electrodes and calculated areal energy density for non-linear charge discharge curves without overestimated values. Briefly, we demonstrated a facile hydrothermal route for the preparation of hierarchical CoMoO<sub>4</sub> NPs directly grown on nickel foam and examined its use as binder free electrodes for supercapacitors. Further, we explored the improvements on electrochemical performances of CoMoO<sub>4</sub> NPs based binder free electrodes in terms of areal capacity

via the introduction of  $\text{K}_3\text{Fe}(\text{CN})_6$  as redox additive into electrolyte solution and their practical applications using full cell configuration.

## **5.2. Experimental methods**

### **5.2.1. Preparation of $\text{CoMoO}_4$ on Ni foam**

The growth of  $\text{CoMoO}_4$  nanostructures on Nickel foam has been achieved via one-pot hydrothermal method. Briefly, precursor solution containing  $\text{Co}(\text{NO}_3)_2 \cdot 6\text{H}_2\text{O}$  and  $\text{Na}_2\text{MoO}_4 \cdot 2\text{H}_2\text{O}$  (in the molar ratio 1:1) has been prepared by dissolving in water. A piece of Ni foam was cleaned 1 M HCl, ethanol, acetone and water to remove impurities on the surface of the nickel foam. Cobalt molybdate precursor solution was transferred into 100 mL Teflon lined autoclave. Precleaned Ni foam was immersed into the precursor solution and kept at a constant temperature of 180 °C for 6 hrs. After the reaction, Teflon was cooled down into room temperature naturally and the color of the nickel foam was changed to pink, which indicated the uniform growth of  $\text{CoMoO}_4$  on nickel foam. The obtained product was thoroughly washed distilled water and ethanol to remove the residual ions. Finally the sample was dried at 80 °C for overnight in a hot air oven.

### **5.2.2. Electrode and electrolyte preparation**

The negative electrode was prepared by mixing activated carbon (AC) as an active material, carbon black as conductive agent, polyvinylene difluoride (PVDF) as binder (in the weight ratio of 80:15:5) together using NMP as solvent and made into

slurry. The prepared slurry was coated onto the cleaned carbon cloth ( $1 \text{ cm}^2$ ) and was kept for drying at  $70 \text{ }^\circ\text{C}$  overnight. Then the electrode was directly used as the working electrode, where  $2 \text{ M KOH}$  electrolytes were used. Silver/silver chloride ( $\text{Ag/AgCl}$ ) and platinum foil were used as the reference and counter electrodes. The weight of active material is  $\sim 2.8 \text{ mg}$ .

The electrochemical properties of the materials were examined through cyclic voltammetry (CV), electrochemical impedance spectroscopy (EIS) and galvanostatic charge discharge (GCD) using an AUTOLAB PGSTAT302N electrochemical workstation. A piece of  $\text{CoMoO}_4$  grown Ni foam ( $1 \times 1 \text{ cm}^2$  area) was directly used as the working electrode. Silver/silver chloride ( $\text{Ag/AgCl}$ ) and platinum foil were used as the reference and counter electrodes. The electrolytes containing  $2 \text{ M KOH}$  and  $2 \text{ M KOH} + 0.02 \text{ M K}_3\text{Fe}(\text{CN})_6$  was used for this study.

### **5.2.3. Fabrication of hybrid supercapacitors**

Hybrid supercapacitor was fabricated by sandwich type electrode using  $\text{CoMoO}_4$  NPAs on Ni foam as positive electrode and commercial activated carbon (AC) as negative electrode and a piece of whatmann filter paper as separator where the  $\text{K}_3\text{Fe}(\text{CN})_6$  added KOH electrolytes was used.

## 5.3. Results and discussion

### 5.3.1. Structural characterization

In this study,  $\text{CoMoO}_4$  nanostructures are directly grown on nickel foam by hydrothermal method using cobalt nitrate and sodium molybdate as starting materials.

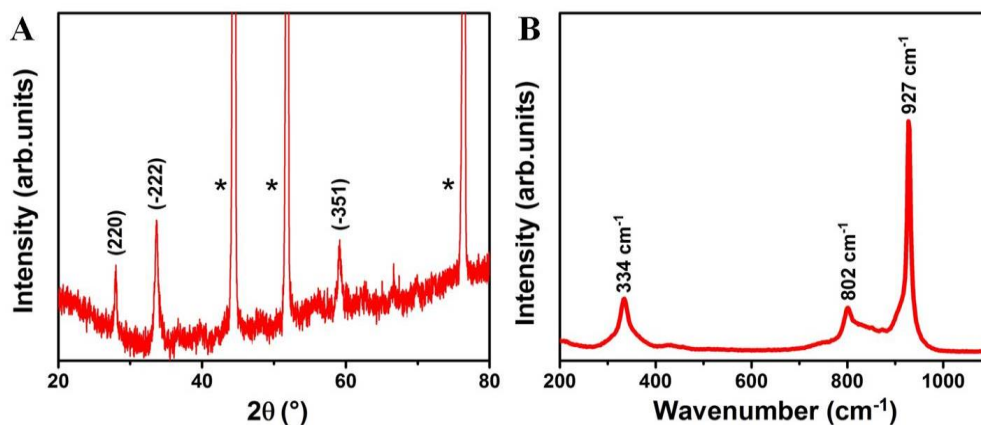


**Figure 5.1.1** X-ray diffraction pattern (A), (\* Ni foam), and Raman spectrum of  $\text{CoMoO}_4$  NPs grown on nickel foam (B).

To determine the crystalline structure, purity and size of the synthesized materials, XRD analysis was performed. **Figure 5.1.1 (A)** shows the XRD pattern of hydrothermally synthesized  $\text{CoMoO}_4$ . The obtained XRD pattern is attributed to the monoclinic phase of  $\text{CoMoO}_4$ . In general,  $\text{CoMoO}_4$  exists in two different phases named as alpha and beta. Both the phases crystallize in a monoclinic structure with the space group of  $C2/m$ , while in our case, the formation of alpha  $\text{CoMoO}_4$  on the nickel foam was observed under the hydrothermal reaction at the temperature of  $180^\circ\text{C}$  with high pressure, but beta  $\text{CoMoO}_4$  exists at high temperature heating [39]. The observed peaks

28.3°, 33.6° and 59.2° are corresponding to the planes (220), (-222) and (-351) respectively. The remaining peaks at 44.5°, 51.8°, and 76.4° are corresponding to the nickel foam. All the diffraction peaks are well matched with the previous reports [39, 40] and standard patterns for CoMoO<sub>4</sub> (Joint Committee on Powder Diffraction Standards card no. 21-0868 and 25-1434). As well, there is no presence of any peaks due to impurities, hydroxyl groups or any other residuals suggesting that the formation of high purity CoMoO<sub>4</sub> by hydrothermal approach. To investigate crystalline and bonding nature of the synthesized material, Raman measurement was performed and shown in **Figure 5.1.1 (b)** in the range of 200 to 1100 cm<sup>-1</sup>. Three major peaks were observed in the spectrum such as 927, 802, and 334 cm<sup>-1</sup>. The band at 927 cm<sup>-1</sup> is associated with the symmetric stretching mode of Mo-O bond. The bands at 802 cm<sup>-1</sup> corresponded to asymmetric stretching modes of oxygen in binding O-Mo-O bond. The band located at 334 cm<sup>-1</sup> can be attributed to the symmetric stretching of the Co-O-Mo bond. The results obtained are in good agreement with the literature [25] and the slight variations in the positions of the vibrational modes can be attributed with the method of synthesis, crystal size, morphology and strength of interaction between the ions and the degree of structural order-disorder of the materials [41].

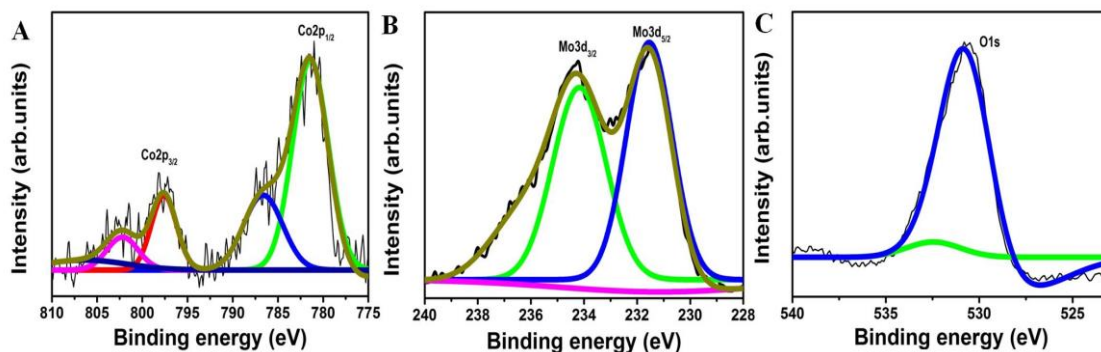


**Figure 5.1.2** X-ray photoelectron spectroscopy of Co 2p core-level spectrum (A), Mo 3d core-level spectrum (B), and O 1s core-level spectrum (C) of CoMoO<sub>4</sub> NPAs on Ni foam.

In order to further examine the surface state of the obtained samples, X-ray photoelectron spectroscopy (XPS) was also studied to analyze the chemical composition of the CoMoO<sub>4</sub> NPAs on Ni foam in **Figure 5.1.2**. As shown in **Figure 5.1.2 (a)**, the Co 2p region shows two peaks at 781.9 and 797.5 eV, attributing to the Co 2p<sub>3/2</sub> and Co 2p<sub>1/2</sub>, respectively, which is the characteristic of Co<sup>2+</sup> in CoMoO<sub>4</sub> [42]. **Figure 5.1.2 (b)** shows the XPS spectrum of Mo 3d with the binding energies at 231.37 and 234.45 eV which corresponding to Mo 3d<sub>5/2</sub> and Mo 3d<sub>3/2</sub> respectively. The binding energy and calculated splitting width (3.08 eV) are in good agreement with Mo<sup>6+</sup> [43]. **Figure 5.1.2 (c)** shows the O 1s region from the synthesized CoMoO<sub>4</sub> NPAs on Ni foam. The band at 530.7 eV shows the presence of lattice oxygen in the prepared CoMoO<sub>4</sub> NPAs. Generally, the presence of hydroxyl group can be identified at the binding energy of ~532.5 eV [44, 45]. But in our case, there is no peak has been observed at the specified binding energy for hydroxyl group formation which supports the XRD analysis.

### 5.3.2. Morphological Analysis

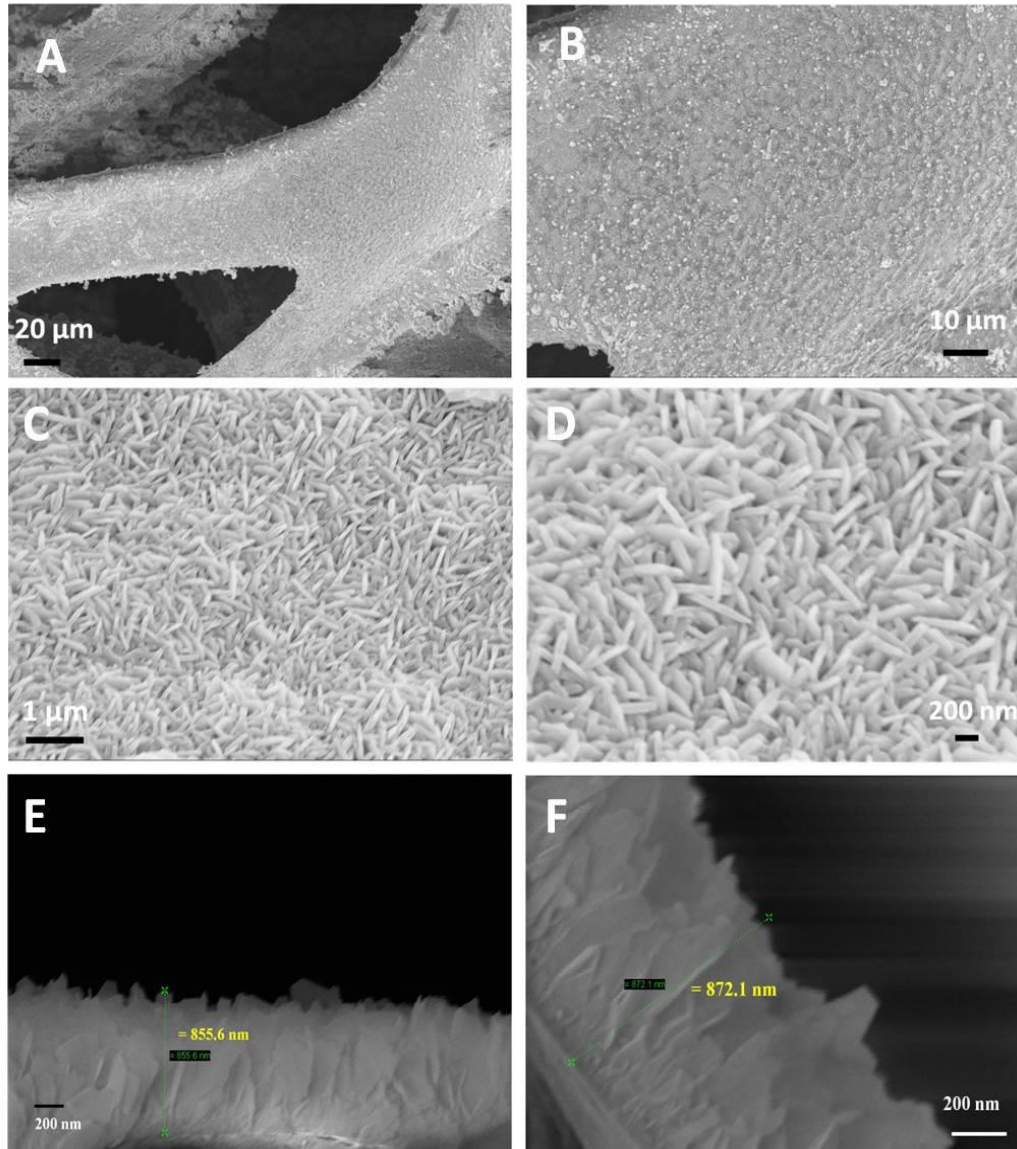


**Figure 5.1.3** Field-emission scanning electron micrographs of CoMoO<sub>4</sub> NPAs directly grown on nickel foam at different magnifications, 20 μm (A), 10 μm (B), 1 μm (C), 200 nm (D). Cross sectional view images at the different regions (E) and (F).

The surface morphology of the  $\text{CoMoO}_4$  grown directly on Ni foam via hydrothermal process was examined by the use of FE-SEM analysis. **Figure 5.1.3 (a-f)** shows the FE-SEM micrographs of the prepared  $\text{CoMoO}_4$  on Ni foam at the different magnifications (20  $\mu\text{m}$ , 10  $\mu\text{m}$ , 1  $\mu\text{m}$  and 200 nm) which confirms the presence of nanoplate arrays (NPAs) on the Ni foam. The low magnification micrographs (**Figure 5.1.3 a and b**) revealed that the  $\text{CoMoO}_4$  was uniformly formed on the surface of the nickel foam. The high magnification micrograph as shown in **Figure 5.1.3 (c and d)** show the growth of tightly bonded uniform  $\text{CoMoO}_4$  NPAs with porous structures was obtained. The length and breadth of the NPAs is about 300-500 and 50-100 nm, respectively. **Figure 5.1.2 (e and f)** shows the cross-sectional view of the  $\text{CoMoO}_4$  on Ni foam. It revealed that less than 1 $\mu\text{m}$  thickness of  $\text{CoMoO}_4$  was grown on the Ni foam. The observed two dimensional nanostructures of  $\text{CoMoO}_4$  is expected to deliver better electrochemical properties via providing more active sites and ion diffusion pathways at the electrode surface.

### 5.3.3. Electrochemical characterization

The electrochemical performances of synthesized  $\text{CoMoO}_4$  NPAs were carried out by CV, GCD, and EIS measurements. **Figure 5.1.4** shows the electrochemical performances of  $\text{CoMoO}_4$  NPAs using 2M KOH as electrolyte solution. Cyclic voltammograms were recorded in the potential range of -0.1 to 0.5 V under the different scan rates of 5 to 100  $\text{mV s}^{-1}$  (**Figure 5.1.4 (a)**).

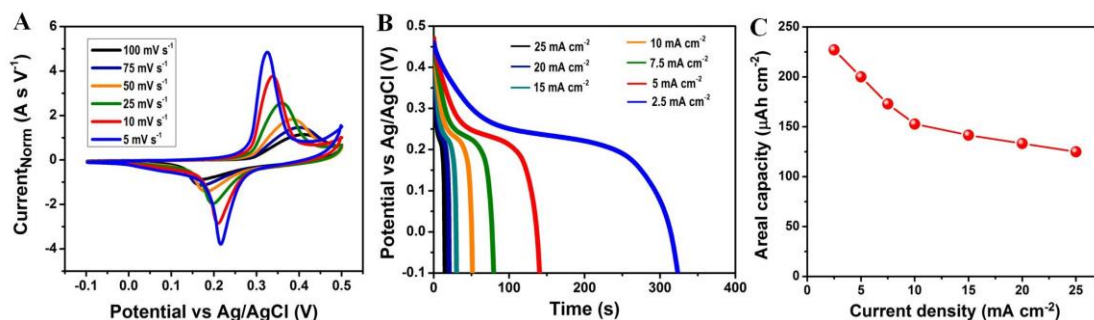


**Figure 5.1.4** Cyclic voltammetry curves measured at different scan rates (5 to 100  $\text{mV s}^{-1}$ ) (A), galvanostatic discharge curves measured at different current densities (2.5 to 25  $\text{mA cm}^{-2}$ ) (B), Areal charge capacities with respect to current densities (C) of  $\text{CoMoO}_4$  NPs directly grown on nickel foam in 2 M KOH electrolyte.

A pair of strong reduction/oxidation curves is observed in each voltammograms, suggesting that the capacitive characteristics are mainly influenced by faradic redox reaction. The shape of the CV curves is not significantly controlled by increasing the scan rate, which indicates improved mass transportation and electron conduction in the host materials [46]. Furthermore, at higher and lower scan rates, the anodic and cathodic peaks shift to higher and lower potentials, respectively. It might be due to the quasi-reversible nature of the electrode (that is, the effect of electro kinetics on peak shape and on the peak separation) [47, 48]. **Figure 5.1.4 (b)** represents the galvanostatic discharge curves of the synthesized  $\text{CoMoO}_4$  NPs collected at the different current densities from 2.5 to 25  $\text{mA cm}^{-2}$ . When increasing the current density, the discharge time was decreased; suggesting that the areal capacity value is inversely proportional to the current densities. It might be due to the fact that the electrolyte ions acquires time constraints which limit their diffusion at the active electrode at higher current density,

where in fact at a lower current density; there is sufficient time available for the electrolyte ions to access the active material. A maximum of areal capacity of  $227 \mu\text{Ah cm}^{-2}$  was achieved from galvanostatic charge discharge analysis for synthesized  $\text{CoMoO}_4$  NPAs at the current density of  $2.5 \text{ mA cm}^{-2}$  (**Figure 5.1.4 (c)**). The obtained higher areal capacity was attributed to the benefit of  $\text{CoMoO}_4$  NPAs formed on Ni foam without addition of polymer binder which can dramatically decrease the contact resistance in the prepared electrode.

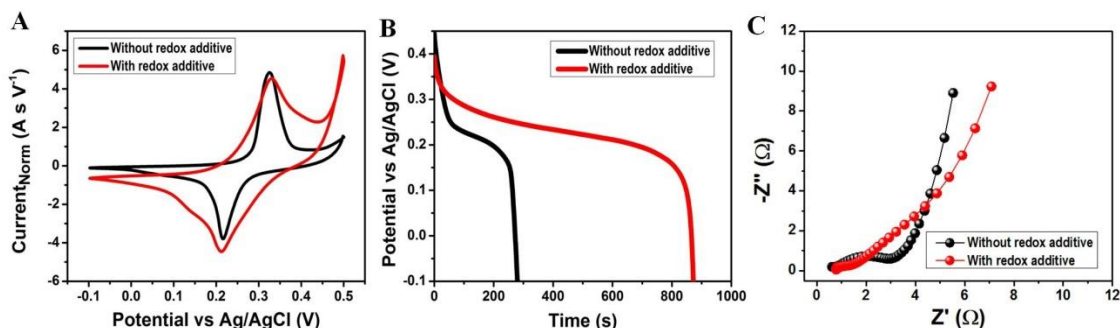


**Figure 5.1.5** Comparison of cyclic voltammetry curves at  $5 \text{ mV s}^{-1}$  (A), discharge curves measured at  $25 \text{ mA cm}^{-2}$  (B) and Nyquist plot (C) of  $\text{CoMoO}_4$  NPAs directly grown on nickel foam measured with and without addition of  $0.02\text{M K}_3\text{Fe}(\text{CN})_6$  redox additive in  $2\text{M KOH}$  electrolyte.

In order to further enhance the capacity behavior of synthesized  $\text{CoMoO}_4$  NPAs, we have used  $0.02\text{M K}_3\text{Fe}(\text{CN})_6$  as redox additive electrolyte into the  $2\text{M KOH}$  electrolyte. **Figure 5.1.5** shows the comparison curves for  $\text{CoMoO}_4$  NPAs with and without the addition of  $0.02\text{M K}_3\text{Fe}(\text{CN})_6$  redox additive. The increased area under the CV curve at  $5 \text{ mV s}^{-1}$  was observed with the addition of  $\text{K}_3\text{Fe}(\text{CN})_6$  redox additive in  $\text{KOH}$  electrolyte compared with the bare  $\text{KOH}$  electrolyte (**Figure 5.1.5 (a)**). The time

taken for discharging is quite high for  $\text{CoMoO}_4$  NPAs with addition of  $\text{K}_3\text{Fe}(\text{CN})_6$  redox additive in KOH electrolyte compared with the bare KOH electrolyte (**Figure 5.1.5 (b)**) resulting the increased charge storage capacity. In order to further elucidate the improved performances with addition of redox additive, we have measured electrochemical impedance spectroscopy (EIS) which is one of the important characteristics of the electrode materials. **Figure 5.1.5 (c)** shows the Nyquist plot in the frequency range between 0.01 Hz to 100000 Hz at the open circuit potential. It shows the binder-free  $\text{CoMoO}_4$  NPAs on Ni foam electrode with and without addition of redox additive into the KOH electrolyte. Both the spectra show common features: a small semi-circle at the higher frequency, a second larger capacitive loop at the lower frequency, and a straight line in the middle frequency part related to the diffusion. In KOH electrolyte, the binder-free  $\text{CoMoO}_4$  NPAs on Ni foam shows that the semi-circle region at the high frequency region and straight line at the low frequency region which close to the imaginary axis. Whereas Nyquist plot of  $\text{K}_3\text{Fe}(\text{CN})_6$  as redox additive in the KOH electrolyte shows the decreased semi-circle region at the high frequency region and inclined line at the lower frequency region, i.e. towards  $45^\circ$  suggests that the improved redox reactions. Also, the charge transfer resistance is less in the presence of redox additive suggests that the improvement of hexacyanoferrate on the conductive mechanism of binder-free  $\text{CoMoO}_4$  NPAs on Ni foam electrode/electrolyte interface [33].

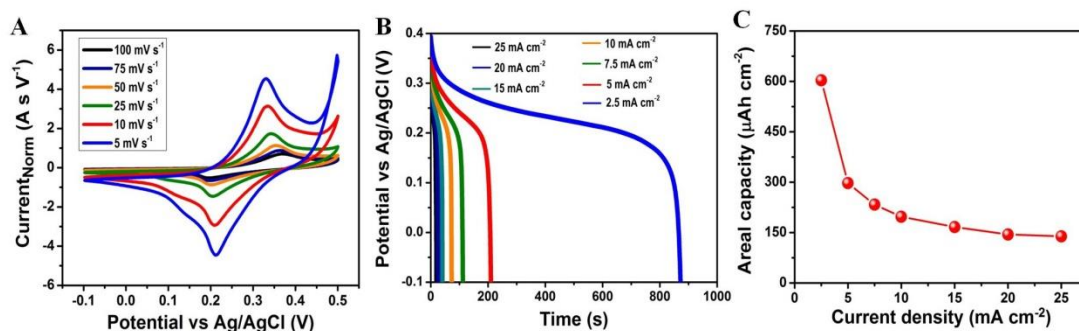


**Figure 5.1.6** Cyclic voltammetry curves at different scan rates (measured at 5 to 100  $\text{mV s}^{-1}$ ) (A), galvanostatic discharge curves at different current densities (measured at 2.5 to 25  $\text{mA cm}^{-2}$ ) (B), Areal charge capacities with respect to current densities (C) of  $\text{CoMoO}_4$  NPAs directly grown on nickel foam in 2M KOH electrolyte with addition of 0.02M  $\text{K}_3\text{Fe}(\text{CN})_6$  redox additive electrolyte.

In **Figure 5.1.6 (a)**, cyclic voltammograms were recorded in the potential range of -0.1 to 0.5 V under the different scan rates of 5 to 100  $\text{mV s}^{-1}$  for  $\text{CoMoO}_4$  NPAs with the addition of 0.02M  $\text{K}_3\text{Fe}(\text{CN})_6$ . The increased area of the CV curve was observed with the addition of redox additive electrolyte compared to the pristine KOH electrolyte resulting the increased charge storage capacity. Generally, the reversibility of the electrode could be determined by the shift of oxidation and reduction peak potentials with respect to the scan rates. When increasing the scan rates, the oxidation/reduction peak potential shifts occurs revealing that the quasi-reversible nature of the electrode [47, 48]. The minimum peak shifts with the addition of redox additive suggest that the reversible nature of the electrode. Further, the well-defined redox peaks were observed even at the higher scan rates (100  $\text{mV s}^{-1}$ ) suggesting the good rate capability of the electrode material. The reproducibility of the redox peaks additionally confirmed that the ionic and electronic transport of the material is rapid enough at the applied scan rates

[24]. **Figure 5.1.6 (b)** shows the galvanostatic discharge profile of synthesized  $\text{CoMoO}_4$  NPAs with the addition of  $0.02\text{M K}_3\text{Fe}(\text{CN})_6$  redox additive electrolyte at the various current densities ( $2.5$  to  $25\text{ mA cm}^{-2}$ ). **Figure 5.1.6 (c)** shows capacity variation with respect to the current densities. A maximum areal capacity of  $603.5\text{ }\mu\text{Ah cm}^{-2}$  was achieved from the galvanostatic charge discharge measurement for the  $\text{CoMoO}_4$  NPAs with the addition of  $0.02\text{M K}_3\text{Fe}(\text{CN})_6$  redox additive at the current density of  $2.5\text{ mA cm}^{-2}$ . The obtained areal capacity value was about three times higher than pristine  $\text{KOH}$  electrolyte.

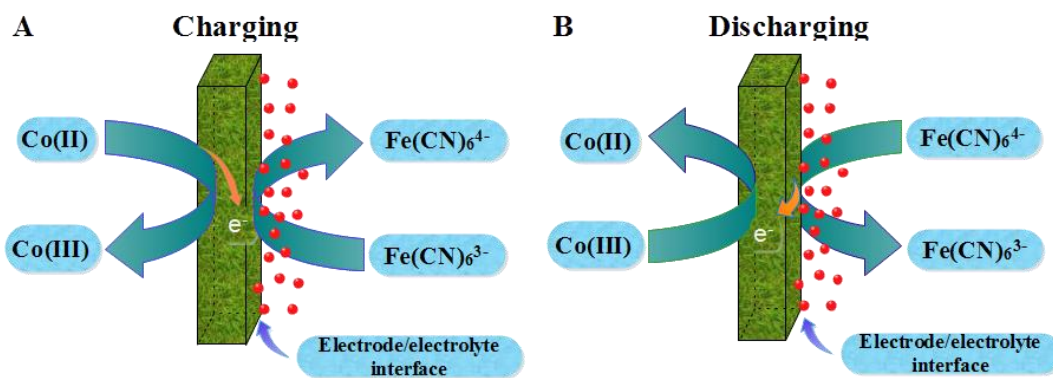
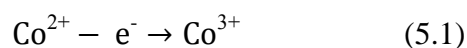


**Figure 5.1.7** Annotation of hexacyanoferrate ions during charge (A) and discharge (B) with the synthesized  $\text{CoMoO}_4$  NPAs on Ni foam electrode.

The improved electrochemical performance of the  $\text{CoMoO}_4$  NPAs via use of redox additive electrolyte can be illustrated as shown in **Figure 5.1.7**. Briefly, during charging process, the  $\text{CoMoO}_4$  undergoes an oxidation process (losing of electron) from  $\text{Co}(\text{II})$  to  $\text{Co}(\text{III})$  state.





The transferred electron from the Co(II) state (electron donor) is the responsible for the whole reactions occurred at the CoMoO<sub>4</sub> electrode. Particularly, the electrochemical performances of the CoMoO<sub>4</sub> NPAs electrode is enhanced if the smooth loose of electron by cobalt element in CoMoO<sub>4</sub> NPAs. It can be enhanced by the high electrochemical reversibility nature of Fe(CN)<sub>6</sub><sup>3-</sup>/Fe(CN)<sub>6</sub><sup>4-</sup> ions [33], which allows the electron from the cobalt element in CoMoO<sub>4</sub> NPAs by the reduction process. Fe(CN)<sub>6</sub><sup>3-</sup> accepts the electron from the Co element gives Fe(CN)<sub>6</sub><sup>4-</sup> ion. When the electrode is discharged, the Fe(CN)<sub>6</sub><sup>4-</sup> loses one electron (oxidation reaction) gives Fe(CN)<sub>6</sub><sup>3-</sup> in hexacyanoferrate to reduction of Co(III) into Co(II) in CoMoO<sub>4</sub> NPAs.



Here, the Fe(CN)<sub>6</sub><sup>4-</sup> acts as “electron donor”. In a word, hexacyanoferrate ions play the role of “electron shuttle” in the charge/discharge processes of CoMoO<sub>4</sub>/Ni foam electrode. In this case, Fe(CN)<sub>6</sub><sup>4-</sup> acts as an electron donor and Co(III) is an electron acceptor. This enhancement in the redox reaction in the presence of redox additive is accelerated the rate of the reaction which leads to the higher charge capacity. The electrochemical cyclic stability of the electrode material is very important parameter to determining the capacitive properties. The cyclic stability of CoMoO<sub>4</sub> NPAs on Ni foam with the redox additive electrolyte was examined over a large number of charge discharge cycles at the current density of 15 mA cm<sup>-2</sup>, as shown in **Figure 5.1.8**.

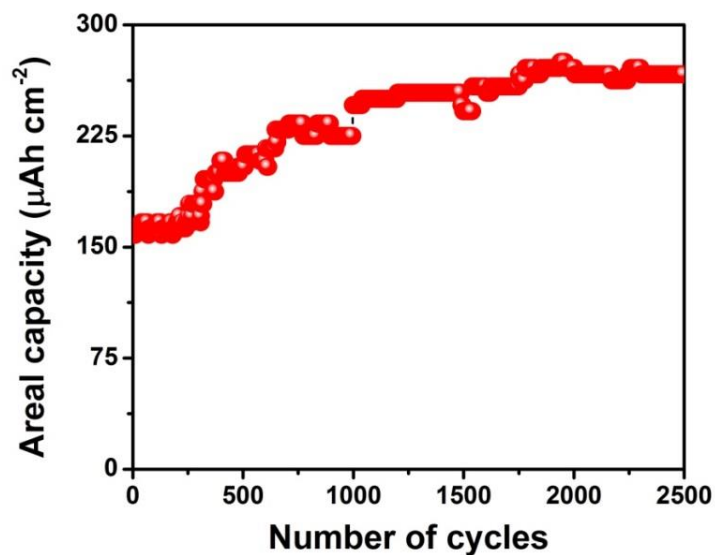


**Figure 5.1.8** Cyclic stability test for CoMoO<sub>4</sub> NPAs on Ni foam using charge discharge analysis measured at the current density of 15 mA cm<sup>-2</sup>.

Interestingly, the capacity of the electrode can be further enhanced to ~240 μAh cm<sup>-2</sup> (nearly 140 %) after 1100 cycles and stays almost stable afterward.

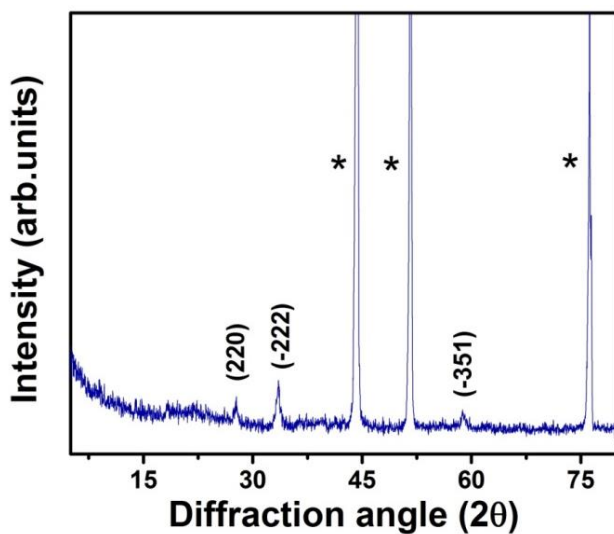


**Figure 5.1.9** XRD pattern of CoMoO<sub>4</sub> NPAs on Ni foam after cycles.

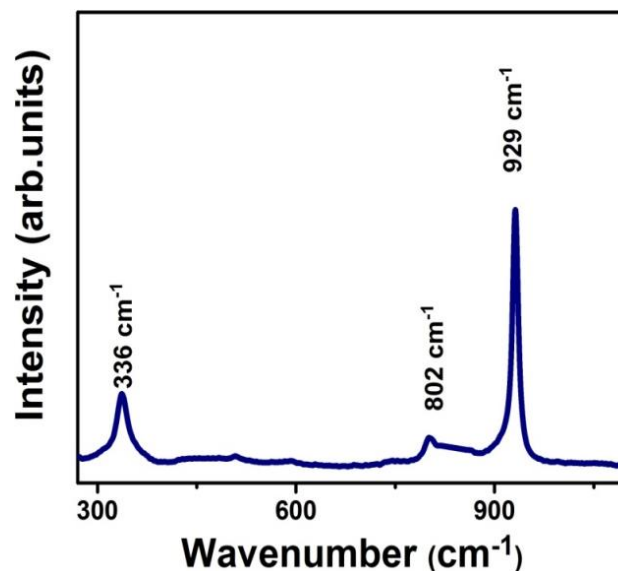


**Figure 5.1.10.** Raman spectrum of CoMoO<sub>4</sub> NPAs on Ni foam after cycles.

Generally, a portion of the material is active during the initial cycles of stability test, whilst the rest of the material is not activated. As the electrolyte ions gradually penetrates into the CoMoO<sub>4</sub> NPAs on Ni foam, more portions of the NPAs become activated and contribute to the increase of capacity. In order to elucidate in detail about the increase in capacity, we measured the XRD and Raman analysis of the electrodes after cyclic tests (shown in **Figure 5.1.9** and **Figure 5.1.10**) which suggested that there is no significant changes in the crystallinity of the material such as the intercalation of Fe(CN)<sub>6</sub> ions, formation of hydroxides are not observed.

Similarly, as shown in **Figure 5.1.11**, the morphological analysis using FE-SEM suggested that there is no change in the NPA structures even after cyclic tests. Thus,

such an activation process may result from the more complete oxidation and reduction of electrochemical species after some initial cycles.

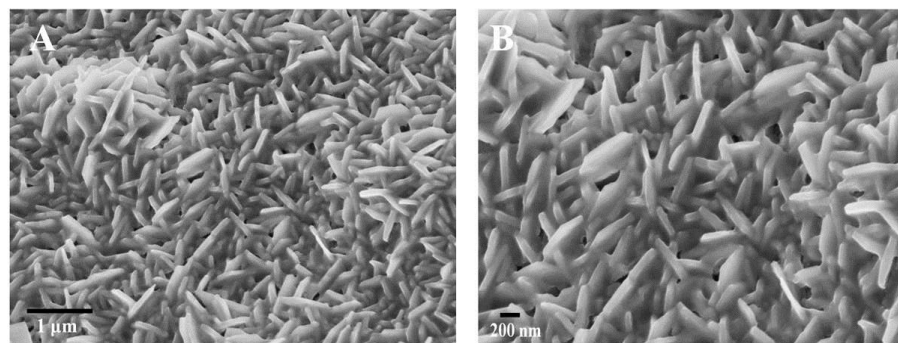


**Figure 5.1.11** FE-SEM images of  $\text{CoMoO}_4$  NPAs on Ni foam after cycles at low (A) and high (B) magnifications.

The similar kind of increasing nature of the binder free electrode material has been observed from the recent literatures by Dong et al [49] and Xia et al [50]. **Figure 5.1.12** shows the self-discharge curve for  $\text{CoMoO}_4$  NPAs on Ni foam with and without redox additive into the electrolyte.

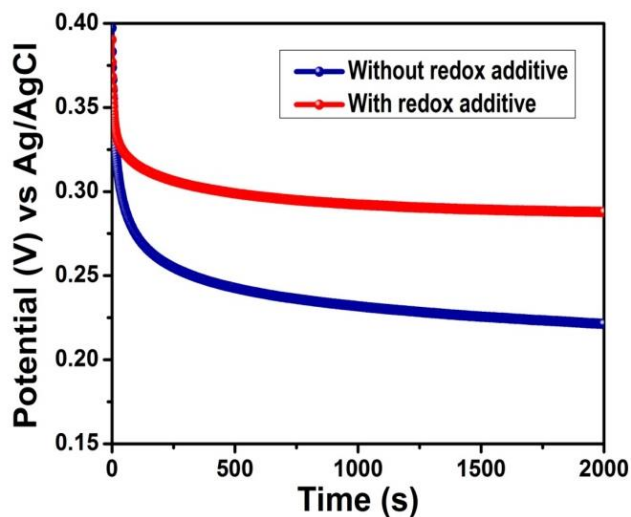


**Figure 5.1.12** Self-discharge curve  $\text{CoMoO}_4$  NPAs on Ni foam electrode with and without redox additive.

For this, the electrode was charged up to 0.4 V at an open circuit potential and discharged for 2000 s. With the addition of redox additive, CoMoO<sub>4</sub> NPAs on Ni foam electrode shows less potential drop and slow self-discharges. Collectively, this study suggested the improved electrochemical properties of the prepared CoMoO<sub>4</sub> NPAs based binder free electrode via redox additive electrolyte with the advantage of high structural stability and improved charge capacity.

In order to further evaluate the practical performances of the CoMoO<sub>4</sub> NPAs on Ni foam with addition of redox additive electrolyte, we have assembled asymmetric supercapacitors with CoMoO<sub>4</sub> NPAs on Ni foam as positive electrode and commercial activated carbon (AC) as negative electrode (see section C and D in supplementary information).

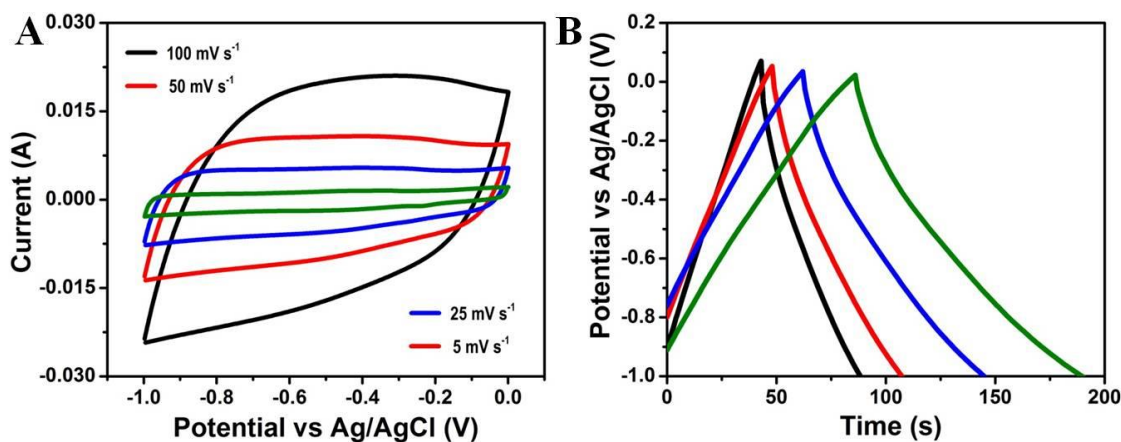


**Figure 5.1.13** Cyclic voltammetry curves at the different scan rates (measured at 5 to 100  $\text{mV s}^{-1}$ ) (A), charge discharge curves at the different current densities (measured at 2.5 to 5  $\text{mA cm}^{-2}$ ) for AC using three electrode system.

The electrochemical performances of activated carbon were shown in **Figure 5.1.13**. The rectangular behavior of CV curves and symmetric nature of GCD curves suggesting the EDLC nature of AC. The charges of both the electrodes have been balanced by balancing the mass of the negative electrode to obtain the maximum output of the supercapacitor device.

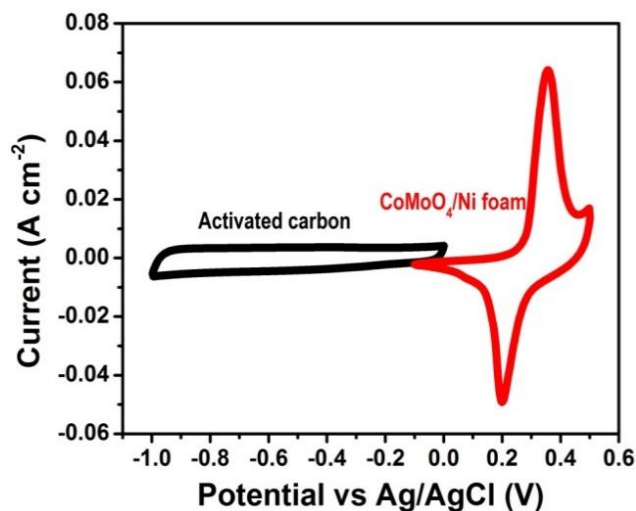


**Figure 5.1.14** Cyclic voltammetry curves of AC and CoMoO<sub>4</sub> NPAs on Ni foam at the scan rate of 50 mV s<sup>-1</sup> in three electrode system

**Figure 5.1.14** shows the CV curves for both positive and negative electrodes at the scan rate of 50 mV s<sup>-1</sup>. As shown in **Figure 5.1.15 (a and b)**, the fabricated asymmetric supercapacitor has been initially checked at the different potential levels from 0.5 V to 1.6 V in order to find out the operating potential window. Above 1.5 V, there is a slight evolution occurred in both CV and GCD curves suggesting that the fabricated device is optimum for up to 1.5 V, since the positive electrode can be scanned from -0.1 to +0.5 V and negative electrode can be scanned from 0 to -1.0 V. **Figure**

**5.1.15 (c)** shows the CV curves of the supercapacitor device at the different scan rates (from 5 to 100 mV s<sup>-1</sup>).

The shape of the CV curves is well maintained even at the high scan rates suggesting the good rate capability of the device. **Figure 5.1.15 (d)** shows the GCD curves at the different current densities measured from 2.5 to 25 mA cm<sup>-2</sup>. By using eqn-2 and 3, the calculated areal energy and power density was shown as Ragone plot in **Figure 5.1.15 (e)**. The fabricated device stores the maximum areal energy density of 125 μWh cm<sup>-2</sup> and delivers high power density of 13457 μW cm<sup>-2</sup>. The energy density decreases from the 125 μWh cm<sup>-2</sup> to 86 μWh cm<sup>-2</sup>, while the power density increases from 1507 μW cm<sup>-2</sup> to 13457 μW cm<sup>-2</sup> at the current density of 2.5 to 25 mA cm<sup>-2</sup>. **Figure 5.1.15 (f)** shows the cyclic stability of the fabricated asymmetric supercapacitors. The increasing nature of the stability study during initial cycles due to the initial activation process of the device and it is stabilized afterwards [49, 50, and 52]. Even after 2000 continuous cycles, there is no specific loss in the capacity suggesting the excellent stability of the device.

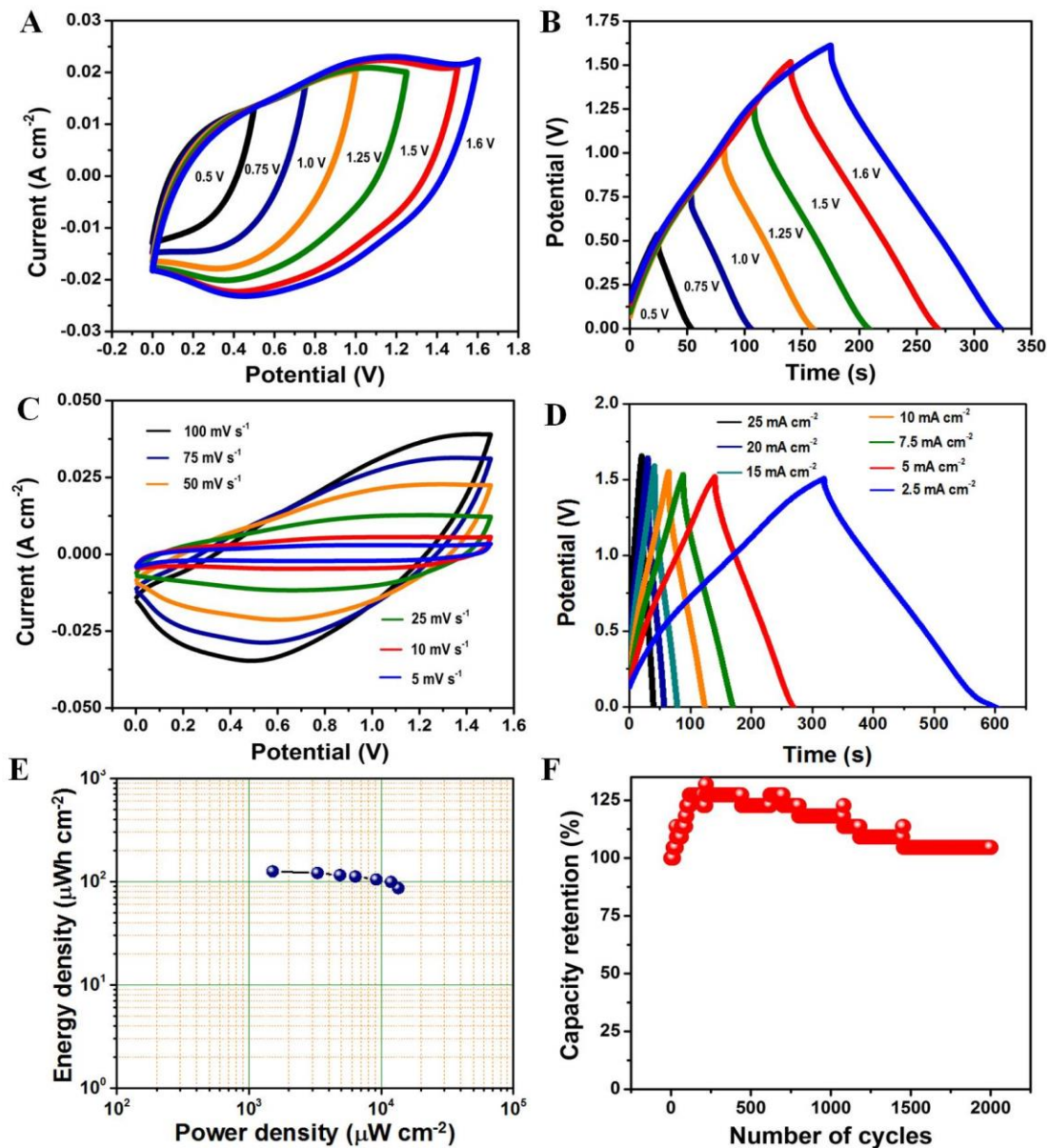


**Figure 5.1.15** Cyclic voltammety curves at the different potentials (measured at 50 mV s<sup>-1</sup>) (A), charge discharge curves at the different potentials (measured at 5 mA cm<sup>-2</sup>) (B), cyclic voltammety curves at the different scan rates (C), charge discharge curves at the different current densities (D), Ragone plot (E) and cyclic stability test measured at 25 mA cm<sup>-2</sup> (F) of fabricated CoMoO<sub>4</sub> NPAs on Ni foam/activated carbon asymmetric supercapacitors with redox additive electrolyte All together, this study suggested the

practical applications of the prepared CoMoO<sub>4</sub> NPAs based binder free electrode via redox additive electrolyte for high performance supercapacitor device applications.

#### 5.4. Conclusion

We have demonstrated the hydrothermal synthesis of CoMoO<sub>4</sub> NPAs on Ni foam for positive electrode material for electrochemical capacitor applications. The CoMoO<sub>4</sub> NPAs on Ni foam exhibited maximum areal capacity of 227  $\mu\text{Ah cm}^{-2}$  at constant current density of 2.5  $\text{mA cm}^{-2}$ . The addition of 0.02M K<sub>3</sub>Fe(CN)<sub>6</sub> redox additive into the 2M KOH solution showed about three fold increment in the charge storage performances of the CoMoO<sub>4</sub> NPAs on Ni foam electrode. Maximum areal capacity of 603.5  $\mu\text{Ah cm}^{-2}$  was achieved with addition of K<sub>3</sub>Fe(CN)<sub>6</sub> redox additive. The presence of redox additive accelerated the transition of Co(II)/Co(III) by the redox reaction  $\text{Fe}(\text{CN})_6^{3-}/\text{Fe}(\text{CN})_6^{4-}$  which results in the improved electrochemical performances. In addition, the fabricated supercapacitor device exhibited a high energy density of 125  $\mu\text{Wh cm}^{-2}$  at a power density of 1507  $\mu\text{W cm}^{-2}$  and excellent cyclic stability even after long cycles. The key findings of this work paves the use of CoMoO<sub>4</sub> NPAs grown on Ni foam via redox additive, which ensure its potential candidate as binder free positive electrodes for high performance supercapacitor applications.

#### 5.5. References

1. P. Simon, Y. Gogotsi, *Nat Mater*, **2008**, 7, 845.
2. L.L. Zhang, X.S. Zhao, *Chem. Soc. Rev.*, **2009**, 38, 2520.

3. Z. Chen, Y. Yuan, H. Zhou, X. Wang, Z. Gan, F. Wang, Y. Lu, *Adv. Mater.* **2014**, 26, 339.
4. L. Dai, D.W. Chang, J.B. Baek, W. Lu, *Small*, **2012**, 8, 1130.
5. L. Yuan, B. Yao, B. Hu, K. Huo, W. Chen, J. Zhou, *Energy Environ Sci.*, **2013**, 6, 470.
6. P.C. Chen, G. Shen, Y. Shi, H. Chen, C. Zhou, *ACS Nano*, **2010**, 4, 4403.
7. L.B. Kong, J.W. Lang, M. Liu, Y.C. Luo, L. Kang, *J. Power Sources*, **2009**, 194, 1194.
8. G. Wang, X. Shen, J. Horvat, B. Wang, H. Liu, D. Wexler, J. Yao, *J. Phys. Chem. C*, **2009**, 113, 4357.
9. H. Jiang, T. Zhao, C. Li, J. Ma, *J. Mater. Chem.* **2011**, 21, 3818.
10. C.C. Hu, K.H. Chang, M.C. Lin, Y.T. Wu, *Nano Lett.* **2006**, 6, 2690.
11. F.L. Zheng, G.R. Li, Y.N. Ou, Z.L. Wang, C.-Y. Su, Y.X. Tong, *Chem Comm*, **2010**, 46, 5021.
12. P.C. Chen, G. Shen, Y. Shi, H. Chen, C. Zhou, *ACS Nano*, **2010**, 4,4403.
13. S. He, C. Hu, H. Hou, W. Chen, *J Power Sources*, **2014**, 246, 754.
14. F. Luan, G. Wang, Y. Ling, X. Lu, H. Wang, Y. Tong, X.-X. Liu, Y. Li, *Nanoscale*, **2013**, 5, 7984.
15. X. Meng, M. Zhou, X. Li, J. Yao, F. Liu, H. He, P. Xiao, Y. Zhang, *Electrochim. Acta*, **2013**, 109, 20.

16. R.R. Salunkhe, B.P. Bastakoti, C.-T. Hsu, N. Suzuki, J.H. Kim, S.X. Dou, C.-C. Hu, Y. Yamauchi, *Chem. Eur. J.* **2014**, *20*, 3084.
17. Q. Yang, Z. Lu, J. Liu, X. Lei, Z. Chang, L. Luo, X. Sun, *Progress in Natural Science: Materials International*, **2013**, *23*, 351.
18. .K. Krishnamoorthy, G.K. Veerasubramani, S. Radhakrishnan, S.J. Kim, *Chemical Eng J*, **2013**, *251*, 116.
19. D. Guo, P. Zhang, H. Zhang, X. Yu, J. Zhu, Q. Li, T. Wang, *J. Mater. Chem. A*, **2013**, *1*, 9024.
20. X. Liu, S. Shi, Q. Xiong, L. Li, Y. Zhang, H. Tang, C. Gu, X. Wang, J. Tu, *ACS Appl. Mater. Inter*, **2013**, *5*, 8790.
21. H.W. Wang, Z.A. Hu, Y.Q. Chang, Y.L. Chen, H.Y. Wu, Z.Y. Zhang, Y.Y. Yang, *J. Mater. Chem*, **2011**, *21*, 10504.
22. C. Yuan, J. Li, L. Hou, X. Zhang, L. Shen, X.W. Lou, *Adv Fun Mater*, **2012**, *22*, 4592.
23. B. Senthilkumar, D. Meyrick, Y.-S. Lee, R.K. Selvan, *RSC Adv.*, **2013**, *3*, 16542.
24. L.Q. Mai, F. Yang, Y.L. Zhao, X. Xu, L. Xu, Y.Z. Luo, *Nat Commun*, **2011**, *2*, 381.
25. S. Peng, L. Li, H.B. Wu, S. Madhavi, X.W. Lou, *Adv. Ener. Mater*, **2015**, *5*, 1401172.
26. M.C. Liu, L.B. Kong, X.J. Ma, C. Lu, X.M. Li, Y.C. Luo, L. Kang, *New. J. Chem*, **2012**, *36*, 1713.

27. G.K. Veerasubramani, K. Krishnamoorthy, S. Radhakrishnan, N.-J. Kim, S.J. Kim, *Int. J. Hydrogen Energy*, **2014**, 39, 5186.
28. X. Yu, B. Lu, Z. Xu, *Adv. Mater.*, **2013**, 26, 1044.
29. G.K. Veerasubramani, K. Krishnamoorthy, S.J. Kim, *RSC Adv.*, **2015**, 5, 16319.
30. C. Yuan, L. Yang, L. Hou, L. Shen, X. Zhang, X.W. Lou, *Energy Environ Sci.*, **2012**, 5, 7883.
31. J. Pu, Y. Tong, S. Wang, E. Sheng, Z. Wang, *J. Power Sources*, **2014**, 250, 250.
32. S. Roldán, M. Granda, R. Menéndez, R. Santamaría, C. Blanco, *J. Phys. Chem C*, **2011**, 115, 17606.
33. L.H. Su, X.G. Zhang, C.H. Mi, B. Gao, Y. Liu, *Phys. Chem. Chem. Phys*, **2009**, 11, 2195.
34. H. Yu, J. Wu, L. Fan, Y. Lin, K. Xu, Z. Tang, C. Cheng, S. Tang, J. Lin, M. Huang, Z. Lan, *J. Power Sources*, **2012**, 198, 402.
35. S.T. Senthilkumar, R.K. Selvan, Y.S. Lee, J.S. Melo, *J. Mater. Chem. A*, **2013**, 1, 1086-1095.
36. B. Akinwolemiwa, C. Peng, G. Z.Chen, *J. Electrochem. Soc*, **2015**, 162(5), A5054.
37. T. Brousse, D. Bélanger, J.W. Long, *J. Electrochem. Soc*, **2015**, 162(5), A5185.
38. S.E. Chun, B. Evanko, X. Wang, D. Vonlanthen, X. Ji, G.D. Stucky, S.W. Boettcher, *Nat Commun*, **2015**, 6, 7818.
39. R. Ramkumar, M. Minakshi, *Dalton Trans.*, **2015**, 44, 6158.
40. K.S. Park, S.-D. Seo, H.W. Shim, D.W. Kim, *Nanoscale Res Lett*, **2012**, 7, 35.

41. A. Moura, L. Oliveira, P. Pereira, I. Rosa, M. Li, E. Longo, J. Varela, *Adv. Chem. Engineer. Sci.*, **2015**, 2 (4), 465.
42. V. Parola, G. Deganello, C.R. Tewell, A.M. Venezia, *Appl Catal A – Gen.* **2002**, 235, 171.
43. X. Xia, W. Lei, Q. Hao, W. Wang, X. Wang, *Electrochim. Acta* **2015**, 99, 253.
44. Z. Gu, H. Nan, B. Geng, X. Zhang, *J. Mater. Chem A*, **2015**, 3, 14578.
45. J. Zhu, L. Huang, Y. Xiao, L. Shen, Q. Chen, W. Shi, *Nanoscale*, **2014**, 6, 6772.
46. D. Guo, H. Zhang, X. Yu, M. Zhang, P. Zhang, Q. Li, T. Wang, *J. Mater. Chem A*, **2013**, 1, 7247.
47. F. Harnisch, S. Freguia, *Chem. Asian J.*, **2012**, 7, 466.
48. Y. Wan, X. Wang, S. Liu, Y. Li, H. Sun, Q. Wang, *Int. J. Electrochem. Sci*, **2013**, 8, 12837.
49. X.C. Dong, H. Xu, X.W. Wang, Y.X. Huang, Mary B. C.Park, H. Zhang, L.H. Wang, W. Huang, P. Chen, *ACS Nano* **2012**, 6 (4), 3206.
50. X. Xia, J.T u, Y. Zhang, X. Wang, C. Gu, X. Zhao, H.J. Fan, *ACS Nano* **2012**, 6, 5531.
51. W. Fu, Y. Wang, W. Han, Z. Zhang, H. Zha, E. Xie, *J. Mater. Chem A*, **2016**, 4, 173.
52. J.H. Zhong, A.L. Wang, G.R. Li, J.W. Wang, Y.N. Ou, Y.X. Tong, *J. Mater. Chem* **2012**, 22, 5656.

## 5.6. Summary

In this chapter, we have discussed about to enhance the performance of  $\text{CoMoO}_4$  faradaic electrode by the binder-free approach and presented. The binder-free  $\text{CoMoO}_4$  was successfully achieved by hydrothermal method. The achieved areal capacity of the  $\text{CoMoO}_4/\text{Ni}$  foam was  $227 \mu\text{Ah cm}^{-2}$  ( $206 \mu\text{Ah g}^{-1}$ ) which is nearly 8 times higher than the sonochemically prepared  $\text{CoMoO}_4$  with binder and conductive agent. In order to further improve the performance of binder-free electrode, we used a novel strategy, which is the addition of redox additive into the electrolyte. The addition of  $0.02\text{M K}_3\text{Fe}(\text{CN})_6$  as redox additive into electrolyte makes the improvement in areal capacity about 2.5 times higher than pristine electrolyte. The achieved areal capacity of  $\text{CoMoO}_4/\text{Ni}$  foam with redox additive was  $603 \mu\text{Ah cm}^{-2}$ . Further, the fabricated  $\text{CoMoO}_4/\text{Ni}$  foam // activated carbon hybrid supercapacitor exhibited an areal energy density of  $125 \mu\text{Wh cm}^{-2}$  at a power density of  $1507 \mu\text{W cm}^{-2}$ . This achieved value is quite higher compare to other reports. However, in order to calculate gravimetric capacity and energy density, for making more comparison, we need to include the weight of addition of redox additive into the electrolyte since the improved capacity is also contributed from the additive. In addition, the negative electrode also should be optimized in presence of redox additive which will provide some interesting aspects for the energy storage society.

## CHAPTER - 6

### **Deposition of CNT on CoMoO<sub>4</sub> by sustainable method and its electrochemical performance as positive electrode for hybrid supercapacitor**

#### **Highlights**

- ❖ Global warming is primarily a problem of excessive carbon dioxide (CO<sub>2</sub>) in the atmosphere, which acts as a blanket, grasping heat and warming the planet
- ❖ One of the inevitable reactions during syngas (SNG) production by dry reforming reaction (DRR) of hydrocarbons is the deposition of carbon over the catalyst which can be eliminated as anthropogenic CO<sub>2</sub>
- ❖ This is the main obstacle for SNG production during DRR, diminishes the performance of the catalysts and enhances the CO<sub>2</sub> formation which leads to global warming
- ❖ In this study, for the first time, we present a novel approach to use the carbon-deposited catalyst formed during DRR as an effective electrode material for supercapacitor applications
- ❖ This disposable carbon-deposited catalyst shows ~22 times higher capacity than the bare catalyst, and act as a positive electrode for hybrid supercapacitors. The fabricated supercapacitor device works with an extended voltage of 1.6 V and exhibits an excellent electrochemical performance
- ❖ Moreover, serially connected supercapacitor devices could power up the various types of LEDs and UV light sensors

## 6.1. Introduction

Recently, the threat of global warming has become one of the most serious environmental concerns worldwide. The increasing emission of greenhouse gases, such as carbon dioxide (CO<sub>2</sub>), methane, nitrous oxide (N<sub>2</sub>O), and some fluorinated gases, is one of the important factors in climate change [1-4]. Thus, it is of great importance to reduce the emission of greenhouse gases, particularly anthropogenic CO<sub>2</sub>, and also to further use processes that are capable of consuming these gases. Fossil fuels are our important source of energy and have immense impact on human prosperity [5]. With the depletion of fossil fuels due to continuously increasing demand, there is a necessity to investigate the ways to utilize the available resources like natural gas reserves that produce fuels and chemicals that are fossil fuels derivatives [6]. Synthesis gas, also called as syngas (SNG), is a mixture of carbon monoxide (CO) and hydrogen (H<sub>2</sub>) gases, which is generally referred to as chemical intermediate that could be readily converted into the abundant value added fuels or chemicals by Fischer-Tropsch synthesis [7, 8]. For last few decades, great attention has been made by the researchers to the production of SNG towards more efficient, sustainable and environmentally benign conversion of fossil fuel feedstocks [9]. There are typically three approaches for hydrocarbon conversion to date, namely, partial oxidation, steam reforming reaction, and dry reforming reaction (DRR) to produce SNG [10]. Among these, DRR shows advantages over rest of two, combining SNG production and greenhouse gas utilization. It uses hydrocarbons (e.g., methane, propane) with CO<sub>2</sub> gas to produce SNG [11, 12]. Among

the various hydrocarbons, propane is much more attractive for DRR because of the associated lower reforming temperature and lower vapor pressure of propane than methane, which makes it more favorable for fuel cell cars with internal reforming. In addition, propane is one of the major constituents of liquid petroleum gas (LPG), which is produced in relatively large amounts by natural gas and crude oil refining and is generally widely available and inexpensive [13-15]. Unfortunately, DRR still faces few technical challenges [16]. The main one is carbon formation which deactivates almost all type of commercial catalyst for DRR. Many attempts have been made to prepare carbon-resistant catalysts. This is very reasonable since if the excess  $\text{CO}_2$  is introduced to alleviate the carbon deposition [17]. It will remain as the main impurity in the effluent which diminishes the performance of the catalyst. Secondly, the DRR is endothermic reaction: it requires high temperatures to achieve maximum conversion efficiencies. This severe operating temperature may cause deactivation of the catalyst by coke formation over the catalyst surface and/or sintering of the catalyst material [18-20]. If the catalyst is deactivated by carbon deposition, it can be reactivated again by removing the carbon as  $\text{CO}_2$  gas using oxygen inlet. However, it is practically difficult, because, we need to use additional oxygen gas and again creating the  $\text{CO}_2$  gas is environmentally noxious since  $\text{CO}_2$  is main green house gas. Thus, it is highly important to create some useful strategy to utilizing the carbon deposited catalyst without harming our earth.

The catalyst used in DRR is the main factor for good conversion efficiency and syngas production. Compared with noble metals or other transition metal based

catalysts, Ni-based catalysts are largely used for the reforming reaction, because of their abundance in nature, lower cost, and excellent activity [21-25]. Mostly, the catalysts for DRR reaction were mainly obtained via impregnation method or sol-gel method which has some disadvantages such as a lack of desirable morphology of the material, less interaction between the catalyst and support, and high temperature synthesis for the formation of the products. In addition, the mass of the catalyst on the support is quite high which increases the cost of the catalyst. Hence, it is important to prepare the catalyst with the low mass, hierarchical structures, strong interaction with the support to sustain even at the high temperatures. Thus, there is a continuing need to find other methods to avoid these disadvantages. Among these efforts, a hydrothermal approach is one important technique that has many advantages, such as low cost, environmentally friendly, excellent morphology, and the possibility of achieving high accessible active sites [26-27]. In this scenario, we have directly grown cobalt molybdate on Ni foam ( $\text{CoMoO}_4/\text{Ni foam}$ ) by using a hydrothermal approach, for use as an effective catalyst for the DRR of propane. Firstly the choice of two catalytic active materials for DRR can provide several advantages such as good catalytic conversion efficiency, good carbon resistant during DRR, and environmentally benign. The presence of Co can be beneficial to resist the deactivation of the catalyst and Mo can act as a promoter as well as better coke-resistant during dry reforming reaction [23, 24]. This approach of using  $\text{CoMoO}_4$  grown on porous Ni foam might facilitate a larger accessible area for the DRR process, hence, it is expected to enhance the catalytic conversion and yield of syngas.

To date, researchers have focused on eliminating the carbon on the catalyst (formed during DRR) via feeding oxygen gas by converting it to anthropogenic CO<sub>2</sub>, since it is the primary greenhouse gas which may leads to global warming [23, 28, 29]. In this study, for the first time, we focused on using this carbon-deposited CoMoO<sub>4</sub>/Ni foam catalyst as an electrode for supercapacitors. The importance of binary metal oxides have gradually been considered as promising effective and scalable alternatives due to their low-cost, environment benignity and abundance [30]. It is well known that the incorporation of carbon based materials with cobalt molybdate nanostructures shows several advantages such as increase in conductivity, surface area, fast ion transportation and good electrochemical stability [31-35]. Thus, the prepared carbon-deposited CoMoO<sub>4</sub>/Ni foam catalyst can be used as an electrode for supercapacitor applications; it would be a novel and promising approach to diminish CO<sub>2</sub> formation during the production of SNG (especially by DRRs). Briefly, this work illustrates an effective method for utilizing the catalyst for dual applications such as energy (fuel gas) production and energy storage (supercapacitors) applications.

## **6.2. Experimental methods**

### **6.2.1. Preparation of CoMoO<sub>4</sub>/Ni foam catalyst**

Initially, the growth of CoMoO<sub>4</sub> nanostructures on the nickel foam was achieved via a one-pot hydrothermal method [36]. Briefly, precursor solution containing Co(NO<sub>3</sub>)<sub>2</sub>·6H<sub>2</sub>O and Na<sub>2</sub>MoO<sub>4</sub>·2H<sub>2</sub>O (molar ratio, 1:1) was prepared by dissolving in

water. A slice of Ni foam was cleaned using dilute HCl, acetone, and water to remove impurities and oxide layers on the surface and the precursor solution was transferred into a 100-mL Teflon-lined autoclave (with stainless steel covering). Precleaned Ni foam was immersed into the solution and kept at a constant temperature of 180°C for 6 h. After the hydrothermal reaction, the autoclave was cooled to room temperature. The color of the nickel foam had changed to pink, indicating the uniform growth of CoMoO<sub>4</sub> on the nickel foam. The product obtained was washed thoroughly in distilled water and ethanol to remove residual ions and was allowed to dry in a hot-air oven overnight at 80°C. Finally, the prepared sample was calcined at 450 °C for 3 h. This prepared material was then used for further characterization and as a catalyst for DRR.

### **6.2.2. Preparation of CNT on CoMoO<sub>4</sub>/Ni foam by dry reforming reaction**

The DRR of propane with CO<sub>2</sub> was carried out in a thermo-catalytic reactor packed with the catalyst in a pellet structure. The catalytic activity of the prepared catalyst was studied over the temperature range of 580–660°C. The reactant gases were fed into the reactor at a ratio of 10:30:60 (C<sub>3</sub>H<sub>8</sub>:CO<sub>2</sub>:N<sub>2</sub>) using a set of mass flow controllers (MKS1179A). The total flow rate was fixed at 300 mL min<sup>-1</sup> throughout the reaction. During the DRR, the concentrations of relevant components were analyzed by gas chromatography (Micro-GCCP-4900; Varian, Palo Alto, CA, USA [10 m PPQ column]) equipped with a thermal conductivity detector (TCD). For the sake of coke deposition

over the catalyst, the DRR of propane was carried out for 24 h at 630°C. After the coke formation, generally, the flow of the feed gas was stopped, the reactor temperature was set to a desired value (500°C), and dry air at 200 mL min<sup>-1</sup> was supplied to the reactor, which regenerated the deactivated catalyst by oxidizing the coke. However, in this study, we used this coke-deposited catalyst directly for further investigations.

### **6.2.3. Fabrication of hybrid supercapacitors**

The electrochemical performances of the materials were investigated through CV, electrochemical impedance spectroscopy (EIS), and GCD using an AUTOLAB PGSTAT302N electrochemical workstation. For the three-electrode system, a piece of CNT-deposited CoMoO<sub>4</sub>/Ni foam (1 × 1 cm<sup>2</sup> area) was used directly as the working electrode. Silver/silver chloride (Ag/AgCl) and platinum foil were used as the reference and counter electrodes, respectively. Electrolyte containing 2 M KOH was used in this study. For the two-electrode system, the CNT-deposited CoMoO<sub>4</sub>/Ni foam catalyst was used as the positive electrode and rGO/CC was used as the negative electrode. Both the electrodes are sandwiched using the commercial filter paper. The areal capacity, areal energy, power density, and mass balance equation for balancing the charges of the positive and negative electrodes can be calculated from the discharge profiles.

## **6.3. Results and discussion**

### **6.3.1. Structural characterization before DRR**

To determine the crystalline structure, purity, and size of the synthesized materials, X-ray diffraction (XRD) analysis was performed.

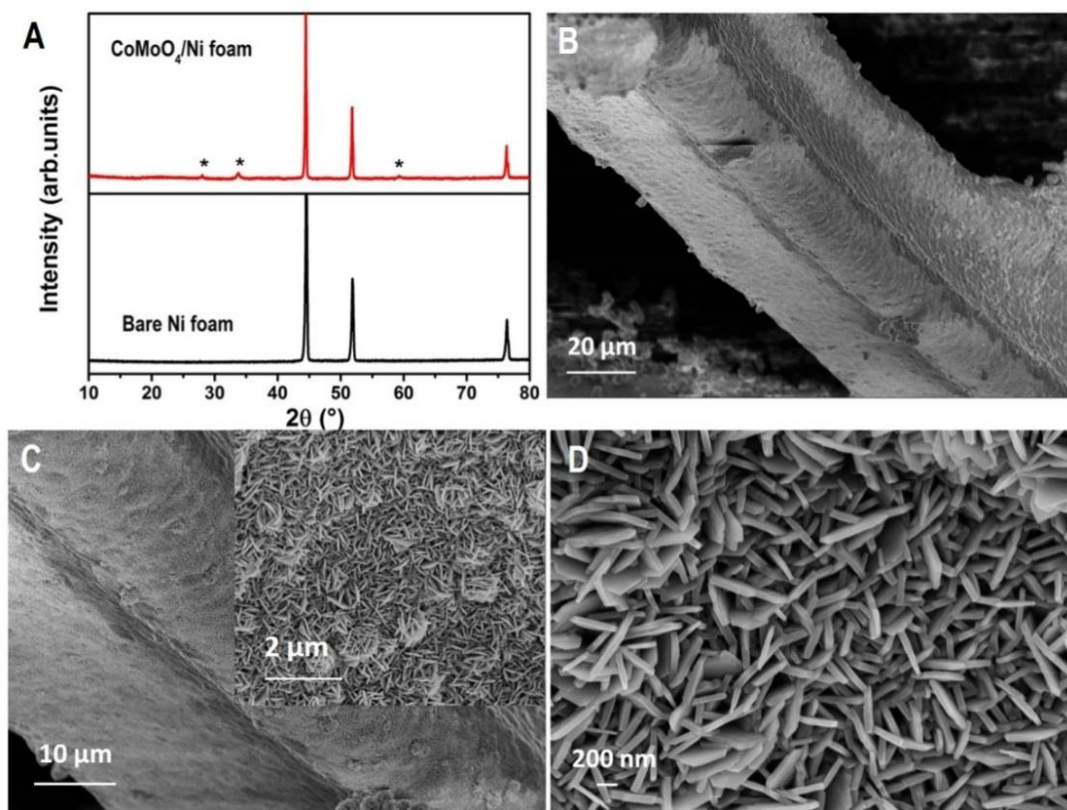


**Figure 6.1.1** Structural characterization of binder-free  $\text{CoMoO}_4$  on nickel Ni foam catalyst before the dry reforming reaction (DRR): the X-ray diffraction (XRD) pattern (A) and Field-emission –scanning electron microscopy (FE-SEM) images at different magnifications, 20  $\mu\text{m}$  (B), 10  $\mu\text{m}$  (C), 2  $\mu\text{m}$  (inset of Fig.1C), 200 nm (D), (B–D) suggest that uniform  $\text{CoMoO}_4$  plate-like arrays grew on the Ni foam (~400 nm in length, 50–100 nm in breadth), which was used directly as a catalyst for the DRR of propane.

**Figure 6.1.1 (a)** shows the XRD pattern of hydrothermally synthesized  $\text{CoMoO}_4/\text{Ni}$  foam and bare Ni foam. The XRD pattern obtained is associated with the monoclinic phase of  $\text{CoMoO}_4$ . Generally,  $\text{CoMoO}_4$  exists in two different phases,  $\alpha$  and  $\beta$ . Both

phases crystallize in monoclinic form with a space group of C2/m. In our case, the formation of  $\alpha$ -CoMoO<sub>4</sub> on the nickel foam was observed under the hydrothermal reaction at a temperature of 180°C with high pressure, followed by calcination [23]. The observed peaks at 28.34°, 33.58°, and 59.24° correspond to the planes (220), (-222), and (-351), respectively and the remaining peaks at 44.5°, 51.8°, and 76.4° correspond to the nickel foam [37-39]. **Figure 6.1.1 (b-d)** shows Field-emission –scanning electron microscopy (FE-SEM) images of the synthesized materials at different magnifications. It suggests that uniform plate like arrays were grown on the Ni foam surface. Furthermore, these plate-like arrays were tightly coordinated with the Ni foam surface with high porous nature. To investigate the crystalline and bonding nature of the synthesized material, Raman measurements were performed and are shown in **Figure 6.1.2** in the range of 250–1,200 cm<sup>-1</sup>. Three major peaks were observed in the spectrum: 928, 803, and 335 cm<sup>-1</sup> which corresponds to the Mo-O bond (symmetric stretching), O-Mo-O bond (asymmetric stretching), Co-O-Mo bond (symmetric stretching) respectively.

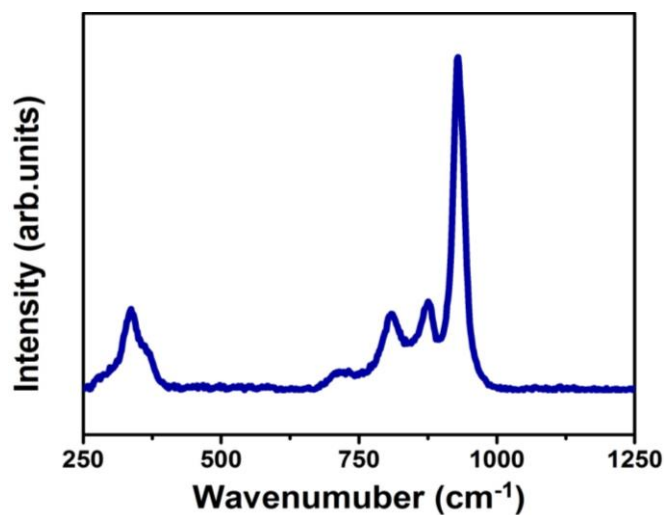


**Figure 6.1.2** Raman spectrum of CoMoO<sub>4</sub> NPAs on Ni foam after calcination

### 6.3.2. Dry reforming reaction of propane

This CoMoO<sub>4</sub>/Ni hierarchical structure was effectively used as a catalyst for DRR reaction for hydrocarbon adsorption to syngas production.

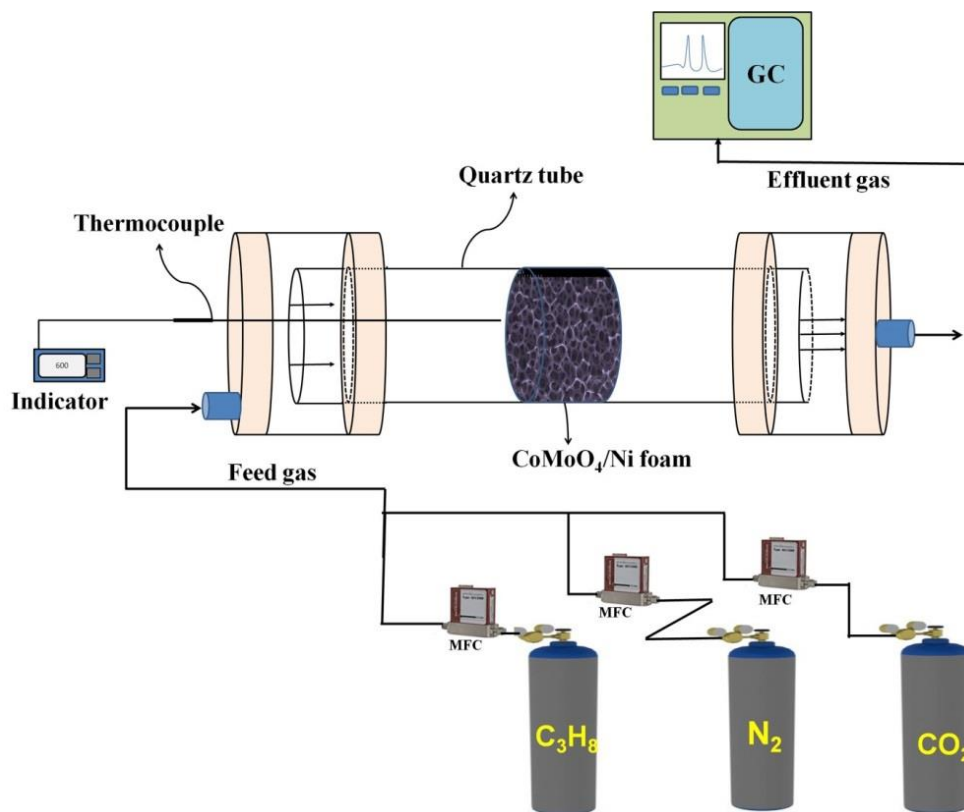
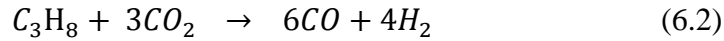


**Figure 6.1.3** Schematic representation of the reactor used for DRR of propane.

The DRR of propane with CO<sub>2</sub> was carried out in a thermo-catalytic reactor, packed with the catalyst in a pellet structure, as shown in **Figure 6.1.3**. The general equation for hydrocarbon reforming [40] is given by



For propane,  $n = 3$ ; thus:



The catalytic activity in terms of propane and  $CO_2$  was studied in the temperature range of 580–660 °C using the  $CoMoO_4/Ni$  foam catalyst and is presented in **Figure 6.1.4**.

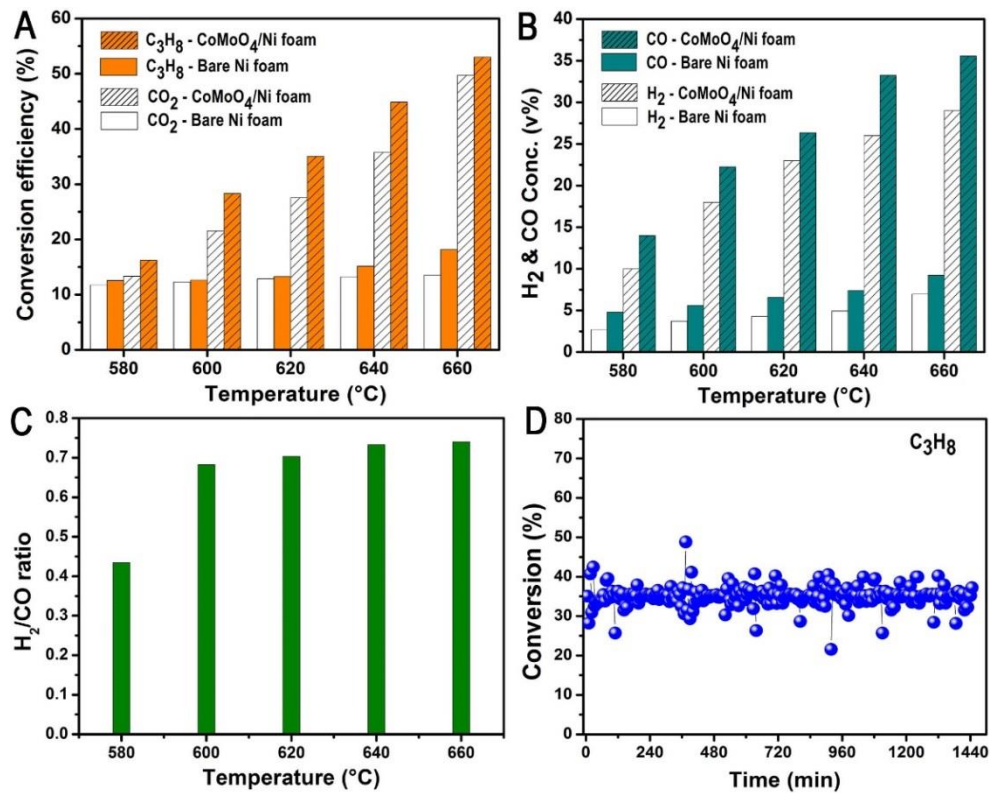


**Figure 6.1.4** Catalytic activity of the catalyst: Conversion efficiencies of propane and carbon dioxide ( $CO_2$ ) (A), concentrations of SNG obtained (B) for bare Ni foam and binder-free  $CoMoO_4/Ni$  foam catalysts,  $H_2/CO$  ratios obtained (C) at different

temperatures, and conversion efficiencies of propane at 630°C over a period of 1,440 min (D) for binder-free CoMoO<sub>4</sub>/Ni foam catalyst.

As shown in **Figure 6.1.4 (a)**, at a temperature of 580 °C, the propane and CO<sub>2</sub> conversions were 16 and 13 %, respectively. When the temperature increased, the conversion efficiency also increased, up to 660 °C. Above 660 °C, saturation of conversion efficiency was observed. The maximum conversion efficiency of propane and CO<sub>2</sub> for the CoMoO<sub>4</sub>/Ni foam exhibited at 53 % and 49.75 %, respectively which is nearly 300 % higher than the pristine Ni foam at the DRR temperature of 660 °C. The concentration of CO and H<sub>2</sub> obtained using the CoMoO<sub>4</sub>/Ni foam catalyst is presented in **Figure 6.1.4 (b)**. It can be seen clearly that the concentrations of both CO and H<sub>2</sub> increase with increasing temperature for CoMoO<sub>4</sub>/Ni foam catalyst. A maximum of 35.5 v% of CO and 29 v% of H<sub>2</sub> was obtained for CoMoO<sub>4</sub>/Ni foam which is about four fold higher than the bare Ni foam. The CoMoO<sub>4</sub> NPAs coated Ni foam showed excellent performances in terms of both conversion efficiency and syngas production compared to bare Ni foam and also higher than the other catalysts [22, 41, 42]. The plate like arrays of the CoMoO<sub>4</sub>/Ni foam catalyst acted as an effective role in the improved conversion efficiency and syngas production [42]. In addition, the presence of Co can be beneficial to resist the deactivation of the catalyst and Mo can act as good coke-resistant during dry reforming reaction [23, 24]. The H<sub>2</sub>/CO ratio is presented in **Figure 6.1.4 (c)** as a function of temperature. The observed H<sub>2</sub>/CO ratio was < 1, which may be ascribed to side reactions during DRR. However, the obtained H<sub>2</sub>/CO product ratio close to unity is suitable for the production of liquid hydrocarbon via Fischer-Tropsch synthesis and the

production of oxygenated hydrocarbon compounds. Thus, from a practical point of view, the obtained H<sub>2</sub>/CO ratio is industrially viable. The catalyst cyclic stability test was studied over a period of 24 h. As can be seen from **Figure 6.1.4 (d)**, the conversion efficiency of the CoMoO<sub>4</sub>/Ni foam catalyst was maximal at a temperature of 630 °C. This shows that the conversion efficiency was retained almost at the initial value, indicating that the catalyst maintained its catalytic activity. However, there was a slight loss in the stability, which might be due to the formation of carbon over the catalyst. The formation of carbon over the catalyst during DRR can be either due to the dehydrogenation of C<sub>3</sub>H<sub>8</sub> (equation 3) or via Boudouard reaction (equation 4) explained as follows:

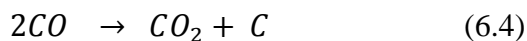
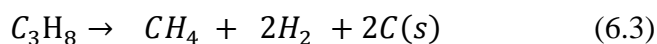


**Figure 6.1.4 (d)** revealed that the conversion efficiency decreases slowly over increasing time, thus indicating that carbon is deposited on the surface of the CoMoO<sub>4</sub>/Ni catalyst upto a mild degree. This carbon-deposited catalyst has been investigated using both structural and electrochemical characterizations.

### 6.3.3. Structural characterization after dry reforming

It is important to determine the morphology of the catalyst after the high-temperature DRR of propane. **Figure 6.1.5 (a-d)** shows the FE-SEM images of the carbon deposited CoMoO<sub>4</sub> catalyst at different magnifications.

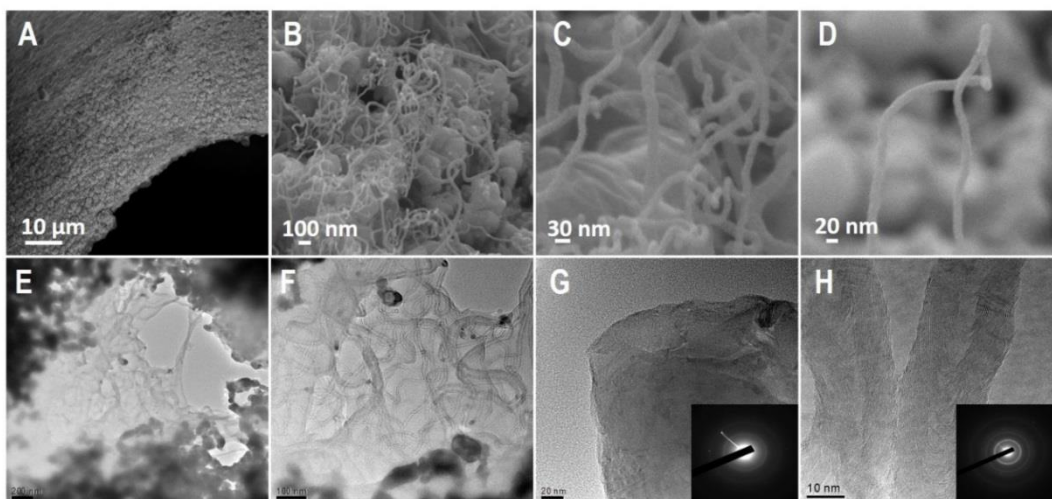


**Figure 6.1.5** Structural morphology of carbon-deposited binder-free CoMoO<sub>4</sub>/Ni foam catalyst after DRR: FE-SEM images (A–D) and HR-TEM (E–H) at different magnifications suggest that carbon nanotubes (CNTs) at the diameter of ~20 nm have been deposited over the catalyst, Inset of G and H, SAED pattern of CoMoO<sub>4</sub> and CNT respectively.

It reveals that the deposited carbon is in the form of tube like nature and the plate like nature of the CoMoO<sub>4</sub> was sintered into the bulk particles. In order to confirm this, we have measured HR-TEM (**Figure 6.1.5 (e-h)**) images of the catalyst after DRR are presented at different magnifications. It again proved that the deposited carbon is in the form of tube like structure with the diameter of about 20 nm and the plate like arrays of CoMoO<sub>4</sub> was changed into the bulk particles. At the high magnification, when focusing on the edge of this particle, the plate like morphology of the CoMoO<sub>4</sub> has been observed even after high temperature DRR. However, compared to morphology of the catalyst

before DRR, the plate like arrays of  $\text{CoMoO}_4$  on Ni foam are agglomerated with each other after DRR due to high temperature sintering. Inset of **Figure 6.1.5 (g and h)** shows the corresponding selected area diffraction pattern of  $\text{CoMoO}_4$  and CNT respectively. The formation of tube like carbon during DRR is well reported [16]. The excess carbon during syngas production which accumulates at the exposed faces is transported by surface diffusion over the peripheral surfaces of the particle to form the skin of the filament [43]. It leads to the deposited carbon is in the form of carbon nanotubes (CNTs) over the catalyst. This might also be a reason for the deactivation of the catalyst [44, 45]. **Figure 6.1.6** shows the FE-SEM images of the bare Ni foam before and after DRR. After DRR, the surface of the bare Ni foam became more eruptions and cracks.

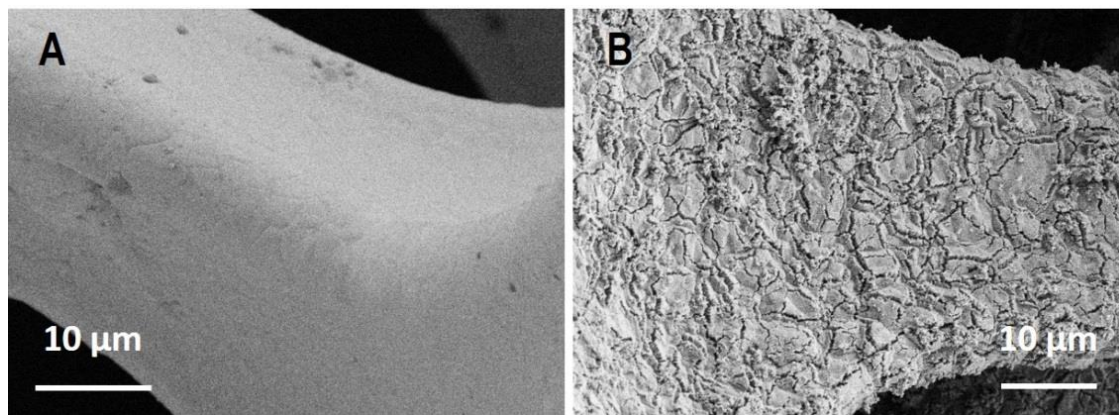


**Figure 6.1.6.** FE-SEM images of bare Ni foam, before DRR (A), after DRR (B).

**Figure 6.1.7 (a)** shows the XRD pattern of the catalyst after the DRR of propane. It indicates that there is no  $\text{CoMoO}_4/\text{Ni}$  foam because the carbon will deposit over the

catalyst. The small broad peak at  $26.2^\circ$  is ascribed to the presence of carbon over the catalyst [46].

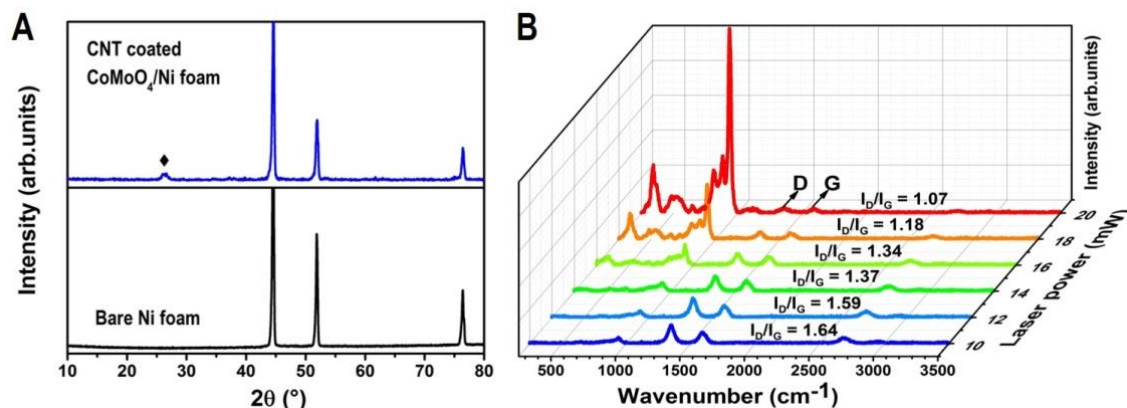


**Figure 6.1.7** Structural characterization of carbon-deposited binder-free  $\text{CoMoO}_4/\text{Ni}$  foam catalyst after DRR: the XRD pattern (A) and Raman spectrum of CNT-deposited catalyst after DRR at different laser powers at a laser wavelength of 514 nm. The laser power dependence was examined for samples exposed in air to examine both the bonding nature of metal-oxygen vibrations for  $\text{CoMoO}_4/\text{Ni}$  foam and the D/G bands for the CNT (B).

When compared with bare Ni foam, the carbon-deposited catalyst shows less intensity peaks because the catalyst was treated at high temperature for a long time, leading to sintering of the catalyst. In order to determine the presence of  $\text{CoMoO}_4/\text{Ni}$  foam catalyst, we have performed Raman spectroscopy using different laser powers. **Figure 6.1.7 (b)** shows the Raman spectrum of CNT-deposited catalyst at different laser powers (from 10 to 20 mW). Three major bands were observed between 1,000 to 3,500  $\text{cm}^{-1}$ , which are related to the presence of CNT over the catalyst. The first band, at 1,348  $\text{cm}^{-1}$  is the D band and is attributable to a loss of translational symmetry and small imperfections. The band at 1,585  $\text{cm}^{-1}$ , or the G band, is a typical graphite mode, and it

is related to  $sp^2$  vibrations in two dimensions from carbon atoms in the hexagonal network. A third band at  $2,679\text{ cm}^{-1}$ , called the  $G'$  or 2D band, is a second-order Raman mode [47, 48]. The small band at  $936\text{ cm}^{-1}$  is attributable to the presence of  $\text{CoMoO}_4$ . As seen from the spectrum, with increasing laser power, the intensity of the D and G peaks also decreases. It may be that increases in laser power induce corresponding increases in the temperatures of the CNTs, resulting in the decreased intensities. A decrease in the  $I_D/I_G$  ratio is observed with increasing laser power from 10 to 20 mW, and at the maximum laser power, D and G bands were diminished which is due to the heating effect. On the other hand, at high laser power, the stretching vibrations between the metal and oxygen bands in the  $\text{CoMoO}_4$  become predominant in the Raman spectrum [49, 50]. The bands less than  $1,000\text{ cm}^{-1}$  are sharper with increasing laser power from 10 to 20 mW, suggesting that less laser power is insufficient for stretching vibrations between metal and oxygen bonds. The bands at  $928$ ,  $803$ ,  $478\text{ cm}^{-1}$  and  $335\text{ cm}^{-1}$  which corresponds to the Mo-O bond (symmetric stretching), O-Mo-O bond (asymmetric stretching), Co-O bond (stretching vibration) and Co-O-Mo bond (symmetric stretching) respectively [37].

Furthermore, X-ray photoelectron spectroscopy (XPS) was used to analyze the chemical composition of the carbon-deposited  $\text{CoMoO}_4/\text{Ni}$  foam; the results are presented in the figures (see **Figure 6.1.8 (a-f)**). The wide scan surface survey is shown in **Figure 6.1.8 a**, which displays the presence of all the elements over the surface of the catalyst.

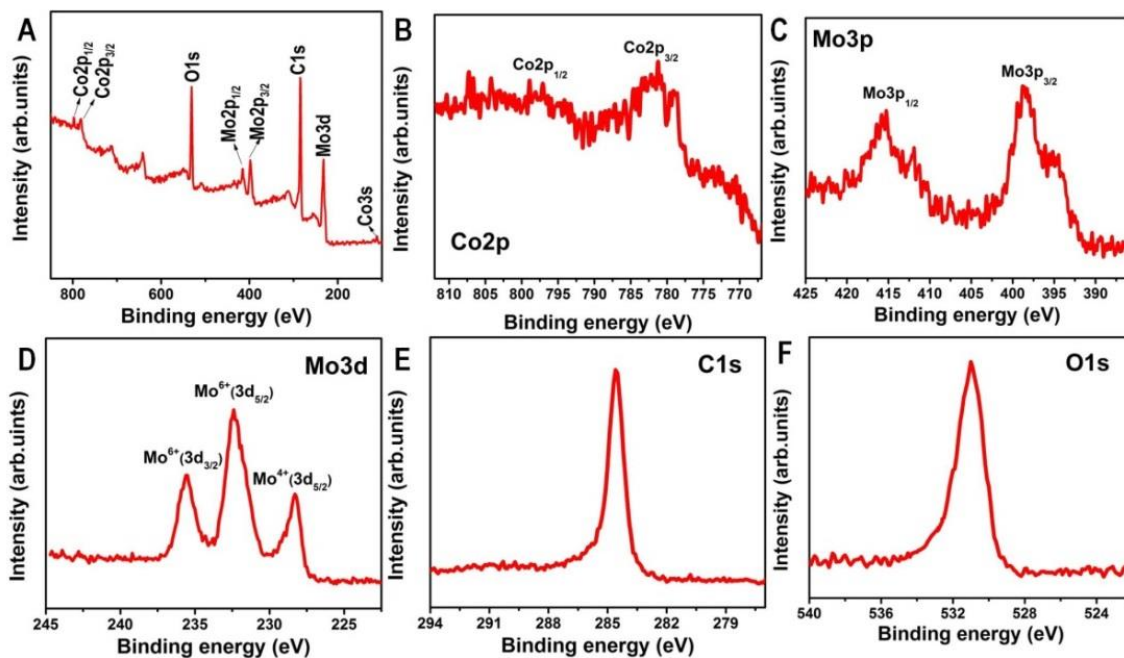


**Figure 6.1.8** XPS spectrum: survey spectrum (A), Co2p core-level spectrum (B), Mo3p core-level spectrum (C), Mo3d core-level spectrum, C1s core-level spectrum (E), O1s core-level spectrum of CNT deposited CoMoO<sub>4</sub> on Ni foam after DRR.

**Figure 6.1.8 b** shows the appearance of two peaks at binding energies of 797.5 eV and 782 eV, corresponding to the core-level spectra of Co2p<sub>1/2</sub> and Co2p<sub>3/2</sub>, respectively, which is characteristic of Co<sup>2+</sup>. **Figure 6.1.8 c** shows the Mo3p peak core-level spectrum. The peaks at 232.4 eV and 235.6 eV in **Figure 6.1.8 d** are attributable to Mo<sup>6+</sup> 3d<sub>5/2</sub> and Mo<sup>6+</sup> 3d<sub>3/2</sub>, respectively. The low-energy peak at 228.3 eV can be assigned to Mo<sup>4+</sup> 3d<sub>5/2</sub>. **Figure 6.1.8 e and f** shows the C1s and O1s core level spectra at 284.6 eV and 530.9 eV, respectively [51, 52]. As a comparison, the XRD and Raman spectrum for CoMoO<sub>4</sub>/Ni foam catalyst under similar condition of DRR without the propane and CO<sub>2</sub> feed gas are provided in **Figure 6.1.9**. XRD pattern from **Figure 6.1.9 A** shows that the presence of well-defined CoMoO<sub>4</sub> peaks at the angle of 26.2° which corresponds to the

(002) plane. Compared to **Figure 6.1.7 A**, the well-defined peaks were observed which is due to there is no formation of carbon over the catalyst since propane and CO<sub>2</sub> gases were not feeded.

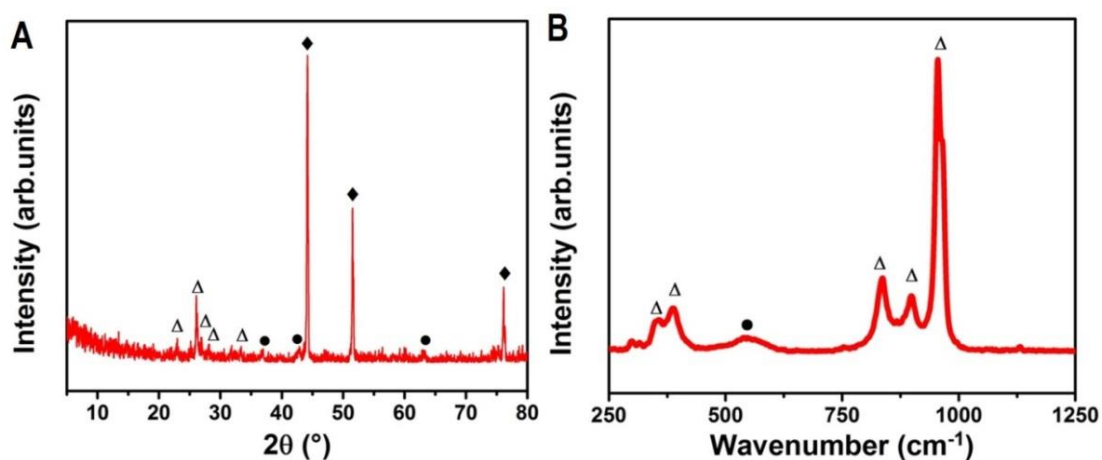


**Figure 6.1.9** XRD pattern (A) and Raman spectrum (B) of CoMoO<sub>4</sub>/Ni foam after treated at 630 °C for 24 h. (Δ – CoMoO<sub>4</sub>, ◆ – Ni foam, ● – NiO)

The presence of slight NiO was observed due to the high temperature treatment which clearly resembles with the Raman spectrum as shown in **Figure 6.1.9 B**.

**Figure 6.1.10** presents an overall view of the focus of this work. Briefly, binder-free CoMoO<sub>4</sub> nanostructures were grown directly on nickel foam by a hydrothermal method using cobalt nitrate and sodium molybdate as precursors, as reported previously [36]. This binder-free CoMoO<sub>4</sub>/Ni foam has been used as a catalyst for the DRR of propane and CO<sub>2</sub>. During DRR, propane reacts with CO<sub>2</sub> to generate synthesis gas. Additionally, carbon is deposited on the catalyst over time. This carbon-deposited

catalyst can then be used directly as a positive electrode for supercapacitor applications, where an rGO is used as the negative electrode.

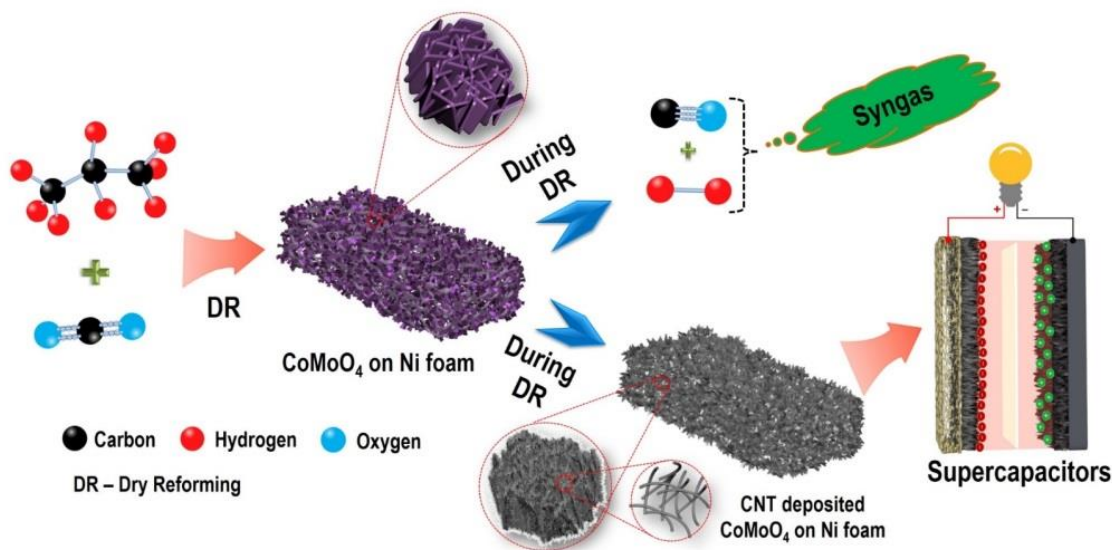


**Figure 6.1.10** Schematic annotation of this work. The binder-free CoMoO<sub>4</sub>/Ni foam was used as a catalyst for the dry reforming reaction (DRR) of propane with carbon dioxide (CO<sub>2</sub>). During the DRR, propane reacts with CO<sub>2</sub> to generate synthesis gas (CO + H<sub>2</sub>) in the presence of the catalyst. In addition, carbon becomes deposited over the catalyst over time. This carbon-deposited catalyst was further used as a positive electrode for supercapacitor applications.

#### 6.3.4. Electrochemical characterization

To utilize this CNT-deposited CoMoO<sub>4</sub>/Ni foam, the electrochemical performances of CNT-deposited CoMoO<sub>4</sub> NPAs were assessed by cyclic voltammogram (CV) and galvanostatic charge–discharge (GCD) measurements. **Figure 6.1.11** shows the electrochemical performances of CNT-deposited CoMoO<sub>4</sub> NPAs using 2 M KOH as

the electrolyte solution. Cyclic voltammograms (CVs) were recorded in the potential range between -0.1 and 0.5 V at different scan rates of 5–100  $\text{mV s}^{-1}$  (Figure 6.1.11 A).

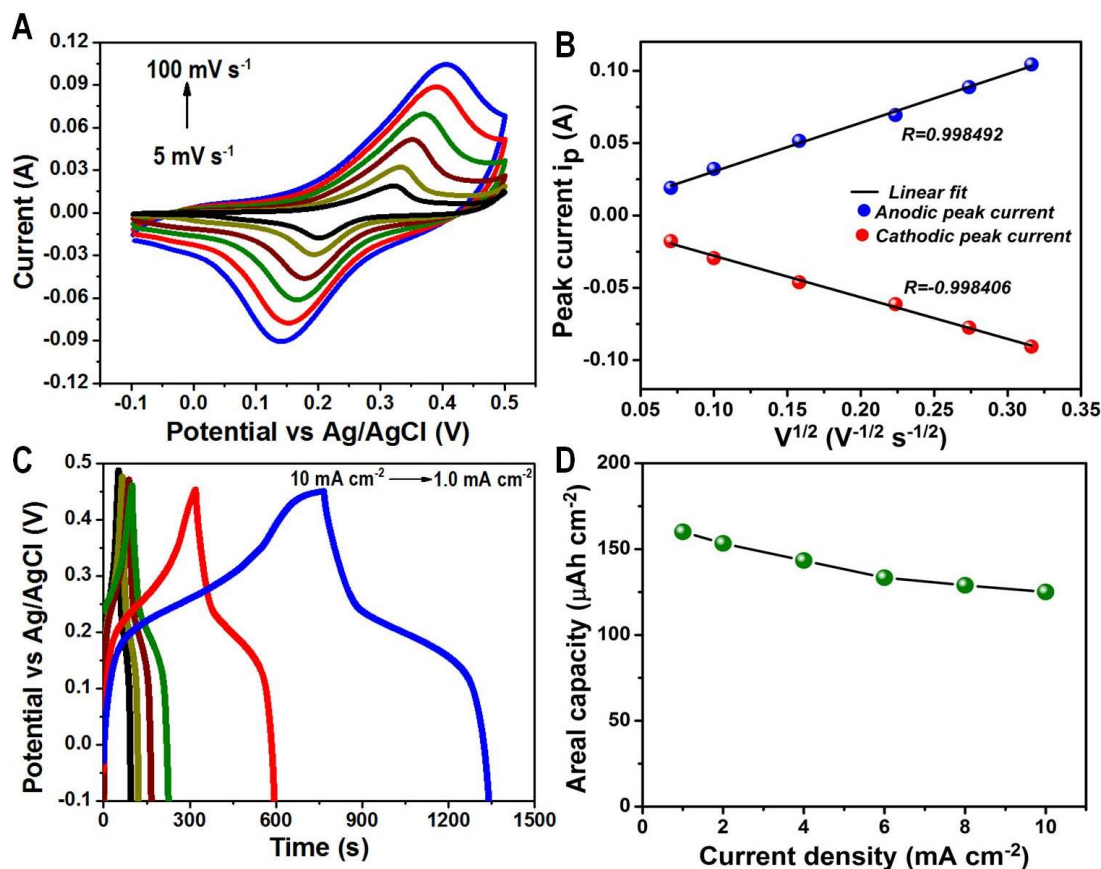


**Figure 6.1.11** Electrochemical performances of CNT-deposited binder-free  $\text{CoMoO}_4/\text{Ni}$  foam catalyst in three electrode systems: cyclic voltammetry curves (CVs) at different scan rates (5–100  $\text{mV s}^{-1}$ ) (A), square root of the scan rates versus charge and discharge peak current (B), galvanostatic charge-discharge (GCD) curves at different current densities (1–10  $\text{mA cm}^{-2}$ ) (C), and comparison of areal capacity with respect to various current densities (D).

A pair of strong reduction/oxidation peaks was observed in the CV curves, suggesting that the capacitive characteristics are governed by Faradic redox reactions. The nature of the CV curves is not significantly controlled by increasing the scan rate,

which is attributable to enhanced mass transportation and electron conduction in the host materials [53]. Moreover, the anodic and cathodic peaks shift to higher and lower potentials at higher and lower scan rates, respectively. This may be due to the effect of electro kinetics on peak shape and peak separation (that is, the quasi-reversible nature of the electrode). As shown in **Figure 6.1.11 B**, the peak current ( $I_p$ ) of a diffusion-controlled reversible reaction increased with increasing scan rates. The peak current follows the Randles-Sevcik equation [54]:  $I_p = (2.687 \times 10^5) n^{3/2} ACD^{1/2} v^{1/2}$ , where  $n$  is the number of electrons transferred in the redox reaction,  $A$  is the effective electrode area in  $\text{cm}^2$ ,  $C$  is the concentration in  $\text{mol cm}^{-3}$ ,  $D$  is the diffusion coefficient in  $\text{cm}^2 \text{s}^{-1}$ , and  $v$  is the scan rate. Using the above equation, the calculated diffusion coefficient of the CNT-deposited  $\text{CoMoO}_4/\text{Ni}$  foam electrode was found to be  $3.42 \times 10^{-7} \text{ cm}^2 \text{ s}^{-1}$ . GCD measurements were further performed in the voltage range between -0.1 and 0.45 V at various current densities to estimate the charge storage behavior of the electrode materials. **Figure 6.1.11 C** shows the GCD curves of CNT-deposited  $\text{CoMoO}_4$  NPAs collected at different current densities of 1–10  $\text{mA cm}^{-2}$ . When decreasing the current density, the discharge time was increased and it might be due to that there is more time available for the electrolyte ions to access the active electrode material. A maximum areal capacity of  $160 \mu\text{Ah cm}^{-2}$  was achieved from GCD analysis for CNT deposited  $\text{CoMoO}_4/\text{Ni}$  foam at a current density of  $1 \text{ mA cm}^{-2}$  (**Figure 6.1.11 D**). This areal capacity was maintained up to  $125 \mu\text{Ah cm}^{-2}$ , even at a higher current density of

10 mA cm<sup>-2</sup>. About 78% of the areal capacity was retained at even 10-fold higher scan rates, suggesting the excellent rate capability of the electrode material.

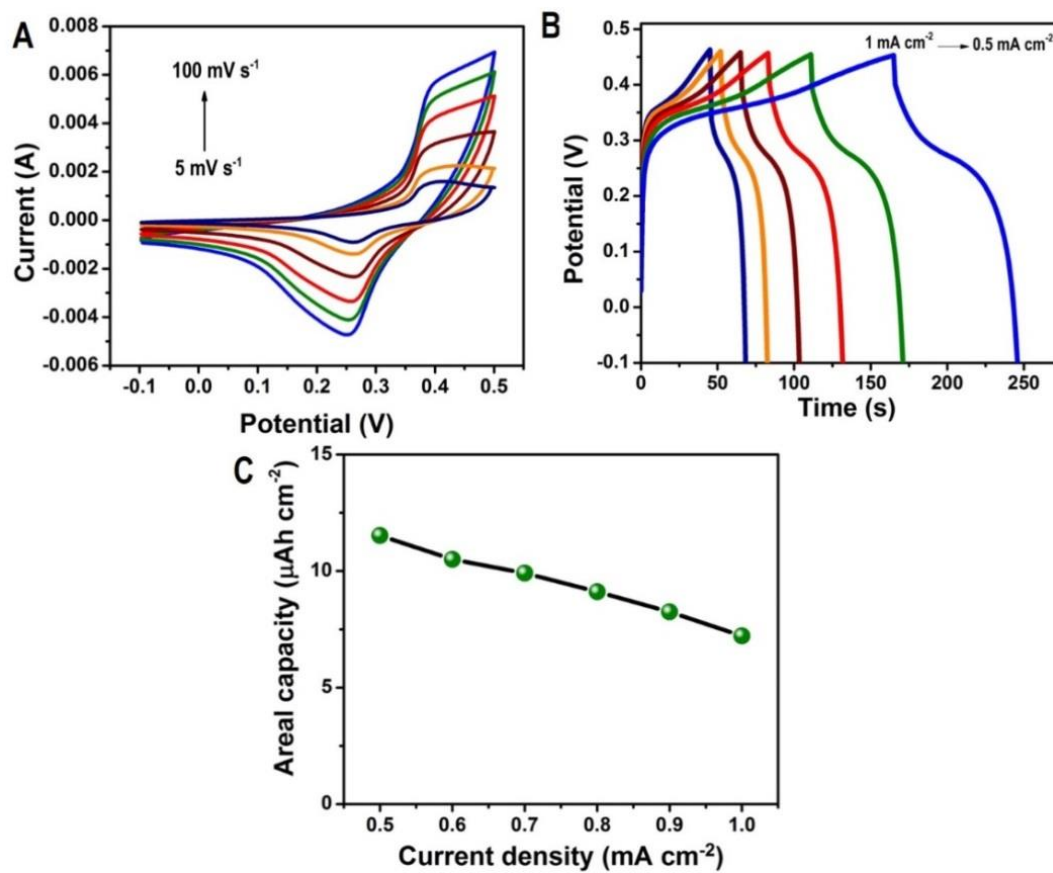


**Figure 6.1.12** CV curve at the different scan rates (A), GCD curves (B), areal capacities with respect current densities (C) of CoMoO<sub>4</sub>/Ni foam after treated at 630 °C for 24 h without propane and CO<sub>2</sub>.

For comparison, heat-treated CoMoO<sub>4</sub> NPAs on Ni foam (without the flow of C<sub>3</sub>H<sub>8</sub> and CO<sub>2</sub>) were tested and are presented in **Figure 6.1.12**. The areal capacity of 7.2 μAh cm<sup>-2</sup> was achieved at a current density of 1 mA cm<sup>-2</sup>. Beneficially, the CNT-deposited CoMoO<sub>4</sub> NPAs on Ni foam showed 22-fold higher performance than the heat-

treated  $\text{CoMoO}_4$  NPAs on Ni foam. **Figure 6.1.13** shows the cyclic stability of CNT deposited  $\text{CoMoO}_4$  electrode for 3000 cycles using GCD analysis. In the initial 200 continuous cycles, the capacity of carbon deposited  $\text{CoMoO}_4/\text{Ni}$  foam has been gradually increased upto  $\sim 111\%$  and stabilized afterwards. At the end of the 3000 continuous cycles,  $\sim 105\%$  of the initial capacity has been retained which suggesting the excellent electrochemical stability of the prepared material.

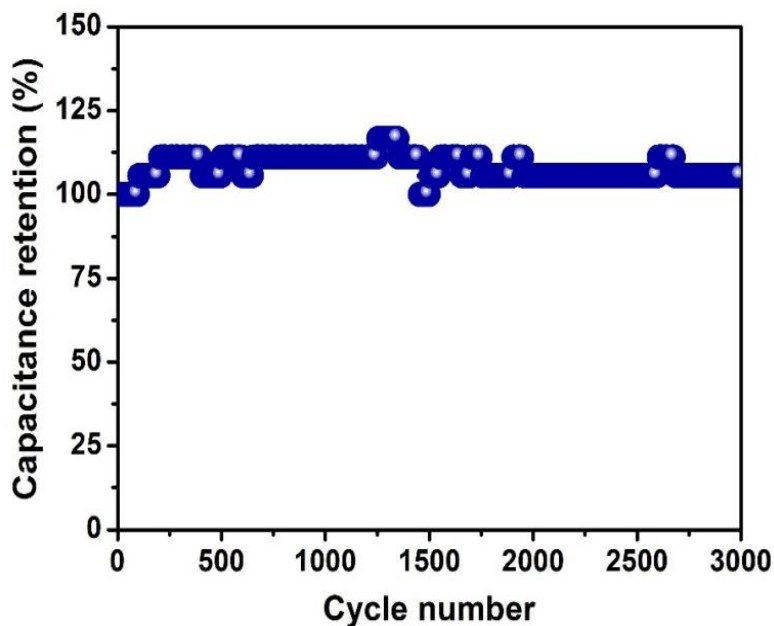


**Figure 6.1.13** Cyclic stability test for CNT deposited  $\text{CoMoO}_4/\text{Ni}$  foam for 3000 cycles using GCD measurement.

Generally, the cycling life of these binder free electrodes consists of three processes; an activation period, steady state, and degradation period [55]. Only a few portions of material is active in initial few cycles, while the rest is not activated. As the electrolyte ions gradually penetrate into the electrode material, more and more electrode

portions are activated and contributed to the increase in nature. The improved performances of CNT-deposited CoMoO<sub>4</sub> NPAs on Ni foam may be explained as follows: the presence of CNTs on the surface of CoMoO<sub>4</sub> NPAs increases the conductivity of the electrode, promotes the ion transport kinetics, and facilitates the controlled diffusion of electrolyte ions on to the electro-active surface compared with the bare CoMoO<sub>4</sub> NPAs/Ni foam, thereby results in better electrochemical performances. The higher areal capacity obtained was attributed to the benefit of CNT-deposited CoMoO<sub>4</sub> NPAs formed on Ni foam without addition of a polymer binder, and also to the presence of carbon, which can dramatically decrease the contact resistance in the prepared electrode material.

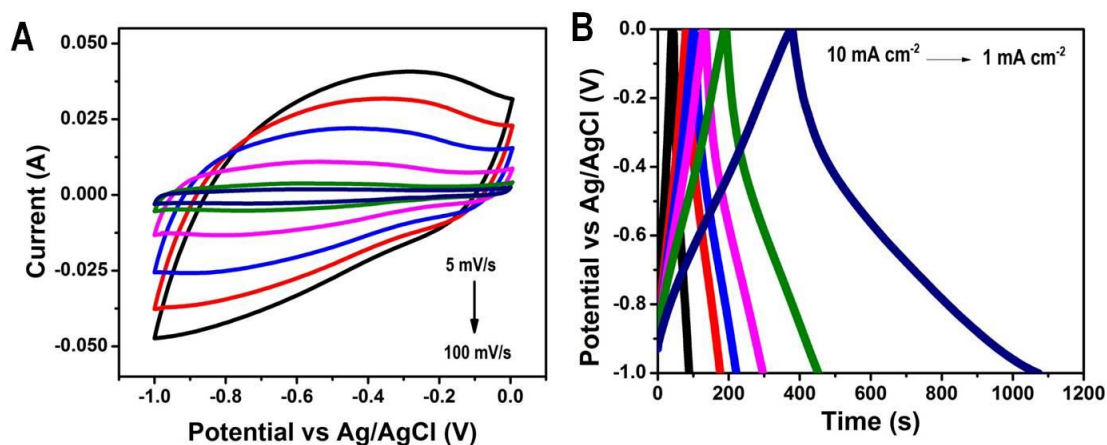


**Figure 6.1.14** Cyclic voltammery curves at the different scan rates (A), galvanostatic charge discharge analysis at the different current densities (B).

The negative electrodes used in this study were rGO on carbon cloth electrode; their electrochemical performances were investigated under the same. **Figure 6.1.14 A**

shows the CV curves for the prepared rGO nanosheets on carbon cloth (CC) at various scan rates (5–100  $\text{mVs}^{-1}$ ). It shows a well-maintained rectangular behavior, suggesting the electrochemical double-layer capacitance of graphene. A GCD study (**Figure 6.1.14 B**) was performed at various current densities (1–10  $\text{mA cm}^{-2}$ ). All of the charge and discharge curves were linear and symmetric in nature, further confirming the capacitive behavior of the electrode. The maximum specific capacitance of 191.56  $\text{F/g}$  was achieved at a current density of 1  $\text{mA cm}^{-2}$  for rGO coated on the CC electrode using the KOH electrolyte.

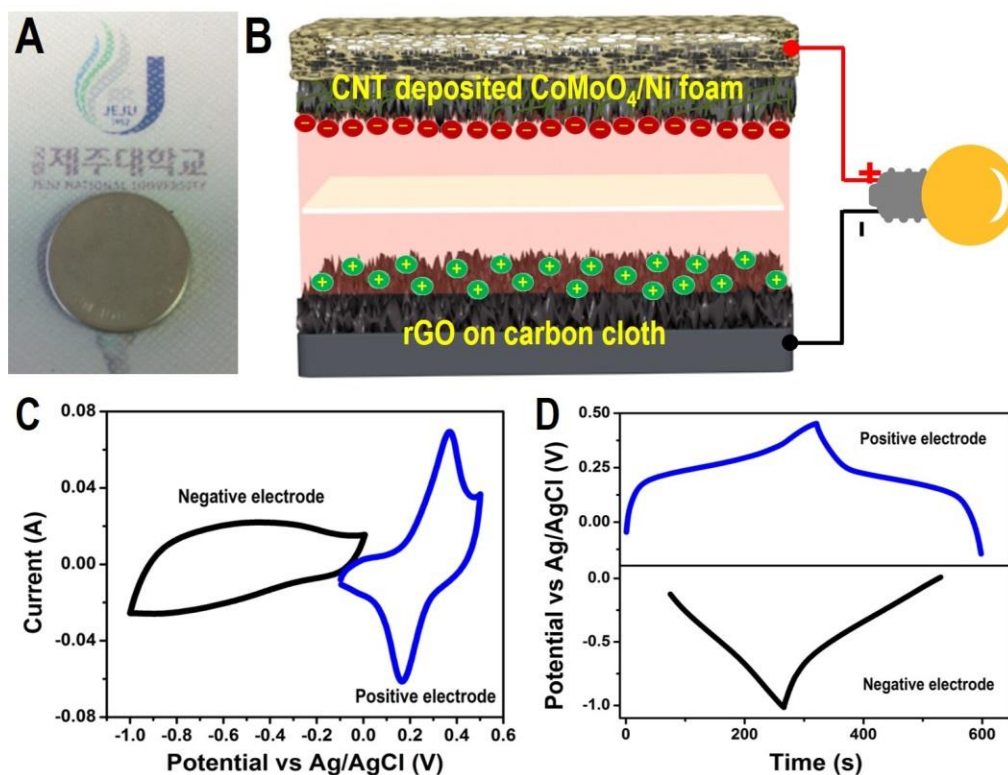


**Figure 6.1.15** Fabricated asymmetric supercapacitor: photographic image of a fabricated coin cell-type device (A), schematic representation of the fabricated asymmetric supercapacitor in the charged state; the device consists of CNT-deposited  $\text{CoMoO}_4/\text{Ni}$

foam as the positive electrode, reduced graphene oxide (rGO)-coated carbon cloth (CC) as the negative electrode, a separator, and electrolyte solution (B), comparison of CV curves at a scan rate of  $50 \text{ mVs}^{-1}$  (C), comparison of charge-discharge curves at a current density of  $2 \text{ mA cm}^{-2}$  (D) for the positive and negative electrodes.

Photographic images of the fabricated coin-cell type device and a schematic representation of the fabricated asymmetric supercapacitor are shown in **Figure 6.1.15 A and B**, respectively. For a comparison of positive and negative working voltage windows of CNT-deposited  $\text{CoMoO}_4$  NPAs on Ni foam and rGO nanosheets, respectively, we show the CV and GCD curves at  $50 \text{ mV s}^{-1}$  (**Figure 6.1.15 C**) and  $2 \text{ mA cm}^{-2}$  (**Figure 6.1.15 D**).

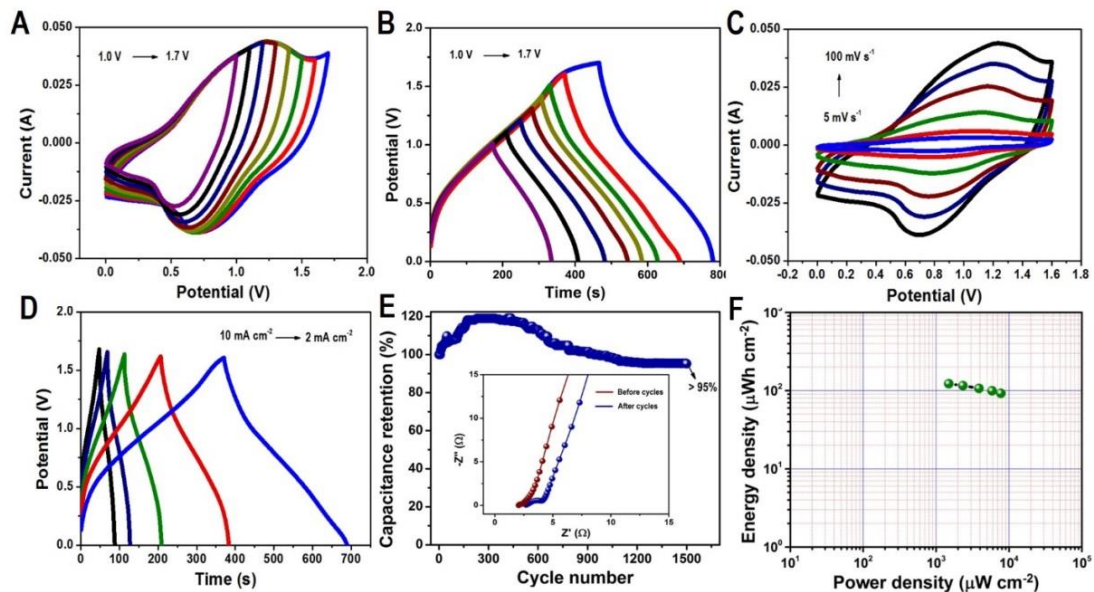


**Figure 6.1.16** Electrochemical performance of an asymmetric supercapacitor: CV curves at different potential windows (at a scan rate of  $100 \text{ mVs}^{-1}$ ) (A), GCD curves at different potential windows (at a current density of  $2 \text{ mA cm}^{-2}$ ) (B), CV curves at a  $1.6 \text{ V}$  potential window (at different scan rates from  $5$  to  $100 \text{ mVs}^{-1}$ ) (C), and GCD curves at the  $1.6 \text{ V}$  potential window (at different current densities from  $2$  to  $10 \text{ mA cm}^{-2}$ ) (D), cyclic stability over many cycles (E), Nyquist plot of before and after cyclic study

(inset in E), Ragone plot of energy density vs. power density (F), for the fabricated CNT-deposited CoMoO<sub>4</sub>/Ni foam // rGO asymmetric supercapacitors.

To ensure the equal charges of the both positive and negative electrode, the mass of the electrodes are balanced using the equation (6). As shown in **Figure 6.1.16 A and B**, the fabricated asymmetric supercapacitor was checked initially at different potential levels from 0.5 V to 1.7 V to ascertain the potential operating window. It suggested the optimal operating potential of the fabricated device is about 1.6 V without any signs of evolution. **Figure 6.1.16 C** shows the CV curves of the supercapacitor device at different scan rates (5–100 mV s<sup>-1</sup>). The fabricated asymmetric supercapacitor exhibited better capacitive behavior with quasi-rectangular CV curves. The shape of the CV curves was maintained well even at the high scan rates, suggesting a good rate capability of the device. To further evaluate the performance of the device, a GCD analysis was performed. **Figure 6.1.16 D** shows the GCD curves at different current densities, measured from 2–10 mA cm<sup>-2</sup>. It can be seen that the fabricated asymmetric device exhibits nearly linear and symmetric behavior with a quick I-V response, consistent with the CV curves. To determine the electrochemical capacitive properties, we performed cyclic stability tests of the fabricated asymmetric supercapacitor device. **Figure 6.1.16 E** shows the cyclic stability of the fabricated asymmetric supercapacitors using GCD analysis at a current density of 25 mA cm<sup>-2</sup>. The increasing nature of the stability study during the initial cycles is due to the initial activation process of the device, which stabilized thereafter [56]. Even after 1,500 continuous cycles, more than 95% of its initial capacitance was maintained, suggesting excellent stability. The inset in **Figure**

**6.1.16 E** shows a Nyquist plot in the frequency range of 0.01 Hz to  $10^5$  Hz in the open circuit potential before and after cycles. It shows common features in both curves: a small semi-circle at the higher frequency, a second, larger capacitive loop at the lower frequency, and a straight line in the middle frequency part, related to diffusion [35]. The solution and charge transfer resistance increased slightly after many cycles, which may be due to a slight loss of capacitance in cyclic stability. Using equations 7 and 8, the calculated areal energy and power density are shown in a Ragone plot in **Figure 6.1.16 F**. The fabricated device stored a maximum areal energy density of  $122 \mu\text{Wh cm}^{-2}$  ( $29.04 \text{ Wh kg}^{-1}$ ) at  $2 \text{ mA cm}^{-2}$  and delivered a high power density of  $7,727 \mu\text{W cm}^{-2}$  ( $1835 \text{ W kg}^{-1}$ )  $10 \text{ mA cm}^{-2}$ . The energy density decreased from  $122 \mu\text{Wh cm}^{-2}$  ( $29.04 \text{ Wh kg}^{-1}$ ) to  $92 \mu\text{Wh cm}^{-2}$  ( $21.92 \text{ Wh kg}^{-1}$ ) while the power density increased from  $1,492 \mu\text{W cm}^{-2}$  ( $354.5 \text{ W kg}^{-1}$ ) to  $7,727 \mu\text{W cm}^{-2}$  ( $1835 \text{ W kg}^{-1}$ ) at current densities of 2–10  $\text{mA cm}^{-2}$ . This high energy density of our device is better than those of some the recent hybrid supercapacitors such as  $\text{ZnCo}_2\text{O}_4@ \text{Ni}_x\text{Co}_{2x}(\text{OH})_{6x} // \text{Activated carbon}$  ( $26.04 \text{ Wh kg}^{-1}$ ) [57],  $\text{NiCo}_2\text{S}_4 // \text{porous carbon}$  ( $22.8 \text{ Wh kg}^{-1}$ ) [58], carbon  $\text{Ni} @ \text{Ni}(\text{OH})_2 // \text{Activated carbon}$  ( $21.8 \text{ Wh kg}^{-1}$ ) [59],  $\text{GF-CNT} @ \text{NiO} // \text{G-CNT}$  ( $23.4 \text{ Wh kg}^{-1}$ ) [60],  $\text{CO}_3\text{O}_4\text{-Ni foam} // \text{Carbon aerogel}$  ( $17.9 \text{ Wh kg}^{-1}$ ) [61], also comparable with the recent reports such as  $\text{CC/graphitic petals} // \text{Ni-Co-Mn hydroxides CC/graphitic petals}$  ( $30 \text{ Wh kg}^{-1}$ ) [62],  $3\text{D Co}_3\text{O}_4/\text{Ni foam} // \text{graphene hydrogel}$  ( $31 \text{ Wh kg}^{-1}$ ) [63]. In addition, it is higher than the other asymmetric supercapacitors such as acetylene black decorated  $\text{NiCo}_2\text{S}_4 // \text{Activated carbon hybrid supercapacitor}$  ( $24.7 \text{ Wh kg}^{-1}$ ) [64],

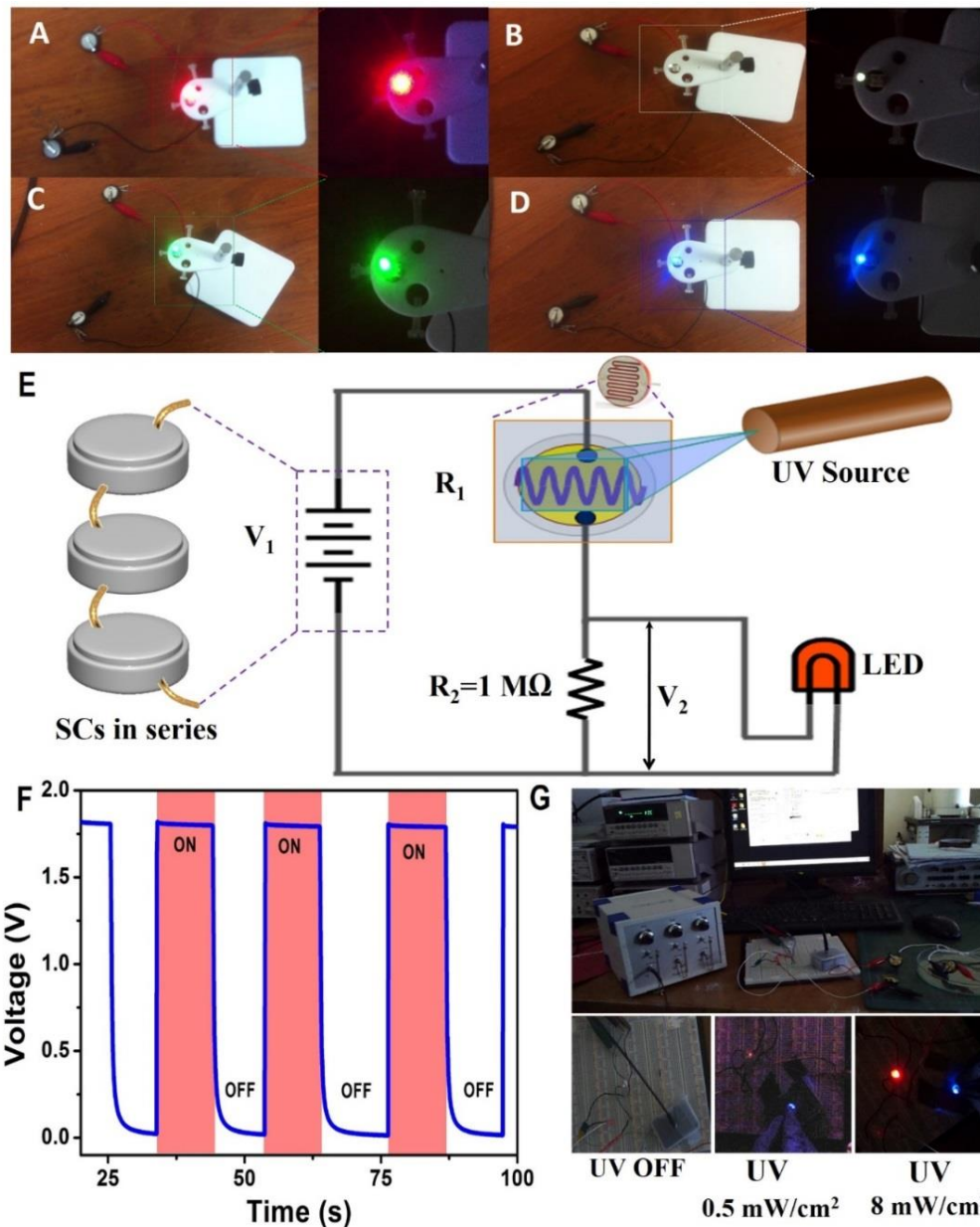


**Figure 6.1.17** Demonstration of driving low power electronic devices for switching applications: series connection of fabricated supercapacitor devices could power up the red (A), white (B), green (C), and blue (D) LEDs, driving a UV light sensor circuit for detection in dark environments (E), switching response of UV photodetector in ON and OFF conditions ( $\lambda=365\text{ nm}$ ) (F), optical photograph of UV light sensor triggering red LED under various illumination intensities,  $0.5\text{ mW cm}^{-2}$  and  $8\text{ mW cm}^{-2}$ , along with fabricated supercapacitors (G).

CoMoO<sub>4</sub> -NiMoO<sub>4</sub>.xH<sub>2</sub>O//Activated carbon (25 Wh kg<sup>-1</sup>) [66], NiCoMnO<sub>4</sub>//rGO supercapacitor (20 Wh kg<sup>-1</sup>) [67], MoO<sub>3</sub>/Activated carbon (16.75 Wh kg<sup>-1</sup>) [68]. Moreover, we demonstrated successfully the fabricated coin-cell type; two serially connected asymmetric devices were able to light up different types of light-emitting diodes, such as red, green, white, and blue LEDs, as presented in **Figure 6.1.17**, respectively.

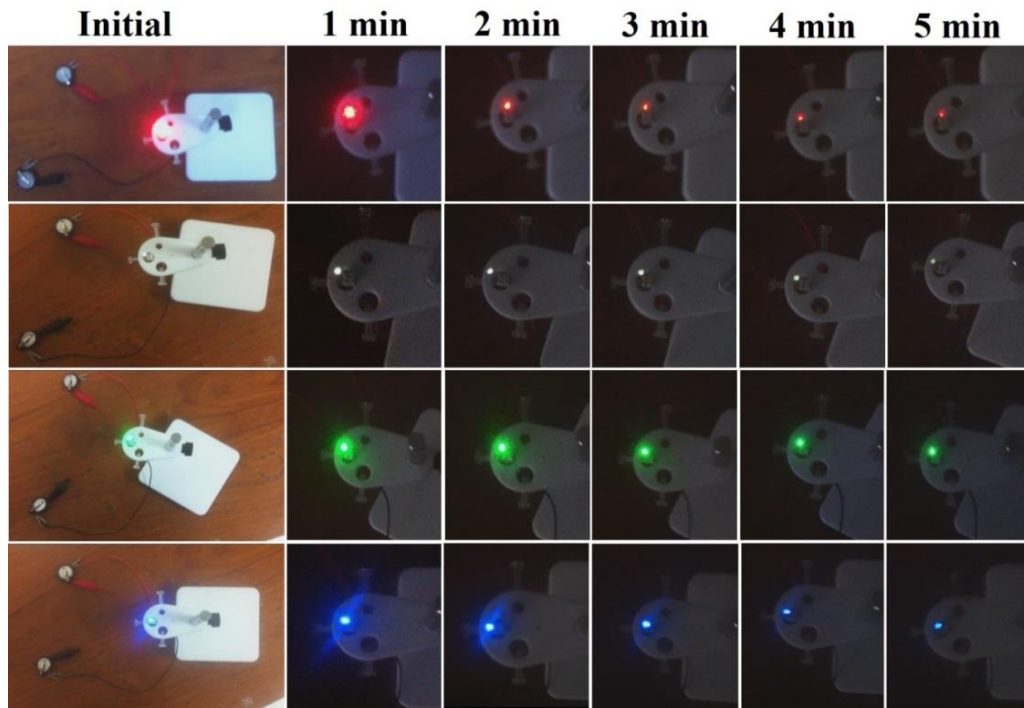


**Figure 6.1.18** Photographic images of various LEDs at the different time intervals of two serially connected asymmetric supercapacitors.

The intensity of each glowing LED for different intervals is shown in supplementary **Figure 6.1.18**. Additionally, we demonstrated that the three-series connection of fabricated asymmetric supercapacitor devices was an effective power

supply to drive UV light sensors for switching and proximity applications, as shown in **Figure 6.1.17 E -G**. The circuit is analogous to a voltage divider circuit having a power supply, two resistances, such as variable resistance  $R_1 \approx 100 \text{ K}\Omega$  to  $100 \text{ M}\Omega$  (cadmium sulfide photo resistor) with respect to the UV light source, and a fixed small resistance  $R_2 \approx 1 \text{ M}\Omega$  along with a red LED. Initially, the red LED is OFF even though the input voltage from the fabricated supercapacitor is sufficient to drive the LED, because the high resistance terminal  $R_1 (\geq 100 \text{ M}\Omega)$  acts as an open circuit under the UV OFF condition. During the UV ON condition ( $8 \text{ mW cm}^{-2}$ ), the resistance  $R_1$  becomes low, such that it can act as a closed path terminal and allows input voltage to the fixed resistance  $R_2$ ; correspondingly, the red LED will light up with high intensity, as shown in **Figure 6.1.17 G**. The experimental demonstration indicated that the fabricated supercapacitor was an excellent power source for switching applications to detect dark environments.

#### 6.4. Conclusion

In summary, we have successfully initiated a novel approach involving use of the disposable carbon-deposited catalyst formed during DRR for supercapacitor applications. Hydrothermally synthesized  $\text{CoMoO}_4/\text{Ni}$  foam has been used to propane DRR to form SNG. The porous nature of the  $\text{CoMoO}_4/\text{Ni}$  foam catalyst exhibited excellent conversion efficiency and SNG production with low mass loading. The inevitable reaction of DRR is the carbon formation over the catalyst in the form of

nanotube which limited the performance of the catalyst. We have successfully utilized this CNT deposited catalyst for supercapacitor applications instead forming CO<sub>2</sub> gas or trashing. The prepared CNT deposited CoMoO<sub>4</sub>/Ni foam electrode shows high specific capacity and excellent cyclic stability. The fabricated asymmetric CNT deposited CoMoO<sub>4</sub>/Ni foam//rGO/CC supercapacitor shows excellent electrochemical performances in terms of specific capacity and energy density. In addition, the fabricated device powered up the various LEDs and UV light sensors suggested its potential use for supercapacitor applications. Overall, this study demonstrated the following important aspects: (i) although the deposition of carbon during DRR diminished the catalyst performance, there is no need to reactivate the catalyst by forming CO<sub>2</sub> gas, which increases global warming, and no need to dispose of the catalyst after it becomes carbon-deposited; (ii) use of the binder-free catalyst for SNG production and the binder-free electrode for supercapacitors will enhance the reactive sites on the surface, leading to excellent catalytic performance and electrochemical performance, respectively; and (iii) even after SNG production, the carbon-deposited catalyst can be used effectively for other energy storage applications, such as batteries, fuel cells and so on.

## 6.5. References

1. T. R. Karl, K. E. Trenberth, *Science*, **2003**, 302, 1719.
2. M. Z. Jacobson, *Energy Environ. Sci.*, **2009**, 2, 148.

3. On Solar Hydrogen & Nanotechnology, (Ed: L. Vayssieres), John Wiley and Sons, Weinheim, Germany **2009**.
4. G. Sneddon, A. Greenaway, Humphrey H.P. Yiu, *Adv. Energy Mater.* **2014**, 4, 1301873.
5. D. Pakhare, J. Spivey, *Chem Soc Rev*, 2014, **43**, 7813-7837
6. M. Maestri, D. G. Vlachos, A. Beretta, G. Groppi and E. Tronconi, *AIChE J.*, 2009, 55, 993–1008
7. M. He, Y. Sun and B. Han, *Angew. Chem., Int. Ed.*, 2013, 52, 9620–9633;
8. T. V. Choudhary and V. R. Choudhary, *Angew. Chem., Int. Ed.*, 2008, 47, 1828–1847.
9. M. E. S. Hegarty, A. M. O'Connor, J. R. H. Ross, *Catal. Today*, 1998, 42, 225–232
10. Bin Hua, Ning Yan, Meng Li, Yi-Fei Sun, Jian Chen, Ya-Qian Zhang, Jian Li, Thomas Etsell, Partha Sarkar and Jing-Li Luo, *J. Mater. Chem. A.* **2016**, DOI: 10.1039/C6TA02809H
11. M. C. J. Bradford, M. A. Vannice, *Appl Catal., A*, **1996**, 142, 73.
12. M. C. J. Bradford, M. A. Vannice, *Catal Rev*, **1999**, 41, 1.
13. L. Pino, A. Vita, F. Cipiti, M. Laganà, V. Recupero, *Appl Catal., A*, **2006**, 306, 68.
14. B. Silberova, H. J. Venvik, J. C. Walmsley, A. Holmen, *Catal. Today*, **2005**, 100, 457.
15. N. Laosiripojana, S. Assabumrungrat, *J. Power Sources*, **2006**, 158, 1348.
16. D. Pakhare, J. Spivey, *Chem Soc Rev*, 2014, 43, 7813-7837

17. B. Hua, N. Yan, M. Li, Y.F. Sun, J. Chen, Y.Q. Zhang, J. Li, T. Etsell, P. Sarkar, J. L. Luo, *J. Mater. Chem.* DOI: 10.1039/C6TA02809H
18. B. Pawelec, S. Damyanova, K. Arishtirova, J. L. G. Fierro, L. Petrov, *Appl Catal., A*, **2007**, 323, 188.
19. N. Sahli, C. Petit, A. C. Roger, A. Kiennemann, S. Libs, M. M. Bettahar, *Catal. Today*, **2006**, 113, 187.
20. J. Zhang, H. Wang, A. K. Dalai, *J. Catal.*, **2007**, 249, 300.
21. J. Sehested, J. A. P. Gelten, I. N. Remediakis, H. Bengaard, J. K. Nørskov, *J. Catal.*, **2004**, 223, 432.
22. L. B. Råberg, M. B. Jensen, U. Olsbye, C. Daniel, S. Haag, C. Mirodatos, A. O. Sjøstad, *J. Catal.*, **2007**, 249, 250.
23. F. M. Althenayan, S. Yei Foo, E. M. Kennedy, B. Z. Dlugogorski, A. A. Adesina, *Chem. Eng. Sci.*, **2010**, 65, 66.
24. A. Siahvashi, D. Chesterfield, A. A. Adesina, *Chem. Eng. Sci.*, **2013**, 93, 313.
25. J. Karupiah, Y. S. Mok, *Int J Hydrogen Energy*, **2014**, 39, 16329.
26. L. Zhang, X. Zhao, W. Ma, M. Wu, N. Qian, W. Lu, *CrystEngComm*, **2013**, 15, 1389.
27. Y. Tan, Q. Gao, C. Yang, K. Yang, W. Tian, L. Zhu, *Sci. Rep.*, **2015**, 5, 12382.
28. X. Yu, B. Lu, Z. Xu, *Adv.Mater.*, **2014**, 26, 1044.
29. Z. Zhang, J. Li, W. Gao, Y. Ma, Y. Qu, *J. Mater. Chem. A*, **2015**, 3, 18074.
30. L.Q. Mai, F. Yang, Y.L. Zhao, X. Xu, L. Xu, Y.Z. Luo, *Nat Comm*, **2011**, 2, 381.

31. M. Zhi, C. Xiang, J. Li, M. Li and N. Wu, *Nanoscale*, **2013**, 5, 72-88
32. J. Wu, P. Guo, R. Mi, X. Liu, H. Zhang, J. Mei, H. Liu, W. M. Lau, L. M. Liu, *J. Mater. Chem. A*, **2015**,3, 15331-15338
33. K. Xu, J. Chao, W. Li, Q. Liu, Z. Wang, X. Liu, R. Zou, J. Hu, *RSC Adv.*, **2014**, 4, 34307
34. Z. Xu, Z. Li, X. Tan, C. M. B. Holt, L. Zhang, B. S. Amirkhiz, D. Mitlin, *RSC Adv*, **2012**, 2, 2753–2755
35. X. Yu, B. Lu, Z. Xu, *Adv. Mater.* **2014**, 26, 1044–1051
36. G.K. Veerasubramani, K. Krishnamoorthy, S. J. Kim, *J. Power Sources*, **2016**, 306, 378.
37. R. Ramkumar and M. Minakshi, *Dalton Trans.*, **2015**, 44, 6158.
38. K.-S. Park, S.-D. Seo, H.-W. Shim, D.-W. Kim, *Nanoscale Res. Lett.*, **2012**, 7, 35.
39. L.-Q. Mai, F. Yang, Y.-L. Zhao, X. Xu, L. Xu, Y.-Z. Luo, *Nat. Commun*, **2011**, 2, 381.
40. A. Siahvashi, A. A. Adesina, *Catal. Today*, **2013**, 214, 30.
41. M.B. Jensen, L.B. Råberg, A.O. Sjøstad, U. Olsbye, *Catal. Today*,**2009**, 145, 114.
42. F. Solymosi, P. Tolmásov, T. S. Zakar, *J. Catal*, **2005**, 233, 51.
43. W.Y. Kim, Y.H. Lee, H. Park, Y.H. Choi, M.H. Lee, J.S. Lee, *Catal. Sci. Technol.*,**2016**,6, 2060.
44. R. E. Ruther, A. F. Callender, H. Zhou, S. K. Martha, J. Nanda, *J. Electrochem. Soc.*, **2015**, 162, A98.

45. H.-C. Chen, S.-F. Lin, K.-T. Huang, *Appl. Opt.*, **2014**, 53, A242.
46. C. Liang, L. Ding, C. Li, M. Pang, D. Su, W. Li, Y. Wang, *Energy Environ. Sci.*, **2010**, 3, 1121.
47. S. Li, J. Gong, *Chem. Soc. Rev.*, **2014**, 43, 7245.
48. J. L. Ewbank, L. Kovarik, C. C. Kevin, C. Sievers, *Green Chem.*, **2014**, 16, 885.
49. G. Grassi, A. Scala, A. Piperno, D. Iannazzo, M. Lanza, C. Milone, A. Pistone, S. Galvagno, *Chem. Comm.*, **2012**, 48, 6836.
50. T. Odedairo, J. Ma, Y. Gu, J. Chen, X. S. Zhao, Z. Zhu, *J. Mater. Chem. A*, **2014**, 2, 1418.
51. W. Ji, R. Shen, R. Yong, G. Yu, X. Guo, L. Peng, W. Ding, *J. Mater. Chem. A*, **2014**, 2, 699.
52. Z. Xu, Z. Li, X. Tan, C.M.B. Holt, L.Zhang, B.S. Amirkhiz, D. Mitlin, *RSC Adv.*, **2012**, 2, 2753.
53. D. Guo, H. Zhang, X. Yu, M. Zhang, P. Zhang, Q. Li, T. Wang *J. Mater. Chem. A*, **2013**, 1, 7247.
54. B. Senthilkumar, K. Vijaya Sankar, R. Kalai Selvan, M. Danielle, M. Manickam, *RSC Adv.*, **2013**, 3, 352.
55. X. Xia, J. Tu, Y. Zhang, X. Wang, C. Gu, X.B. Zhao, H. J. Fan, *ACS Nano*, **2012**, 6, 5531.
56. X.-C. Dong, H. Xu, X.-W. Wang, Y.-X. Huang, M. B. Chan-Park, H. Zhang, L.-H. Wang, W. Huang, P. Chen, *ACS Nano*, **2012**, 6, 3206.

57. W. Fu, Y. Wang, W. Han, Z. Zhang, H. Zha, E. Xie, *J. Mater. Chem. A*, **2016**, 4, 173.
58. W. Kong, C. Lu, W. Zhang, J. Pu, Z. Wang, *J. Mater. Chem. A*, **2015**, 3, 12452.
59. Y.-Z. Su, K. Xiao, N. Li, Z.-Q. Liu and S.-Z. Qiao, *J. Mater. Chem. A*, **2014**, 2, 13845.
60. C. Guan, Y. Wang, Y. Hu, J. Liu, K. H. Ho, W. Zhao, Z. Fan, Z. Shen, H. Zhang, J. Wang, *J. Mater. Chem. A*, **2015**, 3, 23283.
61. W. Liu, C. Li, M. Zhu, X. He, *J Power Sources*, **2015**, 282, 179.
62. G. Xiong, P. He, L. Liu, T. Chen, T. S. Fisher, *J. Mater. Chem. A*, **2015**, 3, 22940.
63. Y. Liang, Y. Yang, Z. Hu, Y. Zhang, Z. Li, N. An, H. Wu, *Int. J. Electrochem. Sci.*, **2016**, 11, 4092 - 4109
64. Y. Zhu, X. Ji, Z. Wu, Y. Liu, *Electrochim. Acta*, **2015**, 186, 562–571.
65. M. Jing, H. Hou, C.E. Banks, Y. Yang, Y. Zhang, X. Ji, *ACS Appl. Mater. Interfaces*, **2015**, 7 (41), 22741.
66. M.C. Liu, L. B. Kong, C. Lu, X. J. Ma, X. M. Li, Y. C. Luo, Kang, *J. Mater. Chem. A*, **2013**, 1, 1380.
67. A. Pendashteh, J. Palma, M. Anderson, R. Marcilla, *RSC Adv*, **2016**, 6, 28970.
68. F. Brazeau, A. Bello, D. Y. Momodu, J. K. Dangbegnon, F. Taghizadeh, M. J. Madito, T.M. Masikhwa, N. Manyala, *RSC Adv.*, **2015**, 5, 37462.
69. T. Brousse, D. Bélanger, J. W. Long, *J. Electrochem. Soc.*, **2015**, 162, A5185.

## 6.6. Summary

As we burn fossil fuels for energy or destroy and burn forests to develop pastures and plantations, carbon gathers and overwhelms our atmosphere. There is always an increasing demand for the research to decrease the CO<sub>2</sub> formation and global warming. For the last few decades, the deposited carbon over the catalyst during syngas production is predominantly eliminating in the form of CO<sub>2</sub> gas by feeding oxygen which further accumulates in the earth's atmosphere which leads to global warming, or disposing the catalyst. This study presents a new platform to utilize the carbon deposited catalyst during reforming reaction of propane without forming CO<sub>2</sub> gas or dispose for efficient energy storage applications. This would be the novel and promising approach to diminish the CO<sub>2</sub> formation during the production of syngas (especially by dry reforming reactions) and the carbon deposited catalyst can be used as an electrode for supercapacitor applications since the carbon is one of the well-known electrode material for energy storage devices.

## CHAPTER - 7

### **Preparation of CoMoO<sub>4</sub> @ Co(OH)<sub>2</sub> core-shell structure on conductive textile as positive electrode for hybrid supercapacitor**

#### **Highlights:**

- ❖ The current challenges in the usage of liquid electrolytes are closely correlated with the flexible and portable electronics
- ❖ Herein a flexible pouch-type hybrid supercapacitor based on binder-less cobalt hydroxide-cobalt molybdate core-shell structure sandwiched with lab-waste tissue derived honeycomb-like porous carbon is reported
- ❖ Briefly, the CoH-CoM core-shell structure is prepared by facile electrochemical deposition (ED) method, whereas honeycomb-like porous carbon is prepared using lab-waste tissue paper by KOH activation and followed by carbonization reaction. Owing to its excellent hierarchical core-shell structure and honeycomb-like porous carbon results in the large electrochemically active surface area, yielding high areal capacity of 265  $\mu\text{Ah cm}^{-2}$  and high specific capacitance of 227  $\text{Fg}^{-1}$  in 2 M KOH electrolyte
- ❖ An assembled pouch type hybrid supercapacitors using the prepared core-shell structure as positive electrode and porous carbon as negative electrode shows an extended working voltage of 1.5V in aqueous KOH electrolyte, thus stores a maximum energy density of 167.5  $\mu\text{Wh cm}^{-2}$
- ❖ Interestingly, the fabricated pouch type supercapacitor shows an excellent flexibility at different bending conditions and also exhibits remarkable cyclic stability with 98% capacitance retention even after long cycles. Further, the capability of the device is demonstrated by driving the various types of LEDs and seven-segment display and by integrating with solar cell for self-powered applications

## 7.1. Introduction

The advent of modern times and increasing demand in the need of global energy due to rapid deterioration of fossil fuels drives the development of alternate energy conversion and storage systems for the progress of mankind including residential, transportation, industry, military and space exploration [1-3]. Owing to the abundant conception of portable electronics, great effort has been committed to fabricate flexible, light weight, and even for wearable applications in the modern electronic society [4-6]. Among the various energy storage systems, supercapacitors, also known as electrochemical capacitors have attracted much attention due its high power density, long durability and good safety. However, supercapacitors display low energy density compared to the batteries which limits its use to advanced electronic applications [7, 8]. In order to overcome this issue, in recent times, the fabrication of hybrid supercapacitors have been emerged as alternate energy storage devices. Hybrid supercapacitor is the combination of battery-type faradaic electrode material and electrochemical double layer capacitive (EDLC) material which can act as a bridge between supercapacitors and batteries [9, 10]. The performance of the hybrid supercapacitor is highly depending on their both electrodes in terms of specific capacity, cyclic stability, rate capability and cost. Many efforts have been made to prepare suitable faradaic electrode with high conductivity and cyclic stability. Among them, rational synthesis of core-shell material is proved to be an excellent approach to modify the properties of the material by its synergetic effect [11, 12]. To date, many core-shell heterostructures have been proposed

such as metal/metal oxide, metal oxide/metal oxide, carbon/metal oxide, and carbon /conducting polymer for design of high energy density supercapacitor [13-16]. However, the lack of flexibility, most of them limits its application for practical usage, especially for flexible electronics. Hence, it is necessary to find out another flexible substrate with high conductivity, good flexibility and high mechanical stability. In this context, metallic layered polyester fabric can be easily lifted up the conducting fibers with desired properties and large scale production with low cost compared to other conducting fabrics. Cobalt oxides and cobalt hydroxides have also been considered as excellent electrode materials for supercapacitor applications [17-19]. Recently, binary metal oxides and mixed metal oxides have been reported to deliver better performance than single component oxides act as the active materials of faradaic electrode due to the mixed oxidation states and high electrical conductivity [20, 21]. Cobalt molybdate ( $\text{CoMoO}_4$ ) is particularly attractive among those materials due it is economical, non-toxic and enhanced electrochemical properties [22, 23]. However, there have only been few reports on the faradaic behavior of  $\text{CoMoO}_4$  so far. Recently, Gu et al, prepared  $\text{Co}_3\text{O}_4@ \text{CoMoO}_4$  nanowire by hydrothermal ion exchange method and fabricated symmetric supercapacitor in liquid electrolyte [24]. More recently, Wang et al reported that  $\text{Co}_3\text{O}_4@ \text{CoMoO}_4$  core-shell structure on Ni foam by hydrothermal technique and fabricated hybrid supercapacitors with CNT [25]. However, those techniques tend to be complicated such as high temperature treatment, time consuming reaction and also obtained electrode is not flexible in nature. To the best of our knowledge, flexible

Co(OH)<sub>2</sub>-CoMoO<sub>4</sub> core-shell structure have never been reported yet. In this report, we have presented the Co(OH)<sub>2</sub>-CoMoO<sub>4</sub> core-shell structure via facile electrochemical deposition technique by controlling growth cycles and growth time. The obtained core-shell delivered high areal capacity of 265 μAh cm<sup>-2</sup> in KOH electrolyte. Electrochemical deposition technique has several advantages compared to other methods such as facile process, possibility of large scale application, low temperature processing and direct control of thickness [26].

In order to make hybrid supercapacitor, the preparation of negative electrode is important as equal to the positive electrode. Carbon based materials such as biomass derived activated carbon, reduced graphene oxide and carbon nanotubes have considered more attention due to its high surface area [24, 27, 28]. Among these, biomass derived activated carbon shows more advantages such as low-cost precursor, easy to synthesis and activation process tailored porous in nature which leads to high specific capacitance. Senthilkumar et al, prepared Eichhornia crassipes derived activated carbon for hybrid supercapacitor and exhibited specific capacitance of 123 F g<sup>-1</sup>[29]. Puthusseri et al. reported that used white paper derived activated carbon for Li ion hybrid capacitor and exhibited 164 Fg<sup>-1</sup>[30]. Based on the above strategies, we have used laboratory waste tissue paper for the preparation of porous carbon by hydrothermal method and followed by carbonization at inert atmosphere via KOH activation process. The obtained honeycomb-like porous carbon shows maximum specific capacitance of 227 Fg<sup>-1</sup> in KOH electrolyte. Moreover, we have fabricated the pouch type flexible hybrid

supercapacitor using the prepared positive core-shell structure and negative porous carbon. The fabricated flexible device shows the excellent electrochemical performance in terms of specific capacitance, energy density and cyclic stability. In addition, the fabricated device was integrated with commercial solar panel and demonstrated lightening of various LEDs and seven segment display to display the self-powered applications. This study constitutes a promising strategy toward design of transition metal oxides based nanostructured positive electrode and porous carbon based negative electrode to fabricate the flexible device with good energy storage performance for hybrid supercapacitors.

## **7.2. Experimental methods**

### **7.2.1. Preparation of $\text{CoMoO}_4$ @ $\text{Co(OH)}_2$ core – shell on conductive textile**

Initially, the growth of  $\text{Co(OH)}_2$  nanostructures as core material on the conductive textile was achieved via a facile electrochemical deposition method. Briefly, precursor solution containing  $\text{Co(NO}_3)_2 \cdot 6\text{H}_2\text{O}$  and  $\text{Na}_2\text{MoO}_4 \cdot 2\text{H}_2\text{O}$  (molar ratio, 1:1) was prepared by dissolving in water. The ECD process has been carried out using a simple three electrode system using CT as working electrode, silver/silver chloride ( $\text{Ag/AgCl}$ ) as reference electrode and platinum (Pt) foil as counter electrode. A slice of CT was cleaned using ethanol and water to remove impurities and dust particles on the surface. The cleaned CT has been attached to the polyethylene terephthalate (PET) film to prevent the deposition of active material on the rear side of the CT. After that, the three electrode system is immersed into the growth solution and performed the ECD process

using cyclic voltammetry for various cycles. After depositing the core  $\text{Co(OH)}_2$  nanostructure, the product obtained was washed thoroughly in distilled water and ethanol to remove residual ions and was allowed to dry in a hot-air oven overnight at  $80^\circ\text{C}$ . In order to deposit the  $\text{CoMoO}_4$  shell, the as-prepared  $\text{Co(OH)}_2/\text{CT}$  electrode taken as working electrode and remaining kept as same as earlier. The three electrode system is immersed into the growth solution ( $\text{Co(NO}_3)_2 \cdot 6\text{H}_2\text{O}$  and  $\text{Na}_2\text{MoO}_4 \cdot 2\text{H}_2\text{O}$  (molar ratio, 1:1)) and performed ECD process with an applied chrono-potentiometry current of  $-0.5$  mA with the voltage range between  $-1.0$  V to  $-0.6$  V for various time intervals. The color of the CT had changed to light pink, indicating the uniform growth of  $\text{CoMoO}_4$  shell on  $\text{Co(OH)}_2/\text{CT}$  core. The obtained core-shell electrode was washed thoroughly in distilled water and ethanol to remove residual ions and was allowed to dry in a hot-air oven overnight at  $80^\circ\text{C}$ .

### **7.2.2. Preparation of porous activated carbon**

The porous activated carbon is prepared using lab waste tissue paper as follows; at first, waste tissue papers were collected from our laboratory and 5 g of lab waste tissue paper (cut into small pieces) is treated in dilute  $\text{H}_2\text{SO}_4$  at  $160^\circ\text{C}$  for 20 hr under hydrothermal reaction. After reaction, the autoclave was cooled down to room temperature naturally, filtered and washed with water several time to remove excess acid, if present. The product was dried at hot air oven at  $80^\circ\text{C}$  for overnight. The grinded powder was further kept for KOH activation overnight. Then the slurry was kept for

carbonization reaction at 700 °C under argon atmosphere for 4 hr. Finally, the resultant powder was washed thoroughly using 10% HCl to remove the inorganic impurities and washed using water to achieve neutral pH. Then, the precipitate is dried under hot air oven for overnight to obtain porous activated carbon. This porous carbon is characterized in detail and directly used as negative electrode for hybrid supercapacitors.

### **7.2.3. Fabrication of pouch type hybrid supercapacitor**

The electrochemical performances of the prepared materials were examined via cyclic voltammetry (CV), electrochemical impedance spectroscopy (EIS), and galvanostatic charge discharge analysis (GCD) using an AUTOLAB PGSTAT302N electrochemical workstation. For the three-electrode system, a piece of  $\text{CoMoO}_4@\text{Co}(\text{OH})_2/\text{CT}$  ( $1 \times 1 \text{ cm}^2$  area) was used directly as the working electrode. Silver/silver chloride (Ag/AgCl) and platinum foil were used as the reference and counter electrodes, respectively. Electrolyte containing 2 M KOH was used in this study. The negative electrode has been prepared by mixing porous activated carbon, carbon block and Polyvinylidene difluoride (PVDF) in the weight ratio of 80:15:5 using N-methylene pyrrolidone (NMP) as solvent to make slurry form. This prepared slurry was drop casted on the conductive carbon cloth and kept for drying at 80°C for overnight. For the two-electrode system, the  $\text{CoMoO}_4@\text{Co}(\text{OH})_2/\text{CT}$  was used as the positive electrode and PAC was used as the negative electrode with commercial filter paper.

## **7.3. Results and discussion**

### **7.3.1. Structural characterization of $\text{CoMoO}_4@\text{Co}(\text{OH})_2/\text{CT}$ core-shell**

The schematic illustration of the preparation of the preparation of  $\text{CoMoO}_4@\text{Co}(\text{OH})_2/\text{CT}$  core-shell structure on the conductive textile was shown in Figure 1A.

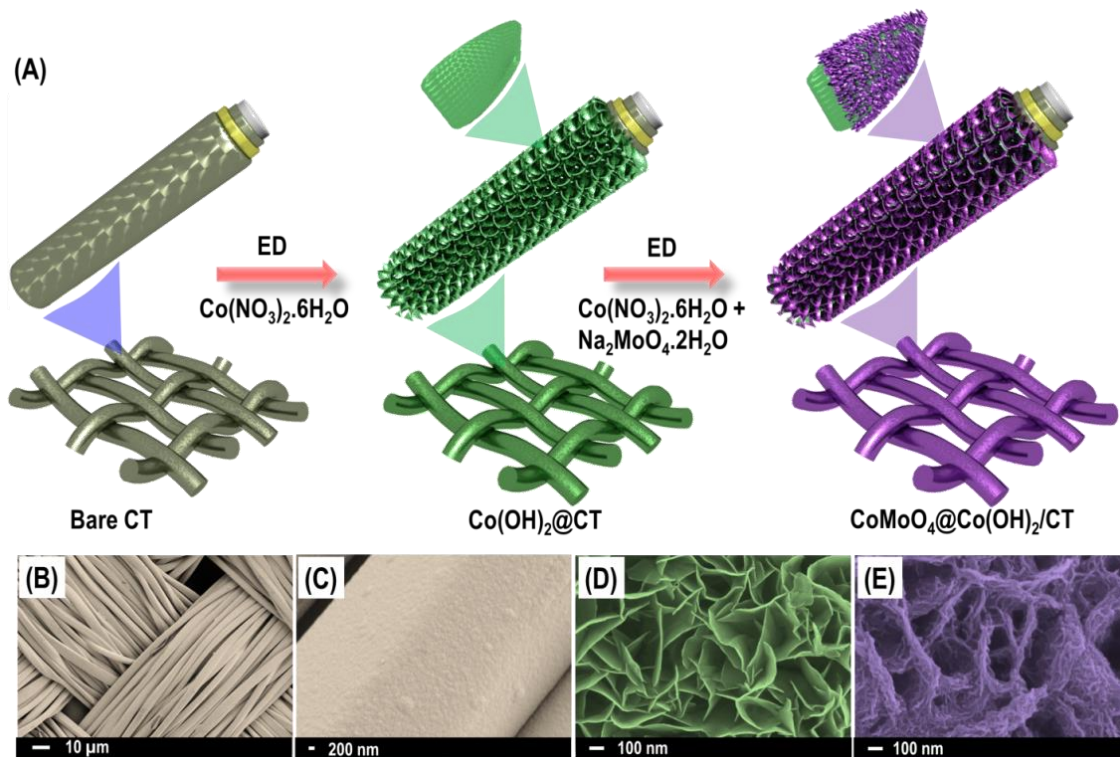


**Figure 7.1.1** Preparation of positive electrode material: Schematic representation of the formation of core-shell (A). The binder-free  $\text{Co}(\text{OH})_2$  core has been initially grown on the CT by cyclic voltammetry method for 30 cycles.  $\text{CoMoO}_4$  shell has been grown on the  $\text{Co}(\text{OH})_2/\text{CT}$  core by chronoamperometry method for 240 sec. FE-SEM images of Bare CT (B), magnified part of bare CT (C),  $\text{Co}(\text{OH})_2/\text{CT}$  core (D) and  $\text{CoMoO}_4@\text{Co}(\text{OH})_2/\text{CT}$  core-shell (E).

Briefly, binder-less  $\text{Co}(\text{OH})_2$  core was grown directly on CT by a facile electrochemical deposition method using cobalt nitrate and followed by  $\text{CoMoO}_4$  shell was directly grown on  $\text{Co}(\text{OH})_2/\text{CT}$  core using cobalt nitrate and sodium molybdate as

precursors. Here, the  $\text{Co}(\text{OH})_2$  acted as seed layer to grow  $\text{CoMoO}_4$  on  $\text{Co}(\text{OH})_2$  core. Initially, the growth of  $\text{Co}(\text{OH})_2$  was measured from the negative sweeping voltage of -0.1 V to -0.6V at the scan rate of  $20 \text{ mV s}^{-1}$  with different cyclic- voltammetry cycles (from 10 to 40 cycles). The reaction of cobalt nitrate precursor solution during on any conductive substrate is well.

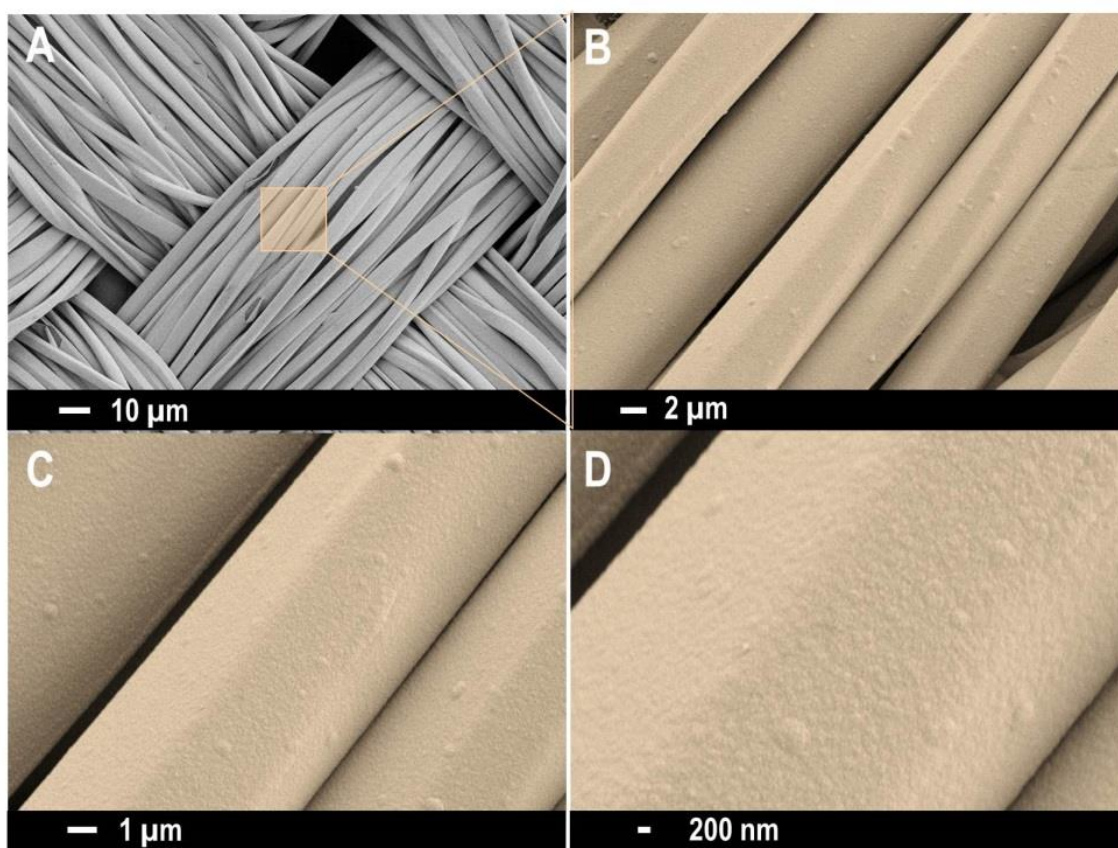


**Figure 7.1.2** FE-SEM images of bare conductive textile at different magnifications 10  $\mu\text{m}$  (A), 2  $\mu\text{m}$  (B), 1  $\mu\text{m}$ (C) and 200 nm (D). Low magnification images shows that uniform fibers are waived together to form textile and high magnification images shows that the surface of the conductive textile are more smooth and polished

The morphology of the as grown sample has been measured using FE-SEM analysis (Figure 7.1.2 to 7.1.6). Figure 7.1.2 shows the morphology of the bare conductive textile. At the 10 number CV cycles, the growth of  $\text{Co(OH)}_2$  is very low. When increasing the number of cycles the growth of  $\text{Co(OH)}_2$  nanosheets also increased. At 30<sup>th</sup> cycle, the uniform growth of  $\text{Co(OH)}_2$  on CT was obtained and the morphology of  $\text{Co(OH)}_2$  also suggested the well growth of nanosheets over the CT.

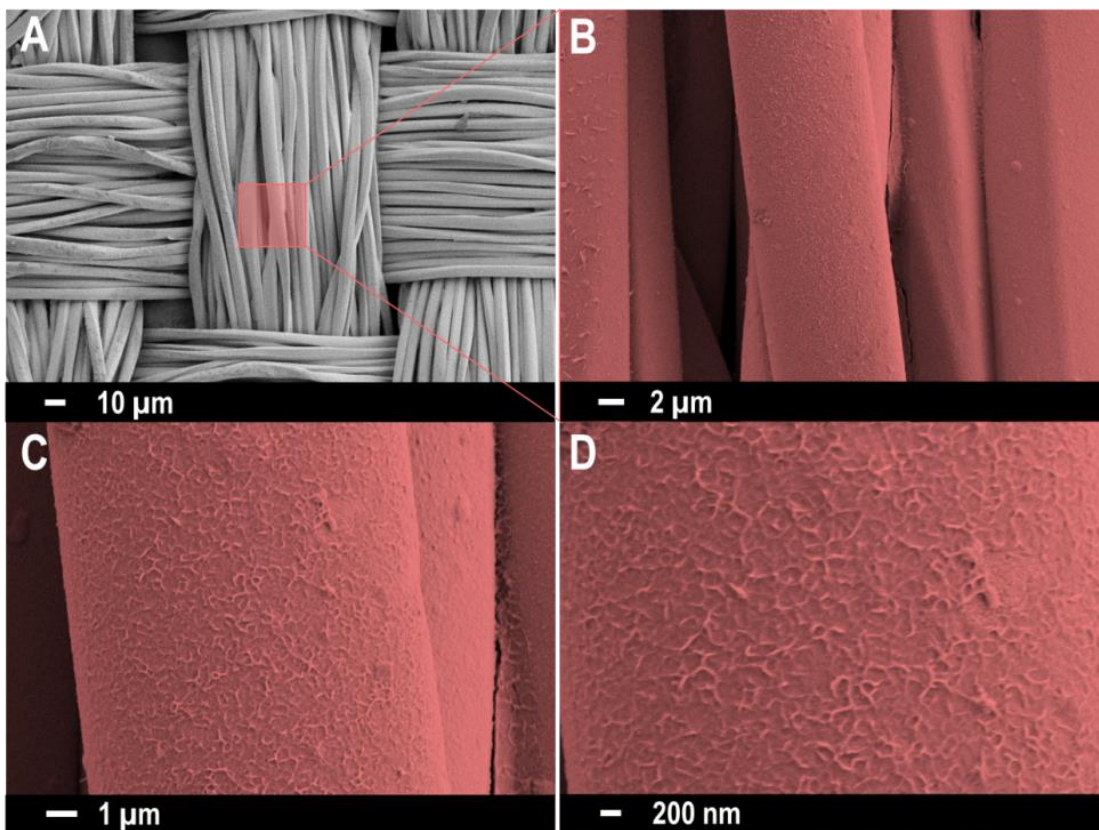


**Figure 7.1.3** FE-SEM images of  $\text{Co(OH)}_2$  grown on conductive textile in 10 cyclic voltammetry cycles at different magnifications, 10  $\mu\text{m}$  (A), 2  $\mu\text{m}$  (B), 1  $\mu\text{m}$  (C) and 200 nm (D) It shows that the 10 number of CV cycles makes the  $\text{Co(OH)}_2$  seed layer on the surface of the conductive textile. Also, the deposited  $\text{Co(OH)}_2$  layer is quite uniform and very thin.

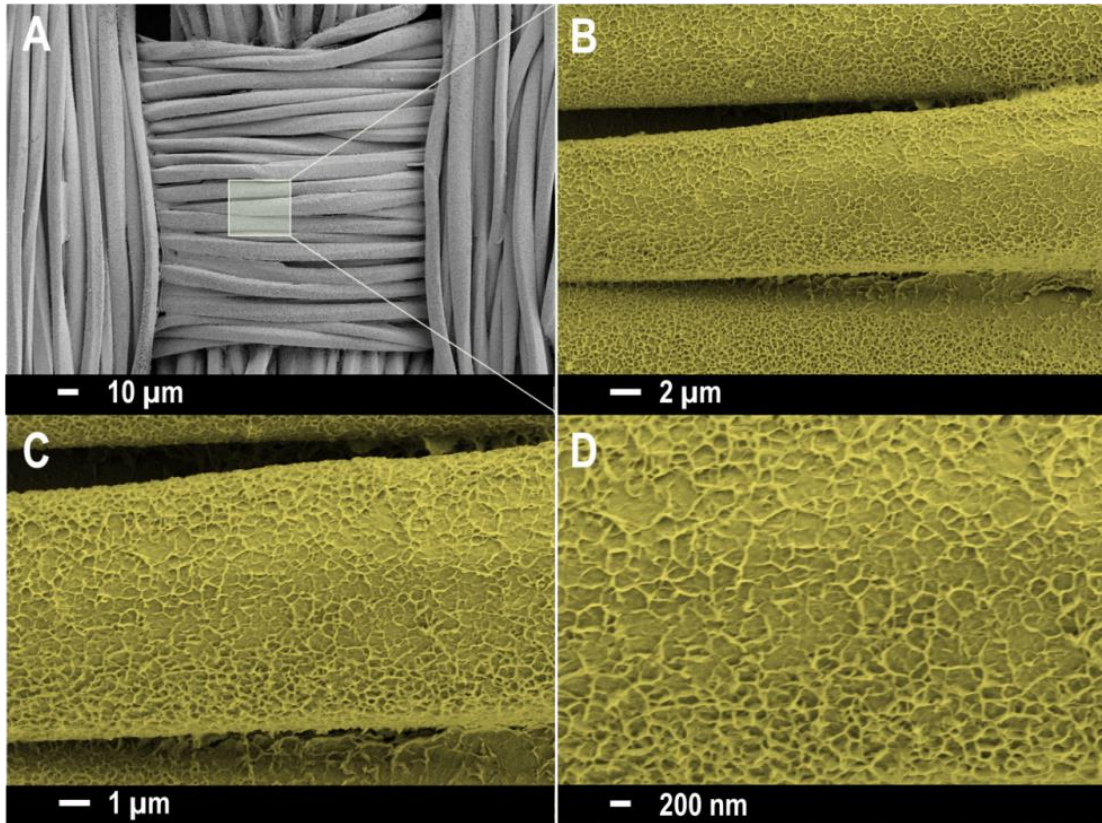


**Figure 7.1.4** FE-SEM images of  $\text{Co(OH)}_2$  grown on conductive textile in 20 number of cyclic voltammetry cycles at different magnifications,  $10\ \mu\text{m}$  (A),  $2\ \mu\text{m}$  (B),  $1\ \mu\text{m}$ (C) and  $200\ \text{nm}$  (D) It clearly depicts that the formation of  $\text{Co(OH)}_2$  in sheet-like structure. Also, when increasing the number of CV cycles to 20, the amount  $\text{Co(OH)}_2$  nanosheets on the surface of the conductive textile is quite high compared to 10 CV cycles.

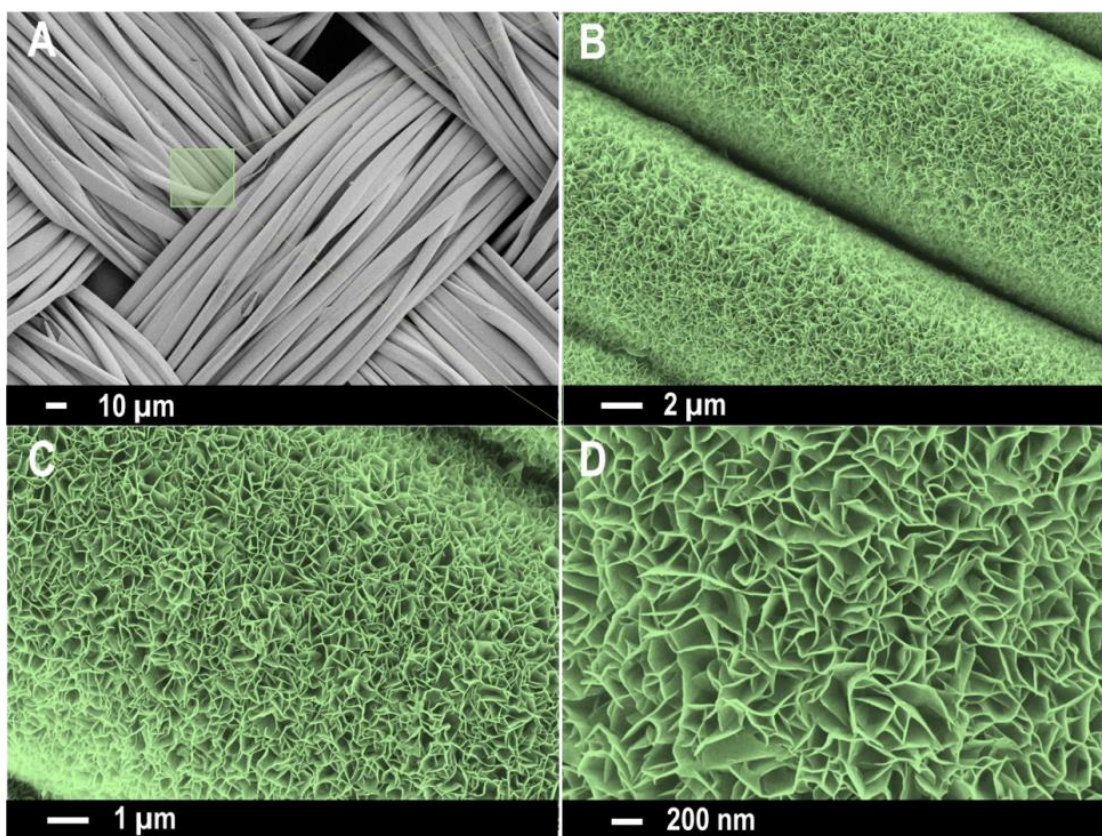


**Figure 7.1.5** FE-SEM images of  $\text{Co(OH)}_2$  grown on conductive textile in 30 number of cyclic voltammetry cycles at different magnifications, 10  $\mu\text{m}$  (A), 2  $\mu\text{m}$  (B), 1  $\mu\text{m}$ (C) and 200 nm (D) It clearly confirms that the formation of  $\text{Co(OH)}_2$  in sheet-like structure. Also, when increasing the number of CV cycles to 30, the amount  $\text{Co(OH)}_2$  nanosheets on the surface of the conductive textile is quite high and controlled growth of the sheet like structure is observed in more uniform and consistent morphology.

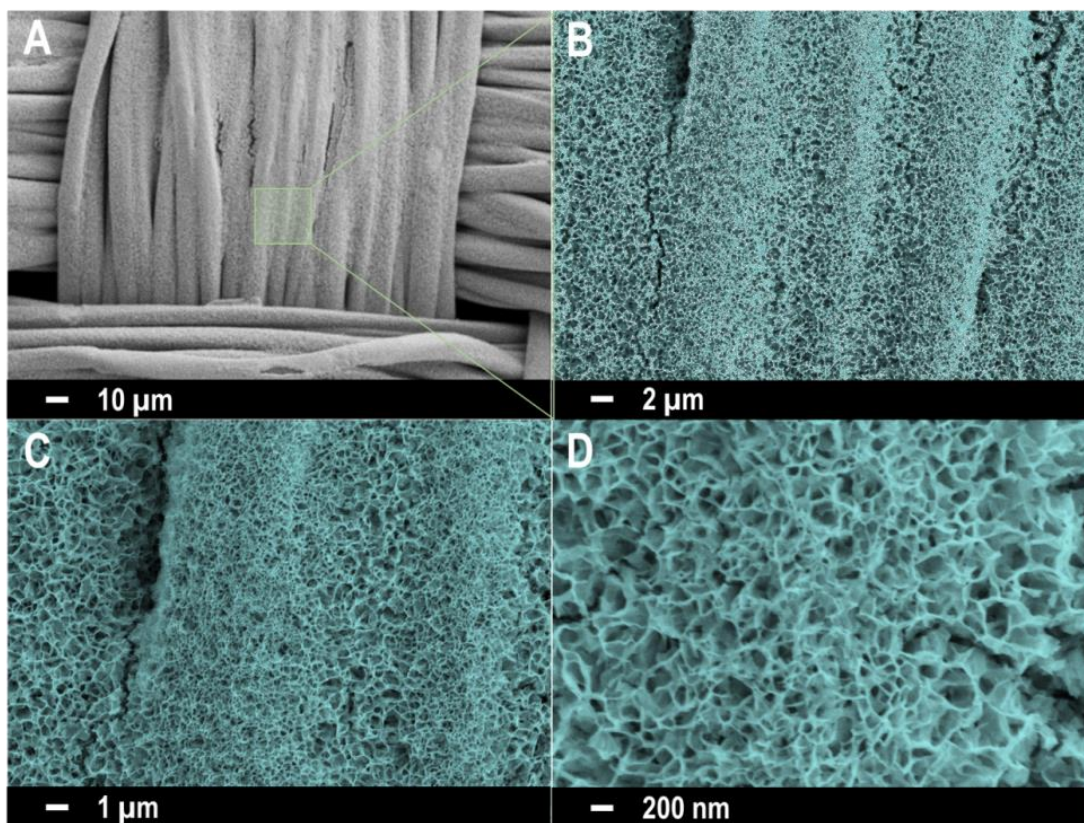


**Figure 7.1.6** FE-SEM images of  $\text{Co(OH)}_2$  grown on conductive textile in 40 number of cyclic voltammetry cycles at different magnifications,  $10\ \mu\text{m}$  (A),  $2\ \mu\text{m}$  (B),  $1\ \mu\text{m}$  (C) and  $200\ \text{nm}$  (D) It clearly confirms that the formation of  $\text{Co(OH)}_2$  in sheet-like structure. Also, when increasing the number of CV cycles to 40, the amount  $\text{Co(OH)}_2$  nanosheets on the surface of the conductive textile is quite high and controlled growth of the sheet like structure was spoiled due to more number of cobalt ions which clearly suggested that the 30 number of CV cycles is more suitable than others.

These nanosheets are interconnected with each other and formed network like structure. When increasing the CV cycles to 40, the morphology of  $\text{Co(OH)}_2$  was random and the uniform sheet like structure was ruined to irregular structure (see **Figure 7.1.5**). Generally, the growth of  $\text{Co(OH)}_2$  is based on the generation of hydroxyl ions on the surface of the working electrode. When the working electrode was immersed into the

precursor solution, the nitrate ( $(\text{NO}_3)^{2-}$ ) ions were reduced electrochemically with water on the working substrate, leading to the formation of hydroxyl ( $\text{OH}^-$ ) ions and nitrite ( $\text{NO}_2^-$ ) ions by the support of electrons. Subsequently, the cobalt ( $\text{Co}^{2+}$ ) ions in the vicinity of the working electrode react with the  $\text{OH}^-$  ions, resulting in the formation of precipitated cobalt hydroxide on the working substrate and providing the subsequent nucleation sites [26].

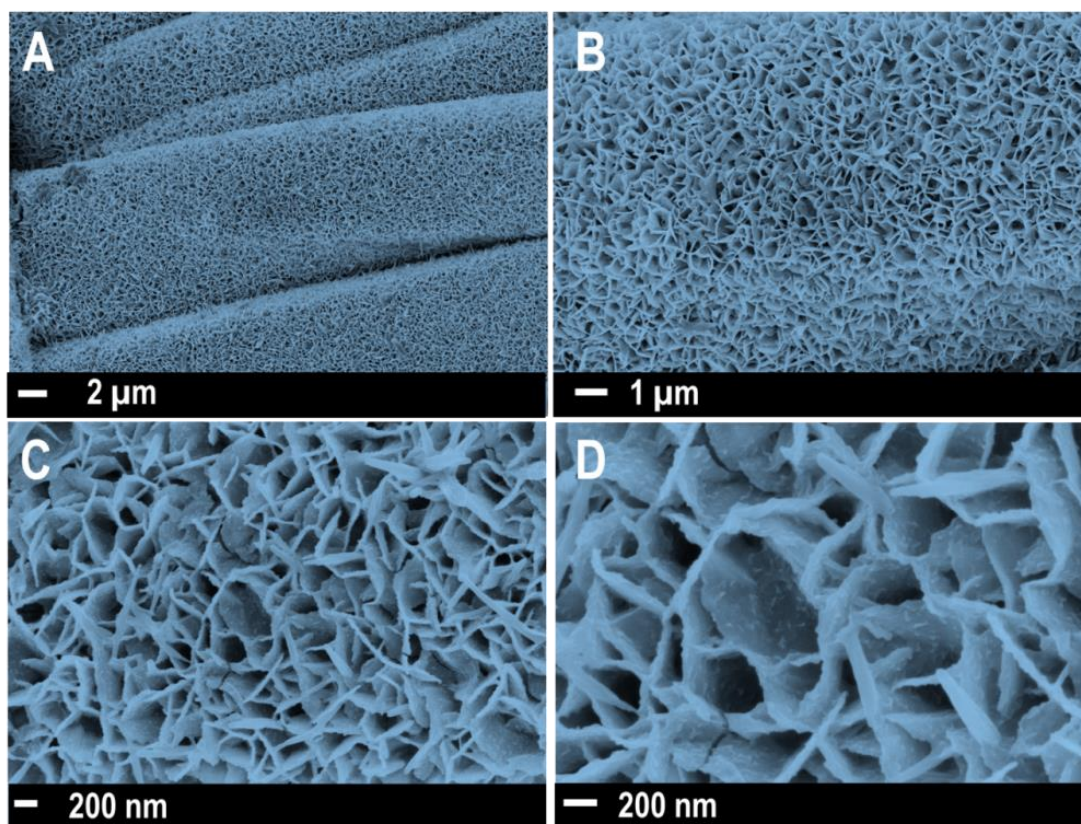


**Figure 7.1.7** FE-SEM images of  $\text{CoMoO}_4$  on  $\text{Co}(\text{OH})_2$  grown on conductive textile in 180 seconds of chrono-potentiometry technique at different magnifications, 10  $\mu\text{m}$  (A), 2  $\mu\text{m}$  (B), 1  $\mu\text{m}$  (C) and 200 nm (D) It suggested that the formation of  $\text{CoMoO}_4$  on  $\text{Co}(\text{OH})_2$  nanosheets is very small.

For further growth of  $\text{CoMoO}_4$  shell has been done on the  $\text{Co(OH)}_2$  nanosheets which obtained from the 30 cycle of CV measurement. The growth of  $\text{CoMoO}_4$  on the  $\text{Co(OH)}_2/\text{CT}$  core structure was performed by chrono-potentiometry technique at constant current of  $-0.5$  mA with different growth times (180 to 270 sec).

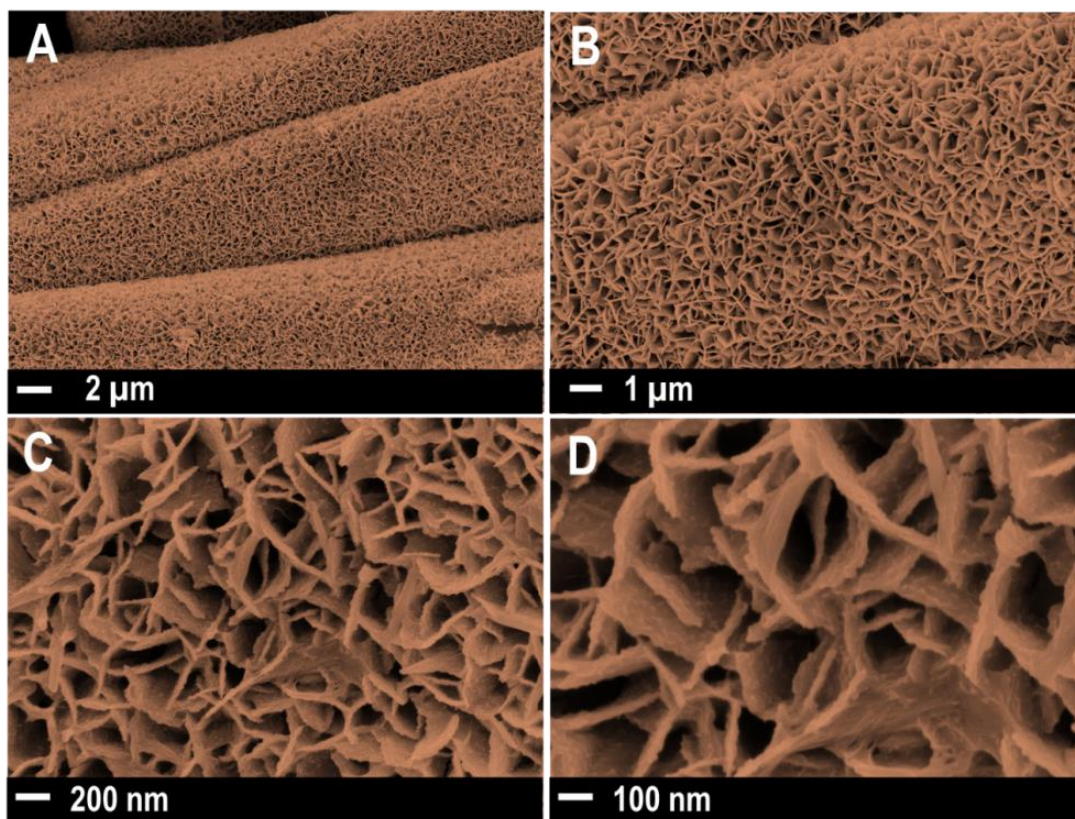


**Figure 7.1.8** FE-SEM images of  $\text{CoMoO}_4$  on  $\text{Co(OH)}_2$  grown on conductive textile in 210 seconds of chrono-potentiometry technique at different magnifications at different magnifications,  $10\ \mu\text{m}$  (A),  $2\ \mu\text{m}$  (B),  $1\ \mu\text{m}$ (C) and  $200\ \text{nm}$  (D) It confirms that the formation of  $\text{CoMoO}_4$  in the form of small wavy shaped. Also, when increasing the time duration of chrono-potentiometry technique, the growth of  $\text{CoMoO}_4$  is also high.

At growth time of 180 sec, small particle like  $\text{CoMoO}_4$  grown on the surface of  $\text{Co(OH)}_2$  nanosheets (**Figure 7.1.7**). When increasing the growth time to 210 sec (**Figure 7.1.8**), the number of particles was increased and the size of shell also increased. At the optimized growth time of 240 sec, the uniform growth of  $\text{CoMoO}_4$  shell was homogeneously covered on the surface of  $\text{Co(OH)}_2$  to form core-shell structure (**Figure 7.1.9**).

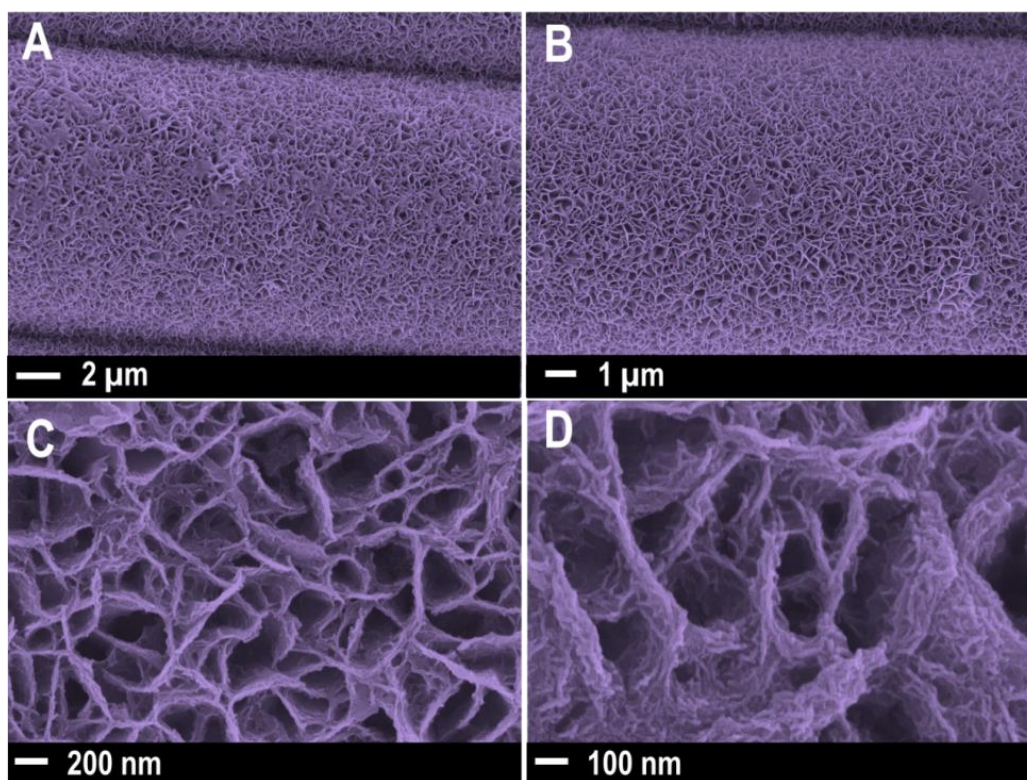


**Figure 7.1.9** FE-SEM images of  $\text{CoMoO}_4$  on  $\text{Co(OH)}_2$  grown on conductive textile in 240 seconds of chrono-potentiometry technique at different magnifications, 10  $\mu\text{m}$  (A), 2  $\mu\text{m}$  (B), 1  $\mu\text{m}$ (C) and 200 nm (D) It clearly confirms that the formation of  $\text{CoMoO}_4$  on  $\text{Co(OH)}_2$  in crumpled sheet-like structure. Also, when increasing the time duration of chrono-potentiometry technique to 240 seconds, the growth of  $\text{CoMoO}_4$  is also quite and controlled growth of the crumpled sheet-like structure is observed in more uniform and consistent morphology.

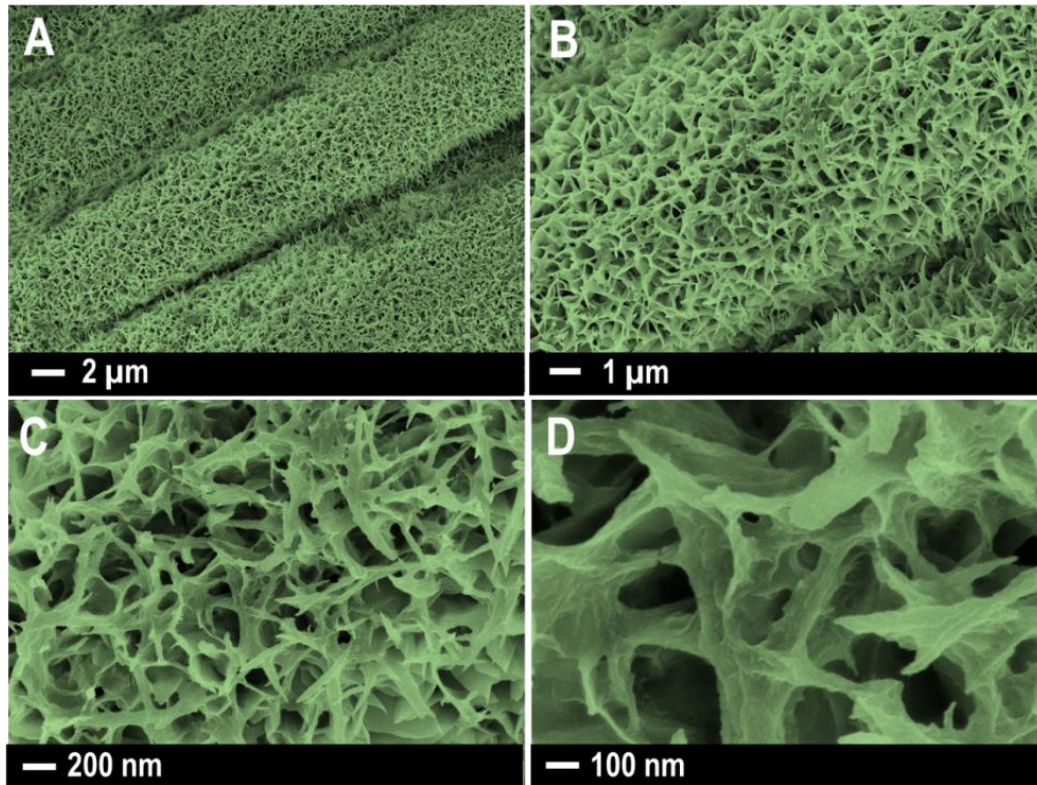


**Figure 7.1.10** FE-SEM images of  $\text{CoMoO}_4$  on  $\text{Co(OH)}_2$  grown on conductive textile in 270 seconds of chrono-potentiometry technique at different magnifications, 10  $\mu\text{m}$  (A), 2  $\mu\text{m}$  (B), 1  $\mu\text{m}$ (C) and 200 nm (D) It is observed that the formation of  $\text{CoMoO}_4$  on  $\text{Co(OH)}_2$  in deformed sheet-like structure. Also, when increasing the time duration of chrono-potentiometry technique to 270 sec, the growth of  $\text{CoMoO}_4$  is also quite high and uniform growth was destroyed due to continuous potential scanning which damages the uniform sheet-like structure of  $\text{Co(OH)}_2$ .

As shown in the **Figure 7.1.10**, when further increasing the time to 270 sec, the sheet like morphology of  $\text{Co(OH)}_2$  was ruined due to the more number of  $\text{CoMoO}_4$  particles are colliding towards nanosheets. From the optimization of growth time, 240 sec of chrono-potentiometry was fixed one for the growth of  $\text{CoMoO}_4$  shell on  $\text{Co(OH)}_2/\text{CT}$  due to the more uniform structure. **Figure 7.1.1 B-E** shows the FE-SEM images of

conductive textile and optimized growth of  $\text{Co(OH)}_2$  core, and  $\text{CoMoO}_4@ \text{Co(OH)}_2$  core-shell respectively. The TEM analysis has been performed by removing the sample from the textile by ethanol solvent and shown in **Figure 7.1.11 A-C**. The images clearly suggest that the formation crumpled  $\text{CoMoO}_4$  shell on the  $\text{Co(OH)}_2$  core. SAED pattern in inset of **Figure 7.1.11C** suggest that the polycrystalline nature of core-shell structure. This vertical interconnected nanosheets array to the CT was beneficial to the fast ion and electron transportation. This core-shell configuration can facilitate a high surface area, which is mainly ascribed to the interconnected  $\text{CoMoO}_4$  crumpled nanosheets and the aligned  $\text{Co(OH)}_2$  nanosheets scaffold that creating a 3D architecture and highly porous surface.

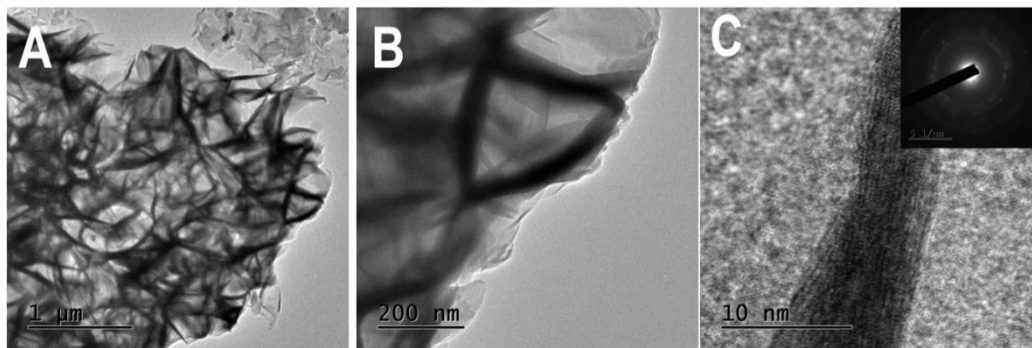


**Figure 7.1.11** TEM images of  $\text{CoMoO}_4@ \text{Co(OH)}_2$  nanosheets on conductive textile at different magnifications (240 sec). The images clearly suggest that the formation crumpled  $\text{CoMoO}_4$  shell on the  $\text{Co(OH)}_2$  core. SAED pattern in inset suggest that the polycrystalline nature of core-shell structure.

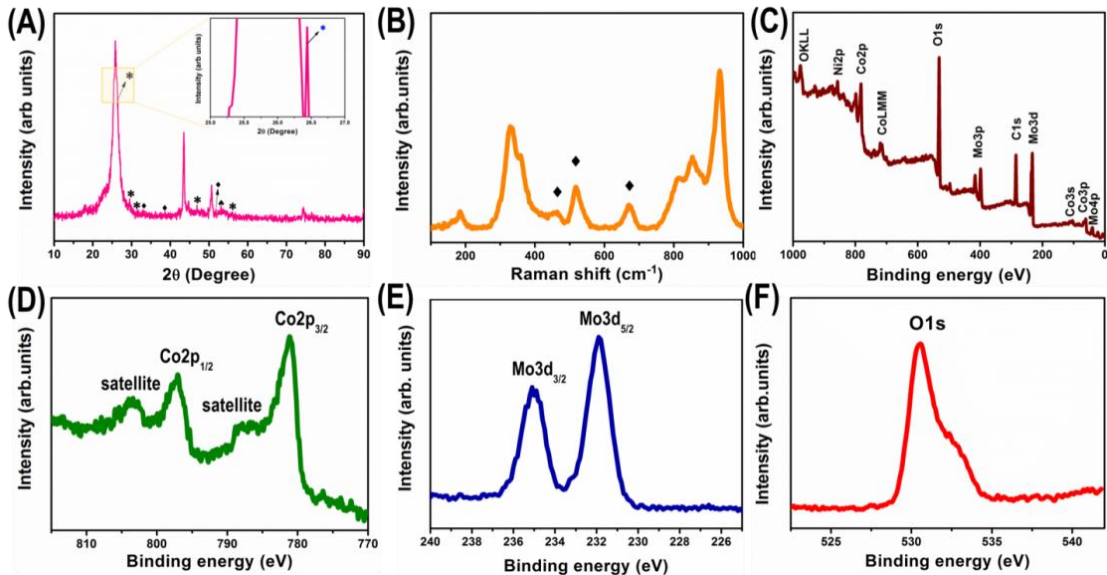


**Figure 7.1.12** Structural characterization of positive electrode material: XRD pattern (A) (inset shows the magnified part of maximum intensity peak of  $\text{CoMoO}_4$ ), Raman spectrum (B) of  $\text{CoMoO}_4@ \text{Co}(\text{OH})_2/\text{CT}$ . XPS core-level spectra: Survey spectrum (C),  $\text{Co}2\text{p}$  core-level spectrum (D),  $\text{Mo}3\text{d}$  core-level (E) and  $\text{O}1\text{s}$  core-level (F) of  $\text{CoMoO}_4@ \text{Co}(\text{OH})_2/\text{CT}$ .

**Figure 7.1.12** shows the structural characterizations of the prepared core-shell structure. **Figure 7.1.12 A** shows the XRD pattern of prepared core-shell structure. The patterns of  $\text{Co}(\text{OH})_2$  core and  $\text{CoMoO}_4$  shell are in good agreement with the standard patterns for the hexagonal cell of brucite-like  $\text{Co}(\text{OH})_2$  (♦, PDF, card No. 30-0443) and monoclinic phase of  $\text{CoMoO}_4$  (\*, PDF, card No.21-0868), respectively [22, 23, 31]. The remaining four major peaks at  $25.78$ ,  $43.62$ ,  $50.76$  and  $74.21^\circ$  are corresponding to the conductive substrate. Besides the diffraction peaks of monoclinic  $\text{CoMoO}_4$ , the peak at the diffraction angle of  $53^\circ$  attributed to  $\text{CoMoO}_6 \cdot 0.9\text{H}_2\text{O}$  are observed [25]. From this XRD pattern of  $\text{Co}_3\text{O}_4@ \text{CoMoO}_4$  core-shell contain the diffraction peaks of both  $\text{Co}_3\text{O}_4$  and  $\text{CoMoO}_4$ , indicating the presence of both phases. Further to identify the crystal

structure, Raman spectroscopy is carried out in the range between  $100\text{ cm}^{-1}$  to  $1000\text{ cm}^{-1}$ . The Raman bands at  $670$ ,  $518$  and  $464\text{ cm}^{-1}$ . The appearance of Raman band at around  $470\text{ cm}^{-1}$  can be explained by high content of  $\text{Co(OH)}_2$ . The second important band is  $518\text{ cm}^{-1}$ , which is attributed to Co-O ( $A_g$ ) symmetric stretching mode. Bøckman et al. reported that the positions of bands originated from  $\text{Co(OH)}_2$  were found to be influenced from the used substrates and the applied methods for preparation, and their positions were also found to vary according to the amount of deposited  $\text{Co(OH)}_2$  content. As can be seen from **Figure 7.1.12 B**, all bands can be assigned as follows:  $464\text{ cm}^{-1}$  band to  $E_g$  mode,  $518\text{ cm}^{-1}$  band to  $F_{2g}$  mode, and  $670\text{ cm}^{-1}$  band to  $A_{1g}$  mode [32, 33]. The remaining bands were assigned to the  $\text{CoMoO}_4$ . The high intensity band at  $932\text{ cm}^{-1}$  is attributable to the symmetric stretching mode of the O-Mo-O bond. The band at  $853$  and  $813\text{ cm}^{-1}$  can be identified for asymmetric stretching modes of oxygen in bending the O-Mo-O bond. The band located at  $359$  and  $329\text{ cm}^{-1}$  can be associated with symmetric torsional mode of stretching of the Co-O-Mo bond [22, 23]. The results obtained are in good agreement with reports in the literature and the slight differences in the positions of the vibrational modes can be ascribed with the sample preparation, crystal size, structural morphology, and the degree of structural order-disorder of the materials. Furthermore, we have performed X-ray photoelectron spectroscopy (XPS) to analyze the chemical composition of the prepared samples; the results are presented in **Figure 7.1.12 C-F**. The survey spectrum is shown in **Figure 7.1.12 C**, which displays the presence of all the elements over the surface of the catalyst. **Figure 7.1.12 D** shows

the appearance of two peaks at binding energies of 797 eV and 781 eV, corresponding to the core-level spectra of  $\text{Co}2p_{1/2}$  and  $\text{Co}2p_{3/2}$ , respectively, which is characteristic of  $\text{Co}^{2+}$  [34]. The peaks at 235.1 eV and 231.9 eV in **Figure 7.1.12 E** are attributable to  $\text{Mo}^{6+} 3d_{3/2}$  and  $\text{Mo}^{6+} 3d_{5/2}$ , respectively. The peak separation between  $\text{Mo}^{6+} 3d_{3/2}$  and  $\text{Mo}^{6+} 3d_{5/2}$  is roughly 3.2 eV, which is in well-fixed with those reported for  $\text{Mo}^{6+}$  [35, 36]. The band at 530.6 eV suggests that the presence of lattice oxygen in the prepared sample, while the oxygen in hydroxyl group show the band at 532.3 eV [36]. **Figure 7.1.13** shows the photographic images of the prepared core-shell structure at different bending conditions suggesting its excellent flexibility.



**Figure 7.1.13** Photographic images of flexibility of the deposited  $\text{CoMoO}_4@ \text{Co}(\text{OH})_2$  on conductive textile at the different bending conditions.

### 7.3.2. Electrochemical characterization of $\text{CoMoO}_4@ \text{Co}(\text{OH})_2/\text{CT}$ core-shell

To use this prepared  $\text{CoMoO}_4@ \text{Co}(\text{OH})_2/\text{CT}$  core-shell as positive electrode for hybrid capacitor, the electrochemical performances of this core-shell electrode were

assessed by cyclic voltammogram (CV) and galvanostatic charge/discharge (GCD) measurements.

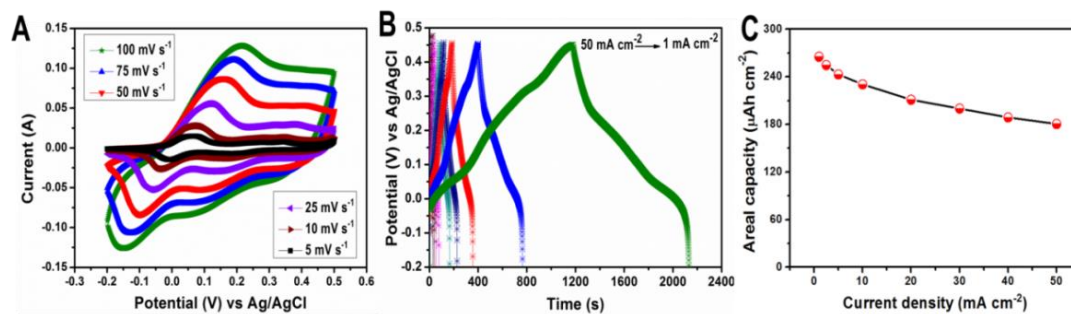


**Figure 7.1.14** Electrochemical performance of the prepared positive core-shell electrode: Cyclic voltammetry curves at different scan rates (100 to 5 mV s<sup>-1</sup>) (A), Galvanostatic charge-discharge curves at different current densities (50-1 mA cm<sup>-2</sup>) (B), areal capacity with respect to the current densities calculated from the charge-discharge analysis (C) of CoMoO<sub>4</sub>@Co(OH)<sub>2</sub>/CT.

**Figure 7.1.14** shows the electrochemical performances of CoMoO<sub>4</sub>@Co(OH)<sub>2</sub>/CT electrode using 2 M KOH as the electrolyte solution. CV curves were recorded in the potential range between -0.2 and 0.5 V at different scan rates of 5–100 mV s<sup>-1</sup> (**Figure 7.1.14 A**). Two pairs of strong reduction/oxidation peaks were observed within each CV curve, suggesting that the capacitive characteristics are governed mainly by Faradic redox reactions. The behavior of the CV curves is not remarkably controlled by increasing the scan rate, which is associated to the enhanced mass transport and electron conduction in the host materials. Moreover, the anodic and cathodic peaks shift to higher and lower potentials at higher and lower scan rates, respectively. This may be due to the effect of electro kinetics on peak shape and peak separation [37]. The major contribution of this redox peak comes from the faradaic

reactions within the active material. The GCD measurements were further studied at various current densities (from 50 – 1 mA cm<sup>-2</sup>) to estimate the charge storage behavior of the electrode materials (**Figure 7.1.14 B**). A maximum areal capacity of 265.3 μAh cm<sup>-2</sup> was achieved from GCD analysis (using equation 1) for synthesized CoMoO<sub>4</sub>@Co(OH)<sub>2</sub>/CT core-shell architecture at a current density of 1 mA cm<sup>-2</sup> (**Figure 7.1.14 C**). This areal capacity was maintained up to 230.6 μAh cm<sup>-2</sup>, even at a higher current density of 10 mA cm<sup>-2</sup>. About 87% of the areal capacity was retained at even 10-fold higher scan rates, suggesting the excellent rate capability of the electrode material. When the current density further increased up to 50-fold, 68% of the capacity has been retained which suggest that the excellent rate capability of the prepared CoMoO<sub>4</sub>@Co(OH)<sub>2</sub>/CT core-shell architecture. Overall, the prepared core-shell structure shows its excellent performance as positive electrode for hybrid supercapacitor.

### 7.3.3. Structural characterization of porous carbon

The schematic annotation of the preparation of porous carbon was shown in **Figure 7.1.15 A**. The lab waste tissue paper was collected from our laboratory and cut into a small pieces. These waste tissue papers were treated with sulfuric acid and kept for hydrothermal reaction. Then collected powder has been activated by KOH activation and followed by carbonization at inert atmosphere which leads to the formation of porous honeycomb-like carbon. **Figure 7.1.15 B-D** shows the corresponding FE-SEM images of the prepared carbon at the different magnification.

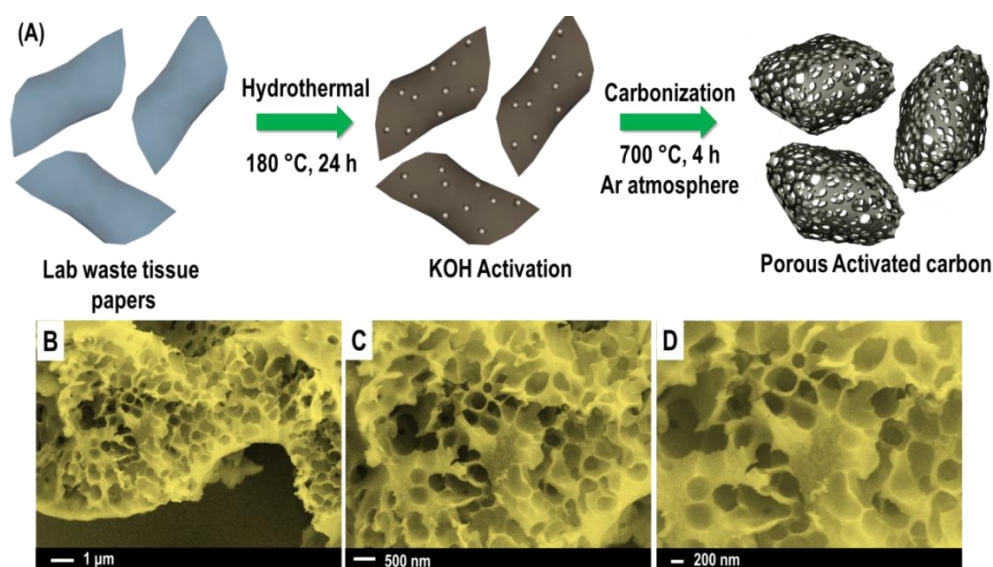


**Figure 7.1.15** Preparation of negative electrode material: Schematic representation of the formation of porous nature (A), FE-SEM images of the prepared lab waste derived activated carbon at different magnifications (B–D).

The morphology shows the formation of honeycomb-like porous carbon is confirmed by the activation process from the laboratory waste tissue papers. These porous structure leads to the high specific surface area which facilitates good ionic transportation during electrochemical reaction. **Figure 7.1.16** show the structural characterization of the prepared carbon material. **Figure 7.1.16A** indicates that the XRD peak show the two broad peaks at  $26^\circ$  and  $43^\circ$  which were attributed to the (002) plane and (001) plane reflection respectively and reveals the presence of amorphous nature of carbon [38, 39]. As shown in **Figure 7.1.16B**, the Raman spectra also substantiate the highly disordered carbon structure. The peak at about  $1354\text{ cm}^{-1}$  suggests that the presence of D band which corresponds to the breathing mode vibration of  $A_{1g}$ , related to

disordered carbon. The peak at  $1591\text{ cm}^{-1}$  corresponds to in-plane stretching vibration mode of  $E_{2g}$  in  $sp^2$  carbons in the prepared activated carbon [40, 41].

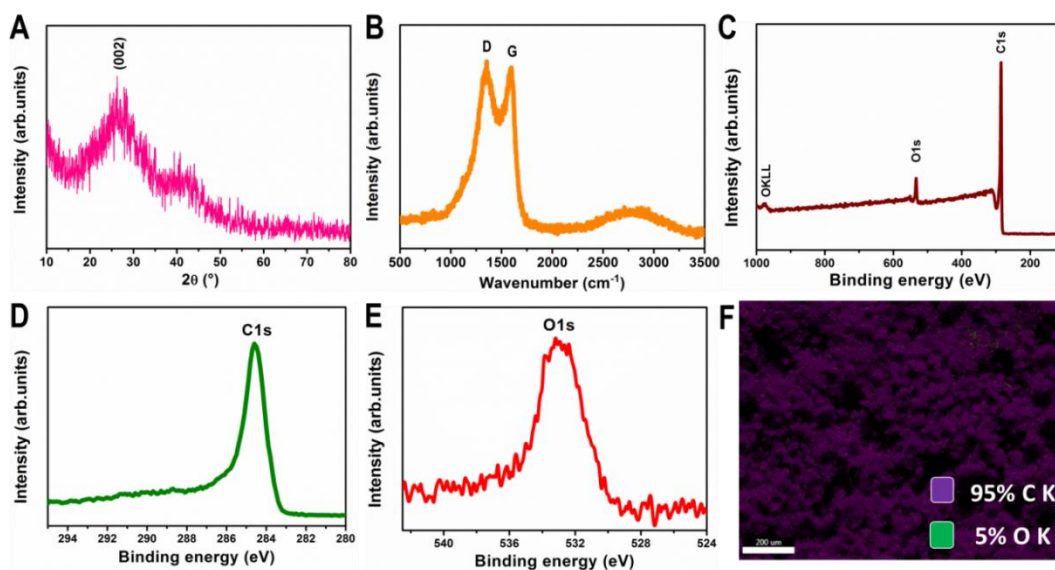


**Figure 7.1.16** XRD pattern (A), Raman spectrum (B) of  $\text{CoMoO}_4@\text{Co}(\text{OH})_2/\text{CT}$ . XPS core-level spectra: Survey spectrum (C), C1s core-level spectrum (D), O1s core-level (E) and elemental mapping (F) of lab waste tissue paper derived activated carbon.

Further, the XPS spectra were performed to characterize the surface functional group of the activated carbon and its survey spectrum shown in **Figure 7.1.16 C**. Besides the core-level spectra of C1s and O1s have shown in **Figure 7.1.16 D and E**. The C1s core-level spectrum holds the broad peak between 284 and 287 eV, which attributes to the presence of graphitic carbon (C-C and C-H), hydroxyl group (C-OH), ether/phenyl carbon (C-O) and carbonyl/quinone groups. The O1s core-level spectrum influenced in the range between 531 and 536 eV, which suggested that the presence of hydroxyl groups (C-OH), carbonyl/quinone groups (C-O) and chemisorbed water molecule on the

surface of the prepared activated carbon [42 – 44]. Moreover, the presence of carbon and oxygen groups were confirmed using the elemental mapping analysis and shown in the **Figure 7.1.16 F**.

### 7.3.4. Structural characterization of porous carbon

In order to use the prepared material as an electrode for hybrid supercapacitor, the electrochemical properties of the prepared porous carbon has been elucidated using cyclic voltammetry and galvanostatic charge discharge analysis and presented in the **Figure 7.1.1** in KOH electrolyte.

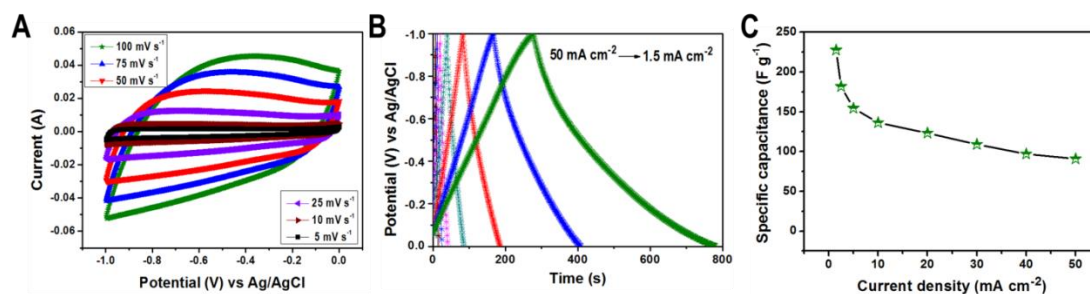


**Figure 7.1.17** Electrochemical performance of the prepared negative porous electrode: Cyclic voltammetry curves at different scan rates (100 to 5 mV s<sup>-1</sup>) (A), Galvanostatic charge-discharge curves at different current densities (50-1.5 mA cm<sup>-2</sup>) (B), specific capacitance with respect to the current densities calculated from the charge-discharge analysis (C) of porous LTAC respectively.

**Figure 7.1.17 A** shows the CV curves of the prepared porous carbon coated on the carbon cloth electrode at the various scan rates (from 5 to 2 to 200 mV s<sup>-1</sup>) in the potential range between -1 V to 0V. When increasing the scan rates from 2 mV s<sup>-1</sup> to 200 mV s<sup>-1</sup>, the rectangular behavior of the CV curve is slightly changed to the fish-shape suggest that the quasi-rectangular behavior of the material. In addition, the CV

curves shows the improved current ranges and excellent EDLC behavior suggest that the prepared lab waste tissue derived activated carbon will be an excellent capacitive electrode material for supercapacitor applications. To support this, the GCD measurement also carried out in the same potential ranges at the different current densities (1.5 to 50 mA cm<sup>-2</sup>), show the symmetric nature of the GCD curves which also ascribed the EDLC nature of the porous carbon. As shown in the **Figure 7.1.17 B**, when increasing the current density, the discharge time was decreased, which may be because the electrolyte ions face time constraints that control their diffusion at the active electrode surface at higher current densities (whereas at lower current densities there is more time available for the electrolyte ions to access the active electrode material). The calculated specific capacitance of the prepared porous carbon is 227 F g<sup>-1</sup> (using equation – 2) at the current density of 1.5 mA cm<sup>-2</sup> (**Figure 7.1.17 C**). This important behavior was ascribed to the excellent diffusion of electrolyte into the electroactive materials due to high porous nature. Overall, the prepared core-shell structure shows its excellent performance as positive electrode for hybrid supercapacitor.

### **7.3.5. Electrochemical characterization of hybrid supercapacitors**

Based on the potential window, the pouch-type hybrid supercapacitor was fabricated using the prepared CoMoO<sub>4</sub>@Co(OH)<sub>2</sub>/CT core-shell structure as positive electrode and honeycomb-like porous activated carbon on carbon cloth as negative electrode which separated by filter paper with KOH electrolyte. Prior to this, based on the specific capacity of the positive core-shell electrode, the mass of the negative carbon

electrode has been balanced in order to achieve the maximum energy density of the hybrid supercapacitor. Initially, the mass balanced electrodes and separator has been wetted with KOH electrolyte for the specified time. Then, the sandwiched device has been inserted into the pouch with the few ml of electrolytes and sealed the device using commercial sealing machine in order to fabricate the flexible device. It also useful to avoid the evaporation of electrolyte ions during electrochemical measurements and prevent from the foreign impurities.

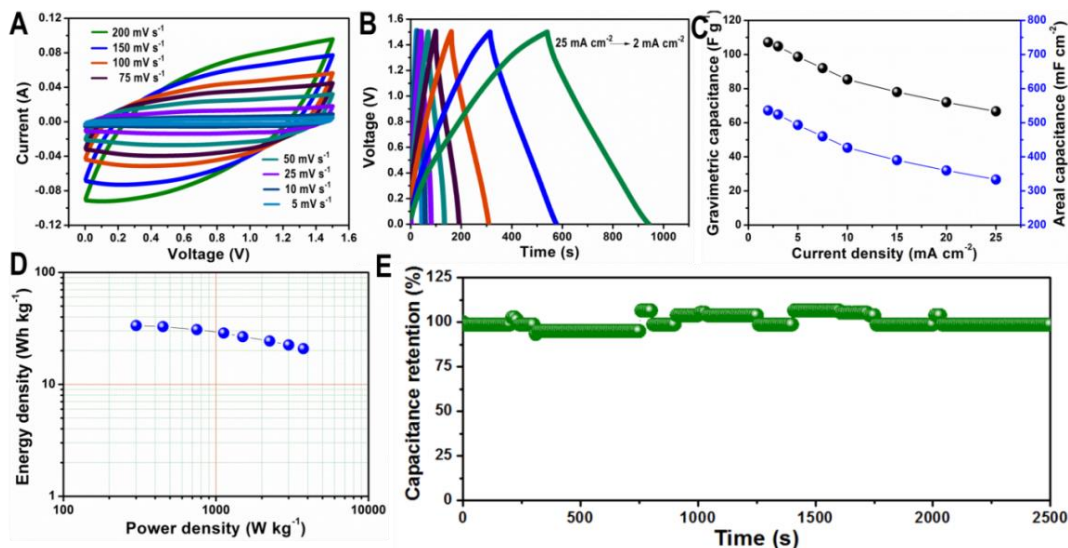


**Figure 7.1.18** Electrochemical performance of the Pouch cell: Cyclic voltammetry curves at different scan rates (200 to 5 mV s<sup>-1</sup>) (A), Galvanostatic charge-discharge curves at different current densities (25-2 mA cm<sup>-2</sup>) (B), specific capacitance with respect to the current densities calculated from the charge-discharge analysis (C) and Ragone plot (D).

**Figure 7.1.18** shows the electrochemical performances of the fabricated hybrid supercapacitors. As shown in **Figure 7.1.18 A**, the fabricated pouch type supercapacitor works up to 1.5V without any deformation in the CV curves at different scan rates (5–

200  $\text{mV s}^{-1}$ ) since the positive electrode can be scanned until 0.5V and negative electrode can be scanned up to -1.0V. The achieved working potential window is higher than that of other asymmetric supercapacitor device, such as  $\text{Co(OH)}_2$  on Ni foam // GO asymmetric supercapacitor [45]. Dissimilar to the sharp redox peak presented in the three-electrode system, the fabricated hybrid supercapacitor shows capacitive behavior with quasi-rectangular CV curves. Also, the shape of the CV curves was maintained well even at the high scan rates, suggesting a good rate capability of the device. To further evaluate the performance of the device, a GCD analysis was performed. **Figure 7.1.18 B** shows the GCD curves at different current densities, measured from 2–25  $\text{mA cm}^{-2}$ . It can be noticed that the fabricated pouch-type hybrid device exhibits nearly linear and symmetric behavior with a quick I-V response, consistent with the CV curves. **Figure 7.1.18 C** shows the areal and mass based specific capacitances with respect to the current densities. The maximum areal capacitance of  $536 \text{ mF cm}^{-2}$  (gravimetric capacitance of  $107.2 \text{ F g}^{-1}$ ) is achieved at the current density of  $2 \text{ mA cm}^{-2}$  which is higher than the previous reports based on hybrid supercapacitors such as  $\text{CoMoO}_4$  vs CNT ( $82 \text{ F g}^{-1}$ ) [46],  $\text{NiMoO}_4\text{-CoMoO}_4\cdot x\text{H}_2\text{O}$  vs activated carbon ( $80 \text{ F g}^{-1}$ ) [47],  $\text{NiMoO}_4$  vs activated carbon ( $96.7 \text{ F g}^{-1}$ ) [48]. By using equations 4 and 5, the energy and power density has been calculated and shown in a Ragone plot in **Figure 7.1.18 D**. The fabricated device stored a maximum areal energy density of  $167.5 \mu\text{Wh cm}^{-2}$  ( $33.5 \text{ Wh kg}^{-1}$ ) at  $2 \text{ mA cm}^{-2}$  and delivered a high power density of  $18750 \mu\text{W cm}^{-2}$  ( $3750 \text{ W kg}^{-1}$ )  $25 \text{ mA cm}^{-2}$ . The energy density decreased from  $167.5 \mu\text{Wh cm}^{-2}$  ( $33.5 \text{ Wh kg}^{-1}$ ) to

104.2  $\mu\text{Wh cm}^{-2}$  (20.83  $\text{Wh kg}^{-1}$ ) while the power density increased from 1,500  $\mu\text{W cm}^{-2}$  (300  $\text{W kg}^{-1}$ ) to 18750  $\mu\text{W cm}^{-2}$  (3750  $\text{W kg}^{-1}$ ) at current densities of 2–10  $\text{mA cm}^{-2}$ . This high energy density of the fabricated pouch-type hybrid device shows better than those of some the recent hybrid supercapacitors such as ZnO@MnO<sub>2</sub> core-shell vs activated carbon (17  $\text{Wh kg}^{-1}$ ) [49], CNT@CoMoO<sub>4</sub>/Ni foam vs rGO (29.4  $\text{Wh kg}^{-1}$ ) [50], ZnCo<sub>2</sub>O<sub>4</sub>@Ni<sub>x</sub>Co<sub>2x</sub>(OH)<sub>6x</sub> // Activated carbon (26.04  $\text{Wh kg}^{-1}$ ) [51], NiCo<sub>2</sub>S<sub>4</sub>//porous carbon (22.8  $\text{Wh kg}^{-1}$ ) [52], carbon Ni@Ni(OH)<sub>2</sub>//Activated carbon (21.8  $\text{Wh kg}^{-1}$ ) [53], Ni<sub>3</sub>Se<sub>2</sub>@conductive textile// activated carbon supercapacitor (32.8  $\text{Wh kg}^{-1}$ ) [54], Co<sub>3</sub>O<sub>4</sub>-Ni foam//Carbon aerogel (17.9  $\text{Wh kg}^{-1}$ ) [55] other asymmetric supercapacitors such as acetylene black decorated NiCo<sub>2</sub>S<sub>4</sub>//Activated carbon hybrid supercapacitor (24.7  $\text{Wh kg}^{-1}$ ) [56], NiCoDH// Activated carbon (25.3  $\text{Wh kg}^{-1}$ ) [57], CoMoO<sub>4</sub> -NiMoO<sub>4</sub>.xH<sub>2</sub>O //Activated carbon (25  $\text{Wh kg}^{-1}$ ) [58]. Also, the fabricated device shows better energy density than that of other symmetric supercapacitors such as NiO-In<sub>2</sub>O<sub>3</sub>-NiF//NiO-In<sub>2</sub>O<sub>3</sub>-NiF (26.24  $\text{Wh kg}^{-1}$ ) [59], Co(OH)<sub>2</sub>/graphene foam//Co(OH)<sub>2</sub>/graphene foam (13.9  $\text{Wh kg}^{-1}$ ) [60]. **Figure 7.1.18 E** shows the cyclic stability study of pouch-type device for 2500 cycles using galvanostatic charge discharge analysis. Even after 2500 cycles, the device shows 98.64% of its initial capacitance suggested the excellent durability of the device. Moreover, this excellent ability of the CoMoO<sub>4</sub>@Co(OH)<sub>2</sub>/CT//Porous carbon hybrid device has remarkably exceeded those previously reported articles. This improved performance of

CoMoO<sub>4</sub>@Co(OH)<sub>2</sub>/CT//Porous carbon hybrid device may be attributed to the synergic effect of the core-shell structure and high surface area of the porous carbon.

In order to display the practical ability of the device, two serially connected pouch-type supercapacitors have the ability to lit-up the four different types of LEDs and shown in **Figure 7.1.19**. As shown in **Figure 7.1.19A-D**, the two supercapacitor devices were able to lighten the red, green, white and blue LEDs respectively. In addition, the flexibility tests have been measured at the different bending conditions and the photographic images were shown in the **Figure 7.1.19E**. CV measurement has been performed at the different bending conditions in both parallel bending and vertical bending to the leads of the device. The area under the CV curves was almost similar at all the bending conditions. However, there is slight loss in the specific capacitance. The calculated specific capacitance at normal condition was 76.1 Fg<sup>-1</sup>. In case of bending at all the conditions, the negligible amount of loss in specific capacitance has been observed (about 0.5 to 0.67 Fg<sup>-1</sup>) suggesting the excellent flexibility of the fabricated device. In addition, the efficiency of the fabricated pouch-type supercapacitor was demonstrated for self-powered application where the commercial small solar-cell panels and LED arrays were integrated with the hybrid supercapacitor.

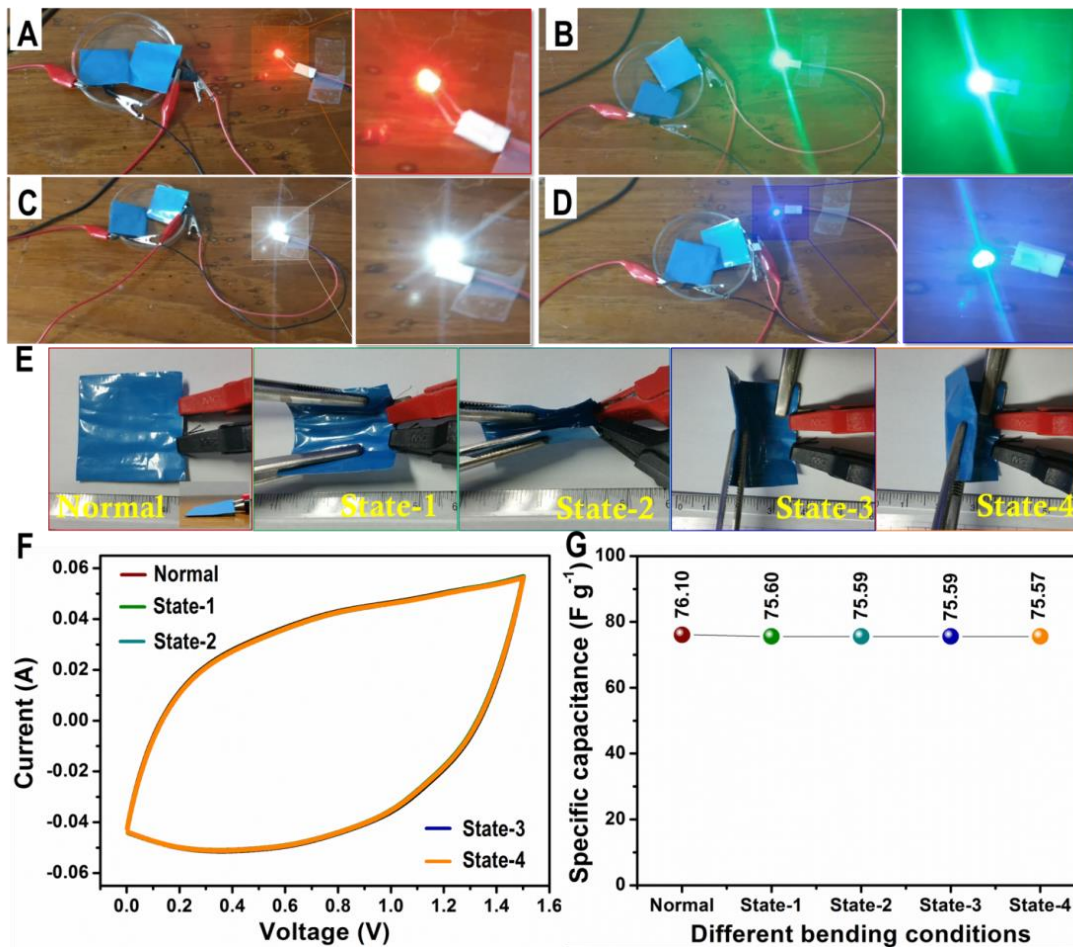


**Figure 7.1.19** Flexibility test of the Pouch cell: Photographic images of the fabricated pouch cell at normal and at different bending conditions (A), Cyclic voltammetry curves for the device at normal and different bending conditions (B), the obtained specific capacitance from the area of the each CV curves at normal and bending conditions (C).

Briefly, two commercial solar-cell devices (connected in series) has been induced using the commercial lamps was integrated with the four serially connected pouch-type hybrid supercapacitors and presented in **Figure 7.1.20**. When the light was ON, the series-wound SCs harvested solar energy and stored the energy in the serially connected pouch-type hybrid supercapacitors maintained at closed position S1 (switch).

Figure 7.1.20 B shows the charging and discharging curve of the serially connected pouch-type hybrid supercapacitors.

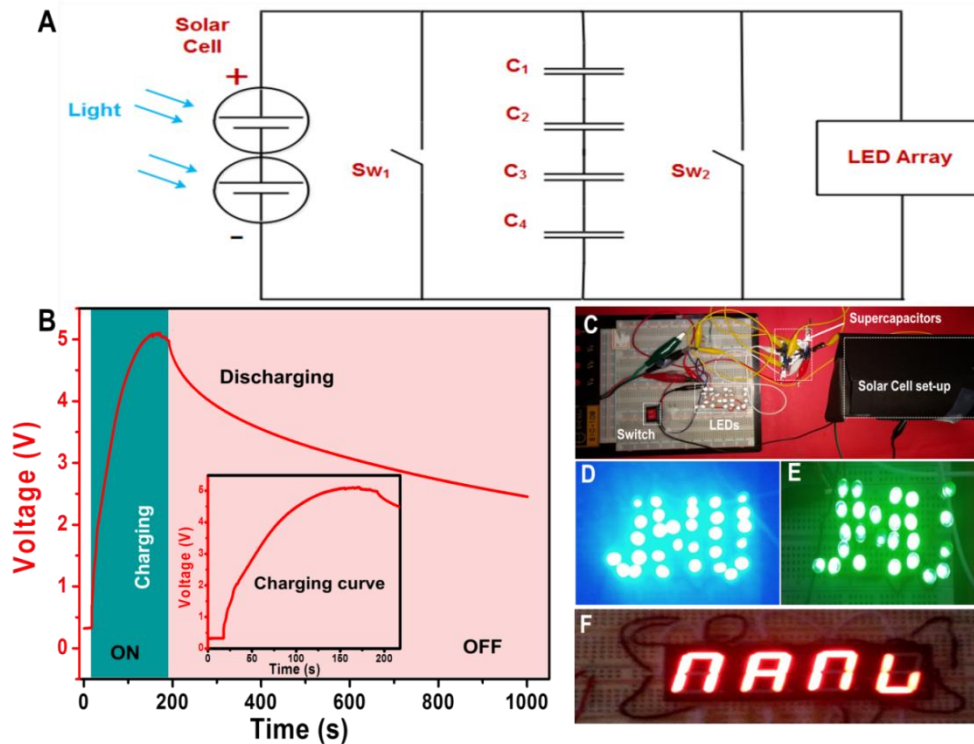


Figure 7.1.20 Self-powered application by solar cell charging: Circuit-diagram (A), charging and self-discharging curve (B), photographic images of self-powered set-up (C), lightening 30 blue LEDs (D), 24 green LEDs (E) and 7-segment display (F) of the two serially connected solar cell, four serially connected fabricated pouch devices.

The four serially connected supercapacitors could be charged to 5V in around 200 s. The overall set-up shown in Figure 7.1.20 C. In order to show self-powered operation, commercial LEDs were connected to the charged supercapacitors, and were illuminated by closing switch S2 and opening switch S1 (the light source was in the OFF condition). The charged supercapacitors could be able to lit-up 40 blue LEDs (Figure

**7.1.20 D**), 30 green LEDs (**Figure 7.1.20 E**) and also capability to lightening the 7-segment display (see supplementary video). This study demonstrated that the fabricated pouch-type supercapacitors could store solar energy produced from solar cells by integration with the commercial small solar panel, which implies their enormous application potential in flexible, wearable and portable electronic devices.

#### **7.4. Conclusions**

In summary, we have successfully fabricated a flexible pouch type hybrid supercapacitor by  $\text{CoMoO}_4@ \text{Co(OH)}_2/\text{CT}$  core-shell structure as positive electrode and porous activated carbon negative electrode. Earlier, core-shell structure prepared via simple electrodeposition method on conductive textile whereas porous activated carbon has been prepared using low-cost lab waste tissue paper by hydrothermal and carbonization methods. Both the electrode materials have been immensely investigated using various techniques. The maximum areal capacity of  $265 \text{ mAhcm}^{-2}$  and specific capacitance of  $227 \text{ Fg}^{-1}$  were achieved for the core-shell structure and porous carbon electrodes respectively. This enhanced output is due to the synergic effect of  $\text{CoMoO}_4$  shell on the walls of the  $\text{Co(OH)}_2/\text{CT}$  core benefits the fast ion transportation for the faradaic reaction which leads to the improved capacity, whereas the porous nature of laboratory waste tissue paper derived activated carbon benefits for the high specific surface area which facilitates the high specific capacitance. Further, the excellent electrochemical performances of pouch-type hybrid supercapacitor have been achieved

in terms of specific capacitance ( $107.2 \text{ Fg}^{-1}$ ), energy density ( $167.5 \text{ } \mu\text{Wh cm}^{-2}$ ) at  $2 \text{ mA cm}^{-2}$ , high power density ( $18750 \text{ } \mu\text{W cm}^{-2}$ ) at  $25 \text{ mA cm}^{-2}$ , cyclic stability (98.64% retention) even after long cycles and flexibility at different bending conditions (no loss in the value of specific capacitance). Moreover, two serially connected pouch-type supercapacitor devices could be able to lit-up four different types of LEDs. The four serially connected supercapacitor devices have an efficient to charge by two serially connected commercial solar panels and demonstrated the lit-up bunch of green and blue LEDs and 7-segment display for self-powered applications. Overall, the fabricated flexible, pouch-type supercapacitor device using facile and low-cost approach.

## 7.5. References

1. P. Simon, Y. Gogotsi, *Nat. Mater.* **2008**, 7, 845.
2. L. Schlapbach, A. Züttel, *Nature*. **2001**, 414, 353.
3. G.Q. Zhang, H.B. Wu, H.E. Hoster, M.B. Chan-Park, X.W. Lou, *Energy Environ. Sci.* **2012**, 5, 9453.
4. J. Liang, X.-Y. Yu, H. Zhou, H.B. Wu, S. Ding, X.W. Lou, *Angew. Chem. Int. Ed.* **2014**, 53, 12803.
5. M.F. El-Kady, V. Strong, S. Dubin, R.B. Kaner, *Science* **2012**, 335, 1326.
6. G.K. Veerasubramani, K. Krishnamoorthy, P. Pazhamalai, S.J. Kim, *Carbon* **2016**, 105, 638-648.

7. Z. Lei, J. Zhang, L.L. Zhang, N.A. Kumar, X.S. Zhao, *Energy Environ. Sci.* **2016**, 9, 1891.
8. S.W. Lee, N. Yabuuchi, B.M. Gallant, S. Chen, B.-S. Kim, P.T. Hammond, Y. Shao Horn, *Nat. Nano* **2010**, 5, 531.
9. F. Zhang, T. Zhang, X. Yang, L. Zhang, K. Leng, Y. Huang, Y. Chen, *Energy Environ. Sci.*, **2013**, 6, 1623.
10. D. P. Dubal, O. Ayyad, V. Ruiz, P. Gómez-Romero, *Chem. Soc. Rev.*, **2015**, 44, 1777.
11. Y. Zhao, L. Hu, S. Zhao, L. Wu, *Adv. Funct. Mater.*, **2016**, 26, 4085.
12. D. Cai, H. Huang, D. Wang, B. Liu, L. Wang, Y. Liu, Q. Li, T. Wang, *ACS Appl. Mater. Interfaces*, **2014**, 6 (18), 15905.
13. Y. Zhang, B. Wang, F. Liu, J. Cheng, Xi-wen. Zhang, L. Zhang, *Nano Energy* 27 (2016) 627–637.
14. H. Chen, X. Q. Qi, M. Kuang, F. Dong, Y. X. Zhang, *Electrochim Acta* **2016**, 212, 671.
15. Y. Zhao, Y. Meng, P. Jiang, *J. Power Sources* **2014**, 259, 219.
16. N. Jabeen, Q. Xia, M. Yang, H. Xia, *ACS Appl. Mater. Interfaces*, **2016**, 8(9) 6093.
17. X.X. Qing, S.Q. Liu, K.L. Huang, K.Z. Lv, Y.P. Yang, Z.G. Lu, D. Fang, X.X. Liang, *Electrochim. Acta* **2011**, 56, 4985.
18. X.H. Xia, J.P. Tu, Y.J. Mai, X.L. Wang, C.D. Gu, X.B. Zhao, *J. Mater. Chem.* **2011**, 21, 9319.

19. C. Zhou, Y. Zhang, Y. Li, J. Liu, *Nano letters* **2013**, 13, 2078.
20. Y. Zhang, L. Li, H. Su, W. Huang, X. Dong, *J. Mater. Chem. A*, **2015**, 3, 43.
21. G.K. Veerasubramani, K. Krishnamoorthy, R. Sivaprakasam, S.J. Kim, *Mater Chem Phys*, **2014**, 147, 836-842.
22. L.Q. Mai, F. Yang, Y.L. Zhao, X. Xu, L. Xu, Y.Z. Luo, *Nat. Commun.* **2011**, 2, 381.
23. G.K. Veerasubramani, K. Krishnamoorthy, R. Sivaprakasam, S.J. Kim, *Int J Hydrogen Energy*, **2014**, 39, 5186.
24. Z. Gu, R. Wang, H. Nan, B. Geng, X. Zhang, *J. Mater. Chem. A*, **2015**, 3, 14578.
25. J. Wang, X. Zhang, Q. Wei, H. Lv, Y. Tian, Z. Tong, X. Liu, J. Hao, H. Qu, Ji. Zhao, Y. Li, L. Mai. *Nano Energy* **2016**, 19, 222–233.
26. Jeffrey R. S. Brownson, C. Lévy-Clément, *Phys. Stat. Sol. (b)* **2008**, 245, 1785–1791.
27. G.K. Veerasubramani, K. Krishnamoorthy, S.J. Kim, *J. Power Sources*, **2016**, 306, 378.
28. X. Yu, B. Lu, Z. Xu, *Adv Mater.* **2014**, 26, 1044.
29. S.T. Senthilkumar, R. Kalai Selvan, M. Ulaganathan, J.S. Melo, *Eletrochim acta.* **2014**, 115, 518.
30. D. Puthusseri, V. Aravindan, B. Anothumakkool, S. Kurungot, S. Madhavi, S. Ogale. *Small.* **2014**, 10(21), 4395-4402.
31. X. Liu, R. Yi, N. Zhang, R. Shi, X. Li, G. Qiu, *Chemistry Asian J*, **2008**, 3, 732.

32. O. Bøckman, T. Østvold, G. A. Voyiatzis, G. N. Papatheodorou, *Hydrometallurgy*, **2000**, 55, 93.
33. J. Yang, H. Liu, W. N. Martens, R. L. Frost, *J. Phys. Chem. C*, **2010**, 114, 111.
34. D. Ghosh, S. Giri and C. K. Das, *Nanoscale*, **2013**, 5, 10428.
35. X. F. Xia, W. Lei, Q. L. Hao, W. J. Wang and X. Wang, *Electrochim. Acta*, **2013**, 13, 253.
36. K. Xu, J. Chao, W. Li, Q. Liu, Z. Wang, X. Liu, R. Zou, J. Hu, *RSC Adv.*, **2014**, 4, 34307.
37. D. Guo, H. Zhang, X. Yu, M. Zhang, P. Zhang, Q. Li, T. Wang, *J. Mater. Chem. A*, **2013**, 1, 7247.
38. V. Subramanian, C. Luo, A.M. Stephan, K. S. Nahm, S. Thomas, B. Wei, *J. Phys. Chem. C* **2007**, 111, 7527.
39. Y. Lv, L. Gan, M. Liu, W. Xiong, Z. Xu, D. Zhu, D. S. Wright, *J. Power Sources* **2012**, 209, 152.
40. S. T. Senthilkumar, R. Kalai Selvan, J. S. Melo, C. Sanjeeviraja, *ACS Appl. Mater. Interfaces* **2013**, 5, 10541–10550.
41. A. Janes, H. Kurig, E. Lust, E. *Carbon* **2007**, 45, 1226.
42. A. M. Puziy, O. I. Podubnaya, R. P. Socha, J. Gurgul, M. Wisniewski, M. *Carbon* **2008**, 46, 2113.
43. C. T. Hsieh, H. Teng, *Carbon* **2002**, 40, 667.
44. H. Valdes, M. S. Polo, J. R. Utrilla, C. A. Zaror, *Langmuir* **2002**, 18, 2111.

45. R. R. Salunkhe, B. P. Bastakoti, C.T. Hsu, N. Suzuki, J. H. Kim, S. X. Dou, C. C. Hu, Y. Yamauchi, *Chem. Eur. J.* **2014**, 20, 3084.
46. R. Ramkumar, M. Minakshi, *Dalton Trans.* **2015**, 44, 6158.
47. B. Senthilkumar, D. Meyrick, Y.-S. Lee, R. K. Selvan, *RSC Adv.*, **2013**, 3, 16542.
48. M.-C. Liu, L. Kang, L.-B. Kong, C. Lu, X.-J. Ma, X.-M. Li and Y.-C. Luo, *RSC Adv.*, **2013**, 3, 6472.
49. A.V. Radhamani, K. M. Shareef, and M. S. Ramachandra Rao, *ACS Appl. Mater. Interfaces*, **2016**, 8(44), 30531.
50. G. K. Veerasubramani, M.S.P. Sudhakaran, N.R. Alluri, K. Krishnamoorthy, Y. S. Mok, S. J. Kim, *J. Mater. Chem. A*, **2016**, 4, 12571.
51. W. Fu, Y. Wang, W. Han, Z. Zhang, H. Zha and E. Xie, *J. Mater. Chem. A*, **2016**, 4, 173.
52. W. Kong, C. Lu, W. Zhang, J. Pu and Z. Wang, *J. Mater. Chem. A*, **2015**, 3, 12452.
53. Y.-Z. Su, K. Xiao, N. Li, Z.-Q. Liu and S.-Z. Qiao, *J. Mater. Chem. A*, **2014**, 2, 13845.
54. G. Nagaraju, S. M. Cha, S. Chandra Sekhar, J. S. Yu, *Adv Energy Mater*, **2016**, 1601362, 1.
55. W. Liu, C. Li, M. Zhu and X. He, *J. Power Sources*, **2015**, 282, 179.
56. Y. Zhu, X. Ji, Z. Wu and Y. Liu, *Electrochim. Acta*, **2015**, 186, 562.
57. M. Jing, H. Hou, C. E. Banks, Y. Yang, Y. Zhang and X. Ji, *ACS Appl. Mater. Interfaces*, **2015**, 7(41), 22741.

58. M. C. Liu, L. B. Kong, C. Lu, X. J. Ma, X. M. Li, Y. C. Luo and L. Kang, *J. Mater. Chem. A*, **2013**, 1, 1380.
59. N. Padmanathan, H. Shao, D. McNulty, Colm O'Dwyer, K. M. Razeed, *J. Mater. Chem. A*, **2016**, 4, 4820.
60. U.M. Patil, S. C. Lee, J.S. Sohn, S.B. Kulkarni, K.V. Gurav, J.H. Kim, J. H. Kim, S. Lee, S. C. Jun, *Electrochim. Acta* **2014**, 129, 334.

## 7.6. Summary

The current challenges in the usage of liquid electrolyte in energy storage devices are closely correlated with the flexibility and portability of the devices. This work is focused to fabricate the flexible and portable supercapacitors in liquid medium. For this, we have prepared novel core-shell on conductive textile as positive electrode and lab waste tissue paper derived activated carbon as negative electrode. The fabricated pouch-type hybrid supercapacitor shows good flexibility and exhibits excellent electrochemical performances in terms of specific capacitance, energy density and cyclic stability. The obtained output has been compared with the recent literatures. In addition, the fabricated supercapacitor integrated with the solar cell and demonstrated its efficiency to power up various LEDs and 7-segment display for self-powered systems. Overall, we trust that the fabricated pouch-type hybrid supercapacitor presents a new way to create liquid electrolyte based hybrid electrode architecture for flexible and portable electronics.

## CHAPTER – 8

### Summary and suggestions for the future work

#### 8.1. Summary

This chapter describes the general conclusions of overall thesis and future directions of this work. This thesis mainly focuses on the improvement of hybrid supercapacitors by improving the battery-type transition metal oxide. For this, we focused on the synthesis of metal molybdates and investigated to improve the electrochemical performances by possible ways.

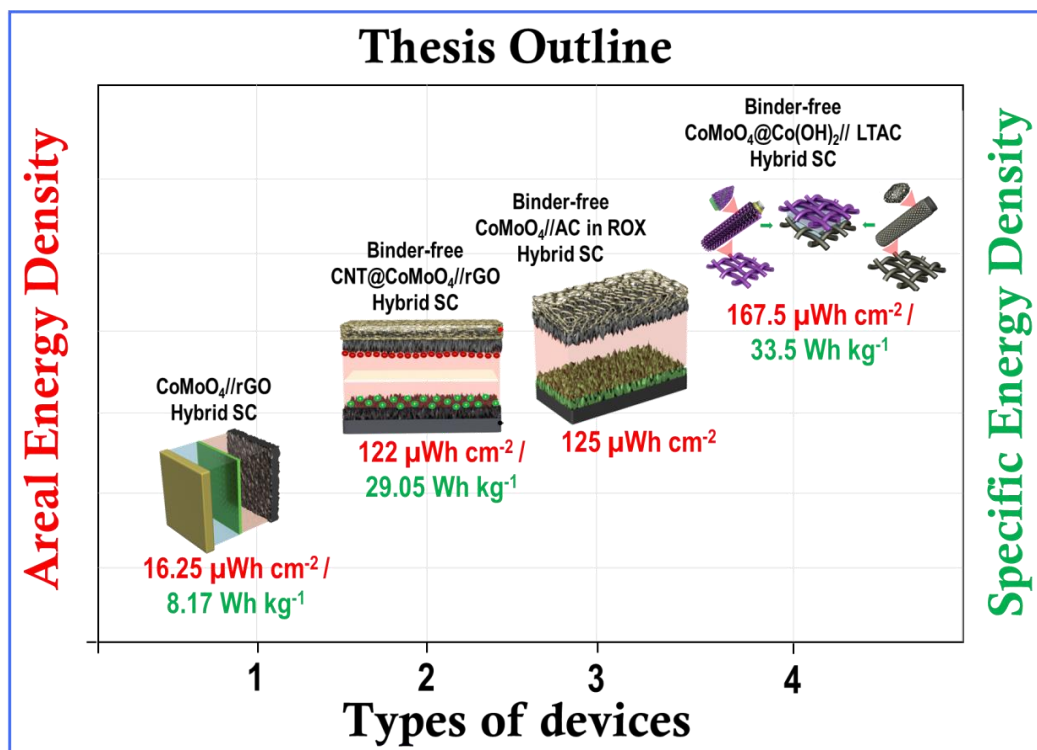


Figure 8.1.1 Overall device-outlook of this thesis

- ✚ First **two Chapters** described about the introduction about the ECs and materials/techniques used in this research work. The nanostructured CoMoO<sub>4</sub> and MnMoO<sub>4</sub> has been prepared by sonochemical technique and investigated its structural and electrochemical properties in **Chapter-3**. The achieved specific capacity for CoMoO<sub>4</sub> nanostructures (25.89 mAh g<sup>-1</sup>) is quite high compared to MnMoO<sub>4</sub> (23 mAh g<sup>-1</sup>) due its nano-sized plate like structure of CoMoO<sub>4</sub>
- ✚ Based on this, in order to further improve the performance of CoMoO<sub>4</sub>, we prepared composite of sonochemically prepared CoMoO<sub>4</sub> with conducting polymer (polyaniline) in first part of **Chapter-4**. The achieved specific capacity of CoMoO<sub>4</sub>/PANI is higher than the bare CoMoO<sub>4</sub>. However, the stability of this composite is very less due to use of acid electrolyte etches CoMoO<sub>4</sub> nanostructures during continuous cycles since PANI is electrochemically active in acid electrolyte, but metals oxides not much. The second part of **Chapter-4** focuses on the fabrication of hybrid supercapacitor using sonochemically prepared CoMoO<sub>4</sub> as positive faradaic electrode and reduced graphene oxide as negative capacitive electrode. The achieved specific capacitance of the device is 26.16 F g<sup>-1</sup> (using GCD analysis) and 27.7 F g<sup>-1</sup> (using CV analysis). The maximum achieved gravimetric energy density is 8.17 Wh kg<sup>-1</sup> at a power density of 187.5 W kg<sup>-1</sup>
- ✚ In order to enhance the performance of CoMoO<sub>4</sub> faradaic electrode, the binder-free CoMoO<sub>4</sub> on Ni foam was prepared and presented in **Chapter-5**. The achieved areal capacity of the CoMoO<sub>4</sub>/Ni foam was 227 μAh cm<sup>-2</sup> (206 mAh g<sup>-1</sup>) which is nearly 8

times higher than the sonochemically prepared  $\text{CoMoO}_4$  with binder and conductive agent. In order to further improve the performance of binder-free electrode, we used a novel strategy, which is the addition of redox additive into the electrolyte. The addition of 0.02M  $\text{K}_3\text{Fe}(\text{CN})_6$  as redox additive into electrolyte makes the improvement in areal capacity about 2.5 times higher than pristine electrolyte. The achieved areal capacity of  $\text{CoMoO}_4/\text{Ni}$  foam with redox additive was  $603 \mu\text{Ah cm}^{-2}$ . Further, the fabricated  $\text{CoMoO}_4/\text{Ni}$  foam // activated carbon hybrid supercapacitor exhibited an areal energy density of  $125 \mu\text{Wh cm}^{-2}$  at a power density of  $1507 \mu\text{W cm}^{-2}$

✚ **Chapter-6** presented a novel sustainable approach to synthesize CNT deposited  $\text{CoMoO}_4/\text{Ni}$  foam without  $\text{CO}_2$  emission. Dry reforming reaction of hydrocarbon (mixture of propane and  $\text{CO}_2$ ) is one which is used to produce syngas ( $\text{CO}+\text{H}_2$ ). The main obstacle of this reaction is the deposition of carbon over the catalyst which can be removed as  $\text{CO}_2$  gas. In this chapter, we have utilized  $\text{CoMoO}_4/\text{Ni}$  foam as catalyst for dry reforming reaction. After reaction, the carbon (in the form of CNT) deposited catalyst have been immensely investigated in both structurally and electrochemically. The achieved areal capacity of  $\text{CNT}@\text{CoMoO}_4/\text{Ni}$  foam was  $163 \text{ Ah cm}^{-2}$  (after DRR) which is 22 times higher than bare  $\text{CoMoO}_4/\text{Ni}$  foam (temperature treated). The fabricated CNT deposited  $\text{CoMoO}_4/\text{Ni}$  foam//rGO hybrid supercapacitor device exhibited an areal energy density of about  $122 \mu\text{Wh cm}^{-2}$  ( $29.04 \text{ Wh kg}^{-1}$ ). This study suggested that the utilization of waste carbon deposited

catalyst can be used as an efficient electrode material for supercapacitor applications instead CO<sub>2</sub> emission

✚ The flexible hybrid supercapacitor device was proposed in **Chapter-7**. In this chapter both faradaic electrode and capacitive electrode have been prepared to fabricate hybrid supercapacitor. CoMoO<sub>4</sub>@Co(OH)<sub>2</sub> has been electrochemically prepared on conductive textile to fabricate flexible electrode. The achieved areal capacity of CoMoO<sub>4</sub>@Co(OH)<sub>2</sub>/CT electrode is 265 μAh cm<sup>-2</sup>. Whereas, the honeycomb like porous carbon as negative electrode is prepared by lab waste tissue paper for the first time using hydrothermal method followed by carbonization reaction. The achieved specific capacitance was 227 F g<sup>-1</sup> which is due to the high specific surface area (1920 m<sup>2</sup> g<sup>-1</sup>). The pouch type hybrid supercapacitor has been fabricated using these prepared electrodes in liquid KOH electrolyte. The achieved capacitance of the fabricated device was 107 F g<sup>-1</sup>. The flexibility test has been done under different bending conditions and measured CV analysis. There was no loss specific capacitance has been observed even at both parallel and vertical bending suggest that excellent flexibility of the device. The achieved areal energy density was 167.5 μWh cm<sup>-2</sup> (33.5 Wh kg<sup>-1</sup>). Moreover, the serially connected devices have the capability of lit up different types of LEDs. In addition, we have demonstrated that the integration of pouch type supercapacitor was integrated with commercial solar cell and could be able to charge up from the charged solar cell (from commercial lamp) to fabricated supercapacitor. The charged device from solar cell

could be able to lit-up 30 blue LEDs, 25 green LEDs and 7-segment display which suggest that the fabricated flexible hybrid supercapacitor is a potential candidate for self-powered applications

Overall, it is identified that the cobalt molybdate ( $\text{CoMoO}_4$ ) is most suitable electrode for the fabrication of flexible hybrid supercapacitors by binder-less approach. Crystal structure, calcination temperature, specific surface area, particle size, carbon content, Co:Mo ratio and mesoporous behavior of the synthesized material influenced the electrochemical properties of the individual electrodes as well as the fabricated devices. The kinetics of the redox reaction and charge transfer reactions mainly depends upon the metal cations and the electrolytes. The charge-storage capability of a hybrid supercapacitor mainly depends on both the material and the structure of electrode. An ideal structure of an electrode material usually has a high surface-to-volume ratio and a balance between the material bulk property and the ionic diffusing distance. Such electrode enables fast kinetics and large-area contacts with the electrolytes. Additionally, the prepared  $\text{CoMoO}_4$  based electrode can provide more electro-active sites for faradaic energy storage, resulting in a high specific capacity even at high current density. Similarly, the diffusion controlled redox reaction of the metal cations in aqueous alkali electrolytes is the main advantage to achieve high capacity and reversibility. The combination of different faradaic positive and capacitive negative electrodes (hybrid) with wide working potential window enhanced the energy density of the supercapacitor.

## 8.2. Suggestions for the future work

It is renowned that the fabrication of flexible hybrid supercapacitor via ecofriendly approach towards self-powered systems. Some more fundamental research developments and modifications are expected to understand the preparation of carbon deposited catalyst for flexible electrode via dry reforming reaction and integration of the flexible supercapacitors with other energy harvesting techniques in future works. As following, the recommendation for the future work and the perspective directions for the development of hybrid supercapacitors are discussed.

- ✚ To enhance the electrochemical properties of hybrid supercapacitors by tuning the shape, size and morphology of the electrode material could be employed. The suitable flexible substrate should be hired to sustain high temperature dry reforming reaction in order to fabricate carbon deposited flexible electrode for hybrid supercapacitors instead CO<sub>2</sub> emission. In order to further improve the energy density of hybrid supercapacitor, new types of redox additive with stable electrochemical window will receive much interest
- ✚ To employ the self-powered systems, the hybrid supercapacitor could be integrated with energy harvesting technique, especially nanogenerator (piezoelectric nanogenerator and tribo electric nanogenerator) with suitable electrode and device structure The appropriate porous piezoelectric separator could be prepared for integrating with the high energy density supercapacitors in order to make high performance self-charging supercapacitor device

## APPENDIX A: List of Publications

1. **Ganesh Kumar Veerasubramani**, M.S.P. Sudhakaran, Nagamalleswara Rao Alluri, Karthikeyan Krishnamoorthy, Young Sun Mok, Sang Jae. Kim, “Effective utilization of an idle carbon deposited catalyst towards energy storage application, **Journal of Materials Chemistry A**, 4, 2016, 12571-12582.
2. **Ganesh Kumar Veerasubramani**, Karthikeyan Krishnamoorthy, Parthiban Pazhamalai, Sang Jae. Kim, High performance solid state flexible cable type supercapacitors using redox mediated polymer gel electrolyte, **Carbon**, 105, 2016, 638-648.
3. Karthikeyan Krishnamoorthy, Parthiban Pazhamalai, **Ganesh Kumar Veerasubramani**, Sang Jae. Kim, Mechanically delaminated few layered MoS<sub>2</sub> nanosheets based high performance wire type solid-state symmetric supercapacitors, **Journal of Power Sources** 321, 2016, 112-119.
4. Tae Hyun Kim, Ananthakumar Ramadoss, Balasubramaniam Saravanakumar, **Ganesh Kumar Veerasubramani**, Sang Jae. Kim, Synthesis and characterization of NiCo<sub>2</sub>O<sub>4</sub> nanoplates as efficient electrode materials for electrochemical supercapacitors, **Applied Surface Science**, 370, 2016, 452-458.
5. **Ganesh Kumar Veerasubramani**, Karthikeyan Krishnamoorthy, S. Radhakrishnan, N-J, Kim, Sang Jae. Kim, In-situ chemical oxidative polymerization of aniline monomer in the presence of cobalt molybdate for supercapacitor applications, **Journal of Industrial and Engineering Chemistry**, 36, 2016, 163-168.

6. Karthikeyan Krishnamoorthy, **Ganesh Kumar Veerasubramani**, P. Pazhamalai, Sang Jae. Kim, Designing two dimensional nanoarchitected MoS<sub>2</sub> sheets grown on Mo foil as a binder free electrode for supercapacitors, **Electrochimica Acta** 190, 2016, 305-312.
7. **Ganesh Kumar Veerasubramani**, Karthikeyan Krishnamoorthy, Sang Jae. Kim, Improved electrochemical performances of binder-free CoMoO<sub>4</sub> nanoplate arrays@ Ni foam electrode using redox additive electrolyte, **Journal of Power Sources**, 306, 2016, 378-386.
8. Karthikeyan Krishnamoorthy, **Ganesh Kumar Veerasubramani**, Sang Jae. Kim, Hydrothermal synthesis, characterization and electrochemical properties of cobalt sulfide nanoparticles, **Materials Science in Semiconductor Processing** 40, 2015, 781-786.
9. Karthikeyan Krishnamoorthy, **Ganesh Kumar Veerasubramani**, Sang Jae. Kim, Gram Scale Preparation, Characterization and Electrochemical Properties of MoO<sub>3</sub> Nanoplates, **Science of Advanced Materials** 7 (7), 2015, 1247-1252.
10. Karthikeyan Krishnamoorthy, **Ganesh Kumar Veerasubramani**, S. Radhakrishnan, Sang Jae. Kim, Preparation of Copper Sulfide Nanoparticles by Sonochemical Method and Study on Their Electrochemical Properties, **Journal of nanoscience and nanotechnology** 15 (6), 2015, 4409-4413.

11. **Ganesh Kumar Veerasubramani**, Karthikeyan Krishnamoorthy, Sang Jae. Kim, Electrochemical performance of an asymmetric supercapacitor based on graphene and cobalt molybdate electrodes, **RSC Advances** 5 (21), 2015, 16319-16327.
12. Karthikeyan Krishnamoorthy, **Ganesh Kumar Veerasubramani**, Sang Jae. Kim, One-pot hydrothermal synthesis, characterization and electrochemical properties of CuS nanoparticles towards supercapacitor application, **Materials Research Express** 1(3), 2014, 035006.
13. **Ganesh Kumar Veerasubramani**, Karthikeyan Krishnamoorthy, S. Radhakrishnan, Sang Jae. Kim, Sonochemical synthesis, characterization, and electrochemical properties of MnMoO<sub>4</sub> nanorods for supercapacitor applications, **Materials Chemistry and Physics** 147 (3), 2014, 836-842.
14. Karthikeyan Krishnamoorthy, **Ganesh Kumar Veerasubramani**, S. Radhakrishnan, Sang Jae. Kim, One pot hydrothermal growth of hierarchical nanostructured Ni<sub>3</sub>S<sub>2</sub> on Ni foam for supercapacitor application, **Chemical Engineering Journal** 251, 2014, 116-122.
15. **Ganesh Kumar Veerasubramani**, Karthikeyan Krishnamoorthy, S. Radhakrishnan, N-J, Kim, S Sang Jae. Kim, Synthesis, characterization, and electrochemical properties of CoMoO<sub>4</sub> nanostructures, **International Journal of Hydrogen Energy** 39 (10), 2014, 5186-5193.

16. Karthikeyan Krishnamoorthy, **Ganesh Kumar Veerasubramani**, S. Radhakrishnan, Sang Jae. Kim, Supercapacitive properties of hydrothermally synthesized sphere like MoS<sub>2</sub> nanostructures, **Materials Research Bulletin** 50, 2014, 499-502.

#### **List of submitted papers**

1. **Ganesh Kumar Veerasubramani**, Arunkumar Chandrasekhar, Sudhakaran MSP, Young Sun Mok, Sang Jae Kim, Flexible Pouch-type Hybrid Supercapacitor Based on Binder-less Core-Shell Nanostructures Congregated with Honeycomb-like Porous Carbon – **Submitted to journal**
2. Tae Hyun Kim, **Ganesh Kumar Veerasubramani**, Sang Jae Kim, Synthesis of binder-less NiCo<sub>2</sub>O<sub>4</sub> porous nanoflowers for supercapacitor application – **Submitted to journal**

#### **APPENDIX-B: Conference Presentations**

1. **Ganesh Kumar Veerasubramani**, Arunkumar Chandrasekhar, Sudhakaran MSP, Young Sun Mok, Sang Jae Kim, “Flexible Pouch-type Hybrid Supercapacitor”, Materials Challenges in Alternative and Renewable Energy – MCARE2017, Feb 20-24 2017, Jeju, Republic of Korea – To be presented (**POSTER**)
2. **Ganesh Kumar Veerasubramani**, Sang Jae. Kim, “Realizing an idle-to-energy material for green environment”, 4<sup>th</sup> International Conference on Electronic

- Materials and Nanotechnology for Green Environment – **ENGE 2016**, Nov 6-9 2016, Jeju, Republic of Korea. **(POSTER). Received Poster Award**
3. K. Krishnamoorthy, P. Pazhamalai, **Ganesh Kumar Veerasubramani**, Sang Jae. Kim, High performance wire-type solid state symmetric supercapacitors using mechanically delaminated few layered MoS<sub>2</sub> nanosheets, 4<sup>th</sup> International Conference on Electronic Materials and Nanotechnology for Green Environment – **ENGE 2016**, Nov 6-9 2016, Jeju, Republic of Korea. **(POSTER)**
  4. **Ganesh Kumar Veerasubramani**, M.S.P. Sudhakaran, Y.S. Mok, Sang Jae. Kim, “Efficient utilization of futile catalyst for energy storage applications”, International Union of Materials research Societies – International Conference of Electronic Materials (July 4-8, 2016), **IUMRS-ICEM 2016**, Suntec, Singapore. **(ORAL)**
  5. **Ganesh Kumar Veerasubramani**, K. Krishnamoorthy, Sang Jae. Kim, “Enhanced electrochemical performance of binder-free electrode via redox additive electrolyte”, International Union of Materials research Societies – International Conference of Electronic Materials (July 4-8, 2016), **IUMRS-ICEM 2016**, Suntec, Singapore. **(POSTER)**
  6. **Ganesh Kumar Veerasubramani**, K. Krishnamoorthy, Sang Jae. Kim, “Electrochemical performances of wire type symmetric supercapacitors”, 14<sup>th</sup> International Union of Materials research Societies – International Conference of Advanced Materials (Oct 25-29, 2015), **IUMRS-ICAM 2015**, Jeju, Republic of Korea. **(ORAL)**

7. **Ganesh Kumar Veerasubramani**, K. Krishnamoorthy, Sang Jae. Kim, “Fabrication and electrochemical performances of Wire type graphene based symmetric supercapacitors”, The 3<sup>rd</sup> International Conference on Advanced Electromaterials (Nov 17-20, 2015), **ICAE 2015**, Jeju, Republic of Korea. **(ORAL)**
8. **Ganesh Kumar Veerasubramani**, K. Krishnamoorthy, S. Radhakrishnan, Sang Jae. Kim, “Fabricaton of asymmetric supercapacitor based on CoMoO<sub>4</sub> as positive electrode and rGO as negative electrodes”. Asian Conference on Nanoscience & Nanotechnology (Oct 26-29, 2014), **ASIA NANO 2014**, Jeju, Republic of Korea. **(POSTER)**
9. K. Krishnamoorthy, **Ganesh Kumar Veerasubramani**, Sang Jae. Kim, “Graphene oxide based nanopaint for multifunctional applications”, Asian Conference on Nanoscience & Nanotechnology (Oct 26-29, 2014), **ASIA NANO 2014**, Jeju, Republic of Korea. **(ORAL)**

## Declaration

I, **Ganesh Kumar Veerasubramani**, hereby declare that the thesis entitled “**A Study on the Synthesis and Electrochemical Properties of Nanostructured Materials towards High Energy Density Hybrid Supercapacitors**”, submitted to the Jeju National University, in partial fulfillment of the requirements for the award of the **Degree of Doctor of Philosophy in Department of Mechatronics Engineering** is a record of original and independent research work done and published by me during the period March 2013 to February 2017 under the supervision and guidance of **Prof. Sang Jae Kim**, Department of Mechatronics Engineering, Jeju National University. This thesis solely based on our publication in reputed journals, and it has not been formed for the award of any other Degree / Diploma / Associateship / Fellowship to any candidate of any University.

**Ganesh Kumar Veerasubramani**



